

New Routes to Inorganic Nanostructure Materials

A thesis submitted to the University of Manchester for
the degree of Doctor of Philosophy in the Faculty of
Science and Engineering

2018

Mundher Al-Shakban

School of Materials, The University of Manchester, Oxford Road

Manchester, M13 9PL

Table of contents

List of Figures	8
List of Tables.....	16
Abstract	18
Declaration	20
Copyright Statement	20
Acknowledgement.....	21
Abbreviations	22
Chapter 1 Introduction	25
1.1 Semiconductor materials	25
1.2 Metal sulfide compounds	26
1.3 Quantum confinement effect.....	27
1.4 Structure properties of semiconductors.....	29
1.4.1 Cubic crystal structure.....	29
1.4.2 Structure of face-centred cubic lattice.....	31
1.5 Electrical properties of semiconductors	34
1.6 Optical properties of semiconductors.....	35
1.7 Metal sulfide thin films	36
1.7.1 Precursors for metal sulfide thin films	37
1.7.1.1 (Dialkyldithiocarbamato) metal complexes.....	37
1.7.1.2 (O-alkyldithiocarbomato)metal complexes	38
1.8 Deposition techniques for metal sulfide thin films	41
1.8.1 Chemical vapour deposition.....	41
1.8.1.1 Low pressure CVD (LPCVD)	42
1.8.1.2 Atmospheric pressure CVD (APCVD)	42
1.8.1.3 Aerosol assisted CVD (AACVD).....	43
1.8.2 Spin coating technique	43
1.8.3 Doctor blade technique.....	44
1.8.4 The hot-injection method	44
1.9 The aims of the present study.....	45

1.10	References	46
Chapter 2	Important compound semiconductors.....	53
2.1	Introduction	53
2.2	Zinc sulfide(ZnS)	55
2.3	Copper indium sulfide (CuInS ₂).....	60
2.4	Copper zinc tin sulfide (Cu ₂ ZnSnS ₄) and copper iron tin sulfide (Cu ₂ FeSnS ₄).....	63
2.4.1	Stannite structure of Cu ₂ FeSnS ₄	66
2.5	References	68
Chapter 3	The synthesis of copper sulfide nanorods from xanthate precursors .	71
3.1	Introduction	71
3.2	Author distribution	71
3.3	References	72
3.4	Manuscript 1: Novel xanthate complexes for the size-controlled synthesis of copper sulfide nanorods.....	73
3.4.1	Abstract.	73
3.4.2	Introduction	73
3.4.3	Experimental section	74
3.4.3.1	General.....	74
3.4.3.2	Synthesis of Precursors.....	75
3.4.3.2.1	Synthesis of Potassium n-Butylxanthate (1).....	75
3.4.3.2.2	Synthesis of Potassium iso-Butylxanthate (2).....	76
3.4.3.2.3	Synthesis of Potassium 2-Methoxyethylxanthate (3).	76
3.4.3.2.4	Synthesis of Potassium 2-Ethoxyethylxanthate (4).....	76
3.4.3.2.5	Synthesis of Potassium 1-Methoxy-2-propylxanthate (5).....	77
3.4.3.2.6	Synthesis of Potassium 3-Methoxy-1-butylxanthate (6).	77
3.4.3.2.7	Synthesis of Potassium 3-Methoxy-3-methyl-1-butylxanthate (7). 77	
3.4.3.2.8	Synthesis of Triphenylphosphine Copper Chloride (8).....	78

3.4.3.3	Synthesis of Copper Xanthates.....	78
3.4.3.3.1	Synthesis of Triphenylphosphine Copper(I) Ethylxanthate (9).	78
3.4.3.3.2	Synthesis Triphenylphosphine Copper(I) n-Butylxanthate (10).	78
3.4.3.3.3	Synthesis of Triphenylphosphine Copper(I) Isobutylxanthate (11).	79
3.4.3.3.4	Synthesis of Triphenylphosphine Copper(I) 2-Methoxyethylxanthate (12).	79
3.4.3.3.5	Synthesis of Triphenylphosphine Copper(I) 2-Ethoxyethylxanthate (13).	80
3.4.3.3.6	Synthesis of Triphenylphosphine Copper(I) 1-Methoxy-2-propylxanthate (14).	80
3.4.3.3.7	Synthesis of Triphenylphosphine Copper(I) 3-Methoxy-1-butylxanthate(15).	80
3.4.3.3.8	Synthesis of Triphenylphosphine Copper(I) 3-Methoxy-3-methyl- 1-butylxanthate (16).	81
3.4.3.4	Synthesis of copper sulfide nanorods.	81
3.4.3.5	Density Functional Theory Calculations.	82
3.4.4	Results and discussion.....	82
3.4.4.1	Xanthate Precursors.....	82
3.4.4.2	Synthesis of Nanorods.....	85
3.4.4.3	DFT Study	89
3.4.5	Conclusions	93
3.4.6	References	94
3.4.7	Supporting information	97
Chapter 4	The synthesis of tin sulfide thin films from tin (II)ethylxanthate	101
4.1	Introduction	101
4.2	Author distribution	101
4.3	References	101

4.4	Manuscript 2: A facile method for the production of SnS thin films from melt reactions.	103
4.4.1	Abstract	103
4.4.2	Introduction	103
4.4.3	Experimental	105
4.4.3.1	Materials and methods.....	105
4.4.3.2	Synthesis of tin(II)(<i>O</i> -ethylxanthate)	105
4.4.3.3	Preparation of SnS thin films by spin coating and heating ..	106
4.4.4	Results and discussion.....	106
4.4.5	Conclusions	114
4.4.6	Acknowledgements	114
4.4.7	References	115
4.4.8	Supplementary information	118
Chapter 5	Phase selective synthesis of CuInS ₂ from xanthate complexes	119
5.1	Introduction	119
5.2	Author distribution	119
5.3	References	120
5.4	Manuscript 3: On the Phase Control of CuInS ₂ Nanoparticles from Cu-/In-Xanthates	121
5.4.1	Abstract	121
5.4.2	Introduction	121
5.4.3	Experimental	122
5.4.3.1	Materials and synthesis.....	122
5.4.3.1.1	Synthesis of Potassium <i>n</i> -propylxanthate (1):	123
5.4.3.1.2	Synthesis of potassium <i>iso</i> -propylxanthate (2):	123
5.4.3.1.3	Synthesis of indium(III) <i>n</i> -propylxanthate (8):	123
5.4.3.1.4	Synthesis of indium(III) <i>iso</i> -propylxanthate (9):.....	124
5.4.3.1.5	Synthesis of indium(III) <i>iso</i> -butylxanthate (10):.....	124
5.4.3.1.6	Synthesis of indium(III) 2-ethoxyethylxanthate (11):.....	124
5.4.3.1.7	Synthesis of indium(III) 2-methoxyethylxanthate (12):.....	125

5.4.3.1.8	Synthesis of indium(III) 3-methoxy-3-methyl-1-butylxanthate (13):	125
5.4.3.1.9	Synthesis of indium(III) 1-methoxy-2-propylxanthate (14):..	125
5.4.3.2	X-ray Crystallography:	126
5.4.3.3	Synthesis of CuInS ₂ nanoparticles:	126
5.4.4	Results and discussion	126
5.4.4.1	Precursors	126
5.4.4.2	Synthesis of Nanoparticles	129
5.4.5	Conclusions	135
5.4.6	Acknowledgements	135
5.4.7	References	135
5.4.8	Electronic Supplementary Information	138
5.4.8.1	References	139
Chapter 6	Alkaline-Transition metal sulfides	140
6.1	Introduction	140
6.2	Author distribution	141
6.3	References	141
6.4	Manuscript 4: A Simple Route to Complex Materials: the Synthesis of Alkaline – Transition Metal Sulfides	142
6.4.1	Abstract	142
6.4.2	Introduction	142
6.4.3	Experimental	144
6.4.3.1	Analytical equipment.....	144
6.4.3.2	Synthesis of xanthate complexes.....	144
6.4.3.2.1	Synthesis of [Ca(S ₂ CO ⁱ P) ₂ (ⁱ PrOH) ₃](1).....	144
6.4.3.2.2	Synthesis of [Ba(S ₂ CO ⁱ Pr) ₂](2)	145
6.4.3.2.3	Synthesis of [KS ₂ CO(CH ₂) ₂ OCH ₃]	145
6.4.3.2.4	Synthesis of [(PPh ₃) ₂ Cu(S ₂ CO(CH ₂) ₂ OCH ₃)] (3)	146
6.4.3.3	Preparation of thin films	146

6.4.4	Results and discussion.....	147
6.4.5	Conclusion.....	152
6.4.6	Acknowledgements	152
6.4.7	Reference.....	153
6.4.8	Supporting information	155
Chapter 7	The synthesis and characterization of $\text{Cu}_2\text{ZnSnS}_4$ thin films from melt reactions using xanthate precursors	159
7.1	Introduction	159
7.2	Author distribution	159
7.3	Reference.....	160
7.4	The synthesis and characterization of $\text{Cu}_2\text{ZnSnS}_4$ thin films from melt reactions using xanthate precursors.....	161
7.4.1	Abstract	161
7.4.2	Introduction	161
7.4.3	Experimental	164
7.4.3.1	Synthesis of metal xanthate complexes	165
7.4.3.1.1	Synthesis of potassium n-butylxanthate ligand	165
7.4.3.1.2	Synthesis of bis(O-ethylxanthato)zinc(II)	165
7.4.3.1.3	Synthesis of bis(O-butylxanthato)zinc(II).....	165
7.4.3.1.4	Synthesis of bis(O-ethylxanthato)tin(II).....	166
7.4.3.1.5	Synthesis of tetrakis(O-ethylxanthato)tin(IV).....	166
7.4.3.1.6	Synthesis of (O-ethylxanthato)copper(I) triphenylphosphine	166
7.4.3.1.7	Synthesis of (O-butylxanthato)copper(I) triphenylphosphine	167
7.4.3.2	Preparation of thin films	167
7.4.3.3	Electrical measurements	167
7.4.4	Results and discussion.....	168
7.4.5	Conclusions	175
7.4.6	Acknowledgements	175
7.4.7	References	176
7.4.8	Supporting information	180

7.4.8.1	References	183
Chapter 8	Conclusion and future work.....	184
8.1	Conclusion.....	184
8.2	Future work	185
8.3	References	186
Appendix	187

Words: 46,623

List of Figures

- Figure 1.1.** Shows a schematic of the cross-substitutional steps for a portion of the periodic table in which the more common II-VI semiconductors are found. 27
- Figure 1.2.** Figure . Comparison between quantum confinement effects of quantum wells, wires, rods and dots, (a) Geometries of the different structures (b) Plots of the increase in the bandgap over the bulk value (ΔE_g) against the thickness or diameter (d) for rectangular quantum wells, cylindrical quantum wires and spherical quantum dots obtained from particle in a box approximations, (c) The dependence of the bandgap on the length/diameter ratio for the InAs quantum rods.²¹ 28
- Figure 1.3.** Electron microscope images of PbTe nanocubes. (a) TEM image of monodisperse lead telluride. (b) slow-processed lead telluride monolayer assembly. (c) Diffraction pattern of slow-processed monolayer assembly (negative pattern). (d) HRTEM image of a PbTe nanocube. (e) PbTe nanocube is stacked on the top of another. (f) 1D-shifted PbTe simple cubic stacking structure (the offset of the top layer along one axis by half a length of the cubic edge).²³ 30
- Figure 1.4.** The precession electron diffraction tomography (PEDT) data obtained from single particle of the π -SnS. (a-c) Views along the [100], [110] and [111] directions, respectively. (d) a single cube-shaped nanoparticle, (e) SAED taken from (d), which matches to the [001] plane of the new π -SnS.^{24, 25} 31
- Figure 1.5.** The zincblende (sphalerite) lattice structure, (a) face-centred cubic lattice arrangement with the positions of the tetrahedral sites (b) the structure of zinc sulfide unit cell, (c) shows the basic tetrahedral structure of ZnS in this structure each atom has four nearest neighbours of the opposite kind. In which each Zn atom has four nearest S neighbours and each S atom has four nearest Zn neighbours.²⁹ 32
- Figure 1.6.** Unit cell representations of $\text{Cu}_2\text{ZnSnS}_4$; (a) the kesterite type structure, (b) stannite type structure, and (c) the primitive mixed CuAu-like structure (PMCA).⁴⁸ 34
- Figure 1.7.** The variation of absorption coefficient α for a semiconductor with the wavelength of incident photons. 36
- Figure 1.8.** Three different coordination modes of dithiocarbamate groups (a) monodentate, (b) asymmetric bidentate, and (c) symmetric bidentate.⁸⁰ 38

Figure 1.9. Xanthate ligands are classified as: (a) monodentate, (b) isobidentate and (c) anisobidentate, and three more rare forms (d, e, f). ⁹³	39
Figure 1.10. Decomposition process of metal alkylxanthate complexes by Chugaev elimination reaction.....	41
Figure 1.11. Fundamental steps that lead to chemical vapor deposition (CVD) of thin films ^{106, 107}	42
Figure 1.12. Schematic representation of the AACVD set up.	43
Figure 1.13. Schematic of spin coating process.	44
Figure 1.14. The Doctor's blade deposition processes. Stage (1): the compound paste is laid onto substrate, stage (2): the blade spreads the paste over the substrate, stage (3): the achieved film is dried. ¹¹⁵	45
Figure 2.1. Close-packed structures (a) side view of hexagonal close-packed (hcp) (b) side view of cubic close-packed (ccp).....	53
Figure 2.2. Schematic diagram of the unit cells of the zinc - blende (ZB) and wurtzite (WZ) structures of ternary CuInS_2 and quaternary $\text{Cu}_2\text{ZnSnS}_4$ which derived from ZnS binary phase. They crystallize in basic ZB and WZ structure, in addition they possess chalcopyrite, WZ - chalcopyrite, CuAu like, WZ - CuAu - like, kesterite, stannite, WZ - kesterite and WZ - stannite. ^{6, 7}	55
Figure 2.3. The unit cell of a ZnS cubic crystal, the parameters of the crystal obtained by Skinner. ¹⁴ (a) The atoms positions in the crystal (b) The tetrahedral structures and (c) crystal parameters. Maroon = Zn and Yellow = S.	56
Figure 2.4. Schematic diagram of the ZnS hexagonal crystal data obtained by Myer. ¹⁴ (a) The atoms positions in the crystal (b) The tetrahedral structures and (c) Crystal parameters. Maroon = Zn and yellow = S.	58
Figure 2.5. Images of nanocable-aligned ZnS tetrapods. (a) Aligned ZnS tetrapods. (b) Nanocable passing through the centre of the tetrapod. (c) Tetrapod image viewed along the [111] direction; (d) Viewed along the $[\bar{1}\bar{1}\bar{1}]$ direction; (e) Viewed along the [100] direction. ²⁰	59

- Figure 2.6.** Schematic diagram of the CuInS₂ Cubic (zinc blende) crystal. (a) The atoms positions in the crystal (b) The tetrahedral structures and (c) crystal parameters. Magenta = Zn/In and yellow = S. 61
- Figure 2.7.** Schematic diagram of the CuInS₂ chalcopyrite crystal (a) The atoms positions (b) Stacking of tetrahedral cations layers (c) The unit cell parameters. Blue = Cu, red = In and yellow = S. 62
- Figure 2.8.** Schematic diagram of a hexagonal CuInS₂ (a) The atoms positions (b) Stacking of tetrahedral anions layers (c) The unit cell parameters. Blue = Cu/In and yellow = S. 63
- Figure 2.9.** The crystal structure of chalcopyrite Cu₂ZnSnS₄ with space group *I42m* (a) The positions of atoms in the unit cells (b) Stacking of tetrahedral cations layers (c) The unit cells parameters. Blue = Cu/Zn, green = Sn, yellow = S, the position 4d(1/2,0,1/4) will be randomly occupied by the Cu⁺² and Zn⁺² cations. 64
- Figure 2.10.** The crystal structure of chalcopyrite Cu₂ZnSnS₄ with space group *I4* (a) The atoms positions in the unit cell (b) Stacking of tetrahedral cations layers (c) The unit cell parameters. Blue = Cu, maroon = Zn, green = Sn, yellow = S. 65
- Figure 2.11.** The crystal structure of Cu₂FeSnS₄ reported by Bonazzi⁴⁷ (a) The positions of atoms (b) The stacking of tetrahedrons of anions and (c) The parameters of the unit cell . Blue = Cu, brown = Fe, green = Sn, yellow = S. 66
- Figure 2.12.** TEM images of the WZ.CZTS nanocrystal synthesised by a hot injection method (a) DF-STEM image of bullet-shaped CZTS nanorods. The inset shows the corresponding SAED pattern. (b) HRTEM image showing that the bullet-shaped CZTS nanorods are elongated in the [002] direction. (c) DF-STEM image of WZ.CZTS nanorods synthesized in the presence of a higher 1-DDT concentration. (d) HRTEM image of a single CZTS nanorod from (c).⁴⁹ 67
- Figure 3.1.** FT-IR spectra of the potassium xanthate precursors (**1-7**). 82
- Figure 3.2.** FT-IR spectra of the triphenylphosphine copper(I) alkylxanthate 83
- Figure 3.3.** Structures of (a) triphenylphosphine copper chloride (**8**), triphenylphosphine copper(I) (b) isobutylxanthate (**11**), (c) 2- methoxyethylxanthate (**12**), (d) 2-ethoxyethylxanthate (**13**), (e) 1- methoxy-2-propylxanthate (**14**), (f) 3- methoxy-1-butylxanthate (**15**), and (g) 3-methoxy-3-methyl-1-butylxanthate (**16**).

Hydrogens omitted for clarity. Green = Cl, orange = Cu, yellow = S, pink = P, red = O, gray = C.....	84
Figure 3.4. TGA of complexes 9–16 indicates that decomposition occurs between 200 and 250 °C leading to the formation of CuS. (inset) Expansion of the 50–250 °C region showing the onset of breakdown.	85
Figure 3.5. The powder XRD patterns of nanocrystals generated from the decomposition of 9-12 for a reaction time of 1 h.....	86
Figure 3.6. Powder XRD patterns of nanocrystals generated from the decomposition of 9–16 for a reaction time of 5 s.....	86
Figure 3.7. Suggested initial breakdown of precursor by Chugaev elimination.	87
Figure 3.8. EDS spectra of the nanorods obtained from a 5 s decomposition of 9-16	88
Figure 3.9. TEM images of the nanocrystals generated from the 5 s decomposition of triphenylphosphine copper(I) (a) ethylxanthate (9), (b) n-butylxanthate (10), (c) isobutylxanthate (11), (d) 2-methoxyethylxanthate (12), (e) 2-ethoxyethylxanthate (13), (f) 1-methoxy-2-propylxanthate (14), (g) 3-methoxy-1-butylxanthate (15), and (h) 3-methoxy-3-methyl-1-butylxanthate (16). (insets) The d-spacings measured for each. d-spacings of 3.27, 3.26, 3.30, 3.34, 3.30, 3.30, 3.30, and 3.30 Å correspond to the (400) reflection.....	88
Figure 3.10. (a) Increasing the chain length of the xanthate ligand leads to a decrease in the width of the rods obtained. One standard deviation for each measurement is displayed. (b) The UV–vis spectra for the copper sulfide nanorod—the number indicates the precursor. (inset) Correlation between band gap and the number of atoms in the xanthate chain.	91
Figure 3.11. (a) The ground-state energies of 9–16 as a function of the chain length. (b) The width of the obtained nanorod compared to the sum of the electronic and thermal energy of the xanthate precursor.....	92
Figure S3.12. A comparison of the ground state energies of the linear chain xanthates [(PPh ₃) ₂ Cu(S ₂ CO(CH ₂) ₂ OR)] (17-R , R = Me, Et, ⁿ Pr, ⁿ Bu, ■) and [(PPh ₃) ₂ Cu(S ₂ COR')] (18-R' , R' = ⁿ Bu, ⁿ Pen, ⁿ Hex, ⁿ Hep, ●).	99

Figure 4.1. Thermogram for the decomposition of $[\text{Sn}(\text{S}_2\text{COEt})_2]$. The final residual weight (44.1 %) is close to the predicted value for residual SnS (41.8%).....	107
Figure 4.2. FTIR spectrum of the precursor $[\text{Sn}(\text{S}_2\text{COEt})_2]$	107
Figure 4.3. SEM images of SnS films grown on glass substrates from $[\text{Sn}(\text{S}_2\text{COEt})_2]$ at (a) 200 °C, (b) 250 °C, (c) 300 °C, and (d) 400 °C (<i>scale bars</i> represent 1 μm); (e) and (f) the elemental maps of the SnS film produced at 300 °C (<i>scale bars</i> represent 10 μm).....	109
Figure 4.4. The Sn/S ratio by EDX for samples heated for 60 min at temperatures between 150 and 400 °C.	110
Figure 4.5. (a) p-XRD patterns of SnS films grown on glass substrate at different temperatures, accompanied by reference patterns of herzenbergite SnS (ICCD pattern No. 00-039-0354) and rock-salt SnS (ICCD pattern No. 04-004-8426). (b) Raman spectra for the SnS films grown on glass substrates from $[\text{Sn}(\text{S}_2\text{COEt})_2]$ at 150, 200, 250, 300, and 400 °C.....	111
Figure 4.6. Absorption coefficient of SnS films grown on glass substrates from $[\text{Sn}(\text{S}_2\text{COEt})_2]$ decomposed at temperatures between 200 and 400 °C.	112
Figure 4.7. (a) UV–Vis and Tauc plots (<i>inset</i>) for the SnS films grown on glass substrates from $[\text{Sn}(\text{S}_2\text{COEt})_2]$ at 200, 250, 300, and 400 °C. (b) Graph showing the relationship between the Sn/S ratio of SnS_{1-x} materials with its measured band gap. Data in black represent the findings in this report, whereas data in <i>red</i> were obtained from literature.....	113
Figure S4.8. The proposed decomposition mechanism of $[\text{Sn}(\text{S}_2\text{COEt})_2]$, which is thought to break down following the Chugaev elimination mechanism of metal xanthates.....	118
Figure S4.9. (a-e) SEM images of SnS films grown on glass substrates from $[\text{Sn}(\text{S}_2\text{COEt})_2]$ at (a) 150 °C, (b) 200 °C (c) 250 °C (d) 300 °C and (e) 400 °C. (a1-e1) and (a2-e2) are the elemental maps of the SnS film produced at the given temperatures.	118
Figure 5.1. The structures of the indium xanthates. (a) $[\text{In}(\text{S}_2\text{CO}^i\text{Pr})_3]$ (8), (b) $[\text{In}(\text{S}_2\text{CO}^i\text{Pr})_3]$ (9), (c) $[\text{In}(\text{S}_2\text{CO}^i\text{Bu})_3]$ (10), (d), $[\text{In}(\text{S}_2\text{CO}(\text{CH}_2)_2\text{OEt})_3]$ (11), (e) $[\text{In}(\text{S}_2\text{CO}(\text{CH}_2)_2\text{OMe})_3]$ (12), (f) $[\text{In}(\text{S}_2\text{CO}(\text{CH}_2)_2\text{C}(\text{OMe})(\text{Me})_2)_3]$ (13) and (g)	

[In(S ₂ COC(H)(Me)CH ₂ OMe) ₃] (14). H atoms are omitted for clarity. Bronze = In, yellow = S, red = O, grey = C.	128
Figure 5.2. TGA of Indium xanthates complexes.	129
Figure 5.3. The pXRD patterns and Raman spectra of (a, b) hexagonal CIS and (c, d) cubic CIS. In each case the upper pattern corresponds to a 45 minute reaction, whilst the lower corresponds to a 10 minute reaction length. Hexagonal CIS reference pattern generated from Tang's ³⁶ work, cubic CIS reference pattern generated from Yang's ³⁷ work,	130
Figure 5.4. TEM images and associated selected area electron diffraction (SAED) patterns for (a)-(c) hexagonal CuInS ₂ from a 10 min reaction and (d)-(f) cubic CuInS ₂ from a 10 min reaction.....	132
Figure 5.5. TEM images and associated selected area electron diffraction (SAED) patterns for (a)-(c) hexagonal CuInS ₂ from a 45 min reaction and (d)-(f) cubic CuInS ₂ from a 45 min reaction.....	132
Figure 5.6. UV-vis spectra and associated band gaps of the CIS nanoparticles.	133
Figure 5.7. pXRD pattern of hexagonal CIS from reacting 12 and [(PPh ₃) ₂ Cu(S ₂ CO(CH ₂) ₂ OMe)] in octadecene/castor oil.	134
Figure 5.8. pXRD pattern of cubic CIS from reacting 12 and [(PPh ₃) ₂ Cu(S ₂ CO(CH ₂) ₂ OMe)] in trioctylphosphine/oleylamine.....	134
Figure S5.9. X-ray emissions lines of zinc blend CuInS ₂ prepared at (a)10 min, (b) 45 min and hexagonal CuInS ₂ prepared at (c) 10 min, (d) 45 min.	139
Figure 6.1. Schematic drawing of the structure of (a) CaCu ₂ S ₂ , (b) β-BaCu ₂ S ₂ and (c) β-BaCu ₄ S ₃ . Teal = Ca, brown = Ba, blue = Cu, yellow = S.....	143
Figure 6.2. Thermogravimetric analysis of [Ca(S ₂ CO ⁱ Pr) ₂ (ⁱ PrOH) ₃] (1 , black), [Ba(S ₂ CO ⁱ Pr) ₂] (2 , red) and [(PPh ₃) ₂ Cu(S ₂ CO(CH ₂) ₂ OMe)] (3 , blue).	147
Figure 6.3 The p-XRD patterns of the thin films. (a) cubic CaS and reference pattern JCPDS 00-08-0464, (b) cubic BaS and reference pattern JCPDS 04-001-3579, (c) hexagonal CaCu ₂ S ₂ and reference pattern generated from Purdy's work, ¹⁶ (d) β-BaCu ₂ S ₂ with reference pattern JCPDS 04-008-2860 and (e) orthorhombic β-BaCu ₄ S ₃ and reference pattern generated from the work of Iglesias <i>et al.</i> ³³	149

Figure 6.4. SEM images of thin films of (a) CaS, (b) BaS, (c) hexagonal CaCu ₂ S ₂ (d) β-BaCu ₂ S ₂ and (e) β-BaCu ₄ S ₃	151
Figure S6.5 p-XRD of BaCu ₂ S ₂ showing the mixed α (orthorhombic) and β (tetragonal) phases present in films prepared at 550 °C.....	156
Figure S6.6. p-XRD of Cu ₂ S showing the chalcocite copper sulfide phase present in film prepared at 300 °C.	156
Figure S6.7. EDX elemental mapping for CaCu ₂ S ₂ showing a homogeneous distribution of the elements.....	157
Figure S6.8. EDX elemental mapping for BaCu ₂ S ₂ showing a homogeneous distribution of the elements.....	157
Figure S6.9. EDX elemental mapping for BaCu ₄ S ₃ showing a homogeneous distribution of the elements.....	158
Figure S6.10. EDX elemental mapping for Cu ₂ S showing a homogeneous distribution of the elements.....	158
Figure 7.1. Side-on SEM image of a film prepared at 375 °C and 450 °C.....	169
Figure 7.2. Decomposition profiles of the six potential CZTS precursors that were assessed by thermogravimetric analysis (TGA). Heating rate of 10 °C min ⁻¹ under N ₂ flow.....	170
Figure 7.3. SEM images showing the surface morphology of the CZTS films obtained by heating spin-coated films at various temperatures.	171
Figure 7.4. (a) p-XRD patterns and (b) Raman scattering spectra of CZTS thin films annealed in an N ₂ atmosphere at the desired temperature (200–475 °C) for 120 min. Chalcocite (Cu _{2-x} S) is identifiable within the p-XRD for temperatures < 300 °C: low-intensity peaks for the (110) plane (2θ = 46.7°) and (103) plane (2θ = 48.8°).....	173
Figure 7.5. (a) The position of the dominant Raman peak at 327–336 cm ⁻¹ in Figure 7.4b and its relationship to the annealing temperature of the films. (b) Raman spectrum of films prepared at 200 °C and (c) 475 °C.....	173
Figure 7.6. TEM images of Cu ₂ ZnSnS ₄ nanocrystals. (a) A CZTS film heated at 225 °C. The insets show selected area electron diffraction (SAED) images, gray box for	

cubic CZTS and white box for hexagonal CZTS. (b) A film heated at 350 °C. The SAED pattern can be indexed to tetragonal CZTS. (c) A film heated at 450 °C, the inset SAED pattern is also indexed to tetragonal CZTS. 175

Figure S7.7. The elemental composition of the films determined by EDX. 180

Figure S7.8. Elemental composition of the CZTS films determined by EDX normalised to Cu₂. 181

List of Tables

Table 1.1. EDS data of the nanorods obtained from a 5 s decomposition.	87
Table S1.2. The unit cell parameters for the nanorods synthesised with a 1 h reaction time, with ICDD 00-009-0328 as the Cu ₂ S reference pattern.....	97
Table S1.3. The unit cell parameters for the nanorods synthesised with a 5 s reaction time, with ICDD 00-064-0278 as the Cu _{1.74} S reference pattern.	97
Table S1.4. Ground state energies of compounds 9-16	98
Table S1.5. Ground state energies of 17-R and 18-R'	98
Table S1.6. Cu-S bond lengths for 17-R and 18-R'	98
Table S1.7. C-S bond lengths for 17-R and 18-R'	99
Table S1.8. Mulliken population of the S atoms in 17-R and 18-R'	99
Table S1.9. Band gap values for the nanorods synthesized from the decomposition of 9-16	100
Table 2.1. Thicknesses, compositions, and unit cell parameters of the SnS films produced by the melt method.....	109
Table S3.1. TGA data analyses of indium xanthate complexes.....	138
Table S3.2. The lattices parameters of CuInS ₂ samples calculated from X-Ray diffraction, lattice parameter (a) of zincblende CuInS ₂ is 5.523 Å, ¹ and lattice parameters of hexagonal CuInS ₂ are a = 3.9065 Å and c= 6.4290 Å. ²	138
Table S3.3. Chemical compositions of CuInS ₂ nanoparticles calculated by energy dispersive X-ray spectroscopy (EDX).	139
Table 4.1. The experimental conditions of preparation of CaS, BaS, CuS, CaCu ₂ S ₂ , β- BaCu ₂ S ₂ , and β - BaCu ₄ S ₃ films heated at different temperatures for 1 h. The picture of β - BaCu ₂ S ₂ is obtained for the film deposited onto glass substrate and heated at 550 °C.....	148
Table 4.2. Compositional analysis of films determined by EDX.....	151
Table S4.3. Lattice parameters of the thin films as determined by p-XRD.	155

Table 5.1. Electrical properties of CZTS films prepared through melt reactions at 225, 375 and 450 °C.....	174
Table S5.2. Composition percentages and ratios for CZTS films after annealing at different temperatures as determined by EDX.....	180
Table S5.3. Lattice parameters calculated from p-XRD and SAED (Figure 7.6a) for hexagonal CZTS film heated at 225 °C.	181
Table S5.4. Lattice parameters calculated from p-XRD and SAED (Figure 7.6a) for cubic CZTS heated at 225 °C.....	182
Table S5.5. Lattice parameters calculated from p-XRD and SAED for tetragonal CZTS prepared at 350 °C (Figure 7.6b).....	182
Table S5.6. Lattice parameters calculated from p-XRD and SAED for tetragonal CZTS prepared at 450 °C (Figure 7.6c).....	182
Table S5.7. Lattice parameters calculated from p-XRD for tetragonal and hexagonal CZTS prepared by heating spin-coated films at various temperatures. The literature values of lattice parameters are $a = b = 5.43 \text{ \AA}$ and $c = 10.84 \text{ \AA}$ for tetragonal ¹ and $a = b = 3.83 \text{ \AA}$, $c = 6.31 \text{ \AA}$ for hexagonal. ²	183

Abstract

Metal sulfide thin films and nanoparticles are important in photovoltaic applications owing to their exciting properties. Xanthate complexes are well known for the deposition of metals sulfide films and nanoparticles. This produces suitable physical and chemical properties to deposit films with a very low level or no contamination at low temperature.

The work shows the synthesis of a series of metal (Cu, Sn, Zn and In) complexes of xanthate ligands, their spectroscopic characterization, crystal structures and thermal decomposition have been studied. Xanthate complexes of calcium and barium have been also synthesised. The complexes were used as single source precursors for the deposition of SnS, CaS, BaS, CaCu_2S_2 , $\beta\text{-BaCu}_2\text{S}_2$, $\beta\text{-BaCu}_4\text{S}_3$ and $\text{Cu}_2\text{ZnSnS}_4$ thin films by spin coating. In addition, Cu(I)-xanthate has been used for the synthesis of highly crystalline copper sulfide nanoparticles. In(III)-xanthate in conjunction with a Cu(I)-xanthate have been used as a single source precursors to the formation of CuInS_2 nanoparticles, both Cu_xS and CuInS_2 nanoparticles have been synthesised by hot injection method at 260 °C. The films and nanoparticles were characterised by powder X-ray diffraction, Raman spectra, scanning electron microscopy and energy dispersive X-ray spectroscopy, transmission electron microscopy and selected area electron diffraction.

Triphenylphosphine copper(I) xanthate complexes [isobutylxanthate, 2-methoxyethylxanthate, 2-ethoxyethylxanthate, 1-methoxy-2-propylxanthate, 3-methoxy-1-butylxanthate, and 3-methoxy-3-methyl-1-butylxanthate] in addition to the ethyl and n-butyl have been used for the formation of copper sulfide nanorods. At 1 h reaction times chalcocite Cu_2S is formed, while at 5 sec result in roxbyite $\text{Cu}_{1.74}\text{S}$ nanorods. The longer chain xanthates lead to the formation of rods of decreased width. These complexes as well as indium complexes have an ability to control the CuInS_2 phase through choice of solvent.

A melt reaction of calcium isopropylxanthate and the novel compounds barium isopropylxanthate and bis(triphenylphosphine)copper 2-methoxyethylxanthate at low temperature, atmospheric pressure and short decomposition time leads to a formation of CaCu_2S_2 , $\beta\text{-BaCu}_2\text{S}_2$ and $\beta\text{-BaCu}_4\text{S}_3$

thin films which have previously been produced from a high temperature, high pressure reaction system.

$\text{Cu}_2\text{ZnSnS}_4$ (CZTS) thin films were obtained from melt reaction after heating the $[(\text{Ph}_3\text{P})_2\text{CuS}_2\text{COEt}]$, $[\text{Zn}(\text{S}_2\text{CO}^n\text{Bu})_2]$ and $[\text{Sn}(\text{S}_2\text{COEt})_2]$ at temperatures between 200 and 475 °C. Higher temperatures give the normal tetragonal phase CZTS, while low temperatures are mixed hexagonal and cubic phases.

Declaration

I declare that no portion of the work referred to in this thesis has been submitted in support of an application for another degree or qualification of this or any other university or other institute of learning.

Copyright Statement

i. The author of this thesis (including any appendices and/or schedules to this thesis) owns certain copyright or related rights in it (the “Copyright”) and s/he has given The University of Manchester certain rights to use such Copyright, including for administrative purposes.

ii. Copies of this thesis, either in full or in extracts and whether in hard or electronic copy, may be made only in accordance with the Copyright, Designs and Patents Act 1988 (as amended) and regulations issued under it or, where appropriate, in accordance with licensing agreements which the University has from time to time. This page must form part of any such copies made.

iii. The ownership of certain Copyright, patents, designs, trademarks and other intellectual property (the “Intellectual Property”) and any reproductions of copyright works in the thesis, for example graphs and tables (“Reproductions”), which may be described in this thesis, may not be owned by the author and may be owned by third parties. Such Intellectual Property and Reproductions cannot and must not be made available for use without the prior written permission of the owner(s) of the relevant Intellectual Property and/or Reproductions.

iv. Further information on the conditions under which disclosure, publication and commercialisation of this thesis, the Copyright and any Intellectual Property and/or Reproductions described in it may take place is available in the University IP Policy (see <http://documents.manchester.ac.uk/DocuInfo.aspx?DocID=24420>), in any relevant Thesis restriction declarations deposited in the University Library, The University Library’s regulations (see <http://www.library.manchester.ac.uk/about/regulations/>) and in The University’s policy on Presentation of Theses.

Acknowledgement

I would like to acknowledge and thank people who support me on my study. My appreciation goes to the Ministry of Higher Education and Scientific Research in Iraq (MHESR) for funding. I am very grateful to my supervisor Professor Paul O'Brien for his encouragement, guidance and useful advice. Thanks also, to Dr Nicky Savjani and Dr. Peter D. Matthews. I appreciate their scientific advice. I am really grateful to Dr. David J. Lewis, Dr Paul McNaughten, and Dr Edward A. Lewis, I have worked with them on some projects and I have taken useful comments. I am very grateful to POB's research group (especially Dr Claire Lydon and Dr Aleksander Tedstone) for their support throughout the study period. Big thanks to technical staff in the school of Chemistry: Dr James Raftery, Dr Inigo Vitorica-Yrezabal, Dr Ralph Adams for their great help in the use of X-ray crystallography and NMR. Also thanks to technical staff in the school of Materials: Dr John Warren, Gary Harrison, Dr Christopher Wilkins, Dr Patrick Hill, Teruo Hashimoto, Michael Faulkner and Xi Zhong for their help and support on the XRD, SEM and TEM.

Finally, I would like to thank my parents for their support and encouragement throughout my study. I would also like to thank my wife for her assistance, thank you Hiyam, I am here because of you.

Abbreviations

1D	1- Dimensional
1-DDT	1-Dodecanethiol
a	Lattice parameter
AACVD	Aerosol Assisted Chemical Vapour Deposition
ALCVD	Atomic Layer Chemical Vapor Deposition
APCVD	Atmospheric Pressure Chemical Vapor Deposition
Bu	Butyl
CCDC	Cambridge Crystallographic Data Centre
CVD	Chemical Vapor Deposition
CCP	Cubic Close Packing
COSY - NMR	Correlation Spectroscopy Nuclear Magnetic Resonance
CZTS	Copper Zinc Tin Sulfide
DF-STEM	Dark Field Scanning Transmission Electron Microscopy
DFT	Density Functional Theory
DLICVD	Direct Liquid Injection Chemical Vapor Deposition
DVT	Direct Vapor Transport Technique
DDT	Dodecanethiol
eV	Electron Volt
EDX	Energy Dispersive X-ray Spectroscopy
Eg	Energy Gap

<i>et al</i>	Et Alia
Et	Ethyl
EQE	External Quantum Efficiency
FCC	Face Centred Cubic
HCP	Hexagonal Close Packing
HAADF	High-Angle Annular Dark-Field imaging
HLW	High Level Wastes
HPCVD	Hybrid Physical Chemical Vapor Deposition
HRTEM	High-Resolution Transmission Electron Microscopy
HOMO	Highest Occupied Molecular Orbitals
ⁱ Pr	Isopropyl
K	Kelvin
LED	Light emitting diode
LPE	Liquid Phase Exfoliation
LPCVD	Low Pressure Chemical Vapor Deposition
LUMO	Lowest Unoccupied Molecular Orbitals
MOCVD	Metalorganic Chemical Vapour Deposition
MOVPE	Metalorganic Vapour Phase Epitaxy
NMP	<i>N</i> -Methyl-2-pyrrolidone
ODA	Octadecylamine
PECVD	Plasma Enhanced Chemical Vapor Deposition

p-XRD	Powder X-ray Diffraction
PEDT	Precession Electron Diffraction Tomography
PMCA	Primitive Mixed CuAu-like
Pr	Propyl
REPCVD	Remote Plasma Enhanced Chemical Vapor Deposition
RTCVD	Rapid Thermal Chemical Vapor Deposition
SAED	Selected Area Electron Diffraction
SEM	Scanning Electron Microscope
SSP	Single Source precursor
T- DDT	Tert-Dodecyl mercaptan
THF	Tetrahydrofuran
TGA	Thermo-Gravimetric Analysis
TMC	Transition Metal Chalcogenide
TOP	Trioctylphosphine
VPE	Vapour Phase Epitaxy
WZ	Wurtzite
ZB	Zinc Blende

Chapter 1 Introduction

1.1 Semiconductor materials

In recent years, semiconductor materials have been intensively studied for constructing solar cells because their bandgaps connect well to the maximum photon power density in the solar spectrum,¹ they have excellent luminescent efficiency,² and they have high promise for applications in a variety of optoelectronic devices for example photodiodes, photoconductive devices, fuel cells and photovoltaic cells.³ In addition, semiconductor materials have good magnetic and electric properties therefore, they have been used for chemical, biochemical field effect transistors and electrochemical sensors.⁴

As well as elemental, semiconductor compounds are found. Gallium arsenide is the most important semiconductor after silicon. It shows excellent electron mobility so that it is widely used in high performance RF devices. Because it presents good lattice mismatch value with other III-V semiconductors, it is also used as substrate for, e.g. InGaAs and GaInN from same group. The fabrication of GaAs as p-type is not achievable since GaAs has a lower hole mobility than silicon. GaAs crystallizes as a zinc-blende or wurtzite lattice,⁵ the value of a lattice parameter a of GaAs unit cell depends on the concentration of dopants and the compositions, doping GaAs with high value of tin (Sn) or tellurium (Te) leads to increase of the lattice parameters up to 0.02%. The value of a also extends by 0.001% for gallium rich composition, a decreases however by 0.004% for the As-rich composition.^{6,7}

Gallium nitride (GaN) semiconductor has found many uses in microwave transistors because they need high temperatures and powers. Similar to GaAs structure, GaN presents a zinc-blend or wurtzite lattice. Change the polarity of GaN to p-type by dopants is, however, intricate.⁸ GaN Mg-doped has a hole concentration of $3 \times 10^{18}/\text{cm}^3$, the hole mobility is $9 \text{ cm}^2/\text{V.s}$ and the resistivity is $0.2 \text{ } \Omega.\text{cm}$ The polarity of the GaN is p-type.⁹

Gallium phosphide (GaP) material is becoming more widely applied in laser and light emitting diode (LED) technology. Gallium phosphide emits a green light. It is relatively easy for a dopant atom, GaP N_2 -doped is used for the yellow-green LED's as well as high efficiency green LED's. Vapour Phase Epitaxy (VPE) system

is widely used for introducing nitrogen into GaP.¹⁰ The crystal structure of a gallium phosphide shows a good correlation with the bandgap, Cubic crystal structure has an indirect band gap however, hexagonal structure has a direct band gap.¹¹

1.2 Metal sulfide compounds

A large number of studies have concentrated on metal sulfide compounds for their application in optoelectronics and energy storage.^{3, 12} Compound semiconductors consist of two or more elements, they can be classified according to the number of elements as follows: (i) two elements, binary system (ii) three elements, ternary system (iii) four elements, quaternary system. The group II-VI semiconductors is the compounds produced from the group 12 elements (Zn, Cd and Hg) and group 16 elements (O, S, Se and Te). ZnS (zinc sulfide) is a good example, the zinc atoms are observed deficient by two electrons which are compensated by two electrons donated to the group VI elements. Zn is in Group 12 (II) and S in Group 16 (VI), and in zinc sulfide, Zn is present as Zn^{2+} and the S is present as the sulfide S^{2-} .

ZnS can form in two types of crystalline structures. ZnS can have a zinc blende structure, also ZnS can become the wurtzite structure type. It is crystallised by single bonds between each atom and preservation of a 1:1 zinc to sulfur ratio. Goodman discussed the replacing one element by pairs from other groups of the periodic table while keeping the valence electrons ratio constant. He used cross substitution process.¹³ A typical example of cross substitution is zinc sulfide (Figure 1.1), the zinc atoms in ZnS can be replaced by copper and indium atoms to generate the compound $CuInS_2$. each anion in $CuInS_2$ is coordinated to two Cu and two In cations. The substitution of atoms to produce $CuInS_2$ system leads to change in optical band gap values from 3.77 eV for zinc sulfide¹⁴ to 1.55 eV for copper indium sulfide.¹⁵ In addition, the cross substitution is true with compounds like cadmium telluride (CdTe) to produce $AgInTe_2$. The bandgap of CdTe is 1.5 eV, the substitution of cadmium atoms by silver and indium atoms gives $AgInTe_2$ ternary compound with band gap of 0.96 eV. Since the bond length is different between new bonds Ag-Te, In-Te and Cd-Te, the Ag-Te bond is higher than CdTe and In-Te, as well as Ag-Te bond has higher electronegativity difference. The cross substitution may lead to a linear relation between bond length and band gap.¹³

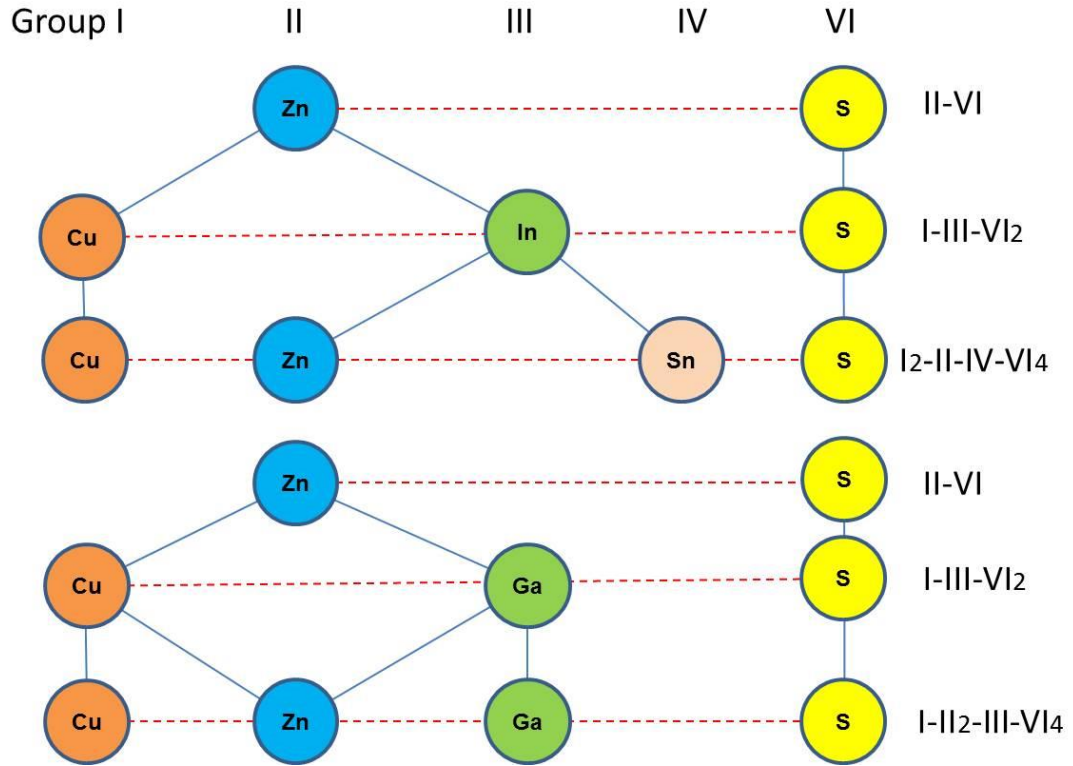


Figure 1.1. Shows a schematic of the cross-substitutional steps for a portion of the periodic table in which the more common II-VI semiconductors are found.

1.3 Quantum confinement effect

Quantum confinement effect in nanomaterials is the change in the properties of materials as a result of influence of small length scale. For typical semiconductor groups II-VI and III-V, the length scale accords to quantum confinement ranges is 1 to 30 nm.^{16, 17} if the particle dimensions of a semiconductor is near to or below the bulk semiconductor Bohr radius, the material properties will be size dependent, in this case the energy of a confined system increases and the energy levels of the system can be calculate by:¹⁸

$$E_n = \frac{n^2 \pi^2 \hbar^2}{2mR^2} \quad (1.1)$$

Where $n = 1, 2, 3, \dots$, \hbar is Plank's constant, m is the particle mass, and R is the radius of the nanoparticle. Furthermore, the quantization effect leads to break down of the continuous energy levels of a bulk material, new different structure of energy levels form a particular absorption spectrum which may differ from the continuous absorption spectrum of a bulk semiconductor.

Nanocrystals have different parameters that can modulate their electronic band gaps such as size and shape. The band gap of semiconductor nanocrystal can shift by 1 eV as a result of quantum confinement. It is also proportional to the thickness or diameter of the quantum nanocrystal.^{19,20} In contrast to bulk semiconductors, confinement effect is very clear in quantum well, wire, rod, and dot, it has a significant influence on band gap. Figure (1.2) shows the influence of different structures on the band gap, the intermediate zone (grey area in figure (1.2b)) between the dot and wire curves corresponds to quantum rods. The vertical dotted line represents the expected variation in the band gap of InAs quantum rods, also the band gap of InAs depends on the length/diameter ratio of the quantum rods which are displayed in figure (1.2 b and c).^{21, 22}

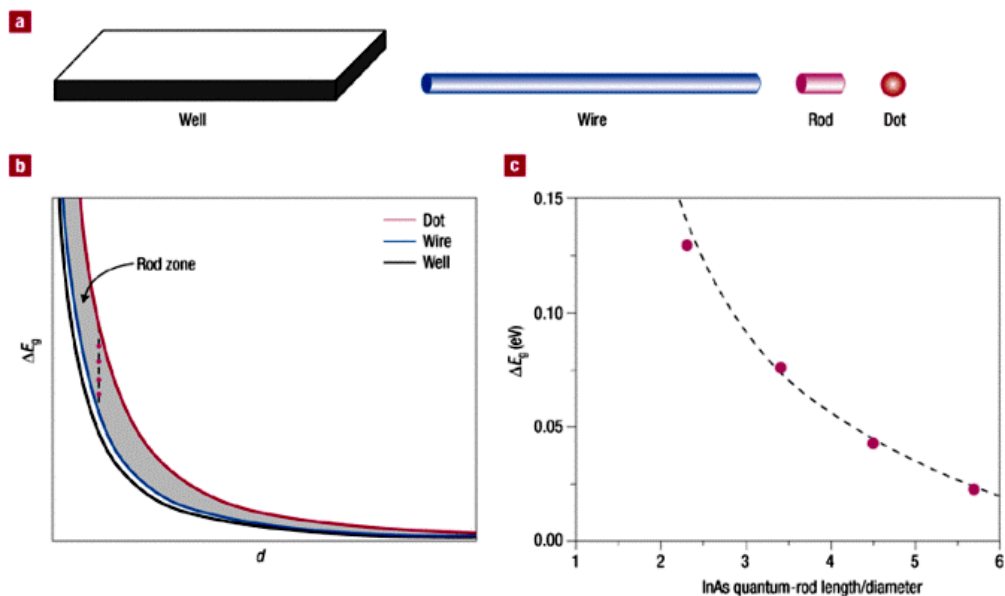


Figure 1.2. Figure . Comparison between quantum confinement effects of quantum wells, wires, rods and dots, (a) Geometries of the different structures (b) Plots of the increase in the bandgap over the bulk value (ΔE_g) against the thickness or diameter (d) for rectangular quantum wells, cylindrical quantum wires and spherical quantum dots obtained from particle in a box approximations, (c) The dependence of the bandgap on the length/diameter ratio for the InAs quantum rods.²¹

1.4 Structure properties of semiconductors

In the early 19th century, fourteen different lattice structures were suggested by Auguste Bravais. The Bravais lattices are the infinite arrays of different points (atoms) at specific positions in three dimensional spaces. Bravais placed the fourteen lattices into seven crystal systems which are cubic, hexagonal, tetragonal, orthorhombic, rhombohedral, monoclinic and triclinic. The physical properties of materials depended strongly on the crystal structure. X-ray diffraction has become an important method for qualitative and quantitative analyses of the properties and structures of materials.

1.4.1 Cubic crystal structure

A simple cubic unit cell consist of eight portions of eight corner atoms to produce one atom, so that each unit cell has one ion or molecule as well as each layer of atoms is in line with previous layer. If r is the radius of the atom, the lattice parameter a will be equal to $2r$. This particular phase is formed for a lot of materials for example PbTe, SnS and CZTS. Fang synthesised simple cubic structure of monodisperse PbTe crystal (Figure 1.3) when he used the mixture of trioctylphosphine (TOP) and oleylamine at 200 °C.²³ Cubic phase (π -SnS) discovered recently by Golan and co- workers.²⁴ Tin- ethylxanthate was used as single source precursor to produce π -SnS phase, the precursor was reacted with 1.53 g of octadecylamine (ODA) at 190 °C under nitrogen for 3 hours of reaction time. π -SnS is new cubic phase with lattice parameters of $a \approx 11.7$ Å. They indexed the dimensions of unit cell, the planes of reciprocal space of π -SnS have been determined along the highest symmetry orientation. Figure (1.4 a, b and c) show sharp reflection nodes of the [100], [110] and [111] planes. The same phase has been synthesised by Golan using the same complex at 150 °C, nanocubes π -SnS were analysed (figure 1.4 d and e), they determined the value of lattice parameter (a) of 11.595 Å by X-ray diffraction pattern. π -SnS has been structurally investigated by Raman spectrum which showed narrow peaks at 59 cm⁻¹, 71 cm⁻¹, 90 cm⁻¹, 112 cm⁻¹, 123 and a wider peak around 190 cm⁻¹.²⁵

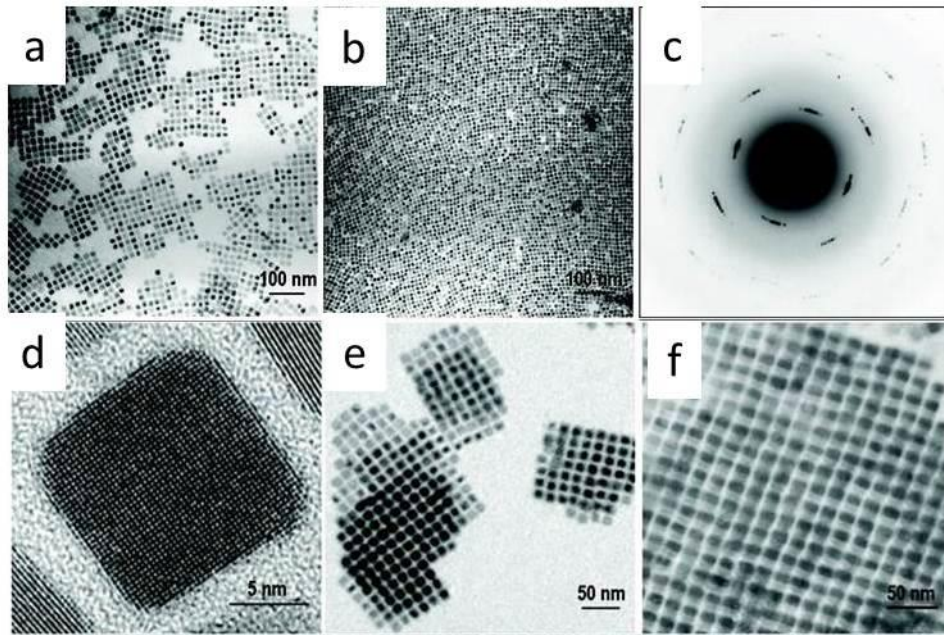


Figure 1.3. Electron microscope images of PbTe nanocubes. (a) TEM image of monodisperse lead telluride. (b) slow-processed lead telluride monolayer assembly. (c) Diffraction pattern of slow-processed monolayer assembly (negative pattern). (d) HRTEM image of a PbTe nanocube. (e) PbTe nanocube is stacked on the top of another. (f) 1D-shifted PbTe simple cubic stacking structure (the offset of the top layer along one axis by half a length of the cubic edge).²³

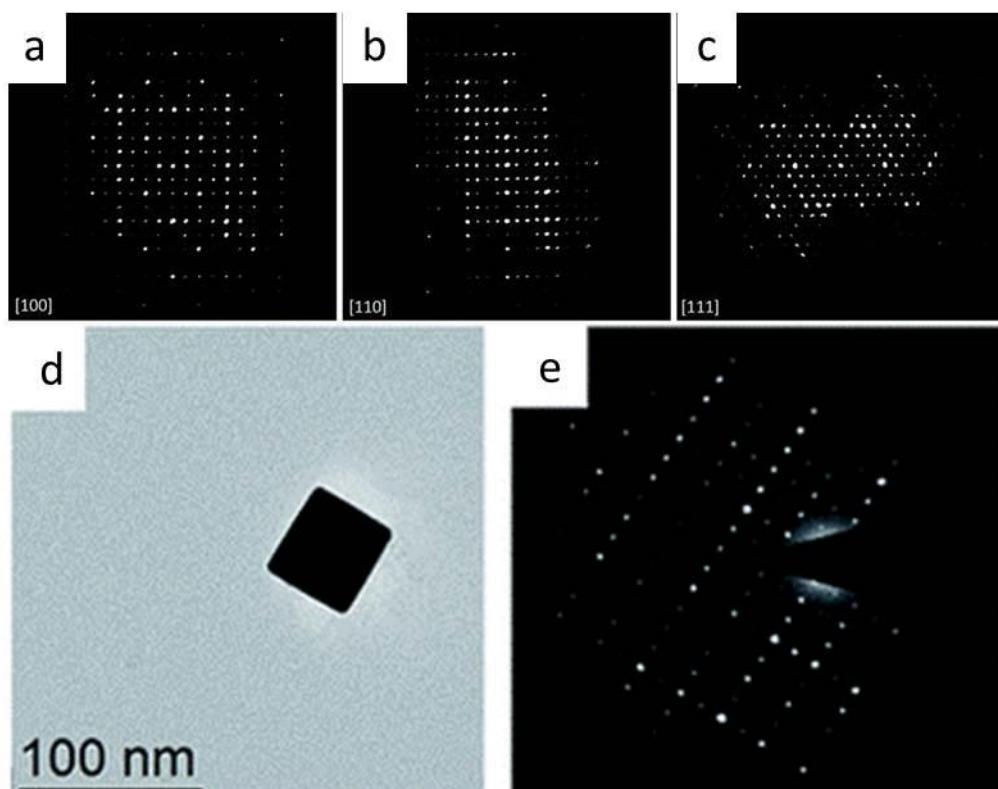


Figure 1.4. The precession electron diffraction tomography (PEDT) data obtained from single particle of the π -SnS. (a-c) Views along the [100], [110] and [111] directions, respectively. (d) a single cube-shaped nanoparticle, (e) SAED taken from (d), which matches to the [001] plane of the new π -SnS.^{24, 25}

1.4.2 Structure of face-centred cubic lattice

Most semiconductor compounds in the solid state can be deposited from close-packed lattices. The crystal structure of ZnS,²⁶ ZnO,²⁷ and GaAs,²⁸ have face-centred cubic lattice (FCC). The FCC unit cell has four anions, one at a corner and three at face centres. The positions of the four anions in the unit cell are 000, $\frac{1}{2}\frac{1}{2}0$, $\frac{1}{2}0\frac{1}{2}$ and $0\frac{1}{2}\frac{1}{2}$, also it has four tetrahedral sites (Figure 1.5 a) in positions 1, 2, 3, 4, and each of them is occupied by a cation. The coordinates of the four cations in FCC unit cell are: $\frac{3}{4}\frac{1}{4}\frac{1}{4}$, $\frac{1}{4}\frac{3}{4}\frac{1}{4}$, $\frac{1}{4}\frac{1}{4}\frac{3}{4}$ and $\frac{3}{4}\frac{3}{4}\frac{3}{4}$ respectively.^{29, 30}

The zincblende (sphalerite) is the structure that is generated when only half of the tetrahedral sites in FCC unit cell anions are captured by cations.²⁹ A typical example of zincblende structure is zinc sulfide (Figure 1.5b); each zinc atom (red sphere) is enclosed by four equidistant sulfur atoms (yellow sphere) at the corners of a tetrahedral site, which is demonstrated in terms of corner-sharing ZnS₄

tetrahedral. The zincblende structure has two FCC sublattices (Figure 1.5c) which are displaced one quarter along the body diagonal of the unit cell. One sublattice is occupied by zinc atoms at the positions 000 , $\frac{1}{2}0\frac{1}{2}$, and $0\frac{1}{2}\frac{1}{2}$ the other by sulfur atoms. The atoms in lattice are crystallized very close to each other. Theoretically the smallest nanoparticle consist of 13 atoms, this can happen only when two closed-packed structures have 12 atoms close to an atom located in the centre of a cube for a FCC structure.³¹

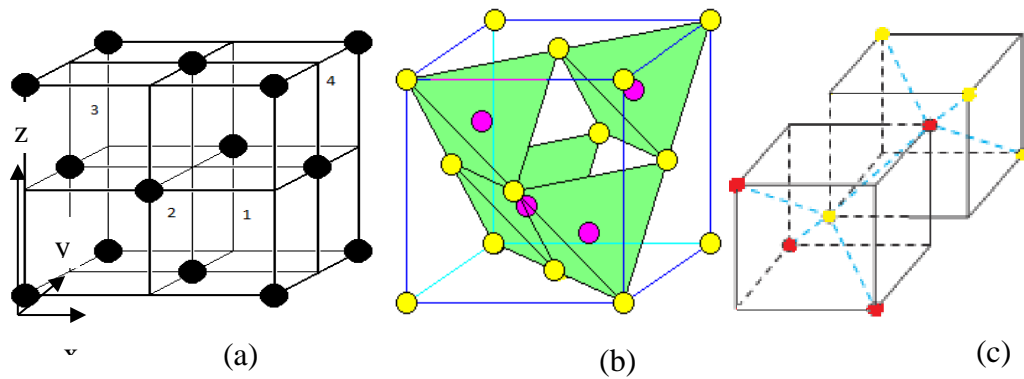


Figure 1.5. The zincblende (sphalerite) lattice structure, (a) face-centred cubic lattice arrangement with the positions of the tetrahedral sites (b) the structure of zinc sulfide unit cell, (c) shows the basic tetrahedral structure of ZnS in this structure each atom has four nearest neighbours of the opposite kind. In which each Zn atom has four nearest S neighbours and each S atom has four nearest Zn neighbours.²⁹

In addition $\text{Cu}_2\text{ZnSnS}_4$ (I-II-IV-VI) compound has zinc blende structure lattice. CZTS compound semiconductors are promising materials for optoelectronics application, the most important reason is their large energy band gap of $(1.45 - 1.6 \text{ eV})$ ³² and it can be further increased by adding (Se) in CZTS.³³ The second, an absorption coefficient of over 10^4 cm^{-1} ,³⁴ another reason is that the CZTS is based on abundant elements, each element of CZTS is plentiful in the Earth's crust (copper: 50 ppm, zinc: 75 ppm, tin: 2.2 ppm, sulfur: 260 ppm),³⁵ environmentally friendly nature of the constituent materials is another advantage.³⁶

$\text{Cu}_2\text{ZnSnS}_4$ thin films have been prepared using several techniques such as chemical vapor deposition (CVD),³⁷ co-sputtering continued with sulfuration from vapor

phase method,³⁸ chemical bath deposition,³⁹ successive ionic layer adsorption and reaction (SILAR) method,⁴⁰ one step solvothermal treatment of layered elemental copper/zinc/tin film with sulfur powder.⁴¹

In recent years there has been increased interest in the design and fabrication of CZTS thin films because of its special optical properties. Chemical vapour deposition method (CVD) is widely used in the fabrication of CZTS nanoparticles. It involves the sulfurization of thermally deposited metallic precursors;⁴² also, doctor's blade and spin coating are promising methods to deposit CZTS nanoparticle films; however, CZTS thin films prepared using these methods need high temperature annealing and contain unidentified impurities; for instance, the CZTS thin films deposited using doctor's blade method by Singh *et al.* using CZTS paste after drying treatment at 100 °C for 30 min in air, followed by annealing at 500°C.⁴³ Schnabel *et al.* reported a $\text{Cu}_2\text{ZnSn}(\text{S},\text{Se})_4$ absorber layer solar cell with an efficiency of 7.5 % using metal salts deposited on a Mo-coated soda lime glass by doctor's blade method, and a subsequent high temperature annealing in a Se-containing nitrogen atmosphere, annealing temperature was 540 °C.⁴⁴

The structure of the $\text{Cu}_2\text{ZnSnS}_4$ unit cell is zinc blende structure similar to zinc sulfide. It derives from the chalcopyrite structure of a CuInS_2 by changing indium atoms for zinc and tin atoms, this result in three different structures that^{45, 46} depend on the position of atoms in tetrahedral coordination. The first structure is kesterite CZTS (Figure 1.6a), it has the space group $I\bar{4}$. In the kesterite structure there are two levels of atoms in tetrahedral site, Zn and one of the Cu atom are ordered at 2d and 2c respectively in the first level, the remaining Cu atom occupies the 2a position in the second level. The Sn atom is located at 2b in first level of tetrahedral site. The second structure is stannite CZTS (Figure 1.6b), it has the space group $I\bar{4}2m$. Tetrahedral site in stannite structure contains; Zn atom is at 2a position, Sn atom at 2b and two Cu atoms occupy the 4d. The third structure is the primitive mixed CuAu-like structure (PMCA) (Figure 1.6c), which is derived from the CuAu-like structure. The space group in this structure is $P42m$.^{47, 48}

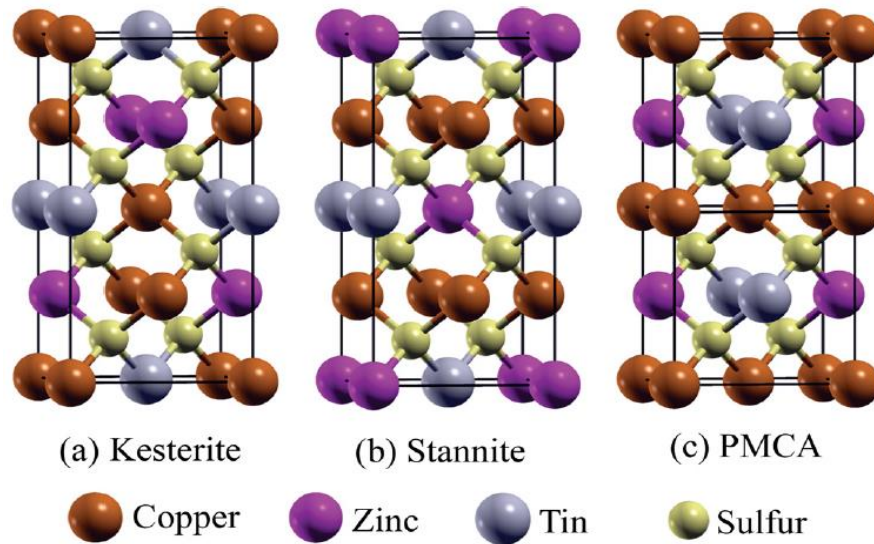


Figure 1.6. Unit cell representations of $\text{Cu}_2\text{ZnSnS}_4$; (a) the kesterite type structure, (b) stannite type structure, and (c) the primitive mixed CuAu-like structure (PMCA).⁴⁸

Zunger *et al.*^{49, 50} have established that strain energy is responsible for stability of CZTS crystal structure. They found that for large lattice mismatch ($\Delta a/a$) ($\Delta a/a$ is a term to characterize the interface between two materials), the kesterite structure has lower strain energy, which means that chalcopyrite is more stable than CuAu-like structure; as a result, the stability of kesterite structure is higher than the stannite and PMCA but there is small difference in strain energy between the kesterite and stannite structure, about 3 meV/atom.

1.5 Electrical properties of semiconductors

The Van der Pauw method is one of the most easily used methods of the four-probe mode of determining the carrier concentration, mobility and Hall coefficient of materials in the form of thin films.⁵¹ The Hall effect is an effect that is generally used to distinguish the polarity of semiconductor. When the Hall probe is placed in an area of the film with a magnetic field and it is crossed by an electric current perpendicular to the field, due to the Lorentz force on a charged particle moving through a magnetic field, a voltage difference appears perpendicular to both the current and magnetic field, known as the Hall voltage. The value of Hall voltage completely depends on the magnetic field and the electric current amplitudes. The Hall voltage is an indicator of the semiconductor type doping (acceptor or donor),

and it presents different signals for n-type or p-type semiconductors. In practice, the magnetic force has the same direction, independently of the type of majority carriers in the semiconductor. In n-type materials the majority of carrier are electrons, in p-type materials the mobile charge that moves is positive. This influences the voltages with opposite polarities in the two mentioned situations. To increase the sensitivity of Hall measurement, the magnetic field should be arranged in the direction of the smallest dimension of the Hall sensor.⁵²

1.6 Optical properties of semiconductors

Studies of optical properties of semiconductor thin films are required; firstly, to calculate important parameters such as absorption coefficient and refractive index that are necessary for designing photovoltaic devices: Secondly, to acquire data on optical band gap.⁵³ One of the most effective techniques to record the optical properties of semiconductor nanoparticles is UV-Visible absorption spectroscopy. It is a practical method of studying the optical band gap. According to the Tauc relation, the optical band gap (E_g) of semiconductor thin films is obtained from transmission spectra by plotting $(\alpha h\nu)^2$ as a function of incident photon energy. The Tauc equation can be written as:^{54, 55}

$$\alpha h\nu = A(h\nu - E_g)^n \quad (1.2)$$

Where α is the absorption coefficient which can be defined as the ability of the materials to absorb photons of a given wavelength,⁵⁶ h is the Planck constant, ν is the photon frequency, A is a constant, and n is an index which assumes the values ($1/2$ or 2) depending on the nature of electronic transition.⁵⁷ For the direct permitted transitions, n has a value of $1/2$ while for indirect permitted transitions, $n = 2$. The absorption regions in materials can accurately be classified into three parts, the value of α can vary from part to part depending on incident photons energies, there is a plentiful absorption of photons with energy larger than E_g in region (1) Figure 1.7, the value of α is $\geq 10^4 \text{ cm}^{-1}$ which is suitable for calculation of the band gap of the materials by applying the Equation 1.2. The exponential region in part 2 of Figure (1.7) has a value of α in the range of $1 \leq \alpha \leq 10^4 \text{ cm}^{-1}$. In the low photon energy range, the spectrum is known as Urbach energy, which is given by the following equation:^{56, 58}

$$\alpha = \alpha_0 e^{hv/E_u} \quad (1.3)$$

Whereas a little absorption happens at long wavelength in region (3) which may be called weak absorption region since the value of α is $\leq 1 \text{ cm}^{-1}$.

One of the examples of using the Tauc relation was reported by Tanaka *et al.* They reported the deposition of $\text{Cu}_2\text{ZnSnS}_4$ thin films by a sputtering-sulfurization method. They found that the optical band gap energy of CZTS was 1.4–1.6 eV and the band gap did not depend on composition of CZTS.⁵⁹ Fernandes *et al.* fabricated a device using CZTS by the electrodeposition method, they used the External Quantum Efficiency (EQE) curve to calculate the energy band gap of CZTS. Plotting $(hv \cdot \ln(1 - \text{EQE}))^2$ against hv , a band gap of 1.65 eV was obtained for the CZTS absorber.⁶⁰ The same method had been used by Deligianni *et al.* to calculate the optical band gap of CZTS, the CZTS layer showed the E_g of 1.57 eV.

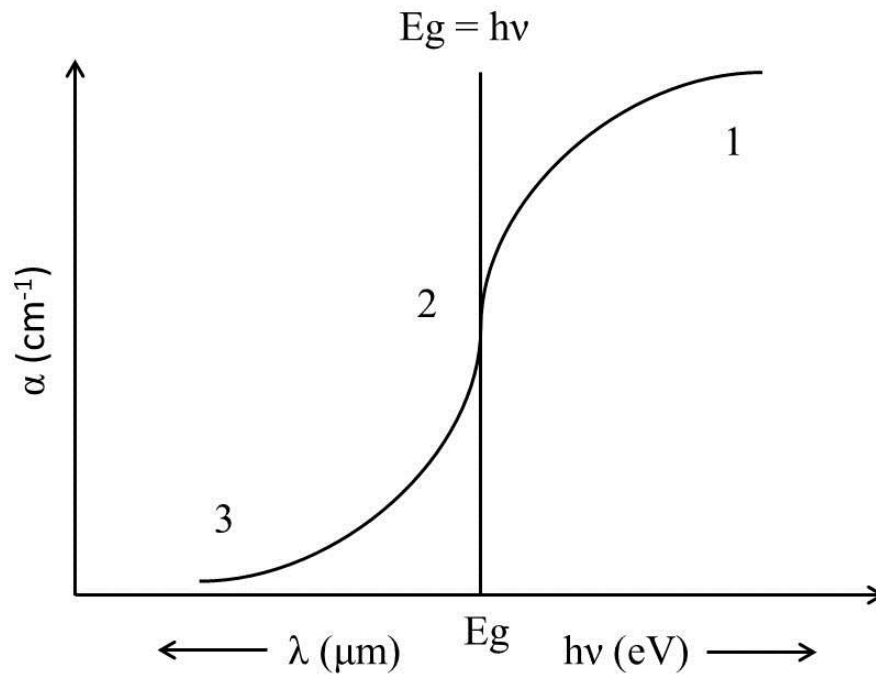


Figure 1.7. The variation of absorption coefficient α for a semiconductor with the wavelength of incident photons.

1.7 Metal sulfide thin films

Metal sulfides are important semiconductors, with a wide range of electronic properties that change with grain size of particles.^{61, 62} This group of materials has

supplied many unique opportunities and indicated different electrical and optical properties, which are potentially useful for technological applications.^{63, 64} They have potential applications in optoelectronic devices for example, metal sulfides smaller than about 10 nm have potential applications in light emitting diodes,⁶⁵ electroluminescent devices as well as photovoltaic conversion.⁶⁶ Larger sulfide particles in the size from 10 to 500 nm can be used as window layer heterojunction solar cells and photonic crystals.⁶⁷

1.7.1 Precursors for metal sulfide thin films

The controlled synthesis of metal sulfide compounds using single source precursor has engaged a great deal of attention in technical applications.⁶⁸ Colloidal and chemical vapour deposition (CVD) methods are mostly used to deposit metal sulfides thin films from single source precursor,^{69, 70} which contain both the metal and sulfur in one molecule.⁷¹ The single-source approach has the advantage such as improved air/moisture stability, low toxicity and control the stoichiometry of materials.⁷² Kukimoto *et al.* reported the deposition of ZnSe from various kinds of source materials (multi-source precursors) including diethyl zinc, dimethyl zinc, diethyl selenide, and dimethyl selenide by MOVPE method. They considered that a reaction may happen between dialkyl selenide and dialkylzinc,⁷³ may that one of disadvantage of single source precursor. This can lead to inhomogeneity and stoichiometry control complications.

1.7.1.1 (Dialkyldithiocarbamato) metal complexes

Dithiocarbamates have the general formula $[M(S_2CNRR')_n]$ and they find wide application in technology as anti-cancer agents, anti-microbial agents,⁷⁴ fungicides,⁷⁵ and in chemistry to detect nitric oxide,⁷⁶ and deposit metal sulfide thin films.⁷⁷ There are many reasons for the continuous interest in these complexes. Dithiocarbamates show high thermal stability⁷⁸ and their thermal decomposition generally starts from about 200°C;⁷⁹ Furthermore, they have the advantage to act as a monodentate or as a bidentate and chelating ligand.⁸⁰ The crystal structure of dithiocarbamate complexes show the metal atoms are surrounded by the octahedral structure of four sulfur atoms and the monomeric nature of complexes.^{81, 82} Coordination of dithiocarbamate ligands is given in figure 1.8.

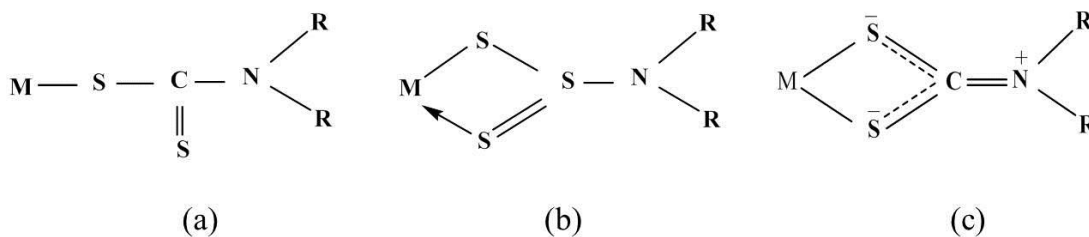
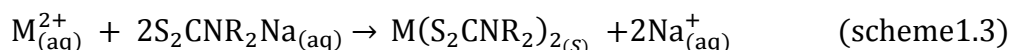


Figure 1.8. Three different coordination modes of dithiocarbamate groups (a) monodentate, (b) asymmetric bidentate, and (c) symmetric bidentate.⁸⁰

Dithiocarbamate ligands are synthesized by the reaction between carbon disulfide and a primary or secondary dialkyl amine with sodium or potassium hydroxide as follows:^{83, 84}



Where R = alkyl group, M=metals. According to scheme (1.3), dithiocarbamate complex is obtained by the reaction between a solution of sodium dithiocarbamate ligand and an aqueous transition metal salt.



There have been various studies on the use of dithiocarbamate for the growth of metal sulfide nanomaterials. For example, O'Brien *et al.* reported the preparation of $Co_{1-x}S$ films from $[Co(N-(SCNMe_2)_2)_3]$ complex,⁸⁵ ZnS and CdS films from $[Zn(N-(SCNMe_2)_2)_2]$, $[Cd(N-(SCNMe_2)_2)_2]$ respectively using an aerosol assisted chemical vapour deposition (AACVD) method.⁸⁶ In addition, they reported recently the synthesis of symmetric and asymmetric diorganotin dithiocarbamates as precursors for the deposition of orthorhombic SnS nanoparticles.⁷⁷

1.7.1.2 (O-alkyldithiocarbomato)metal complexes

Xanthates have the general chemical formula $[M(S_2COR)^n]$.⁸⁷ They have been prepared as precursors to deposit metal sulfide nanoparticles; in fact, great success has been achieved with xanthate single source precursors,^{88, 89} which are more promising due to their typically lower decomposition temperatures.^{90, 91} Similar to

the dithiocarbamate groups, xanthates are also constituted in three main forms,⁹² (Figure 1.9) ; monodentate, isobidentate, and anisobidentate. They are divided into three more unusual forms, which are obtained by metal- oxygen interaction or when bimetallic bond happens between sulfur atoms or sulfur and oxygen atoms.⁹³

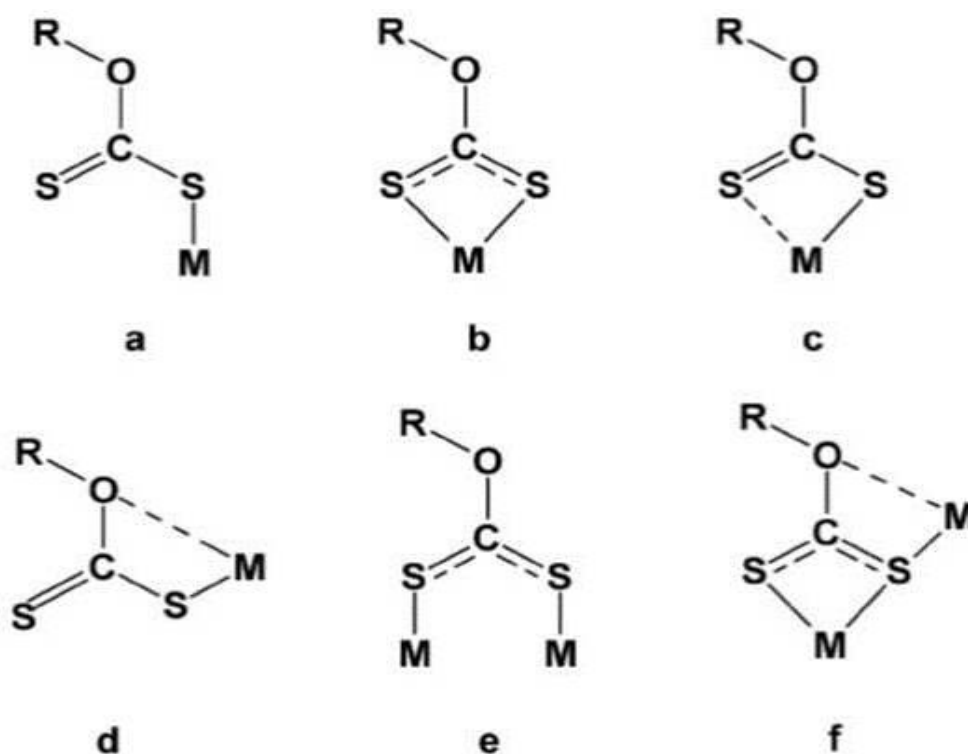
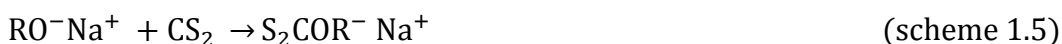


Figure 1.9. Xanthate ligands are classified as: (a) monodentate, (b) isobidentate and (c) anisobidentate, and three more rare forms (d, e, f).⁹³

One of the first reports on the study of C-O vibration frequencies and S-C-S bond angles of iron, nickel, copper, zinc, and lead ethylxanthate was by Winter *et al.* They suggested that the frequency depends on the coordination around the oxygen atom and the type of bond with alkoxy group, the reason of the variation in the position of the C-O band is the variation of the S-C-S angles. Low frequency would be expected for S-C-S greater than 120° while for S-C-S less than 120° the frequency will be higher.⁹⁴

Xanthate ligands are formed by the reaction between sodium or potassium hydroxide, alcohol, and carbon disulfide as follows:



A reaction between a transition metal salt and a solution of sodium ethylxanthate produces the metal complex.



The scheme (1.6) is used to synthesise most of the metal xanthate complexes like lead alkyl xanthate,⁹⁵ cadmium(II) xanthate and zinc(II) xanthate⁹⁶. However, copper(II) xanthate decompose to copper(I) xanthate and dixanthogen (ROC(S)S–SC(S)OR) where R = Me, Et, Pr and Bu.^{97, 98}

Thermal decomposition processes of metal xanthates have been investigated intensively, a Chugaev reaction derives this process.⁹⁹ In this reaction (Figure 1.10), metal xanthate is decomposed into a metal thioalkyl, alkene, and carbonyl sulfide. Metal sulfide is obtained by a subsequent carbonyl sulfide and hydrogen sulfide elimination processes.⁸⁸

Butler *et al.* analysed the decomposition mechanisms of the metal xanthato, iron, zinc, copper, lead, and nickel ethylxanthates, they found that the decomposition reaction of iron and zinc complexes produce a constant ratio of CS₂ to COS, and the triatomic species eliminate to form a metal alkoxide or thioalkyl species. They described the same result for copper, lead, nickel ethylxanthates, but the decomposition rate was very low in comparison with iron and zinc ethylxanthates. Also the reactions generated more highly oxygenated metal.¹⁰⁰

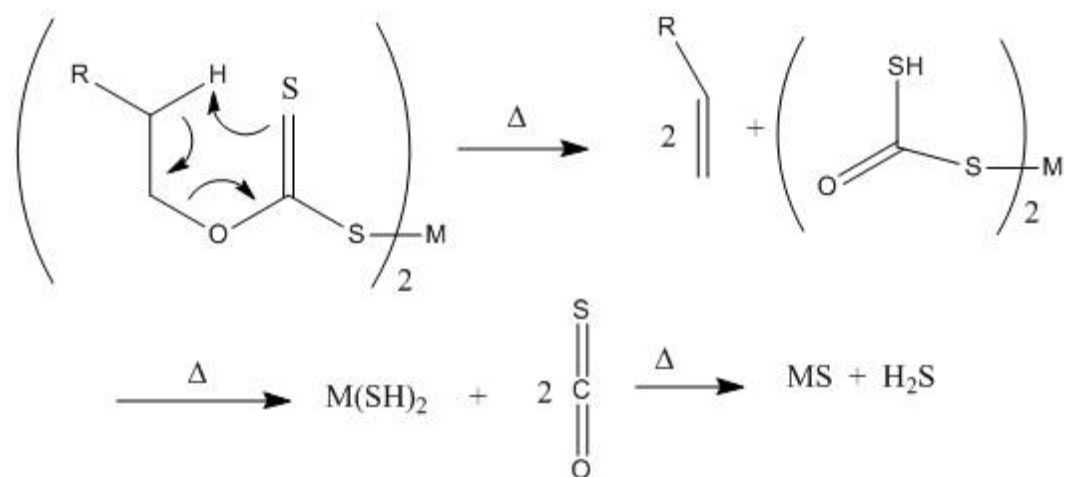


Figure 1.10. Decomposition process of metal alkylxanthate complexes by Chugaev elimination reaction.

1.8 Deposition techniques for metal sulfide thin films

1.8.1 Chemical vapour deposition

Chemical vapor deposition (CVD) has been employed to prepare nanoparticles material uniformly distributed on surface of the substrate,¹⁰¹ high crystalline,¹⁰² and high purity.¹⁰³ Varieties of materials have been deposited by CVD because it has several important technical features, the reactions are done in hot wall and cold wall, at wide range of temperature from 200 to 1800 °C, and at high vacuum to high atmospheric pressure.^{104, 105}

In a typical CVD process (Figure 1.11) precursors evaporate and transfer into the reaction zone by gas flow. Argon or nitrogen has been mostly used as main gas flow in CVD, one or more volatile precursors react to produce new reactive species in gas phase. In the reaction zone the substrate is directly exposed to volatile precursors, which react on the substrate surface to produce the solid film formation.

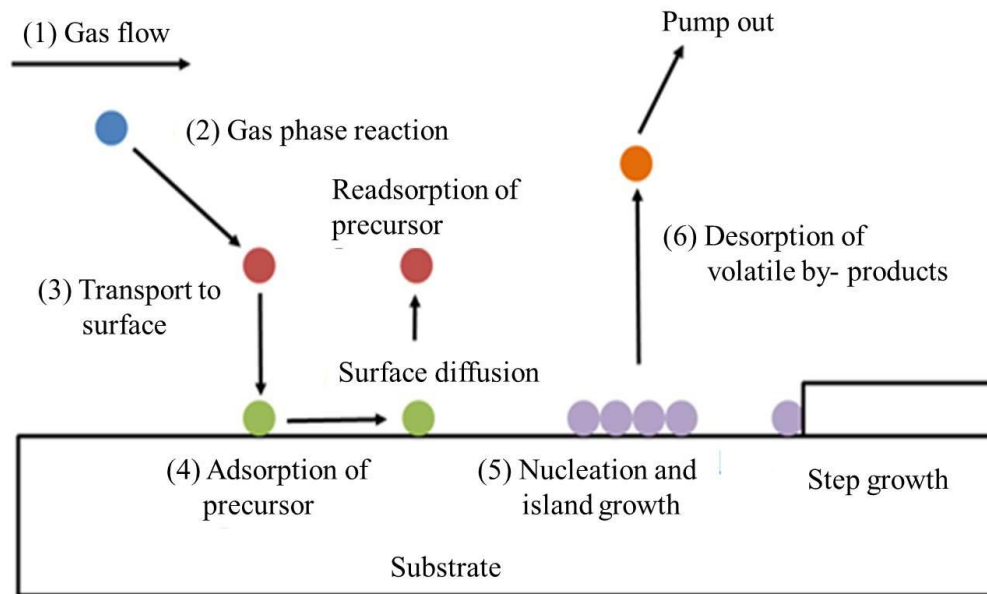


Figure 1.11. Fundamental steps that lead to chemical vapor deposition (CVD) of thin films^{106, 107}

Parameters such as the volatility and solubility of the precursor, the deposition temperature, and the carrier gas flow rate will determine the quality of the film.¹⁰⁶ Various types of CVD have been used to deposit metal sulfide thin films. Use of these different types is dependent on solubility and volatility of precursors.

1.8.1.1 Low pressure CVD (LPCVD)

LPCVD has been used to produce highly uniform films at relatively low deposition temperature.¹⁰⁸ LPCVD reaction can occur in a closed reactor system, and a low pressure reactor is generally operated at a wide range of temperatures. In this method a rotary mechanical pump has been used to evacuate the reaction chamber thus; LPCVD uses low volatility precursors. Growth rate depends on the variations in flow rates and reactor temperature profiles.¹⁰⁹

1.8.1.2 Atmospheric pressure CVD (APCVD)

APCVD technique can be used when the precursors are volatile enough for transport at atmospheric pressure. The APCVD has the advantage over LPCVD method in that it can be done at atmospheric pressure and it has fast growth rates.^{110, 111}

1.8.1.3 Aerosol assisted CVD (AACVD)

AACVD reaction can occur in open reactor systems, the reactants are carried from precursor solution into the reaction chamber by a carrier gas (Figure 1.12). AACVD is suitable for deposition of thin films from high solubility precursors because of its simple operation.¹¹² Growth rate and film thickness depends on the gas flow rates and deposition temperature.

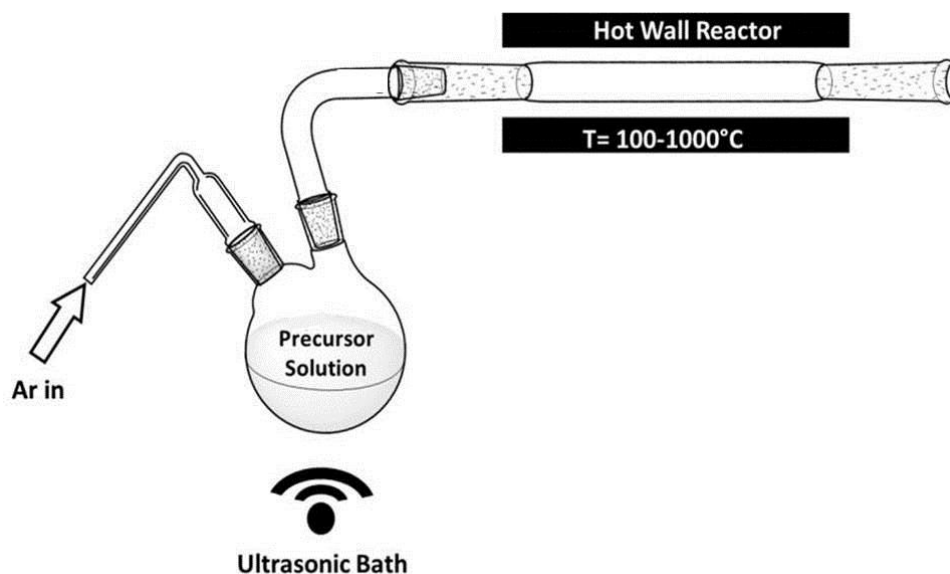


Figure 1.12. Schematic representation of the AACVD set up.

1.8.2 Spin coating technique

Spin coating has been applied for several years for device application and films. A typical process entails: First the substrate is coated in the ink containing the precursors dissolved in an appropriate solvent (Figure 1.13), then the substrate is rotated and the majority of the ink will be scattered around, or during the continuous rotation of the substrate the ink is dropped on it. The film obtained from the spin coating method should be fully dried and annealed.¹¹³ In order to produce thin film with high quality, substrate cleaning, rotation speed of substrate and the time of rotation must be carefully controlled. The advantages of using spin coating are the simplicity and it is easy to control the parameters,¹¹⁴ however it has low throughput since only one substrate can be coated at one time.¹¹⁵

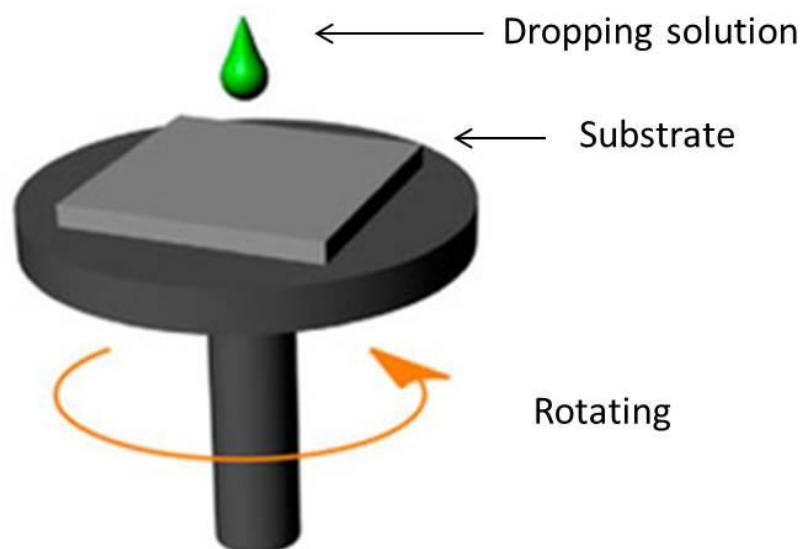


Figure 1.13. Schematic of spin coating process.

1.8.3 Doctor blade technique

Doctor blading is a perfectly-understood laboratory method to deposit a semiliquid precursor (paste) resulting in high uniformly thin film,¹¹⁶ the paste is deposited moderately over the substrates using a coating knife. In this method, an amount of precursor is placed directly onto the substrate. If the precursor has low viscosity, it is laid in the gap between the substrate and the blade.¹¹⁵ Subsequently the knife is transferred gently along the substrate with an adjustable motion. A humid thin film is left behind, which dries because of the evaporation of the liquid after drying treatment in appropriate temperature. A schematic picture of the doctor blade process is given in (Figure 1.14). The film thickness is dependent on both the precursor properties and the blading parameters for instance, the gap width between blade and substrate, the temperature of the substrate, the viscosity of the precursor, and blading speed.¹¹⁵

1.8.4 The hot-injection method

The method that involved the injection of precursor solution at a room temperature into a hot solvent is the hot injection.

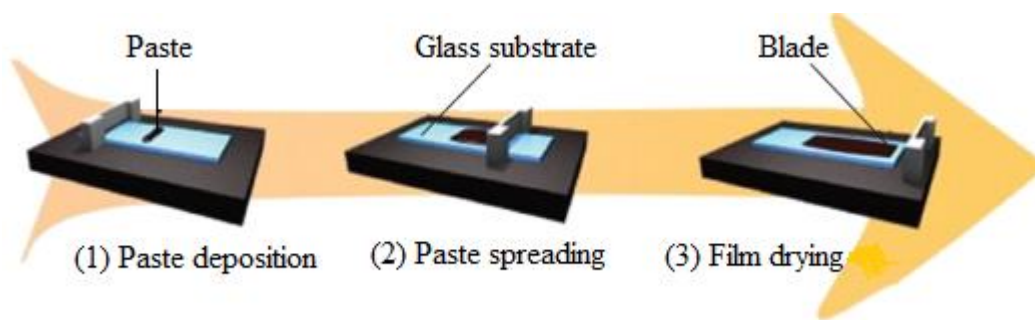


Figure 1.14. The Doctor's blade deposition processes. Stage (1): the compound paste is laid onto substrate, stage (2): the blade spreads the paste over the substrate, stage (3): the achieved film is dried. ¹¹⁵

This method is widely used to synthesise nanocrystalline materials such as CdTe,¹¹⁷ InP¹¹⁸ and CdS/ZnS core-shell nanocrystals.⁶⁵ The hot injection has been employed to control the sizes and shapes of the nanocrystal, to produce monodisperse nanoparticles and prepare the highly luminescent semiconductor nanocrystals. The crystal defects may be influenced by growth rate, the ability of using non-ionic precursors in organic solvents makes the hot injection a good method to control the growth rate.^{119, 120} Oleylamine and trioctylphosphine are the most common solvents that have been used in hot injection.

1.9 The aims of the present study

The objective of this study is to synthesise xanthate single-source precursors for the formation of nanoparticles and deposition of thin films. Metal xanthate complexes show interesting thermal behaviour, and these complexes could be a good choice to produce binary, ternary and quaternary metal sulfide at low temperatures, since the complexes decompose at low temperature. Furthermore, we hypothesise their xanthate complexes may lead to low - temperature synthesis of alkali metal chalcogenide thin films that have previously only been produced from a high temperature, high pressure reaction system. Finally, the synthesis of xanthate complexes with different chain length could be useful to study the variations of physical properties of metal sulfide compounds.

Chapter two will present the structures and some properties of sulfide phases directly relevant to this research.

1.10 References

1. X. Huang, S. Han, W. Huang and X. Liu, *Chem. Soc. Rev.*, 2013, **42**, 173-201.
2. J. Liqiang, Q. Yichun, W. Baiqi, L. Shudan, J. Baojiang, Y. Libin, F. Wei, F. Honggang and S. Jiazhong, *Sol. Energy Mater Sol. Cells*, 2006, **90**, 1773-1787.
3. C.-H. Lai, M.-Y. Lu and L.-J. Chen, *J. Mater. Chem.*, 2012, **22**, 19-30.
4. N. Chaniotakis and N. Sofikiti, *Anal. Chim. Acta.*, 2008, **615**, 1-9.
5. M. Heiss, S. Conesa-Boj, J. Ren, H.-H. Tseng, A. Gali, A. Rudolph, E. Uccelli, F. Peiró, J. R. Morante and D. Schuh, *Phys. Rev. B*, 2011, **83**, 045303.
6. J. Blakemore, *J. Appl. Phys.*, 1982, **53**, R123-R181.
7. K. Hjort, J. Soderkvist and J.-A. Schweitz, *J. Micromech. Microeng.*, 1994, **4**, 1.
8. S. Strite and H. Morkoç, *J. Vac. Sci. Technol. B*, 1992, **10**, 1237-1266.
9. S. Nakamura, M. Senoh and T. Mukai, *Jpn. J. Appl. Phys.*, 1991, **30**, L1708.
10. G. Stringfellow, H. Hall Jr and R. Burmeister, *J. Appl. Phys.*, 1975, **46**, 3006-3011.
11. S. Assali, I. Zardo, S. Plissard, D. Kriegner, M. Verheijen, G. Bauer, A. Meijerink, A. Belabbes, F. Bechstedt and J. Haverkort, *Nano Lett.*, 2013, **13**, 1559-1563.
12. X. Xia, C. Zhu, J. Luo, Z. Zeng, C. Guan, C. F. Ng, H. Zhang and H. J. Fan, *small*, 2014, **10**, 766-773.
13. C. Goodman, *J. Phys. Chem. Solids*, 1958, **6**, 305-314.
14. H. Ong and R. Chang, *Appl. Phys. Lett.*, 2001, **79**, 3612-3614.
15. A. Martinez, L. Arriaga, A. Fernandez and U. Cano, *Mater. Chem. Phys.*, 2004, **88**, 417-420.
16. H. Yu, J. Li, R. A. Loomis, L.-W. Wang and W. E. Buhro, *Nat. Mater.*, 2003, **2**, 517.
17. A. Dong, H. Yu, F. Wang and W. E. Buhro, *J. Am. Chem. Soc.*, 2008, **130**, 5954-5961.
18. P. Trwoga, A. Kenyon and C. Pitt, *J. Appl. Phys.*, 1998, **83**, 3789-3794.
19. A. Yoffe, *Adv. Phys.*, 2002, **51**, 799-890.

20. A. Dong, H. Yu, F. Wang and W. E. Buhro, *J. Am. Chem. Soc.*, 2008, **130**, 5954-5961.
21. W. E. Buhro and V. L. Colvin, *Nat. Mater.*, 2003, **2**, 138.
22. S. Kan, T. Mokari, E. Rothenberg and U. Banin, *Nat. Mater.*, 2003, **2**, 155.
23. J. Zhang, A. Kumbhar, J. He, N. C. Das, K. Yang, J.-Q. Wang, H. Wang, K. L. Stokes and J. Fang, *J. Am. Chem. Soc.*, 2008, **130**, 15203-15209.
24. A. Rabkin, S. Samuha, R. E. Abutbul, V. Ezersky, L. Meshi and Y. Golan, *Nano Lett.*, 2015, **15**, 2174-2179.
25. R. E. Abutbul, E. Segev, L. Zeiri, V. Ezersky, G. Makov and Y. Golan, *RSC Adv.*, 2016, **6**, 5848-5855.
26. C. Ma, D. Moore, J. Li and Z. L. Wang, *Adv. Mater.*, 2003, **15**, 228-231.
27. M. Hakamada, M. Yuasa, T. Yoshida, F. Hirashima and M. Mabuchi, *Appl. Phys. A*, 2014, **114**, 1061-1066.
28. S. Golin, S. Kirkwood, D. Klug, D. Villeneuve, D. Rayner, C. T. Herrero and P. Corkum, *J. Phys. B*, 2014, **47**, 204025.
29. H. V. Keer, *Principles of the solid state*, New Age International, 1993.
30. A. R. West, *Solid state chemistry and its applications*, John Wiley & Sons, 2007.
31. P. Charles and O. Frank, *Published by John Wiley & Sons, Inc., Hoboken, New Jersey*, 2003, 226-234.
32. N. Shinde, R. Deokate and C. Lokhande, *J. Anal. Appl. Pyrolysis*, 2013, **100**, 12-16.
33. H. Wei, Z. Ye, M. Li, Y. Su, Z. Yang and Y. Zhang, *CrystEngComm*, 2011, **13**, 2222-2226.
34. H. Araki, A. Mikaduki, Y. Kubo, T. Sato, K. Jimbo, W. S. Maw, H. Katagiri, M. Yamazaki, K. Oishi and A. Takeuchi, *Thin Solid Films*, 2008, **517**, 1457-1460.
35. H. Katagiri, K. Jimbo, W. S. Maw, K. Oishi, M. Yamazaki, H. Araki and A. Takeuchi, *Thin Solid Films*, 2009, **517**, 2455-2460.
36. P. Kush, S. K. Ujjain, N. C. Mehra, P. Jha, R. K. Sharma and S. Deka, *ChemPhysChem*, 2013, **14**, 2793-2799.
37. K. Ramasamy, M. A. Malik and P. O'Brien, *Chemical Science*, 2011, **2**, 1170-1172.

38. R. Schurr, A. Hölzing, S. Jost, R. Hock, T. Voß, J. Schulze, A. Kirbs, A. Ennaoui, M. Lux-Steiner and A. Weber, *Thin Solid Films*, 2009, **517**, 2465-2468.
39. A. Wangperawong, J. King, S. Herron, B. Tran, K. Pangan-Okimoto and S. Bent, *Thin Solid Films*, 2011, **519**, 2488-2492.
40. Z. Su, C. Yan, K. Sun, Z. Han, F. Liu, J. Liu, Y. Lai, J. Li and Y. Liu, *Appl. Surf. Sci.*, 2012, **258**, 7678-7682.
41. L.-J. Chen and Y.-J. Chuang, *Mater. Lett.*, 2013, **91**, 372-375.
42. K. Ramasamy, M. A. Malik and P. O'Brien, *Chemical Communications*, 2012, **48**, 5703-5714.
43. B. Pani and U. P. Singh, *J. Renew. Sustain. Energy*, 2013, **5**, 053131.
44. T. Schnabel, M. Löw and E. Ahlswede, *Sol. Energy Mater. Sol. Cells*, 2013, **117**, 324-328.
45. S. Chen, X. Gong, A. Walsh and S.-H. Wei, *Appl. Phys. Lett.*, 2009, **94**, 041903.
46. J. Paier, R. Asahi, A. Nagoya and G. Kresse, *Phys. Rev. B*, 2009, **79**, 115126.
47. D. S. Su and S.-H. Wei, *Appl. Phys. Lett.*, 1999, **74**, 2483-2485.
48. A. Khare, B. Himmetoglu, M. Johnson, D. J. Norris, M. Cococcioni and E. S. Aydil, *Journal of Applied Physics*, 2012, **111**, 083707.
49. J. E. Bernard, L. Ferreira, S.-H. Wei and A. Zunger, *Phys. Rev. B*, 1988, **38**, 6338.
50. R. Magri, S.-H. Wei and A. Zunger, *Phys. Rev. B*, 1990, **42**, 11388.
51. A. Ramadan, R. Gould and A. Ashour, *Thin Solid Films*, 1994, **239**, 272-275.
52. J. Orton and M. Powell, *Rep. Prog. Phys.*, 1980, **43**, 1263.
53. T. P. Dhakal, C. Y. Peng, R. R. Tobias, R. Dasharathy and C. R. Westgate, *Solar Energy*, 2014, **100**, 23-30.
54. Y. Wang, C. Li, X. Yin, H. Wang and H. Gong, *ECS J. Solid State Sci. Technol.*, 2013, **2**, Q95-Q98.
55. M. Y. Yeh, Y.-J. Liao, D.-S. Wu, C.-L. Huang and C.-D. Yang, in *Adv. Mater.*, Springer, 2014, pp. 45-53.
56. K. Gupta and N. Gupta, *Advanced semiconducting materials and devices*, Springer, 2016.
57. A. Tanuševski and D. Poelman, *Sol. Energy Mater Sol. Cells*, 2003, **80**, 297-303.

58. A. Hassanien and A. A. Akl, *Superlattices Microstruct.*, 2016, **89**, 153-169.
59. K. Tanaka, T. Shinji and H. Uchiki, *Sol. Energy Mater Sol. Cells*, 2014, **126**, 143-148.
60. P. Fernandes, P. Salomé, A. Da Cunha and B.-A. Schubert, *Thin Solid Films*, 2011, **519**, 7382-7385.
61. Y. Xia, B. Gates, Y. Yin and Y. Lu, *Adv. Mater.*, 2000, **12**, 693-713.
62. Y. Yin, Y. Lu, B. Gates and Y. Xia, *J. Am. Chem. Soc.*, 2001, **123**, 8718-8729.
63. W. U. Huynh, J. J. Dittmer and A. P. Alivisatos, *science*, 2002, **295**, 2425-2427.
64. B. Sun, E. Marx and N. C. Greenham, *Nano Lett.*, 2003, **3**, 961-963.
65. J. S. Steckel, J. P. Zimmer, S. Coe-Sullivan, N. E. Stott, V. Bulović and M. G. Bawendi, *Angew. Chem. Int. Ed.*, 2004, **43**, 2154-2158.
66. V. Biju, T. Itoh, A. Anas, A. Sujith and M. Ishikawa, *Anal. Bioanal. Chem.*, 2008, **391**, 2469-2495.
67. B. Sun, Y. Hao, F. Guo, Y. Cao, Y. Zhang, Y. Li and D. Xu, *The Journal of Physical Chemistry C*, 2011, **116**, 1395-1400.
68. K. Sukola, F. Wang and A. Tessier, *Anal. Chim. Acta.*, 2005, **528**, 183-195.
69. M. Afzaal, M. A. Malik and P. O'Brien, *J. Mater. Chem.*, 2010, **20**, 4031-4040.
70. S. L. Cumberland, K. M. Hanif, A. Javier, G. A. Khitrov, G. F. Strouse, S. M. Woessner and C. S. Yun, *Chem. Mater.*, 2002, **14**, 1576-1584.
71. P. S. Nair, T. Radhakrishnan, N. Revaprasadu, G. Kolawole and P. O'Brien, *J. Mater. Chem.*, 2002, **12**, 2722-2725.
72. B. P. Bade, S. S. Garje, Y. S. Niwate, M. Afzaal and P. O'Brien, *Chem. Vap. Deposition*, 2008, **14**, 292-295.
73. H. Mitsuhashi, I. Mitsuishi and H. Kukimoto, *J. Crys. Growth*, 1986, **77**, 219-222.
74. E. R. Tiekink, *Appl. Organomet. Chem.*, 2008, **22**, 533-550.
75. R. Kesari and V. Gupta, *Talanta*, 1998, **45**, 1097-1102.
76. S. Fujii and T. Yoshimura, *Coord. Chem. Rev.*, 2000, **198**, 89-99.
77. K. Ramasamy, V. L. Kuznetsov, K. Gopal, M. A. Malik, J. Raftery, P. P. Edwards and P. O'Brien, *Chem. Mater.*, 2013, **25**, 266-276.

78. M.-L. RIEKKOLA, T. PAKKANEN and L. Niinisto, *Acta Chem. Scand. A.*, 1983, **37**, 807-816.
79. D. Ondrušová, E. Jona and P. Šimon, *J. Therm. Anal. Calorim.*, 2002, **67**, 147-152.
80. C. Sharma, N. Kumar, M. Khandpal, S. Chandra and V. Bhide, *J. Inorg. Nucl. Chem.*, 1981, **43**, 923-930.
81. S. Zemskova, L. Glinskaya, R. Klevtsova, S. Gromilov, V. Durasov, V. Nadolinnyi and S. Larionov, *J. Struct. Chem.*, 1995, **36**, 484-495.
82. N. A. Bell, E. Johnson, L. A. March, S. D. Marsden, I. W. Nowell and Y. Walker, *Inorganica Chim. Acta*, 1989, **156**, 205-211.
83. S. J. Joris, K. I. Aspila and C. L. Chakrabarti, *J. Phys. Chem. B*, 1970, **74**, 860-865.
84. J. M. Bevilacqua and R. Eisenberg, *Inorg. Chem.*, 1994, **33**, 2913-2923.
85. K. Ramasamy, M. A. Malik, J. Raftery, F. Tuna and P. O'Brien, *Chem. Mater.*, 2010, **22**, 4919-4930.
86. K. Ramasamy, M. A. Malik, M. Helliwell, J. Raftery and P. O'Brien, *Chemistry of Materials*, 2011, **23**, 1471-1481.
87. J.-G. Kang, J.-S. Shin, D.-H. Cho, Y.-K. Jeong, C. Park, S. F. Soh, C. S. Lai and E. R. Tiekink, *Cryst. Growth Des.*, 2009, **10**, 1247-1256.
88. N. Alam, M. S. Hill, G. Kociok-Köhn, M. Zeller, M. Mazhar and K. C. Molloy, *Chem. Mater.*, 2008, **20**, 6157-6162.
89. Y. W. Koh, C. S. Lai, A. Y. Du, E. R. Tiekink and K. P. Loh, *Chem. Mater.*, 2003, **15**, 4544-4554.
90. D. Barreca, A. Gasparotto, C. Maragno and E. Tondello, *J. Electrochem. Soc.*, 2004, **151**, G428-G435.
91. C. Sceney, J. Hill and R. Magee, *Thermochimica Acta*, 1973, **6**, 111-117.
92. M. Shankaranarayana and C. Patel, *Can. J. Chem.*, 1961, **39**, 1633-1637.
93. J. S. Casas, A. Castineiras, I. Haiduc, A. n. Sánchez, R. F. Semeniuc and J. Sordo, *J. Mol. Struct.*, 2003, **656**, 225-230.
94. M. Hunt, A. Kruger, L. Smith and G. Winter, *Aust. J. Chem.*, 1971, **24**, 53-57.
95. E. A. Lewis, P. D. McNaughter, Z. Yin, Y. Chen, J. R. Brent, S. A. Saah, J. Raftery, J. A. Awudza, M. A. Malik and P. O'Brien, *Chem. Mater.*, 2015, **27**, 2127-2136.

96. N. Pradhan, B. Katz and S. Efrima, *J. Phys. Chem. B*, 2003, **107**, 13843-13854.
97. M. Afzaal, C. L. Rosenberg, M. A. Malik, A. J. White and P. O'Brien, *New J. Chem.*, 2011, **35**, 2773-2780.
98. S. R. Rao, 1971.
99. N. O. Boadi, M. A. Malik, P. O'Brien and J. A. Awudza, *Dalton Transactions*, 2012, **41**, 10497-10506.
100. A. J. Vreugdenhil, S. H. Brienne, I. S. Butler, J. A. Finch and R. D. Markwell, *Spectrochim. Acta A*, 1997, **53**, 2139-2151.
101. S. Bhaviripudi, X. Jia, M. S. Dresselhaus and J. Kong, *Nano Lett.*, 2010, **10**, 4128-4133.
102. N. Han, F. Wang, Z. Yang, S. Yip, G. Dong, H. Lin, M. Fang, T. Hung and J. C. Ho, *Nanoscale Res. Lett.*, 2014, **9**, 347.
103. L. Wang, X. Hu, X. Xu, S. Jiang, L. Ning and M. Jiang, *J. Mater. Sci. Technol.*, 2007, **23**, 118-122.
104. W. S. Cheong, N. M. Hwang and D. Y. Yoon, *J. Cryst. Growth*, 1999, **204**, 52-61.
105. N. F. Baril, R. He, T. D. Day, J. R. Sparks, B. Keshavarzi, M. Krishnamurthi, A. Borhan, V. Gopalan, A. C. Peacock and N. Healy, *J. Am. Chem. Soc.*, 2011, **134**, 19-22.
106. K. Choy, *Progress in materials science*, 2003, **48**, 57-170.
107. J. S. Ritch, T. Chivers, M. Afzaal and P. O'Brien, *Chem. Soc. Rev.*, 2007, **36**, 1622-1631.
108. B. Meester, L. Reijnen, A. Goossens and J. Schoonman, *Chem. Vap. Deposition*, 2000, **6**, 121-128.
109. K. F. Jensen and D. Graves, *J. Electrochem. Soc.*, 1983, **130**, 1950-1957.
110. C. S. Blackman, C. Piccirillo, R. Binions and I. P. Parkin, *Thin Solid Films*, 2009, **517**, 4565-4570.
111. C. Blackman, C. Carmalt, S. O'Neill, I. Parkin, L. Apostilco and K. Molloy, *J. Mater. Chem.*, 2001, **11**, 2408-2409.
112. H. Wang, C. Xia, G. Meng and D. Peng, *Materials Letters*, 2000, **44**, 23-28.
113. Y. Natsume and H. Sakata, *Thin Solid Films*, 2000, **372**, 30-36.
114. P. Jiang and M. J. McFarland, *J. Am. Chem. Soc.*, 2004, **126**, 13778-13786.

115. S. Ahmadi, N. Asim, M. Alghoul, F. Hammadi, K. Saeedfar, N. A. Ludin, S. H. Zaidi and K. Sopian, *Int. J. Photoenergy*, 2014, **2014**.
116. F. Padinger, C. Brabec, T. Fromherz, J. Hummelen and N. Sariciftci, *Optoelectronics Review*, 2000, 280-283.
117. D. V. Talapin, S. Haubold, A. L. Rogach, A. Kornowski, M. Haase and H. Weller, *J. Phys. Chem. B*, 2001, **105**, 2260-2263.
118. D. V. Talapin, N. Gaponik, H. Borchert, A. L. Rogach, M. Haase and H. Weller, *J. Phys. Chem. B*, 2002, **106**, 12659-12663.
119. C. de Mello Donegá, P. Liljeroth and D. Vanmaekelbergh, *Small*, 2005, **1**, 1152-1162.
120. S. G. Kwon and T. Hyeon, *Small*, 2011, **7**, 2685-2702.

Chapter 2 Important compound semiconductors.

2.1 Introduction

The crystal structure of the metal sulfides can be described by the coordination of atoms in the unit cells. The description of crystal structure based on close-packed structure provides a greater understanding into the crystal chemistry. There are two types of close packing, hexagonal (hcp) and cubic (ccp), hcp has an ABABAB stacking sequence, any atom from the B plane located at interstitial site of the A plane (Figure 2.1a). The third layer A is the first layer repeated. The stacking sequence type ABCABC presents in ccp, the planes A, B and C in the ccp type are stacked in different manners (Figure 2.1b).¹

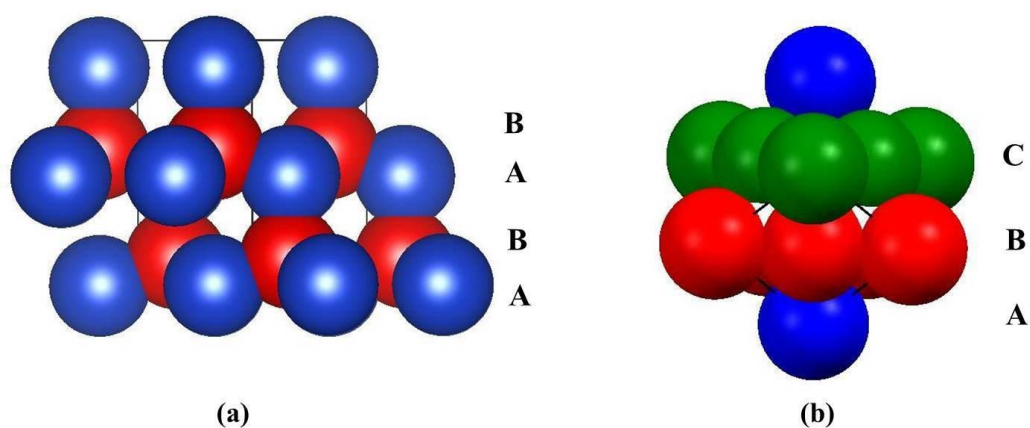


Figure 2.1. Close-packed structures (a) side view of hexagonal close-packed (hcp) (b) side view of cubic close-packed (ccp).

The classification of the transition metal sulfide relies on the distribution of atoms in the tetrahedral sites. Many tetrahedral bonded compounds can be formed from diamond structure based on the ordering of atoms in the substructures. Figure 2.2 shows the structural derivation of binary, ternary and quaternary compounds. These compounds are said to be adamantine maybe because the strong bond between atoms in substructures.²

Silicon and carbon unit cells have the basic structure of tetrahedron which is equidistant from four atoms. It is located at $[1/4, 1/4, 1/4]$, every silicon atom has four nearest neighbours, the average bond length is 2.36 \AA , four valence electrons are available per atom, in covalent bonding each valence electron is shared by two

atoms, when each bond has exactly two electrons the covalent bond become strongest. Dutta³ studied the diamond crystal structure of silicon with the space group $Fd\bar{3}m$ and the value of lattice parameter is 5.45 Å for the samples heated at 878 °C, however the value of lattice constant is 5.43 Å for the samples heated at 345 °C.

The general formula of the binary metal sulfides is $A^{II}B^{VI}$ (A = Zn, Cd, Hg, Mg, Ca, Ba, Sr; B = O, S, Se, Te), the crystal structure of this group is cubic sphalerite type belonging to the $F\bar{4}3m$ space group. Some of the $A^{II}B^{VI}$ compounds also crystallize as hexagonal wurtzite structure which has $P6_3mc$ space group. The ternary compounds have the general formula $A^IB^{III}C_2^{VI}$ (A = Ag, Cu; B = Ga, In ;C = O, S, Se, Te), the chalcopyrite type structure is a quite common structure known for this group (space group $I\bar{4}2d$). This structure is obtained from zinc blende by the replacement of the cations in the sublattice by two different atoms in which the unit cell define a is doubled. This leads to a tetragonal distortion (η), η can be calculated by ($\eta = c/2a$).⁴ In addition these semiconductors crystallize in the hexagonal wurtzite structure (space group $P6_3mc$). The formula for quaternary compounds is $A_2^IB^{II}C^{IV}D^{VI}_4$ (A = Ag, Cu; B = Zn, Cd, Hg, Mg, Ca, Ba, Sr; C = Si, Ge, Sn, Pb, Ti, Zr, Hf; D = O, S, Se, Te), they form in kesterite structure (space group $I\bar{4}$) and stannite (space group $I\bar{4}2m$).^{5,6}

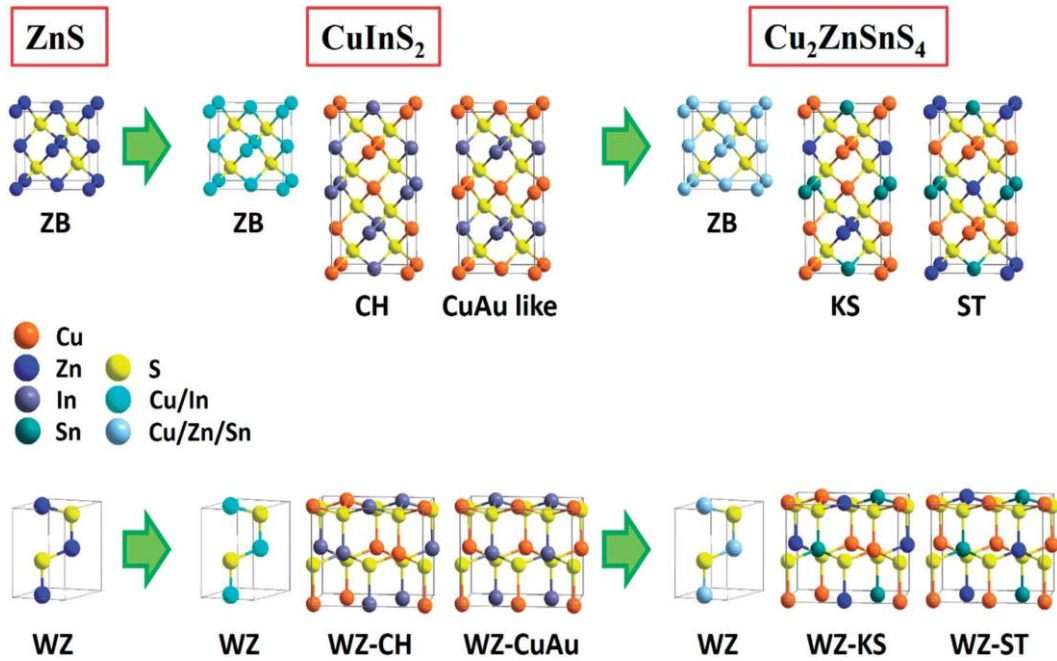


Figure 2.2. Schematic diagram of the unit cells of the zinc - blende (ZB) and wurtzite (WZ) structures of ternary CuInS_2 and quaternary $\text{Cu}_2\text{ZnSnS}_4$ which derived from ZnS binary phase. They crystallize in basic ZB and WZ structure, in addition they possess chalcopyrite, WZ - chalcopyrite, CuAu like, WZ - CuAu - like, kesterite, stannite, WZ - kesterite and WZ - stannite.^{6,7}

2.2 Zinc sulfide(ZnS)

It is known, that the zinc sulfide (ZnS) is a promising material for a wide range of application such as photoreactions,⁸⁻¹⁰ drug delivery systems¹¹ and kinetic analysis of bioleaching.¹² The cubic type ZnS consists essentially of two face centre cubic (FCC) substructures which are determined as the interpenetration sublattices along the body diagonal. First substructure occupied by cation atom (Zn) and the other contains anion atom(S). The origin of one of them is displaced by $\frac{1}{4}$ the body diagonal. The cubic single crystals of ZnS were characterized by Czyzak,¹³ the crystals present cubic structure because they have fourfold symmetry, the lattice is a faced centered cubic with lattice parameter ($a = 5.4145 \pm 0.0009 \text{ \AA}$), the crystal tends to grow on (110) plane. They studied the absorption and photoconductivity of the ZnS crystals, they found that conductivity of ZnS cubic crystals are largely intrinsic and have good dielectric properties. Figure (2.3) shows the unit cell of ZnS cubic crystal, this structure was reported by Skinner,¹⁴ the space group is $F\bar{4}3m$, the position of zinc atom is (0,0,0) and the sulfur atom is located at (1/4,1/4,1/4), the

atoms are tetrahedrally bonded. Cubic nanocrystal of ZnS has synthesised in different shapes such as nanoflakes,¹⁵ nanotube¹⁶ and nanoball.¹⁷ Depending on the state of the reaction, the synthetic methods of cubic ZnS crystal can be classified into the vapour phase medium, liquid phase medium and solid phase medium. Vapour phase medium was used by Mazhar¹⁸ *et al.* Single source precursors $[\text{Zn}(\text{S}_2\text{CNCy}_2)_2(\text{py})]$ and $[\text{Zn}(\text{S}_2\text{CN}(\text{CH}_2\text{Ph})(\text{Me}))_2(\text{py})]$ were employed to deposit ZnS thin films, the reactions were carried out on FTO substrates by AACVD at different temperatures. They conclude that the above zinc complexes give mixed phase cubic and hexagonal. The cubic phase is dominating at 375 °C. While at high temperature 475 °C hexagonal phase is observed as major phase. Liquid phase medium was used by Hyeon¹⁹ *et al.* to synthesise rod shaped ZnS nanocrystals, the injection of diethylzinc (0.5 mmol) into the 3 mmol (0.096 g) of elemental sulfur dissolved in five grams of 1-hexadecylamine (21 mmol). The reaction was carried out at 125 °C in an argon atmosphere. The yellow coloured ZnS nanocrystals formed after heating up the resulting solution to 300 °C. Solid phase reaction medium was used by Zhu²⁰ *et al.*, ZnS and carbon powders were mixed as solid precursors, the mixture placed in a graphite tube enclosed within a quartz tube. The precursors were heated firstly at 900 °C for 1 h in a N₂ flow to prepare ZnS - C nanocables, in the second stage the temperature increases to 1100 °C for another hour to form nanocable - aligned tetrapods.

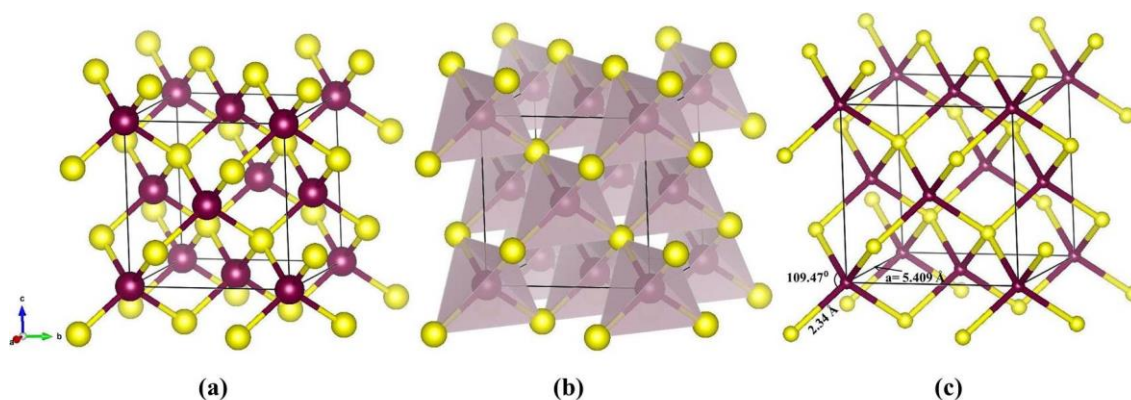


Figure 2.3. The unit cell of a ZnS cubic crystal, the parameters of the crystal obtained by Skinner.¹⁴ (a) The atoms positions in the crystal (b) The tetrahedral structures and (c) crystal parameters. Maroon = Zn and Yellow = S.

The second most common phase of ZnS is hexagonal. Similar to the cubic ZnS which derives from the (FCC) lattices, the ZnS of wurtzite type structure derives from the hexagonal close packed (hcp). Zn and S atoms are tetrahedrally bonded. A unit cell of wurtzite ZnS generally has two (hcp) anions, one at the origin and one inside the cell. Their coordinates are (0,0,0) and (1/3,2/3,1/2). Close packed layers occur in planes at $c = 0$, at $c = 1/2$ and at $c = 1$.¹⁰ Figure (2-4) shows the unit cell parameters of ZnS hexagonal crystal. The data reported by Myer in the American Mineralogist crystal structure database¹⁴ has been used to draw the cells of the crystal which presents the space group of P63mc. The lattice parameters a and c are 3.81 and 18.68 Å respectively; euhebral crystals are identified as the 6H polytype. Zinc atoms are located at (0, 0, 0), (1/3, 2/3, 1/6) and (2/3, 1/3, 1/3), while the position of sulfur atoms are in (0, 0, 0.125), (1/3, 2/3, 0.291) and (2/3, 1/3, 0.458). The layer arrangement is repeated every other layer, so that the stacking sequence in the ZnS cell is hexagonal.

Vapour phase medium was used by O'Brien²¹ *et al.* They reported Zn complex of [Zn(N(SCNMe₂)₂)₂] as a single molecular precursor for deposition of ZnS thin films by AACVD. Films were cubic ZnS at 300 and 350 °C, the cubic phase begins to change however to hexagonal at the substrate temperature of 400 °C. Liquid phase medium to obtain hexagonal ZnS has been used by Zhao²² *et al.* The solution of 7.34 mmol of thiourea into 50 mL of ethylene glycol was prepared and quickly injected into the solution of (7.34 mmol) of anhydrous ZnCl₂ and (14.86 mmol) of tetramethylammonium hydroxide into 50 ml ethylene glycol at 100 °C. Milky white solution of ZnS nanocrystals was formed after heating the mixture to 150 °C for 10 min. Soxman²³ reported the synthesis of ZnS hexagonal hollow crystals from zinc sulfide powder which was heated in a double crucible arrangement at 1150°C for one to three hours. X-ray diffraction revealed the presence of hexagonal ZnO (zincite) with the ZnS phase.

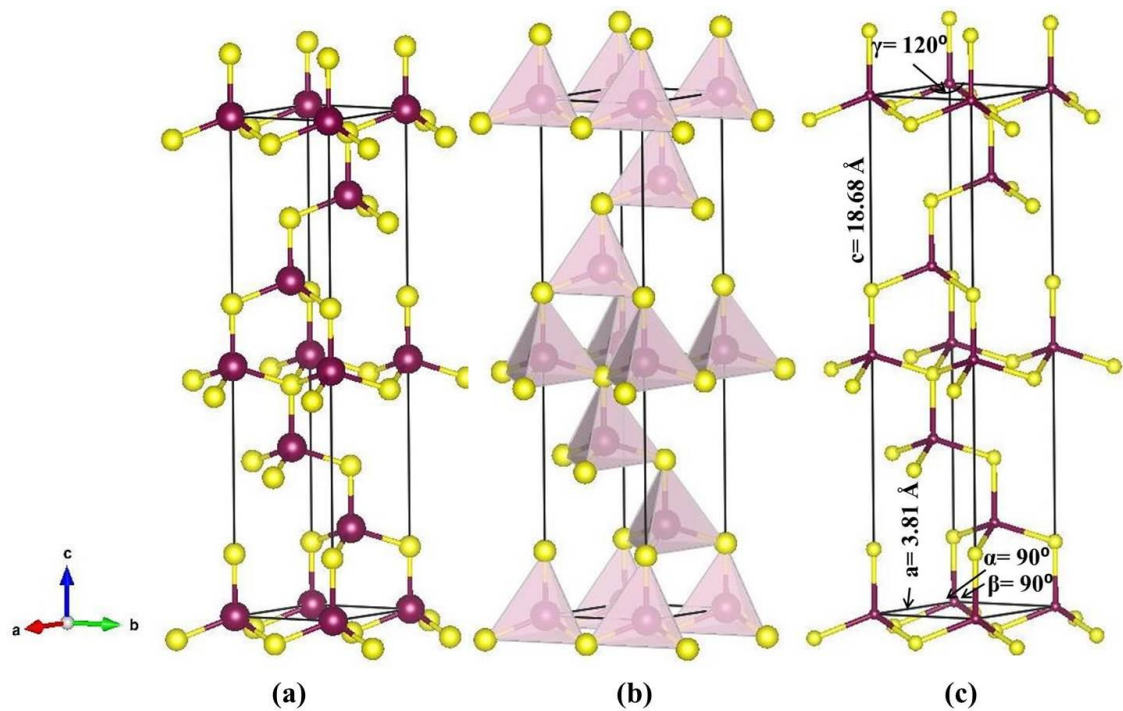
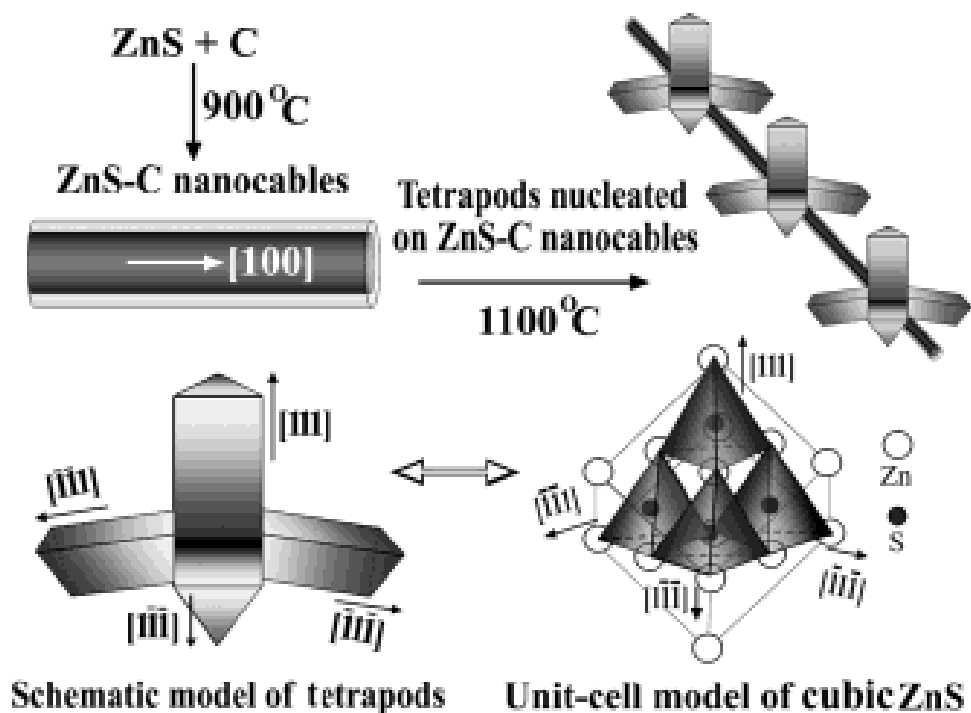


Figure 2.4. Schematic diagram of the ZnS hexagonal crystal data obtained by Myer.¹⁴ (a) The atoms positions in the crystal (b) The tetrahedral structures and (c) Crystal parameters. Maroon = Zn and yellow = S.

ZnS structures have polymorphic modifications, the cubic ZnS is a low temperature phase and it is a more stable than the hexagonal structure. The transformation from a cubic to hexagonal structure takes place at 1024°C.^{24, 25} Recently, Alivisator²⁶ *et al.* studied the polytypism phenomenon in the inorganic nanocrystals; polytypism is popular in tetrahedrally bonded structures. The crystal structures of the II-VI semiconductors have identical crystal faces, both the $\pm (111)$ and $\pm (0001)$ planes of the cubic and hexagonal respectively are identical. Therefore a tetrapod is the most branched polytypic crystal that can be obtained with these materials. A tetrapod is of single crystalline materials structure, whose branches are triangular prisms stretching out in four directions. The mechanism of the formation a tetrapod depends on the stability of the two phases during growth process. The tetrapods of ZnS nanocrystals have been intensively investigated by Zhu²⁰ *et al.* The branches are triangular prisms stretching out in four directions which are $(1\ 1\ 1)$, $(\bar{1}\ \bar{1}\ 1)$, $(1\ \bar{1}\ \bar{1})$ and $(\bar{1}\ 1\ \bar{1})$ axes (scheme1 and figure 2-5). Four tetrahedrons have four corners showing in the unit cell at the $(1\ 1\ 1)$, $(\bar{1}\ \bar{1}\ 1)$, $(1\ \bar{1}\ \bar{1})$ and $(\bar{1}\ 1\ \bar{1})$ directions respectively.



Scheme 1. Preparation and Schematic Model of Nanocable-Aligned ZnS Tetrapod Crystals.²⁰

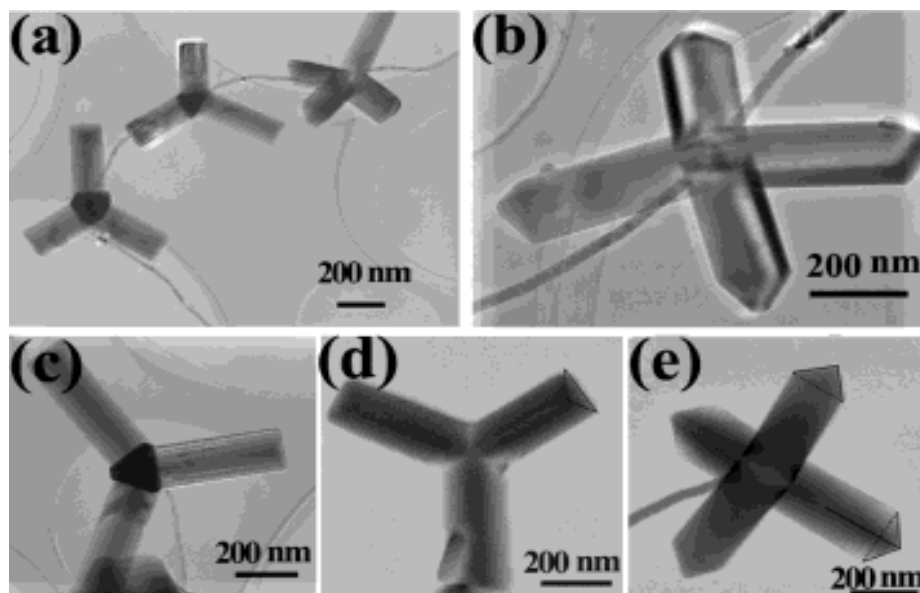


Figure 2.5. Images of nanocable-aligned ZnS tetrapods. (a) Aligned ZnS tetrapods. (b) Nanocable passing through the centre of the tetrapod. (c) Tetrapod image viewed along the $[111]$ direction; (d) Viewed along the $[\bar{1}\bar{1}\bar{1}]$ direction; (e) Viewed along the $[100]$ direction.²⁰

2.3 Copper indium sulfide (CuInS₂)

CuInS₂ has attracted considerable attention due to its potential use in photovoltaic solar cells, photodetectors and light-emitting diodes.²⁷ The crystal structure of a CuInS₂ can be considered as the ternary interpretation of the ZnS, as a result of the two types of atoms copper and indium in the CuInS₂ symmetry, the unit cells of CuInS₂ crystallise into two structures, chalcopyrite structure which has a primitive cell of eight atoms as well as zincblende structure with two atoms per unit cell. The lattices of the zinc blende CuInS₂ are face centred cubic, the copper and indium atoms are coordinated randomly in the lattices of the zinc blende (sphalerite) structure; however, the chalcopyrite CuInS₂ has face centre cubic lattices, the crystal unit cell is doubled in this structure along the c axis.⁷ Because of the CuInS₂ structure derived from the ZnS structure after substitution of the Zn atoms by copper and indium atoms, the new atoms will occupy the tetrahedrons. Each tetrahedron in the CuInS₂ crystal has four cations at the corners with one sulfur atom at the centre. The tetrahedron of the chalcopyrite structure has two types of cations bonded to the sulfur atom. The atomic radii of cations are not identical, so that the value of tetragonal distortion (η) which has the ideal value of 2 will diverge. Moreover, the sulfur atom in the centre of tetrahedron will move from its ideal position, Bernstein²⁸ *et al* suggested that the distortion in the sublattices is related to electronegativity differences among the Cu, In, and S atoms. They calculated the sublattice distortions of some A^{II}B^{IV}C₂ compounds and they found that the CuInS₂ compound has a Cu-S distance of 2.335(1) Å and the value of sublattice distortion is (- 0.0165(6) Å).

In the zinc blende (cubic) CuInS₂ structure, the cations occupy the same position and have a random distribution in the zinc blende unit cell. This phase was prepared by the injection of Na₂S solution (0.062 mmol) into the mixture of the metal salts solutions at room temperature. The reaction mixture was heated to 95°C for 40 min.²⁹ Lu³⁰ *et al*, reported the zinc blende phase of CuInS₂ from liquid reaction medium by using copper and indium as a single source precursor, in this reaction the mixture of copper diethyldithiocarbamate [Cu(S₂CNEt₂)] (18 mg, 0.05 mmol), indium diethyldithiocarbamate [In(S₂CNEt₂)₃] (28 mg, 0.05 mmol), 1.0 mL of oleic acid and 9.0 mL of octadecene was heated to 200 °C. Subsequently, 1 mL oleylamine was injected into mixture, and after 4 minutes the mixture was cooled down to room temperature and the CuInS₂ nanocrystals were extracted by adding 30 ml ethanol.

The phase was cubic (zinc blende) with lattice parameter of 5.523 Å and space group $F\bar{4}3m$. The atomic coordinate of sulfur is $4c(1/4, 1/4, 1/4)$ and both of the copper and indium have $4a(0, 0, 0)$ Wyckoff position. Figure (2-6) is drawn using the data that reported by Lu³⁰ *et al*, which provide the data of zinc blende CuInS₂ crystal.

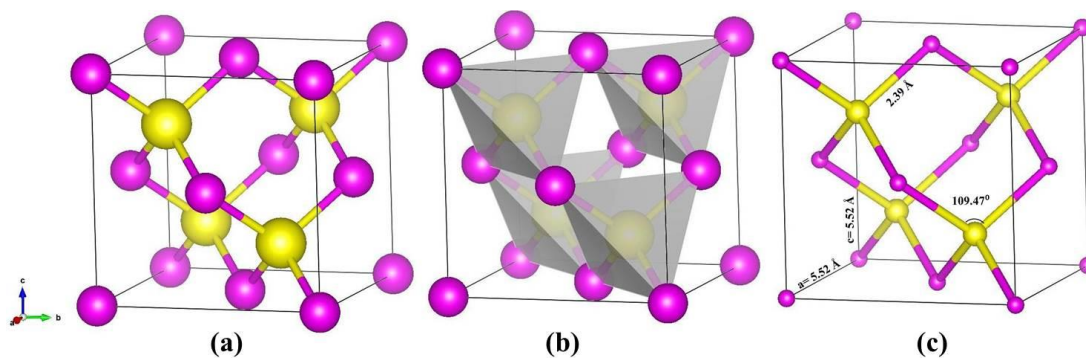


Figure 2.6. Schematic diagram of the CuInS₂ Cubic (zinc blende) crystal. (a) The atoms positions in the crystal (b) The tetrahedral structures and (c) crystal parameters. Magenta = Zn/In and yellow = S.

Chalcopyrite CuInS₂ is a stable phase at room temperature and has a tetragonal structure,³¹ in this structure, copper and indium atoms occupy the different positions. Aitken³² *et al* reported the chalcopyrite type structure (Figure 2-7)of CuInS₂. The structure shows that a half of the cation site is occupied by Cu on the (0,0,0) and the other half by In on the (0,0,1/2), forming the chalcopyrite structure of CuInS₂. They prepared a polycrystalline CuInS₂ by the reaction of stoichiometric mixtures of high purity elements. They used copper, indium and sulfur in evacuated and sealed fused silica tubes. The samples were heated to 1150 °C in 12 h, after 72 h, the samples were cooled to room temperature in 12 h. The samples were characterised by X-ray diffraction and neutron powder diffraction. The system is tetragonal unit cell, the space group is $I\bar{4}2d$, and the unit cell parameters are: $a = 5.521 \text{ \AA}$ and $c = 11.141 \text{ \AA}$.

The occupation of the metal cations of ternary compounds in the corresponding position of binary systems is random, which can form the metastable nature of two structures zinc blende and wurtzite. Wurtzite (WZ) crystal structure of CuInS₂ was investigated by Tang³³ *et al*. Solvothermal method was used to form WZ-CuInS₂ nanocrystals. Stoichiometric amounts of CuCl₂ · 2H₂O and InCl₃ · 4H₂O were mixed with 20% molar excess of thiourea in 40 ml of ethanolamine. The mixture was put in

the autoclave, which was sealed and maintained at 180 °C for 24 h, the product was separated by centrifugation and cooled down to room temperature naturally.

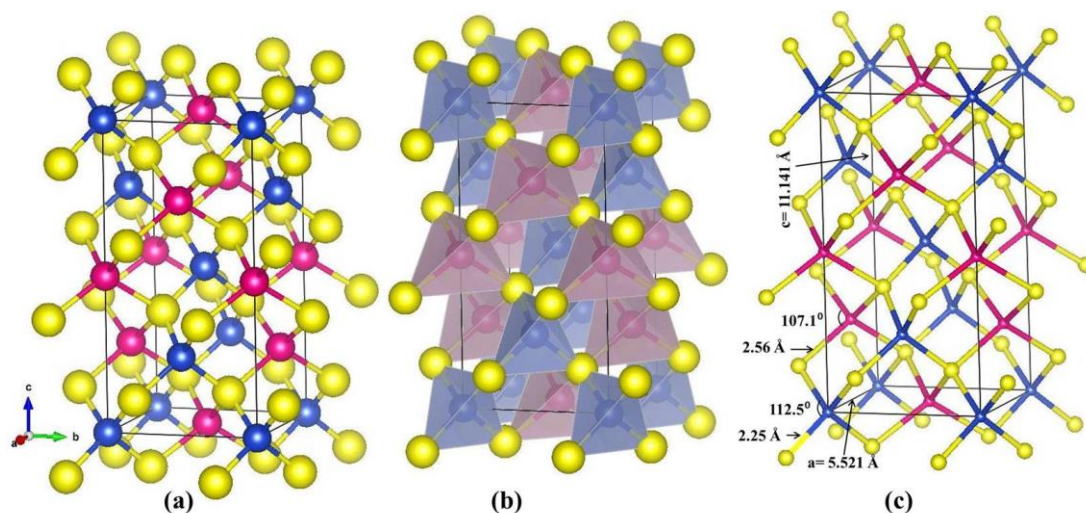


Figure 2.7. Schematic diagram of the CuInS₂ chalcopyrite crystal (a) The atoms positions (b) Stacking of tetrahedral cations layers (c) The unit cell parameters. Blue = Cu, red = In and yellow = S.

They studied growth mechanism of WZ-CuInS₂, they found that the coordination between Cu²⁺ and ethanolamine has a major impact to growth of a hexagonal phase of CuInS₂. Also, DSC analysis proved that this phase is metastable, heating the sample to 500 °C leads to the formation of chalcopyrite CuInS₂ as the major crystalline phase. They reported WZ-CuInS₂ (Figure 2.8) in a space group of *P63mc*, the crystal parameters *a* and *c* are 3.906, 6.428 Å respectively. Cu and In atoms occupied the level 2b at (1/3, 2/3, 0). S is in the same level but in the position of (1/3, 2/3, 0.375).

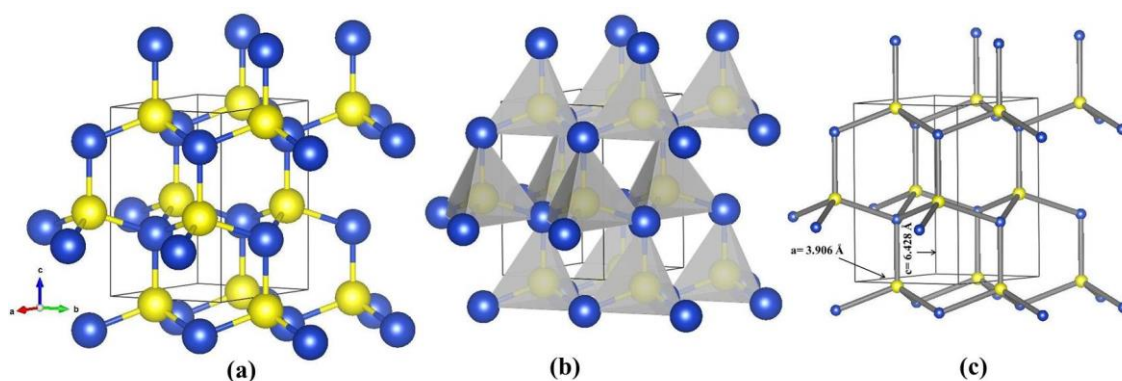


Figure 2.8. Schematic diagram of a hexagonal CuInS_2 (a) The atoms positions (b) Stacking of tetrahedral anions layers (c) The unit cell parameters. Blue = Cu/In and yellow = S.

2.4 Copper zinc tin sulfide ($\text{Cu}_2\text{ZnSnS}_4$) and copper iron tin sulfide ($\text{Cu}_2\text{FeSnS}_4$)

Ternary chalcopyrite compounds can be easily obtained from binary analogues, the same analogy can be drawn to derive the quaternary compounds from ternary ones. The substitution of an element in a ternary $\text{A}^{\text{I}}\text{B}^{\text{III}}\text{C}_2^{\text{VI}}$ from other groups of the periodic table leads to form new quaternary compounds while keeping the four electrons per lattice site rule without change. For instance, the quaternary compound $\text{Cu}_2\text{ZnSnS}_4$ can be considered as a substitution of indium ions in CuInS_2 with zinc and tin ions, cation cross-substitution in ternary systems should happen without violating the octahedral sites. In addition, the substitution of the elements is possible when the elements have the same oxidation state and quite close radii. As a result a series of quaternary compound were reported for example $\text{Cu}_2\text{ZnSiS}_4$ and $\text{Cu}_2\text{CdSnS}_4$.^{34, 35} It should also be noted that following the relationship between the oxidation states of elements, quaternary compounds can be also derived via isovalent substitution, when the ions that are substituting the original ions are of the same oxidation state as the ions they are replacing. The new quaternary compounds will still have a chalcopyrite structure. Grossberg³⁶ *et al.* studied the effect of the cations isovalent substitution on the optoelectronic and structural properties of $\text{Cu}_2\text{Zn}(\text{Sn}_{1-x}\text{Ge}_x)\text{Se}_4$ (CZTGSe) alloy compounds. They found that increasing Ge concentration leads to a linear decrease of the lattice parameter (a) from 0.569 nm to 0.561 nm, and the A symmetry Raman modes of kesterite crystal structure show a shift towards higher wavenumbers with increasing Ge content. However, anion substitutions for

the $\text{Cu}_2\text{ZnGeSe}_{4-x}\text{S}_x$ compounds show a constant increase of the lattices parameters (a) and (c) with increasing selenium content, also revealed a reduction of the lattice thermal conductivity of 42%.³⁷ Non-isovalent substitutions are where the ions that are substituting the original ions have a different oxidation state, this type of substitution forms vacancies which leads to the defects in the crystal lattices.³⁸

Similar to the family of ternary compounds, cation and anions in the quaternary compounds are crystallised in tetrahedral structures. There are three lattice sites for tetrahedral, copper, zinc and tin in $\text{Cu}_2\text{ZnSnS}_4$, also copper, iron and tin in $\text{Cu}_2\text{FeSnS}_4$, may that cause an increase in the cations ordering. The different crystal structures are then identified by the ways in which the set of tetrahedra occur. The kesterite and stannite types are the most common structures. Both structures can be described as cubic closed packed array of anions, with cations occupying one half of the tetrahedral voids. Figure (2.9) shows the complete disordered type of tetragonal $\text{Cu}_2\text{ZnSnS}_4$ compound, this structure was reported in the space group $I\bar{4}2m$ by Schorr³⁹ *et al.* The structure gives a good example to describe the complete disordered case of tetrahedrons in chalcopyrite $\text{Cu}_2\text{ZnSnS}_4$ crystal, the Wyckoff positions of the cations Cu^{+1} and Zn^{+2} are 4d (1/2, 0, 1/4), Sn is occupied at 2b(1/2, 1/2, 0) Wyckoff position. The sulfur is located at 8i (0.7524,0.7524,0.8712).

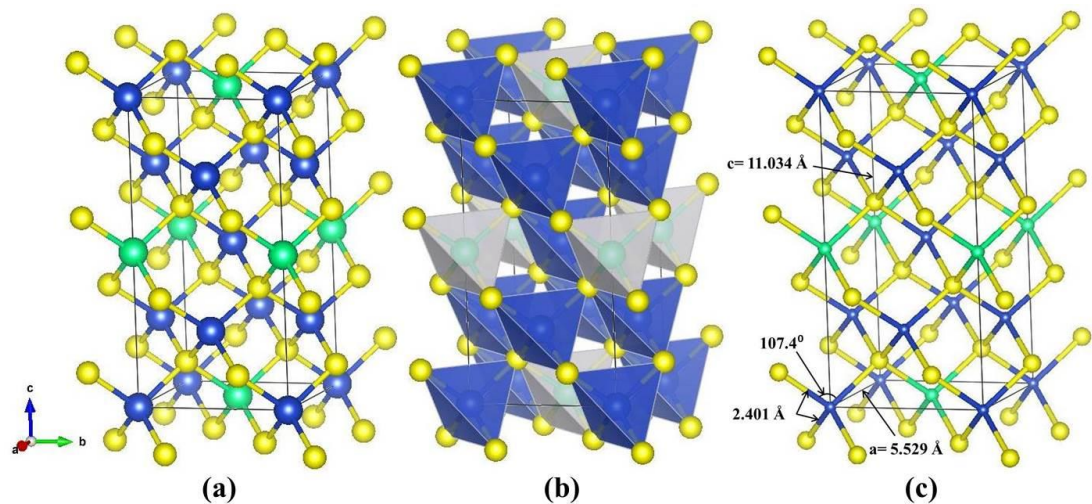


Figure 2.9. The crystal structure of chalcopyrite $\text{Cu}_2\text{ZnSnS}_4$ with space group $I\bar{4}2m$ (a) The positions of atoms in the unit cells (b) Stacking of tetrahedral cations layers (c) The unit cells parameters. Blue = Cu/Zn, green = Sn, yellow = S, the position 4d(1/2,0,1/4) will be randomly occupied by the Cu^{+2} and Zn^{+2} cations.

They used a solid state reaction method of the pure elements in sealed evacuated silica tubes to synthesise the sample, the samples were heated at different temperatures: 250 °C, 450 °C and 750 °C, then was cooled down to room temperature with a rate of 1 K/h. If the cations are partially disordered in the tetrahedral structure, the space group $I\bar{4}$ should be used to analyse the crystal structure of chalcopyrite $\text{Cu}_2\text{ZnSnS}_4$. Lafond⁴⁰ *et al*, reported the kesterite structure of $\text{Cu}_2\text{ZnSnS}_4$ with space group $I\bar{4}$ (figure 2.10). They found that the Cu, Zn and Sn cations are located in (2a), (2d), and (2b) respectively, the whole structure is noncentrosymmetric because the position of the S atoms is (8e), also the 2a crystallographic site is partially occupied, also they found that the lattice parameters a and c of the structure are 5.434 and 10.838 Å respectively. No difference was observed in the X-ray diffraction patterns of kesterite and stannite $\text{Cu}_2\text{ZnSnS}_4$. In addition, kesterite $\text{Cu}_2\text{ZnSnS}_4$ with the Cu and Zn cations disordered exhibit the same space group with stannite ($I\bar{4}2m$), therefore, it is impossible to distinguish between them.

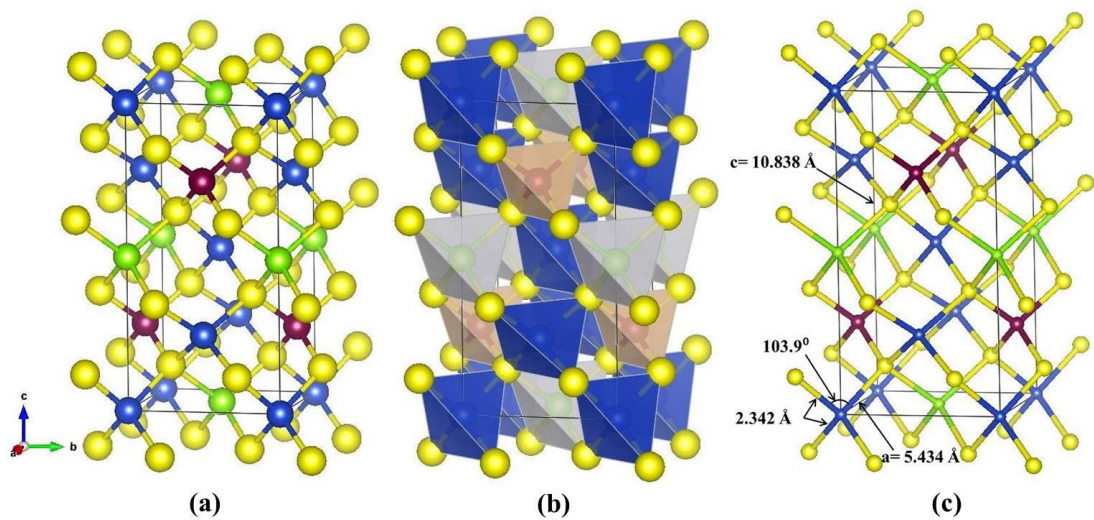


Figure 2.10. The crystal structure of chalcopyrite $\text{Cu}_2\text{ZnSnS}_4$ with space group $I\bar{4}$ (a) The atoms positions in the unit cell (b) Stacking of tetrahedral cations layers (c) The unit cell parameters. Blue = Cu, maroon = Zn, green = Sn, yellow = S.

2.4.1 Stannite structure of $\text{Cu}_2\text{FeSnS}_4$

$\text{Cu}_2\text{FeSnS}_4$ (CFTS) a quaternary compound has a good semiconducting properties, which makes it one of the important absorber layers in photovoltaic solar cells, CFTS exhibits carrier mobilities of $\sim 2\text{--}11 \text{ cm}^2/\text{V}\cdot\text{s}$,⁴¹ carrier concentration of $3.3 \times 10^{17} \text{ cm}^{-3}$ and resistivity of $2 \times 10^{-2} \Omega \text{ cm}$ with p-type conductivity.⁴² Different crystal structures have been reported for CFTS such as: cubic⁴³, tetragonal⁴⁴ and hexagonal⁴⁵. One of the first studies of stannite CFTS was performed in 1934 by Brockway.⁴⁶ Recently, Bonazzi⁴⁷ *et al*, reported the crystal structure of stannite CFTS, the space group is $I\bar{4}2m$ (Figure 2.11), the Wyckoff position of the Cu is $(0, 1/2, 1/4)$ in the level of 4d, Fe is occupied at $2a(0, 0, 0)$. The Sn and S are located at $2b(0, 0, 1/2)$, $8i(0.755, 0.755, 0.870)$ respectively. The lattice parameters of the structure, a and c, have been refined to 5.449 and 10.726 Å, respectively, using means of least-squares refinements.

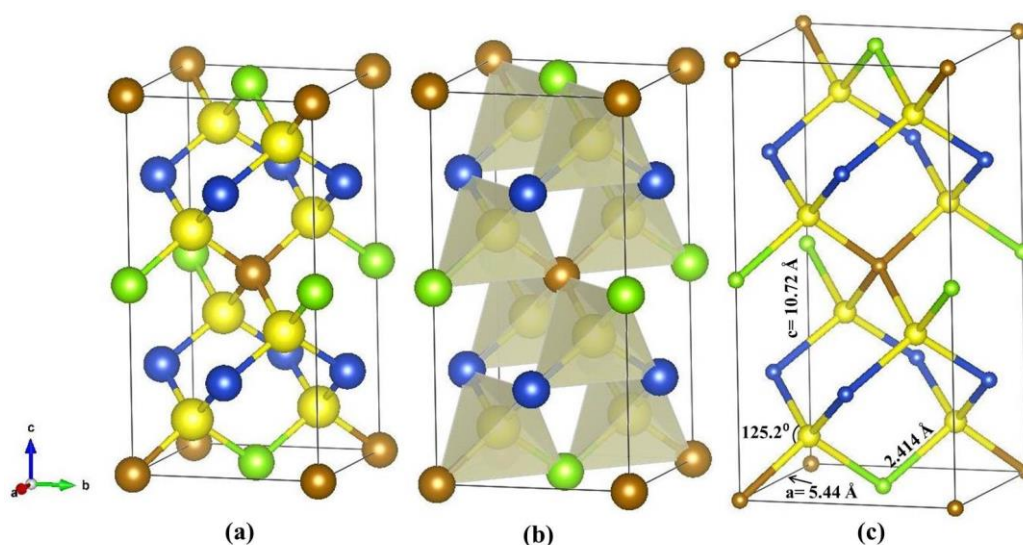


Figure 2.11. The crystal structure of $\text{Cu}_2\text{FeSnS}_4$ reported by Bonazzi⁴⁷ (a) The positions of atoms (b) The stacking of tetrahedrons of anions and (c) The parameters of the unit cell . Blue = Cu, brown = Fe, green = Sn, yellow = S.

Wurtzite $\text{Cu}_2\text{ZnSnS}_4$ (WZ.CZTS) is a kinetic product beyond thermodynamic equilibrium; however the equilibrium state could be achieved using a solvent such as dodecanethiol (DDT) to grow WZ.CZTS nanocrystal.⁷ DDT produces a homogenous precursor solution of metal thiolates, which will form WZ.CZTS directly via heating. Thus, WZ.CZTS phase can be obtained using faster growth reactions. This phase

was synthesised by Peng⁴⁸ *et al* by the hot injection method, they synthesised the metal thiolates precursor from the dissolving of 0.10 mmol of $\text{CuCl}_2 \cdot 2\text{H}_2\text{O}$, 0.05 mmol of ZnCl_2 and 0.05 mmol of $\text{SnCl}_4 \cdot 5\text{H}_2\text{O}$ in 1 ml (DDT) at 120 °C, then the metal thiolates precursor was injected into 2 ml of (DDT) and 2 ml of oleylamine (OAM) or 4 ml of oleic acid (OA) at 240 °C. Ryan⁴⁹ *et al* also reported the synthesis of WZ.CZTS nanocrystal from a mixture of 0.25 ml of 1-dodecanethiol (1-DDT) and 1.75 ml of tert-dodecyl mercaptan(t-DDT). WZ.CZTS crystallised as monodisperse nanorods with an average length of 35 ± 3 nm and diameter of 11 ± 0.5 nm (Figure 2.12).

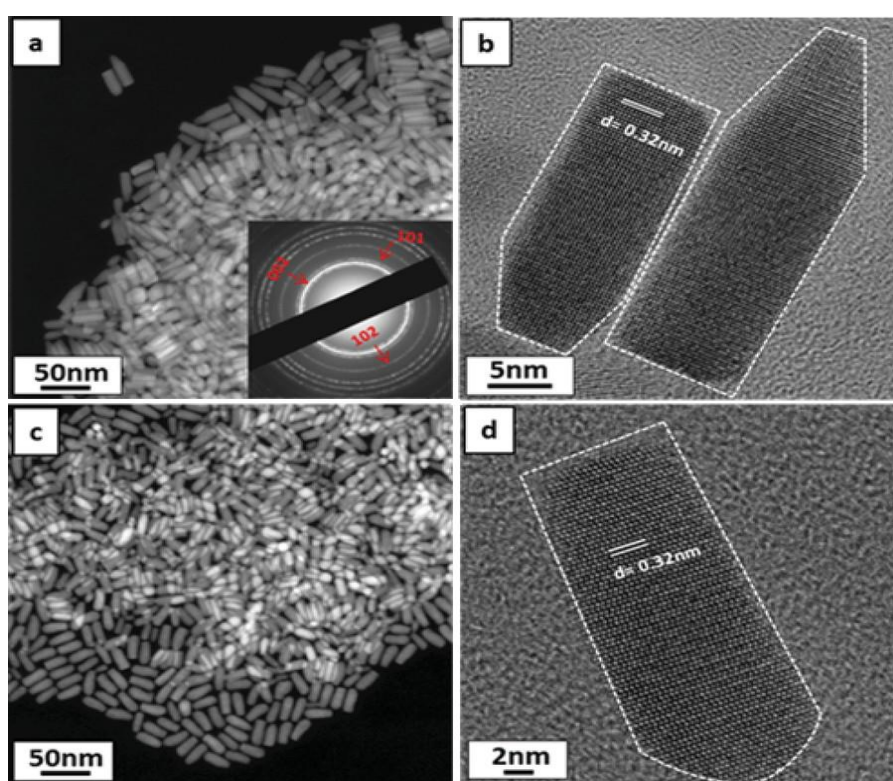


Figure 2.12. TEM images of the WZ.CZTS nanocrystal synthesised by a hot injection method (a) DF-STEM image of bullet-shaped CZTS nanorods. The inset shows the corresponding SAED pattern. (b) HRTEM image showing that the bullet-shaped CZTS nanorods are elongated in the [002] direction. (c) DF-STEM image of WZ.CZTS nanorods synthesized in the presence of a higher 1-DDT concentration. (d) HRTEM image of a single CZTS nanorod from (c).⁴⁹

2.5 References

1. P. Partridge, *Metallurgical reviews*, 1967, **12**, 169-194.
2. P. Newman, *J. Phys. Chem. Solids*, 1963, **24**, 45-50.
3. B. Dutta, *Phys. Status Solidi B*, 1962, **2**, 984-987.
4. A. Verma, *Solid State Commun.*, 2009, **149**, 1236-1239.
5. S. Chen, A. Walsh, Y. Luo, J.-H. Yang, X. Gong and S.-H. Wei, *Phys. Rev. B*, 2010, **82**, 195203.
6. J. Chang and E. R. Waclawik, *RSC Adv.*, 2014, **4**, 23505-23527.
7. F. J. Fan, L. Wu and S. H. Yu, *Energy Environ. Sci.*, 2014, **7**, 190-208.
8. A. Stroyuk, A. Raevskaya, A. Korzhak and S. Kuchmii, *J. Nanopart. Res.*, 2007, **9**, 1027-1039.
9. D. Son, D. R. Jung, J. Kim, T. Moon, C. Kim and B. Park, *Appl. Phys. Lett.*, 2007, **90**, 101910.
10. X. Fang, T. Zhai, U. K. Gautam, L. Li, L. Wu, Y. Bando and D. Golberg, *Prog. Mater. Sci.*, 2011, **56**, 175-287.
11. R. Xing and S. Liu, *Nanoscale*, 2012, **4**, 3135-3140.
12. Y. Konishi, H. Kubo and S. Asai, *Biotechnol. Bioeng.*, 1992, **39**, 66-74.
13. S. Czyzak, D. Reynolds, R. Allen and C. Reynolds, *JOSA*, 1954, **44**, 864-867.
14. R. T. Downs and M. Hall-Wallace, *Am. Mineral.*, 2003, **88**, 247-250.
15. J. Patil, S. Dhasade, A. Babar, S. Patil and V. Fulari, *Superlattices Microstruct.*, 2015, **83**, 565-574.
16. H. Zhang, S. Zhang, S. Pan, G. Li and J. Hou, *Nanotechnology*, 2004, **15**, 945.
17. X. Xue, J. Chen and Y. Hu, *Mater. Lett.*, 2007, **61**, 115-118.
18. M. A. Ehsan, T. N. Peiris, K. U. Wijayantha, H. Khaledi, H. N. Ming, M. Misran, Z. Arifin and M. Mazhar, *Thin Solid Films*, 2013, **540**, 1-9.
19. J. H. Yu, J. Joo, H. M. Park, S.-I. Baik, Y. W. Kim, S. C. Kim and T. Hyeon, *J. Am. Chem. Soc.*, 2005, **127**, 5662-5670.
20. Y. C. Zhu, Y. Bando, D.-F. Xue and D. Golberg, *J. Am. Chem. Soc.*, 2003, **125**, 16196-16197.
21. K. Ramasamy, M. A. Malik, P. O'Brien and J. Raftery, *MRS Online Proceedings Library Archive*, 2008, **1145**.

22. Y. Zhao, Y. Zhang, H. Zhu, G. C. Hadjipanayis and J. Q. Xiao, *J. Am. Chem. Soc.*, 2004, **126**, 6874-6875.
23. E. Soxman, *J. Appl. Phys.*, 1963, **34**, 948-950.
24. A. Baronnet, *Prog. Cryst. Growth Charact.*, 1978, **1**, 151-211.
25. F. A. La Porta, J. Andrés, M. S. Li, J. R. Sambrano, J. A. Varela and E. Longo, *Phys. Chem. Chem. Phys.*, 2014, **16**, 20127-20137.
26. L. Manna, D. J. Milliron, A. Meisel, E. C. Scher and A. P. Alivisatos, *Nat. Mater.*, 2003, **2**, 382-385.
27. J. Kolny-Olesiak and H. Weller, *ACS Appl. Mater. Interfaces*, 2013, **5**, 12221-12237.
28. S. Abrahams and J. Bernstein, *J. Chem. Phys.*, 1973, **59**, 5415-5422.
29. Y. Chen, S. Li, L. Huang and D. Pan, *Inorg. Chem.*, 2013, **52**, 7819-7821.
30. D. Pan, L. An, Z. Sun, W. Hou, Y. Yang, Z. Yang and Y. Lu, *J. Am. Chem. Soc.*, 2008, **130**, 5620-5621.
31. C. Yu, L. Zhang, L. Tian, D. Liu, F. Chen and C. Wang, *Cryst. Eng. Comm.*, 2014, **16**, 9596-9602.
32. J. Yao, B. W. Rudyk, C. D. Brunetta, K. B. Knorr, H. A. Figure, A. Mar and J. A. Aitken, *Mater. Chem. Phys.*, 2012, **136**, 415-423.
33. Y. Qi, Q. Liu, K. Tang, Z. Liang, Z. Ren and X. Liu, *J. Phys. Chem. C.*, 2009, **113**, 3939-3944.
34. K. A. Rosmus, C. D. Brunetta, M. N. Srnc, B. Karuppanan and J. A. Aitken, *Z. Anorg. Allg. Chem.*, 2012, **638**, 2578-2584.
35. K. A. Rosmus, J. A. Brant, S. D. Wisneski, D. J. Clark, Y. S. Kim, J. I. Jang, C. D. Brunetta, J.-H. Zhang, M. N. Srnc and J. A. Aitken, *Inorg. Chem.*, 2014, **53**, 7809-7811.
36. M. Grossberg, K. Timmo, T. Raadik, E. Kärber, V. Mikli and J. Krustok, *Thin Solid Films*, 2015, **582**, 176-179.
37. C. P. Heinrich, T. W. Day, W. G. Zeier, G. J. Snyder and W. Tremel, *J. Am. Chem. Soc.*, 2013, **136**, 442-448.
38. W. Xiao, J. Wang, X. Zhao, J. Wang, G. Huang, L. Cheng, L. Jiang and L. Wang, *Solar Energy*, 2015, **116**, 125-132.
39. S. Schorr and G. Gonzalez-Aviles, *Phys. Status Solidi A*, 2009, **206**, 1054-1058.

40. L. Choubrac, A. Lafond, C. Guillot-Deudon, Y. Moëlo and S. Jobic, *Inorg. Chem.*, 2012, **51**, 3346-3348.
41. R. R. Prabhakar, N. Huu Loc, M. H. Kumar, P. P. Boix, S. Juan, R. A. John, S. K. Batabyal and L. H. Wong, *ACS Appl. Mater. Interfaces*, 2014, **6**, 17661-17667.
42. K. Mokurala and S. Mallick, *RSC Adv.*, 2017, **7**, 15139-15148.
43. T. Evstigneeva and Y. K. Kabalov, *Crystallography Reports*, 2001, **46**, 368-372.
44. X. Jiang, W. Xu, R. Tan, W. Song and J. Chen, *Mater. Lett.*, 2013, **102**, 39-42.
45. X. Zhang, N. Bao, K. Ramasamy, Y.-H. A. Wang, Y. Wang, B. Lin and A. Gupta, *Chem. Commun.*, 2012, **48**, 4956-4958.
46. L. Brockway, *Z. Kristallog. – Cryst. Mater.*, 1934, **89**, 434-441.
47. P. Bonazzi, L. Bindi, G. P. Bernardini and S. Menchetti, *The Canadian Mineralogist*, 2003, **41**, 639-647.
48. X. Lu, Z. Zhuang, Q. Peng and Y. Li, *Chem. Commun.*, 2011, **47**, 3141-3143.
49. A. Singh, H. Geaney, F. Laffir and K. M. Ryan, *J. Am. Chem. Soc.*, 2012, **134**, 2910-2913.

Chapter 3 The synthesis of copper sulfide nanorods from xanthate precursors

3.1 Introduction

Copper sulfide is an important semiconductor with a strong potential for use as a p-type material for solar cell application^{1, 2} and in a wide range of biomedical utilizations.^{3, 4} The variations in composition of copper sulfide from sulfur rich region like covellite (CuS) to the copper rich region like chalcocite (Cu₂S) lead to different physical properties^{5, 6} such as shape variation, size distribution⁷ and band gap. The band gap of copper sulfide can change depending on the chemical composition, the E_g of covellite is 2 eV, however for chalcocite is 1.8 eV.⁸

The formation of copper sulfide nanorods from xanthate complexes by the hot-injection of a series of novel copper(I) xanthate single-source precursors [(PPh₃)₂Cu(S₂COR), (R = iso-butyl, 2-methoxyethyl, 2-ethoxyethyl, 1-methoxy-2-propyl, 3-methoxy-1-butyl and 3-methoxy-3-methyl-1-butyl) was investigated, the crystal structures of complexes are also reported. These complexes, in addition to the ethyl and n-butyl analogues have been tested as single-source precursors for the formation of copper sulfide nanoparticles. The thermal decomposition of copper(I) xanthate complexes in oleylamine at 260 °C gives copper sulfide nanorods. The width of the nanoparticles obtained is dependent on the length of the xanthate chain which is agreement with previous results.⁹

3.2 Author distribution

In this work, I synthesised and then characterised xanthate complexes via IR, NMR, elemental analysis and TGA. The experimental work to produce nanoparticles was carried out by me, I characterised the nanoparticles by XRD, EDX, UV-Visible spectroscopy. Peter D. Matthews checked the characterization of complexes and materials, he analysed the COSY NMR data for xanthate ligands and complexes. Geradius Deogratias provided the DFT study for this project. Paul McNaughton carried out TEM for the samples. The crystallographic data of the complexes has been collected by James Raftery and Inigo Vitorica-Yrezabal. The project was provided by Paul O'Brien, who edited the draft. The experimental work was done in the laboratory of Paul O'Brien.

3.3 References

1. S. Sartale and C. Lokhande, *Mater. Chem. Phys.*, 2000, **65**, 63-67.
2. H. Lee, S. W. Yoon, E. J. Kim and J. Park, *Nano Lett.*, 2007, **7**, 778-784.
3. S. Goel, F. Chen and W. Cai, *Small*, 2014, **10**, 631-645.
4. J. Bai and X. Jiang, *Anal. Chem.*, 2013, **85**, 8095-8101.
5. D. Koch and R. McIntyre, *J. Electroanal. Chem.*, 1976, **71**, 285-296.
6. Y. Xie, A. Riedinger, M. Prato, A. Casu, A. Genovese, P. Guardia, S. Sottini, C. Sangregorio, K. Miszta and S. Ghosh, *J. Am. Chem. Soc.*, 2013, **135**, 17630-17637.
7. W. P. Lim, C. T. Wong, S. L. Ang, H. Y. Low and W. S. Chin, *Chem. Mater.*, 2006, **18**, 6170-6177.
8. I. Grozdanov and M. Najdoski, *J. Solid State Chem.*, 1995, **114**, 469-475.
9. P. D. McNaughter, S. A. Saah, M. Akhtar, K. Abdulwahab, M. A. Malik, J. Raftery, J. A. Awudza and P. O'Brien, *Dalton Trans.*, 2016, **45**, 16345-16353.

3.4 Manuscript 1: Novel xanthate complexes for the size-controlled synthesis of copper sulfide nanorods

Mundher Al-Shakban,[†] Peter D. Matthews,[‡] Geradius Deogratias,[§] Paul D. McNaughten,[‡] James Raftery,[‡] Inigo Vitorica-Yrezabal,[‡] Egid B. Mubofu,[§] and Paul O'Brien*^{†,‡}

[†]School of Materials and [‡]School of Chemistry, University of Manchester, Oxford Road, Manchester M13 9PL, U.K.

[§]Chemistry Department, University of Dar es Salaam, P.O. Box 35061, Dar es Salaam, Tanzania

3.4.1 Abstract.

We present a simple, easily scalable route to monodisperse copper sulfide nanocrystals by the hot injection of a series of novel copper(I) xanthate single-source precursors [(PPh₃)₂Cu(S₂COR)] (R = isobutyl, 2-methoxyethyl, 2-ethoxyethyl, 1-methoxy-2-propyl, 3-methoxy-1-butyl, and 3-methoxy-3-methyl-1-butyl), whose crystal structures are also reported. We show that the width of the obtained rods is dependent on the length of the xanthate chain, which we rationalize through a computational study, where we show that there is a relationship between the ground-state energy of the precursor and the copper sulfide rod width.

3.4.2 Introduction

The colloidal synthesis of semiconductor nanoparticles has become a key area of research, with much attention focused on II–VI, III–V, and IV–VI compounds. However, many of these, such as Pb/Hg/Cd chalcogenides or In/Ga phosphide/arsenide, contain toxic and/or rare and expensive elements making them undesirable for widespread production and mass utilization. There remains a demand for simple, cheap semiconductor nanoparticles, consisting of earth-abundant elements. Transition-metal chalcogenides (TMC) such as copper sulfide, iron sulfide, and tin sulfide are promising candidates,¹ and among these, copper(I) sulfide is a promising material for photoapplications. It is an indirect band gap semiconductor with a band gap of 1.21 eV,^{2, 3} and additionally nanocrystals of Cu_xS exhibit plasmonic properties⁴ the result of oxidation leading to Cu vacancies. The net result

is that copper sulfides, unlike other TMC semiconductors, have both electronic and photonic modes, allowing greater opportunities for light-harvesting applications and quantum information processing.⁵⁻⁷ Copper sulfides have found extensive use in photovoltaics, as well as in biomedical applications as sensors⁸ and in theranostics.⁹

Copper sulfide (Cu_xS) crystallizes in a number of different phases between the two end members of $x = 1$ (covellite) and $x = 2$ (chalcocite). There are at least 14 different phases of copper sulfide, each with a unique Cu/S ratio.¹⁰ These include yarrowite ($\text{Cu}_{1.12}\text{S}$), spionkopite ($\text{Cu}_{1.40}\text{S}$), geerite ($\text{Cu}_{1.60}\text{S}$), roxbyite ($\text{Cu}_{1.74-1.82}\text{S}$), anilite ($\text{Cu}_{1.75}\text{S}$), digenite ($\text{Cu}_{1.80}\text{S}$), and djurleite ($\text{Cu}_{1.97}\text{S}$).¹¹⁻¹⁵ The vast range of accessible phases of bulk copper sulfides is also observed in the nanocrystal domain. This leads to the interesting range of properties demonstrated by Cu_xS , but to exploit these it is necessary to be able to exert control over size and phase during the synthesis.

Copper sulfide has been prepared by a number of different routes,¹⁶ such as the ubiquitous hot-injection method,^{3, 5,17-20} solvothermal synthesis,²¹ and cation exchange.^{22, 23} Previous attempts at phase control have been based on choice of solvent,²⁴ sulfur choice,²⁵ Cu/S ratio,¹⁸ and reaction temperature.²⁶ Many synthetic protocols require a complex mixture of reagents to generate monodisperse nanocrystals of copper sulfide, often including environmentally unfriendly ligands. Here we present a simple and easily scalable route to Cu_xS nanocrystals using a series of copper (I) xanthates as single source precursors (SSP), which are an established route to nanodimensional metal chalcogenide semiconductors, though a true SSP has been rarely used to generate copper sulfide.^{10,27-29} Metal xanthates are an excellent SSP for nanoparticles and thin films of metal sulfide,³⁰⁻³² as they breakdown via a Chugaev elimination producing volatile byproducts that should be removed at the reaction temperature.³³⁻³⁶

3.4.3 Experimental section

3.4.3.1 General.

All chemicals were purchased from Sigma-Aldrich and were used as received. Elemental analysis (EA) and thermogravimetric analysis (TGA) were performed by

the Microelemental Analysis service at the University of Manchester. EA was performed using a Flash 2000 Thermo Scientific elemental analyzer, and TGA data were obtained with Mettler Toledo TGA/DSC1 stare system in the range of 30–600 °C at a heating rate of 10 °C min⁻¹ under nitrogen flow. NMR spectra were recorded in CDCl₃ and D₂O solutions on a Bruker Ascend spectrometer operating at 400 MHz. Single-crystal X-ray diffraction (XRD) was performed using a Bruker diffractometer with a Cu K α source ($\lambda = 1.5418 \text{ \AA}$) at 100 K and Agilent diffractometer with a Mo K α source ($\lambda = 0.71073 \text{ \AA}$) at 150 K. For more information see tables A1 and A2. Crystallographic data available from the CCDC, numbers: 1550291–550300. Transmission electron microscope (TEM) images were collected at 300 keV using an FEI Tecnai TF30 equipped with a field emission gun. Energy-dispersive X-ray spectroscopy (EDS) measurements were performed using an FEI Quanta 200 SEM equipped with a DAX Genesis spectrometer. Grazing incidence X-ray diffraction (XRD) patterns were obtained with a Bruker D8 Advance diffractometer using a Cu K α source ($\lambda = 1.5418 \text{ \AA}$). UV–vis spectra were collected on a Shimadzu UV-1800, using 1.57 mM solution of nanorods in toluene.

3.4.3.2 Synthesis of Precursors.

3.4.3.2.1 Synthesis of Potassium n-Butylxanthate (1).

Potassium n-butylxanthate was prepared following a literature procedure.³⁷ Potassium hydroxide (5.64 g, 0.10 mol) and n-butyl alcohol (50 mL) were stirred for 2 h at room temperature, and then CS₂ (7.73 g, 6.11 mL, 0.10 mol) was added dropwise to the reaction, resulting in an orange solution. The unreacted alcohol was removed in vacuo, and the yellow solid product was dried and recrystallized from n-butyl alcohol to give [K(S₂COⁿBu)] (13.5 g, 0.0717 mol, 71.7% yield). mp = 232–235 °C. Calc. for C₅H₉KOS₂ (%): C 31.9, H 4.82, S 34.0, K 20.8; found: C 32.2, H 4.83, S 33.8, K 20.4. Fourier transform infrared (FT-IR) (cm⁻¹): 2958 (m), 2869 (w), 1461 (m), 1445 (w), 1261 (s), 1149 (m), 1173 (m), 1062 (m), 1014 (m), 747.3 (m), 669.0 (s), 566.2 (s). ¹H NMR (400 MHz, D₂O) δ (ppm) = 0.85 (t, J = 7.4 Hz, 3H, CH₃), 1.35 (s, J = 7.5 Hz, 2H, CH₂CH₂CH₃), 1.65 (p, J = 6.8 Hz, 2H, CH₂CH₂CH₂), 4.37 (t, J = 6.5 Hz, 2H, OCH₂CH₂).

3.4.3.2.2 Synthesis of Potassium iso-Butylxanthate (2).

[K(S₂COⁱBu)] was prepared via the same method, using isobutanol (50 mL). The product was recrystallized from isobutanol. (9.66 g, 65% yield). mp = 241–243 °C. Calc. for C₅H₉KOS₂ (%): C 31.9, H 4.82, S 34.0, K 20.8; found: C 31.7, H 4.72, S 34.0, K 21.0. FT-IR (cm⁻¹): 2958 (m), 2927 (w), 2870 (w), 1463 (w), 1386 (w), 1366 (w), 1179 (w), 1165 (w), 1141 (m), 1092 (s), 968.8 (m), 937.6 (w), 912.7 (w), 802.1 (w), 653.3(w), 571.9(w). ¹H NMR (400 MHz, D₂O) δ (ppm) = 0.89 (d, J = 6.8 Hz, 6H, CH(CH₃)₂), 1.99 (sep, J = 6.8 Hz, 1H, CH(CH₃)₂), 4.16 (d, J = 6.5 Hz, 2H, OCH₂CH).

3.4.3.2.3 Synthesis of Potassium 2-Methoxyethylxanthate (3).

[KS₂CO(CH₂)₂OMe] was synthesized by dissolving KOH (11.2 g, 0.20 mol) in (75 mL) of 2-methoxyethanol. The reactors were stirred for 6 h at 0 °C, and then a solution of CS₂ (15.2 g, 12 mL, 0.20 mol) in 2-methoxyethanol (25 mL) was added dropwise, resulting in a clear yellow solution. [KS₂CO(CH₂)₂OMe] was isolated from solution by adding tetrahydrofuran (THF; 100 mL) and shaking the mixture for 15 min. The yellow solid product was dried in *vacuo* and recrystallized from 2-methoxyethanol to give [K(S₂CO(CH₂)₂OMe)] (19.8 g, 0.104 mol, 52.1% yield). mp = 216–219 °C. Calc. for C₄H₇KO₂S₂ (%): C 25.3, H 3.71, S 33.6, K 20.6; found: C 25.5, H 3.79, S 33.5, K 20.8. FTIR (cm⁻¹): 2935 (w), 2888 (w), 1442 (m), 1445 (w), 1230 (m), 1134 (m), 1099 (m), 1066 (s), 1018 (m), 844.3 (w), 676.7 (m), 532.5 (m). ¹H NMR (400 MHz, D₂O) δ (ppm) = 3.35 (s, 3H, OCH₃), 3.72 (t, J = 4.5 Hz, 2H, CH₂CH₂O), 4.50 (t, J = 4.3 Hz, 2H, CH₂CH₂O).

3.4.3.2.4 Synthesis of Potassium 2-Ethoxyethylxanthate (4).

[K(S₂CO(CH₂)₂OEt)] was prepared via the same method, using 2-ethoxyethanol alcohol (75 mL). The product was recrystallized from 2-ethoxyethanol. (22.2 g, 0.108 mol, 54.3% yield). mp = 201–204 °C. Calc. for C₅H₉KO₂S₂ (%): C 29.4, H 4.44, S 31.3, K 19.2; found: C 29.4, H 4.38, S 30.9, K 19.6. FT-IR (cm⁻¹): 2972 (w), 2859 (w), 1443 (m), 1421(w), 1290 (w), 1246 (w), 1107(m), 1053 (s), 934 (w), 826 (w), 795 (w). ¹H NMR (400 MHz, D₂O) δ (ppm) = 1.13 (t, J = 7 Hz, 3H, CH₂CH₃), 3.57 (q, J = 7 Hz, 2H, CH₂CH₃), 3.76 (t, J = 4.5 Hz, 2H, CH₂CH₂O), 4.49 (t, J = 4.5 Hz, 2H, CH₂CH₂O).

3.4.3.2.5 Synthesis of Potassium 1-Methoxy-2-propylxanthate (5).

[K(S₂COC(H)(Me)CH₂OMe)] was prepared via the same method, using 1-methoxy-2-propanol (75 mL). The product was recrystallized from 1-methoxy-2-propanol to give 5 (27.1 g, 0.132 mol, 66.3% yield). mp = 221–226 °C. Calc. for C₅H₉KO₂S₂ (%): C 29.4, H 4.44, S 31.3, K 19.2; found: C 29.7, H 4.38, S 31.5, K 19.5. FT-IR (cm⁻¹): 2974 (w), 2935(w), 2897 (w), 1442 (m), 1474(w), 1445 (w), 1247 (m), 1172 (m), 1108(m), 1045 (s), 949.6 (w), 938.7 (m), 628.2 (w), 572 (w). ¹H NMR (400 MHz, D₂O) δ (ppm) = 1.2 (d, J = 6.5 Hz, 3H, CHCH₃), 3.33 (s, 3H, OCH₃), 3.58 (m, 2H, CH₂O), 5.59 (m, 1H, CHCH₃).

3.4.3.2.6 Synthesis of Potassium 3-Methoxy-1-butylxanthate (6).

[K(S₂CO(CH₂)₂C(H)(OMe)Me)] was prepared via the same method, using 3-methoxy-1-butanol (75 mL). The product was recrystallized from 3-methoxy-1-butanol to give 6 (30.7 g, 0.14 mol, 70.3% yield). mp = 202–206 °C. Calc. for C₆H₁₁KO₂S₂ (%): C 33.0, H 5.08, S 29.3, K 17.9; found: C 33.3, H 5.06, S 29.2, K 18.0. FTIR (cm⁻¹): 2963 (w), 2924(w), 2820 (w), 1449 (m), 1372(w), 1171 (m), 1131 (s), 1100 (s), 1060(s), 958.4 (w), 935.6 (w), 916.1 (w), 830.8(m), 780.4 (w), 559.2 (w). ¹H NMR (400 MHz, D₂O) δ (ppm) = 1.13 (d, J = 6.3 Hz, 3H, CHCH₃), 1.87 (m, 2H, CH₂CHOCH₃), 3.28 (s, 3H, CH₂CHOCH₃), 3.56 (s, J = 6.3 Hz, 1H, CH₂CHOCH₃), 4.42 (m, 2H, CH₂CH₂CHOCH₃).

3.4.3.2.7 Synthesis of Potassium 3-Methoxy-3-methyl-1-butylxanthate (7).

[K(S₂CO(CH₂)₂C(OMe)(Me)₂)] was prepared via the same method, using 3-methoxy-3-methyl-1-butanol (75 mL). The product was recrystallized from 3-methoxy-3-methyl-1-butanol to give 7. (29.2 g, 0.125 mol, 62.8% yield). mp = 237–240 °C. Calc. for C₇H₁₃KO₂S₂ (%): C 36.2, H 5.65, S 27.6, K 16.8; found: C 36.5, H 5.75, S 27.6, K 17.0. FT-IR (cm⁻¹): 2973 (w), 2955 (w), 1463 (w), 1385 (w), 1366 (w), 1293 (w), 1157 (m), 1087 (s), 1050 (s), 988.4 (w), 945.7 (w), 870.3 (m), 779.4 (w), 754.6 (m). ¹H NMR (400 MHz, D₂O) δ (ppm) = 1.17 (s, 6H, CH₂C(CH₃)₂OCH₃), 1.95 (t, J = 7 Hz, 2H, CH₂C(CH₃)₂OCH₃), 3.16 (s, 3H, CH₂C(CH₃)₂OCH₃), 4.44 (t, J = 7 Hz, 2H, CH₂CH₂C(CH₃)₂OCH₃).

3.4.3.2.8 Synthesis of Triphenylphosphine Copper Chloride (8).

$[(\text{Ph}_3\text{P})_2\text{CuCl}]_2 \cdot 2\text{CHCl}_3$ was prepared through a modified literature method.³⁸ PPh_3 (21.5 g, 0.082 mol) and copper(I) chloride (3.96 g, 0.04 mol) were heated to reflux for 12 h in chloroform (150 mL) under N_2 . After filtration the product was allowed to cool to give crystalline $[(\text{Ph}_3\text{P})_2\text{CuCl}]_2$. White crystals suitable for diffraction were obtained from a chloroform solution at $-20\text{ }^\circ\text{C}$. (17.6 g, 0.011 mol, 61.0% yield). mp = $214\text{--}217\text{ }^\circ\text{C}$. Calc. for $\text{C}_{74}\text{H}_{62}\text{C}_{18}\text{Cu}_2\text{P}_4$ (%): C 59.8, H 4.21, P 8.34; found: C 59.4, H 4.21, P 8.05. FT-IR (cm^{-1}): 3052 (w), 2969 (w), 1479 (w), 1432 (m), 1234 (w), 1183 (w), 1092 (m), 1069 (w), 1026 (w), 997.5 (w), 741.7 (s), 691.3 (s), 665.8 (w), 618.2 (w). ^1H NMR (400 MHz, CDCl_3) δ (ppm) = 7.13–7.35 (m, 30H, Ph). ^{31}P NMR (400 MHz, CDCl_3) δ (ppm) = -4.2 .

3.4.3.3 Synthesis of Copper Xanthates.

3.4.3.3.1 Synthesis of Triphenylphosphine Copper(I) Ethylxanthate (9).

A solution of potassium ethylxanthate (0.641 g, 0.0040 mol) in chloroform (40 mL) was added to a solution of triphenylphosphine (2.09 g, 0.008 mol) and CuCl (0.40 g, 0.0040 mol) in the same amount of chloroform. A white precipitate was obtained after continuous stirring for 1 h at room temperature. The solution was filtered to obtain a clear yellow solution. Cooling the yellow solution to $-20\text{ }^\circ\text{C}$ gave yellow crystals of triphenylphosphine copper(I) ethylxanthate (2.40 g, 0.0033 mol, 82.5% yield). mp = $185\text{--}191\text{ }^\circ\text{C}$. Calc. for $\text{C}_{39}\text{H}_{35}\text{CuOP}_2\text{S}_2$ (%): C 66.1, H 4.97, S 9.02, P 8.74, Cu 8.96; found: C 65.7, H 5.08, S 8.77, P 8.44, Cu 8.74. FT-IR (cm^{-1}): 3048 (w), 2992 (w), 1478 (m), 1433 (m), 1290 (s), 1142 (m), 1041 (m), 1009 (s), 849.5 (s), 740.8 (m), 617.7 (s), 559.2 (s). ^1H NMR (400 MHz, CDCl_3) δ (ppm) = 1.27 (t, $J = 7\text{ Hz}$, 3H, CH_2CH_3), 4.34 (q, $J = 7\text{ Hz}$, 2H, OCH_2CH_3), 7.02–7.37 (m, 30H, Ph).

3.4.3.3.2 Synthesis Triphenylphosphine Copper(I) n-Butylxanthate (10).

$[(\text{Ph}_3\text{P})_2\text{Cu}(\text{S}_2\text{COBu})]$ was also synthesized by the same method using potassium butylxanthate (1, 0.75 g, 0.0040 mol), triphenylphosphine (2.09 g, 0.0080 mol), and CuCl (0.40 g, 0.0040 mol). Yield = 2.10 g, 0.0028 mol, 70.0%. mp = $131\text{--}135\text{ }^\circ\text{C}$. Calc. for $\text{C}_{41}\text{H}_{39}\text{CuOP}_2\text{S}_2$ (%): C 66.8, H 5.33, S 8.67, P 8.40, Cu 8.62; found: C 66.9, H 5.34, S 8.44, P 8.72, Cu 8.80. FT-IR (cm^{-1}): 3061 (w), 2998 (w), 1478 (m), 1433

(m), 1313 (s), 1168 (m), 1092 (m), 1052 (s), 996.1 (s), 743.6 (m), 618.5 (s), 574.1 (s). ^1H NMR (400 MHz, CDCl_3) δ (ppm) = 0.96 (t, J = 7.5 Hz, 3H, $\text{CH}_2\text{CH}_2\text{CH}_3$), 1.45 (m, J = 7.5 Hz, 2H, $\text{CH}_2\text{CH}_2\text{CH}_3$), 1.75 (quin, J = 7 Hz, 2H, $\text{CH}_2\text{CH}_2\text{CH}_2$), 4.38 (t, J = 6.5 Hz, 2H, OCH_2CH_2), 7.11–7.47 (m, 30H, Ph).

3.4.3.3.3 Synthesis of Triphenylphosphine Copper(I) Isobutylxanthate (11).

$[(\text{Ph}_3\text{P})_2\text{Cu}(\text{S}_2\text{CO}^i\text{Bu})]$ was synthesized by the same method using potassium isobutylxanthate (2, 0.76 g, 4.00 mmol), triphenylphosphine (2.09 g, 8.0 mmol), and CuCl (0.40 g, 4.0 mmol) in a 1.94 g, 66.0% yield. mp = 133–136 °C. Calc. for $\text{C}_{41}\text{H}_{39}\text{CuOP}_2\text{S}_2$ (%): C 66.78, H 5.34, S 8.68, P 8.41, Cu 8.63; found: C 66.3, H 5.46, S 8.00, P 8.64, Cu 8.93. FT-IR (cm^{-1}): 3054 (w), 2960 (w), 1583 (w), 1477 (m), 1433 (m), 1307 (w), 1167 (m), 1120 (m), 1062 (w), 1026 (w), 996.6 (s), 742.4 (m), 691.8 (s). ^1H NMR (400 MHz, CDCl_3) δ (ppm) = 0.99 (d, J = 6.8 Hz, 6H, $\text{CH}(\text{CH}_3)_2$), 2.12 (sep, J = 6.8 Hz, 1H, $\text{CH}(\text{CH}_3)_2$), 4.17 (d, J = 6.8 Hz, 2H, OCH_2CH), 7.10–7.5 (m, 30H, Ph).

3.4.3.3.4 Synthesis of Triphenylphosphine Copper(I) 2-Methoxyethylxanthate (12).

A solution of potassium methoxyethylxanthate [$\text{K}(\text{S}_2\text{CO}(\text{CH}_2)_2\text{OMe})$] (3, 0.76 g, 4.0 mmol) in chloroform (40 mL) was added to a solution of triphenylphosphine (2.09 g, 8.0 mmol) and CuCl (0.40 g, 4.0 mmol) in the same amount of chloroform. A white precipitate was obtained after continuous stirring for 1 h at room temperature. The solution was filtered to obtain a clear yellow solution. Cooling the yellow solution to -20 °C gave yellow crystals of triphenylphosphine copper(I) methoxyethylxanthate [$(\text{Ph}_3\text{P})_2\text{Cu}(\text{S}_2\text{CO}(\text{CH}_2)_2\text{OMe})$] (2.03 g, 0.0027 mol, 67.8% yield). mp = 139–143 °C. Calc. for $\text{C}_{40}\text{H}_{37}\text{CuO}_2\text{P}_2\text{S}_2$ (%): C 65.0, H 5.05, S 8.66, P 8.38, Cu 8.60; found: C 64.5, H 4.99, S 8.39, P 8.01, Cu 8.25. FT-IR (cm^{-1}): 3046 (w), 2930 (w), 1583 (m), 1478 (m), 1432 (m), 1307 (w), 1152 (m), 1169 (m), 1120 (m), 1091 (s), 1064 (m), 1015 (w), 996.9 (w), 844.3 (w), 745.3 (s), 619.9 (s), 574.4 (w). ^1H NMR (400 MHz, CDCl_3) δ (ppm) = 3.42 (s, 3H, OCH_3), 3.69 (t, J = 5.2 Hz, 2H, $\text{CH}_2\text{CH}_2\text{O}$), 4.52 (t, J = 5 Hz, 2H, $\text{CH}_2\text{CH}_2\text{O}$), 7.05–7.47 (m, 30H, Ph).

3.4.3.3.5 Synthesis of Triphenylphosphine Copper(I) 2-Ethoxyethylxanthate (13).

A solution of potassium 2-ethoxyethylxanthate (4, 0.82 g, 4.0 mmol) in chloroform (40 mL) was added to a solution of triphenylphosphine copper chloride (8, 2.89 g, 4.0 mmol) in the same amount of chloroform. A white precipitate was obtained after continuous stirring for 1 h at room temperature. The solution was filtered to obtain a clear yellow solution. Cooling the yellow solution to $-20\text{ }^{\circ}\text{C}$ gave yellow crystals of triphenylphosphine copper(I) ethoxyethylxanthate $[(\text{Ph}_3\text{P})_2\text{Cu}(\text{S}_2\text{CO}(\text{CH}_2)_2\text{OEt})]$ in a 1.89 g, 0.0025 mol, 62.9% yield. mp = $147\text{--}151\text{ }^{\circ}\text{C}$. Calc. for $\text{C}_{41}\text{H}_{39}\text{CuO}_2\text{P}_2\text{S}_2$ (%): C 65.4, H 5.22, S 8.49, P 8.22; found: C 65.5, H 5.19, S 8.26, P 8.29. FT-IR (cm^{-1}): 3039 (w), 2943 (w), 1584 (m), 1477 (m), 1432 (m), 1305 (w), 1188 (m), 1121 (m), 1092 (s), 1060 (m), 1018 (w), 850.3 (w), 746.7 (s), 691.4 (s), 618.6 (w). ^1H NMR (400 MHz, CDCl_3) δ (ppm) = 1.24 (t, $J = 7\text{ Hz}$, 3H, CH_2CH_3), 3.57 (q, $J = 7\text{ Hz}$, 2H, CH_2CH_3), 3.74 (t, $J = 4.3\text{ Hz}$, 2H, $\text{CH}_2\text{CH}_2\text{O}$), 4.52 (t, $J = 4.5\text{ Hz}$, 2H, $\text{CH}_2\text{CH}_2\text{O}$), 7.03–7.46 (m, 30H, Ph).

3.4.3.3.6 Synthesis of Triphenylphosphine Copper(I) 1-Methoxy-2-propylxanthate (14).

$[(\text{Ph}_3\text{P})_2\text{Cu}(\text{S}_2\text{COC}(\text{H})(\text{Me})\text{CH}_2\text{OMe})]$ was synthesized by the same method using potassium 1-methoxy-2-propylxanthate (5, 0.82 g, 4.0 mmol) and triphenylphosphine copper chloride (8, 2.89 g, 4.0 mmol) in a 2.37 g, 0.0031 mol, 79.4% yield. mp = $143\text{--}148\text{ }^{\circ}\text{C}$. Calc. for $\text{C}_{41}\text{H}_{39}\text{CuO}_2\text{P}_2\text{S}_2$ (%): C 65.4, H 5.22, S 8.49, P 8.23, Cu 8.44; found: C 66.2, H 5.25, S 7.90, P 7.91, Cu 7.99. FT-IR (cm^{-1}): 3037 (w), 2949 (w), 1478 (m), 1434 (m), 1310 (w), 1180 (m), 1110 (m), 1027 (s), 997.6 (m), 969.4 (w), 746.8 (s), 692.7 (s), 618.7 (w). ^1H NMR (400 MHz, CDCl_3) δ (ppm) = 1.33 (d, $J = 6.5\text{ Hz}$, 3H, CHCH_3), 3.39 (s, 3H, OCH_3), 3.43–3.63 (m, 2H, CH_2O), 5.50 (m, 1H, CHCH_3), 7.1–7.47 (m, 30H, Ph).

3.4.3.3.7 Synthesis of Triphenylphosphine Copper(I) 3-Methoxy-1-butylxanthate(15).

$[(\text{Ph}_3\text{P})_2\text{Cu}(\text{S}_2\text{CO}(\text{CH}_2)_2\text{C}(\text{H})(\text{OMe})\text{Me})]$ was synthesized by the same method using potassium 3-methoxy-1-butylxanthate (6, 0.87 g, 4.0 mmol) and

triphenylphosphine copper chloride (8, 2.89 g, 4.0 mmol) in a 1.78 g, 0.0023 mol, 59.3% yield. Mp = 141–146 °C. Calc. for C₄₂H₄₁CuO₂P₂S₂ (%): C 65.7, H 5.39, S 8.34, P 8.08, Cu 8.29; found: C 65.1, H 5.33, S 8.21, P 7.63, Cu 8.16. FT-IR (cm⁻¹): 3041 (w), 2966 (w), 1479 (m), 1433 (m), 1376 (w), 1165 (m), 1093 (m), 1076 (s), 1047 (m), 997.5 (m), 969.4 (w), 743.7 (s), 693.4 (s), 618.3 (w). ¹H NMR (400 MHz, CDCl₃) δ (ppm) = 1.18 (d, J = 6 Hz, 3H, CHCH₃), 1.93 (m, 2H, CH₂CHOCH₃), 3.33 (s, 3H, CH₂CHOCH₃), 3.51 (s, J = 6.5 Hz, 1H, CH₂CHOCH₃), 4.48 (m, 2H, CH₂CH₂CHOCH₃), 7.17–7.59 (m, 30H, Ph).

3.4.3.3.8 Synthesis of Triphenylphosphine Copper(I) 3-Methoxy-3-methyl-1-butylxanthate (16).

[(Ph₃P)₂Cu(S₂CO(CH₂)₂C(OMe)(Me)₂)] was synthesized by the same method using potassium 3-methoxy-3-methyl-1-butylxanthate (7, 0.93 g, 4.0 mmol) and triphenylphosphine copper chloride (8, 2.89 g, 4.0 mmol) in a 1.92 g, 0.0024 mol, 61.4% yield. mp = 124–128 °C. Calc. for C₄₃H₄₃CuO₂P₂S₂ (%): C 66.1, H 5.55, S 8.19, P 7.93, Cu 8.14; found: C 66.2, H 5.60, S 7.94, P 7.48, Cu 7.92. FT-IR (cm⁻¹): 3062 (w), 2977 (w), 1479 (m), 1433 (m), 1366 (w), 1309 (w), 1167 (m), 1146 (m), 1090 (m), 1073 (s), 1043 (m), 996.7 (m), 917(w), 742.7 (s), 693.1 (s), 618.3 (w). ¹H NMR (400 MHz, CDCl₃) δ (ppm) = 1.22 (s, 6H, CH₂C(CH₃)₂OCH₃), 1.98 (t, J = 7.5 Hz, 2H, CH₂C(CH₃)₂OCH₃), 3.22 (s, 3H, CH₂C(CH₃)₂OCH₃), 4.49 (t, J = 7.5 Hz, 2H, CH₂CH₂C(CH₃)₂OCH₃), 7.21–7.33 (m, 30H, Ph).

3.4.3.4 Synthesis of copper sulfide nanorods.

The copper sulfide nanorods were synthesized under an inert atmosphere of nitrogen gas. Oleylamine (15 mL) was heated to 270 °C for 30 min. The temperature was reduced to 260 °C and 0.40 g of the relevant copper(I) xanthate in oleylamine (6 mL) was injected into the hot reaction medium via a syringe. After a period of time (5 s or 1 h), the solution was cooled to room temperature with the addition of isopropyl alcohol, and the rods were separated by centrifugation. The nanorods were extracted by diluting the resultant product with methanol.

3.4.3.5 Density Functional Theory Calculations.

The molecular geometry optimization and vibrational frequencies for 9–16 and two additional copper xanthate series [(PPh₃)₂Cu(S₂CO(CH₂)₂OR)] (17- R, R = Me, Et, ⁿPr, ⁿBu) [(PPh₃)₂Cu(S₂COR')] (18-R', R' = ⁿBu, ⁿPen, ⁿHex, ⁿHep) were calculated by using the Gaussian09³⁹ package at the M06/6-31(d, p) level of theory.

3.4.4 Results and discussion

3.4.4.1 Xanthate Precursors.

Compounds 1–7 were synthesized from the reaction of the relevant potassium alkoxide with carbon disulfide to generate the xanthate ligand. Figure (3.1) shows the IR curves of ligands 1–7 and figure (3.2) shows the IR of copper xanthate complexes.

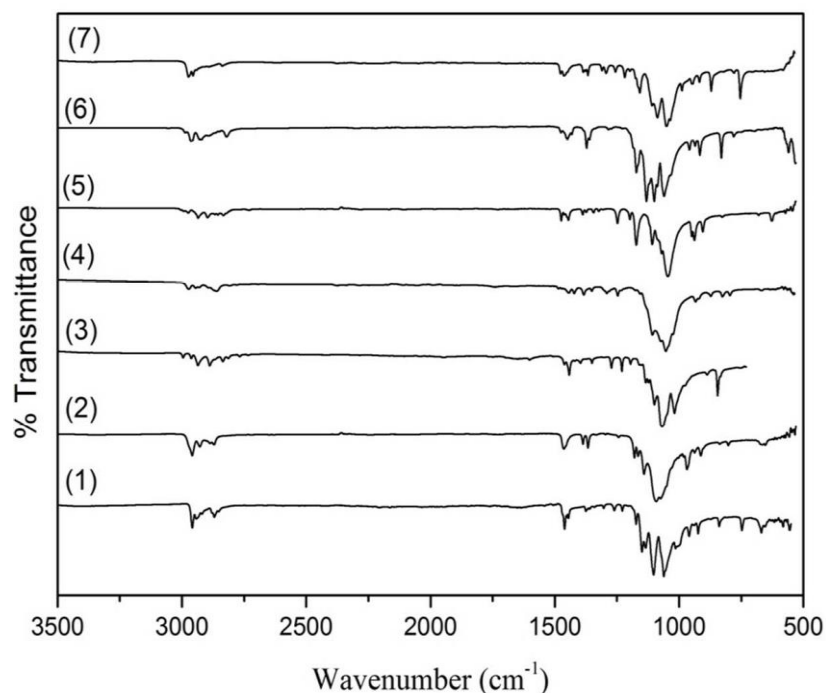


Figure 3.1. FT-IR spectra of the potassium xanthate precursors (1–7).

The ¹H NMR spectra were taken as evidence for the purity of the complexes (Figures A2 – A21). We were able to obtain the structure of 3–5 from single-crystal X-ray diffraction (Table A1 and Figure A1). 9–12 were formed via complexing commercially available potassium ethylxanthate or 1–3, respectively, with copper(I) chloride in the presence of triphenylphosphine as a stabilizing ligand. Compounds

13–16 were synthesized from reaction of xanthate ligands **4–7** with triphenylphosphine copper chloride (**8**, Figure 3.3a).

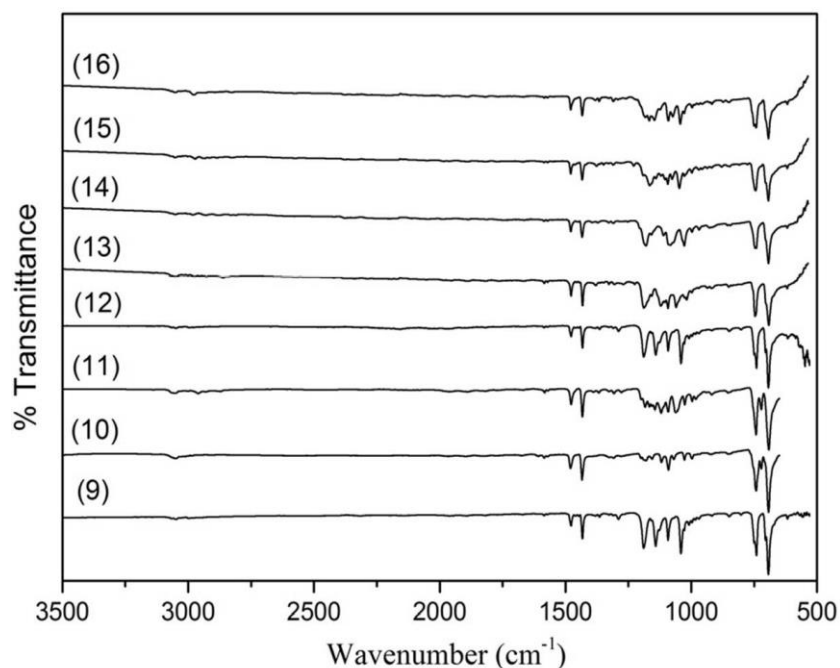


Figure 3.2. FT-IR spectra of the triphenylphosphine copper(I) alkylxanthate complexes (**9-16**).

Crystals suitable for X-ray diffraction were grown from a chloroform solution at -20 °C. We report the crystal structure of the triphenylphosphine isobutyl (**11**, Figure 3.3b), 2-methoxyethyl (**12**, Figure 3.3c), 2-ethoxyethanol (**13**, Figure 3.3d), 1-methoxy-2-propyl (**14**, Figure 3.3e), 3-methoxy-1-butyl (**15**, Figure 3.3f), and 3-methoxy-3-methyl-1-butyl (**16**, Figure 3.3g) copper xanthates for the first time, while the ethylxanthate (**9**) and n-butylxanthate (**10**) complexes have previously been reported.^{40, 41} Compounds **11–16** all adopt a tetrahedral coordination arrangement around the central copper ion (Figure 3.3), in a manner analogous to the previously reported ethyl and n-butyl counterparts. The additional O as part of the alkoxy groups for **12–16** does not coordinate to any neighboring copper atoms. The bond lengths for **11–16** are all very similar, with Cu–S bond lengths of 2.4083(7)–2.4312(6) Å, 2.3705(9)–2.4791(9) Å, 2.417(1)–2.420(1) Å, 2.417(1)–2.434(1) Å, 2.3903(8)–2.4468(8) Å, and 2.3956(6)–2.4411(7) Å, respectively. For **11–16** the S–C–S bond angles are 120.7(1)°, 121.5(2)°, 120.5(3)°, 119.7(3)°, 120.4(2)°, and 121.1(1)°. The S–Cu–S bond angle is fairly consistent for **11–16** at 74.92(2)°, 74.82(3)°, 74.75(5)°, 74.41(4)°, 74.70(3)°, and 74.94(2)°.

respectively. The copper(I) xanthates' decomposition pathway was observed by TGA (Figure 3.4) and, with the exception of **10**, which has a small weight loss between 150 and 200 °C, gave a clean, one-step route. The major decomposition occurs from 200 to 275 °C, with fully breaking down by 270 °C. The final weight % of the residue indicates the conversion to CuS for all of the complexes **9–16**.

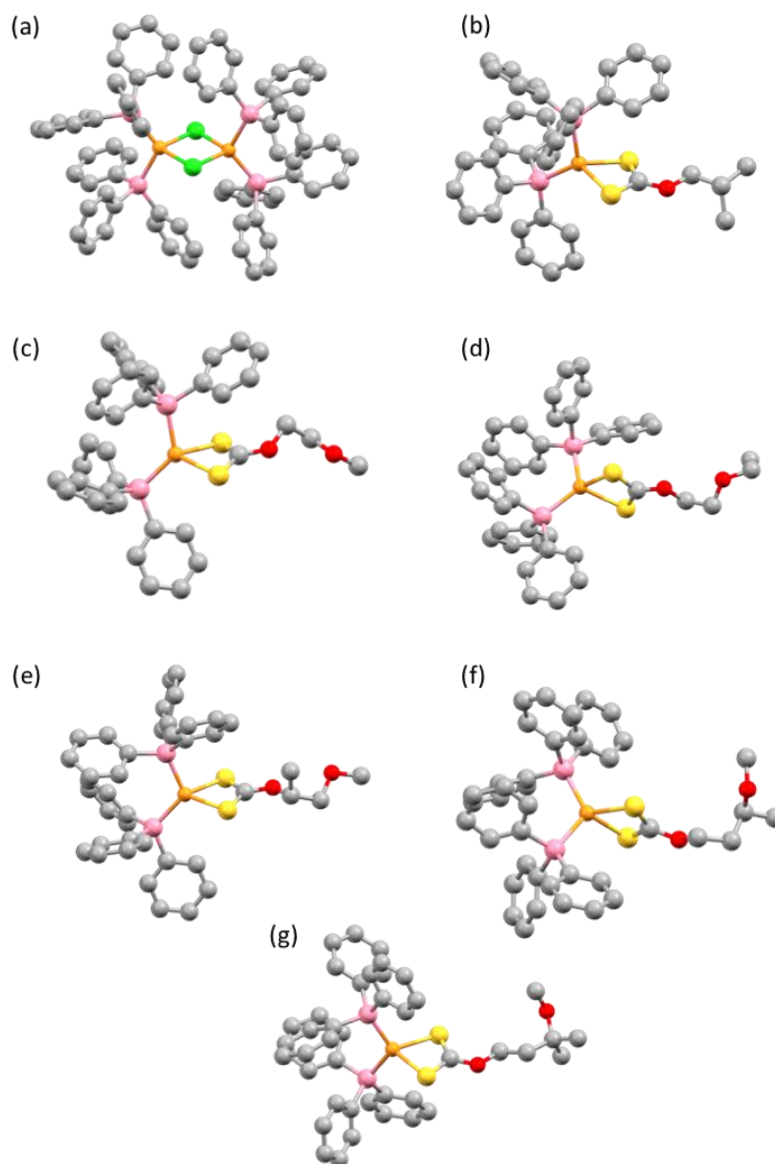


Figure 3.3. Structures of (a) triphenylphosphine copper chloride (**8**), triphenylphosphine copper(I) (b) isobutylxanthate (**11**), (c) 2- methoxyethylxanthate (**12**), (d) 2-ethoxyethylxanthate (**13**), (e) 1- methoxy-2-propylxanthate (**14**), (f) 3- methoxy-1-butylxanthate (**15**), and (g) 3-methoxy-3-methyl-1-butylxanthate (**16**). Hydrogens omitted for clarity. Green = Cl, orange = Cu, yellow = S, pink = P, red = O, gray = C.

3.4.4.2 Synthesis of Nanorods.

The copper(I) xanthates were utilized as single source precursors via decomposition in oleylamine to generate copper sulfide at 260 °C. We observed no ligand exchange during the dissolution of the xanthates in oleylamine (figure A22). At long reaction times (1 h) complexes **9–12** gave nanocrystals that were exclusively Cu₂S (Figure 3.5). At short reaction times (5 s) all eight precursors (**9–16**)

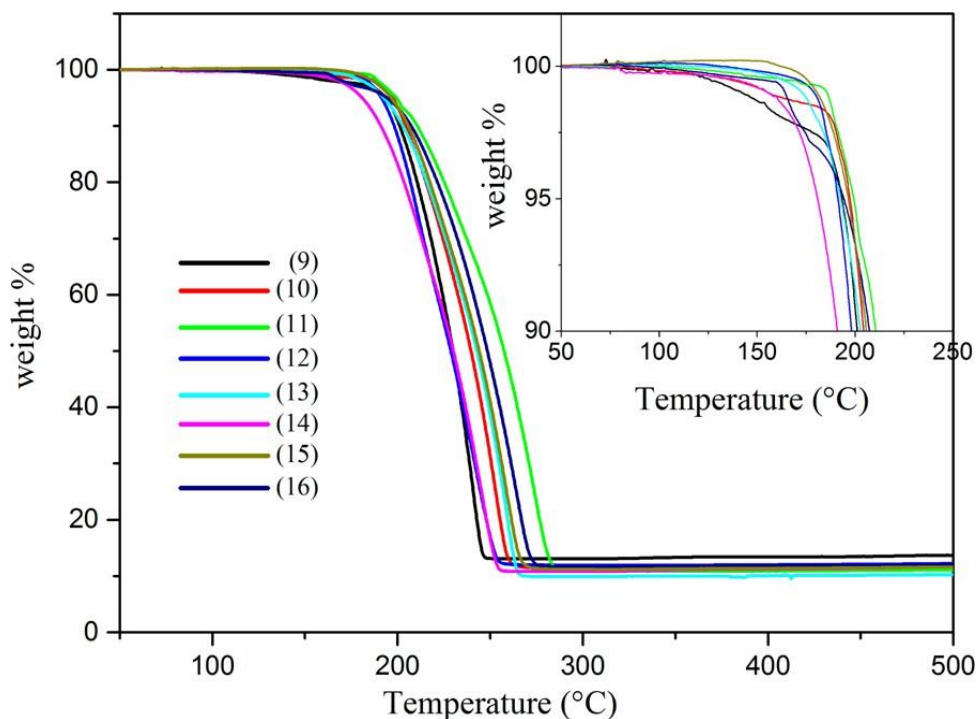


Figure 3.4. TGA of complexes **9–16** indicates that decomposition occurs between 200 and 250 °C leading to the formation of CuS. (inset) Expansion of the 50–250 °C region showing the onset of breakdown.

generated Cu_{1.74}S, with a pattern that matches that of roxbyite (JCPDS 00–064–0278, Figure 3.6). The unit cells for the nanocrystals are in good agreement with the literature values for the two phases (Supporting Information Tables S3.2 and S3.3).

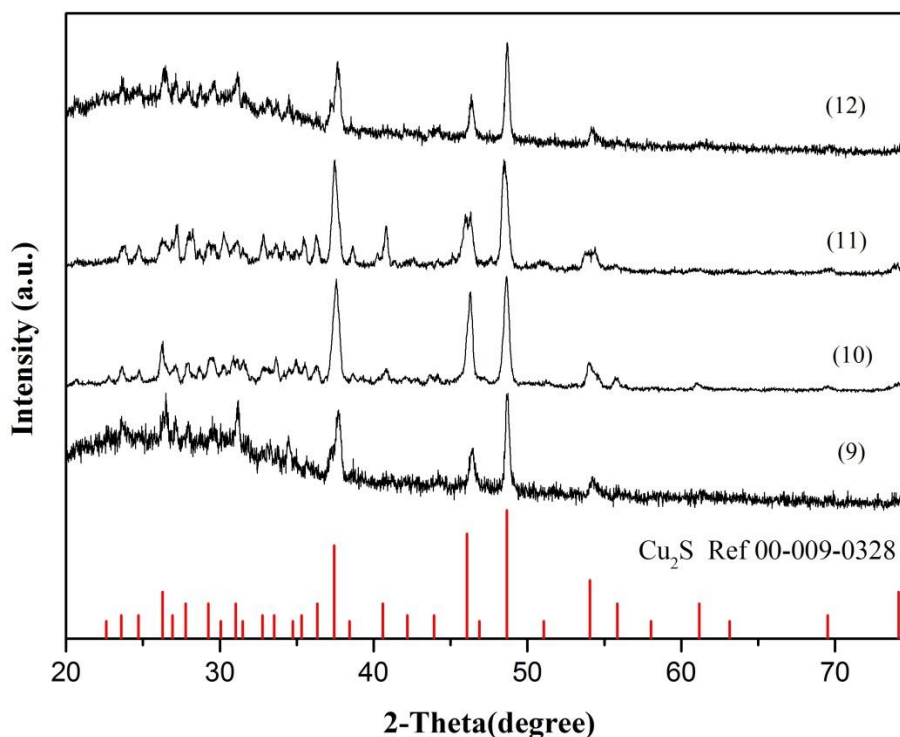


Figure 3.5. The powder XRD patterns of nanocrystals generated from the decomposition of **9-12** for a reaction time of 1 h.

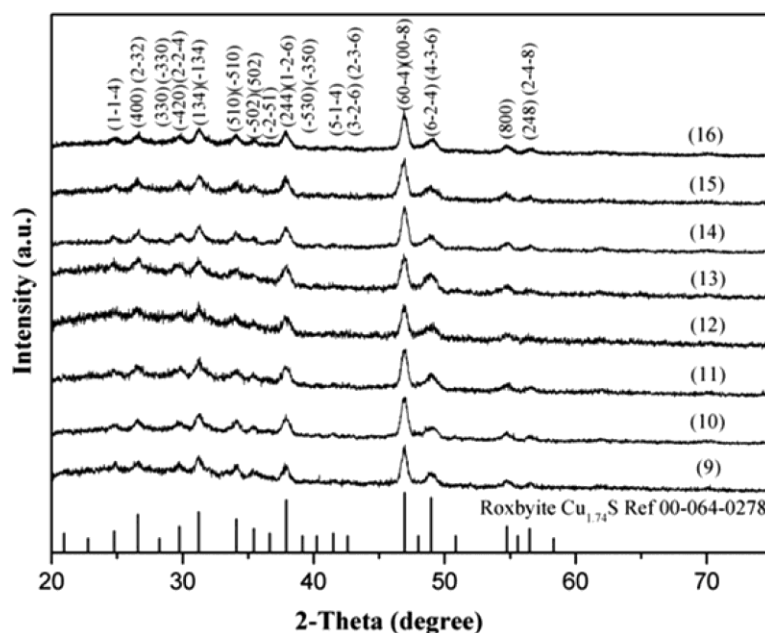


Figure 3.6. Powder XRD patterns of nanocrystals generated from the decomposition of **9–16** for a reaction time of 5 s.

The nanorods have a Cu/S stoichiometry of nearly 2:1, while the precursors have the reverse of this (1:2). This indicates that the precursors appear to decompose with the retention of the copper +1 oxidation state. One of the suggested mechanisms of

metal xanthate decomposition is the Chugaev elimination mechanism, which results in the formation of CuSH units (Figure 3.7).^{35, 42} This retains the copper in the +1 oxidation state that the precursor was in.

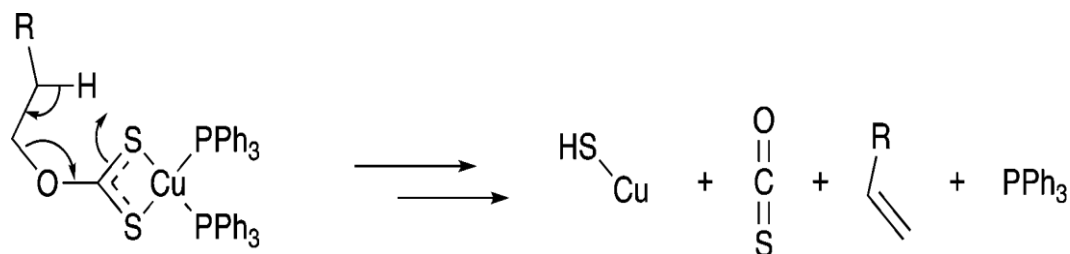


Figure 3.7. Suggested initial breakdown of precursor by Chugaev elimination.

For copper sulfide to crystallize there must be further loss of hydrogen and sulfur. In the idealized instance this would involve the loss of H₂S from two “CuSH” units to give Cu₂S, which keeps the +1 oxidation state. In the case of the 5 s reaction time we observe an incomplete loss of sulfur to give Cu_{1.74}S roxbyite, whereas, as noted previously, for the longer reaction time we obtain Cu₂S chalcocite. The elemental composition of the nanorods was determined by energy dispersive X-ray spectroscopy (EDS). The ratio of Cu/S is fairly consistent for all of the nanorods formed from the breakdown of **9–16** (Table 3.1, Figure 3.8), ranging from 1.83:1 (**9**) to 1.73:1 (**16**).

Table 3.1. EDS data of the nanorods obtained from a 5 s decomposition.

Precursor	Cu	S	Cu/S
9	64.7	35.3	1.83
10	64.6	35.4	1.83
11	64.6	35.4	1.82
12	64.4	35.6	1.81
13	64.3	35.7	1.80
14	64.3	35.7	1.80
15	64.0	36.0	1.78
16	63.3	36.7	1.73

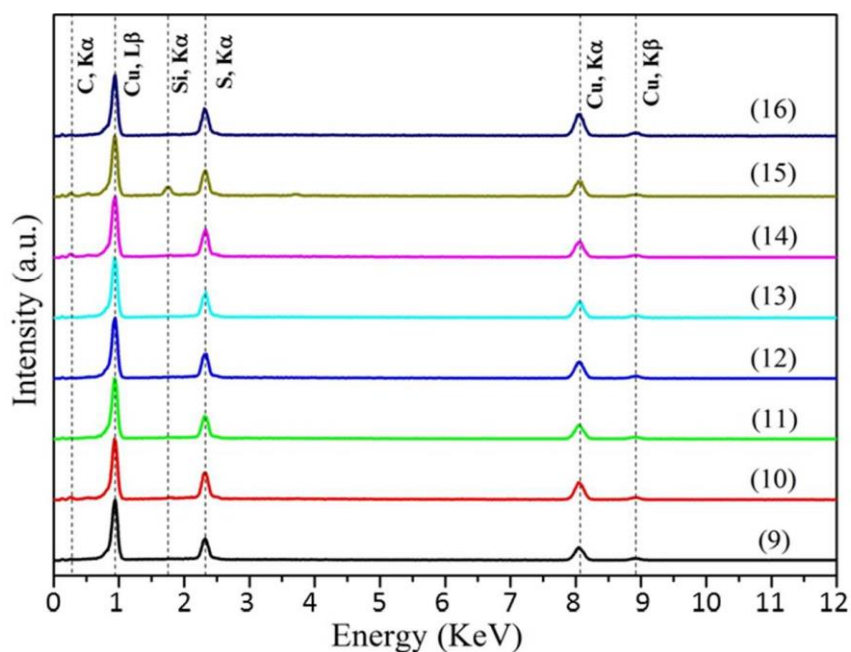


Figure 3.8. EDS spectra of the nanorods obtained from a 5 s decomposition of **9-16**.

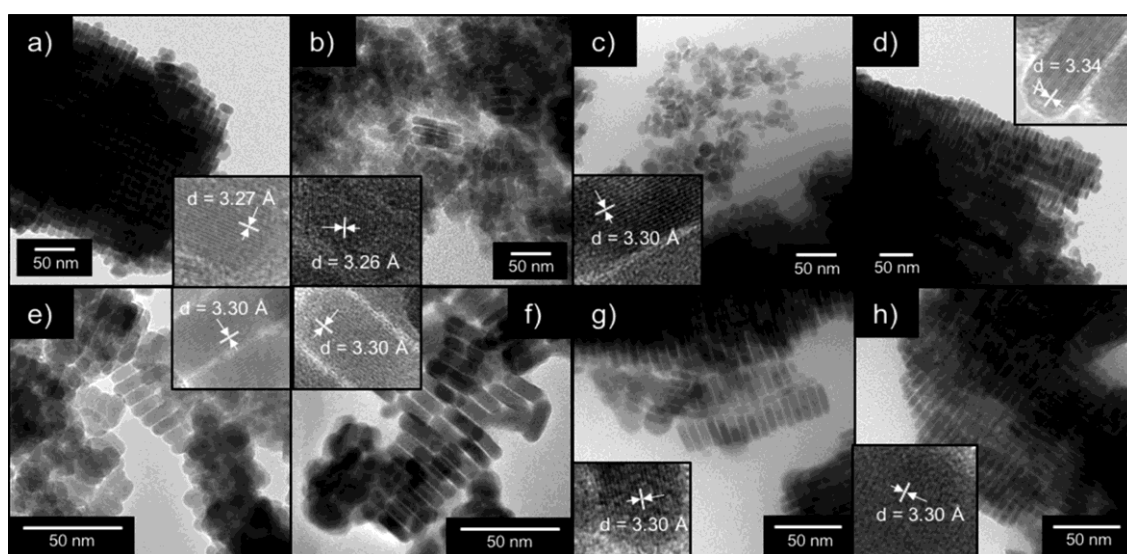


Figure 3.9. TEM images of the nanocrystals generated from the 5 s decomposition of triphenylphosphine copper(I) (a) ethylxanthate (**9**), (b) n-butylxanthate (**10**), (c) isobutylxanthate (**11**), (d) 2-methoxyethylxanthate (**12**), (e) 2-ethoxyethylxanthate (**13**), (f) 1-methoxy-2-propylxanthate (**14**), (g) 3-methoxy-1-butylxanthate (**15**), and (h) 3-methoxy-3-methyl-1-butylxanthate (**16**). (insets) The d-spacings measured for each. d-spacings of 3.27, 3.26, 3.30, 3.34, 3.30, 3.30, 3.30, and 3.30 Å correspond to the (400) reflection.

Initially the xanthates were decomposed over a long period of time (1 h), and while this generated clean Cu_2S , analysis of the particle size via TEM indicated that there was excessive agglomeration of the nanocrystals (Figure A23). Therefore, a shorter reaction time period of 5 s was chosen. This led to the synthesis of nanorods of $\text{Cu}_{1.74}\text{S}$, which align themselves along their long axis (Figure 3.9). The choice of xanthate ligand appears to exert some control over the size of the obtained nanorod. Some of the precursors lead to highly uniform nanorods (i.e., **9**, **10**, **12**, **14**, and **16**), while the others are a little more polydisperse (Figures A24–A31). There are further examples of TEM images of the rods in the appendix A, figures A32–A39. The xanthate chains that have more carbon/ oxygens give slightly narrower particles (Figure 3.10); that is, the obtained width of the copper sulfide nanorod has an inverse relationship with the chain length of the precursor. This is in agreement with a result that we have provisionally reported for PbS nanorod.³⁵

The UV–vis spectra of the $\text{Cu}_{1.74}\text{S}$ nanorods are shown in Figure 3.10b. There is a slight variation in band gap in the rods obtained, and this correlates very well with the choice of xanthate ligand used in the precursor (inset of Figure 3.10b).

3.4.4.3 DFT Study

To understand the way the xanthate ligand influences the size of the obtained nanorod, we turned to density functional theory (DFT). We optimized the geometry of **9–16** and obtained the ground-state energies of these complexes (Supporting Information Table S3.4). We also studied two series of linear chain xanthates $[(\text{PPh}_3)_2\text{Cu}(\text{S}_2\text{CO}(\text{CH}_2)_2\text{OR})]$ (17-R, R = Me, Et, ⁿPr, ⁿBu) and $[(\text{PPh}_3)_2\text{Cu}(\text{S}_2\text{COR}')] (18\text{-R}', \text{R}' = \text{}^n\text{Bu}, \text{}^n\text{Pen}, \text{}^n\text{Hex}, \text{}^n\text{Hep})$, which have comparable xanthate chain lengths (i.e., 17-Me has the same chain length as 18-ⁿBu; Supporting Information Table S3.5).

For 17-R and 18-R', there are some notable differences in the geometry-optimized structures. For 17-R, there is a loss of symmetry about the Cu center with respect to the Cu–S bond lengths. For each complex in the 18-R' series, the two Cu–S bonds, and correspondingly the C–S bonds, are nearly identical (Supporting Information Tables S3.6 and S3.7). However, for 17-R one Cu–S lengthens, while one C–S contracts slightly. This is mirrored in the experimental crystal data, where **12** (which corresponds to **17**-Me) has Cu–S bond lengths of 2.3705(9) and 2.4791(9) Å, while

9 (i.e., **18-nBu**) has ones of 2.421(2) and 2.423(2) Å.⁴¹ This distinction between the two S atoms for **17-R** is also observed in a Mulliken population analysis, where the S that is most closely bonded to the Cu has a greater electronic charge. This suggests that there is decreased delocalization across the S–C–S unit for **17-R** than **18-R'**, which must be brought about by the introduction of the second oxygen into the xanthate chain. There is a good relationship between length of the xanthate chain and ground-state energy, which is to be expected for **17-R** and **18-R'** (Supporting Information Figure S3.12), but is also true for **9–16** (Figure 3.11a). This clearly indicates that the longer chain complexes are lower in energy than the shorter chain ones. Additionally, we note that the introduction of an O into the alkyl chain of the xanthate results in a lowering of energy. This again is the expected result, as an “O” is lower in energy than a CH₂ motif and can be seen in Supporting Information Figure S3.12, where **17-R** is lower in energy than **18-R'** for each chain length.

A plot of the ground-state energy of **9–16** against width of the nanorods reveals a reasonable correlation (Figure 3.11b). The lower-energy complexes appear to result in the formation of narrower nanorods, while the higher-energy complexes give wider nanorods. This is presumably due to the complexes with a higher ground-state energy being easier to decompose into copper sulfide. Additionally, this is in agreement with the previous assertion that the longer-chain complexes give narrower rods (Figure 3.10), as they are also lower in energy. Therefore, it is possible to suggest that control over the size of the obtained nanorods may be exerted by the choice of xanthate ligand.

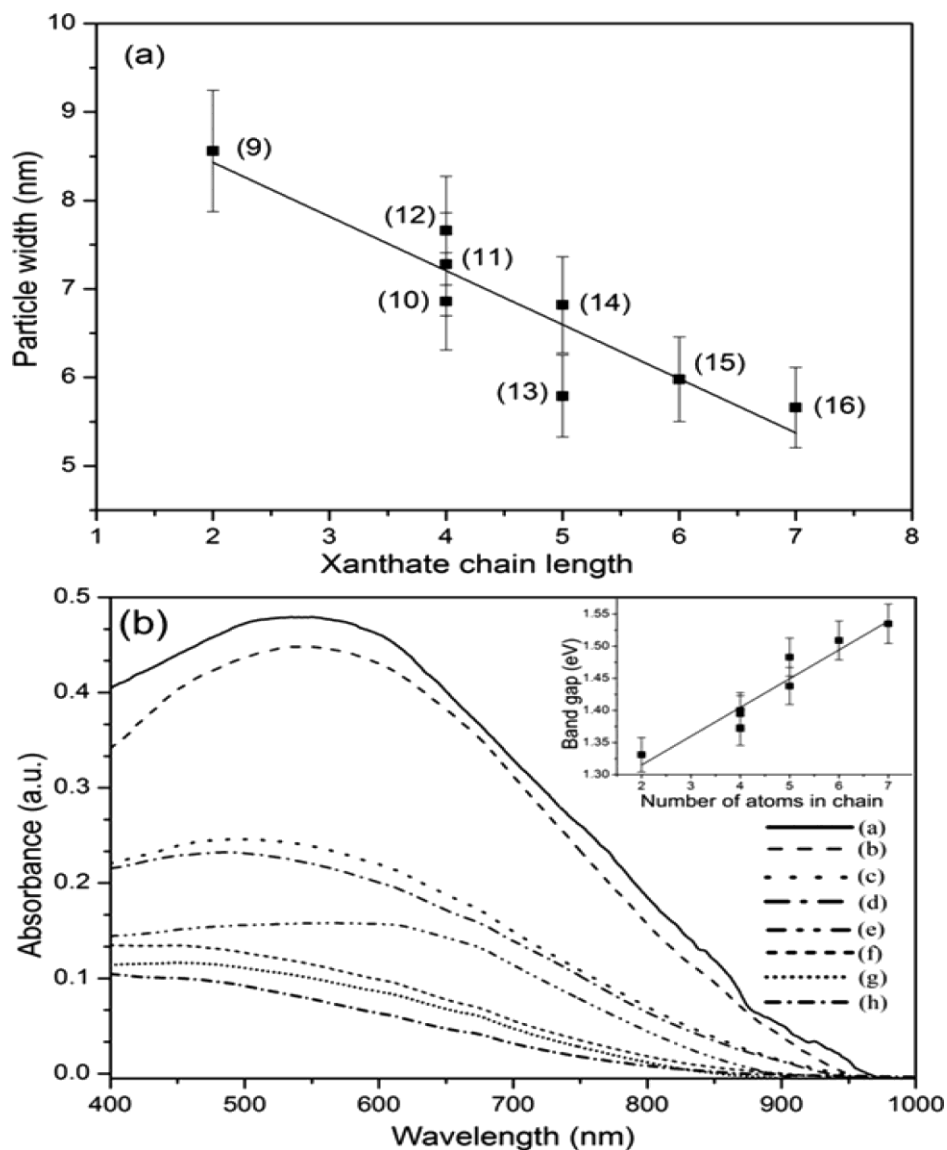


Figure 3.10. (a) Increasing the chain length of the xanthate ligand leads to a decrease in the width of the rods obtained. One standard deviation for each measurement is displayed. (b) The UV-vis spectra for the copper sulfide nanorod—the number indicates the precursor. (inset) Correlation between band gap and the number of atoms in the xanthate chain.

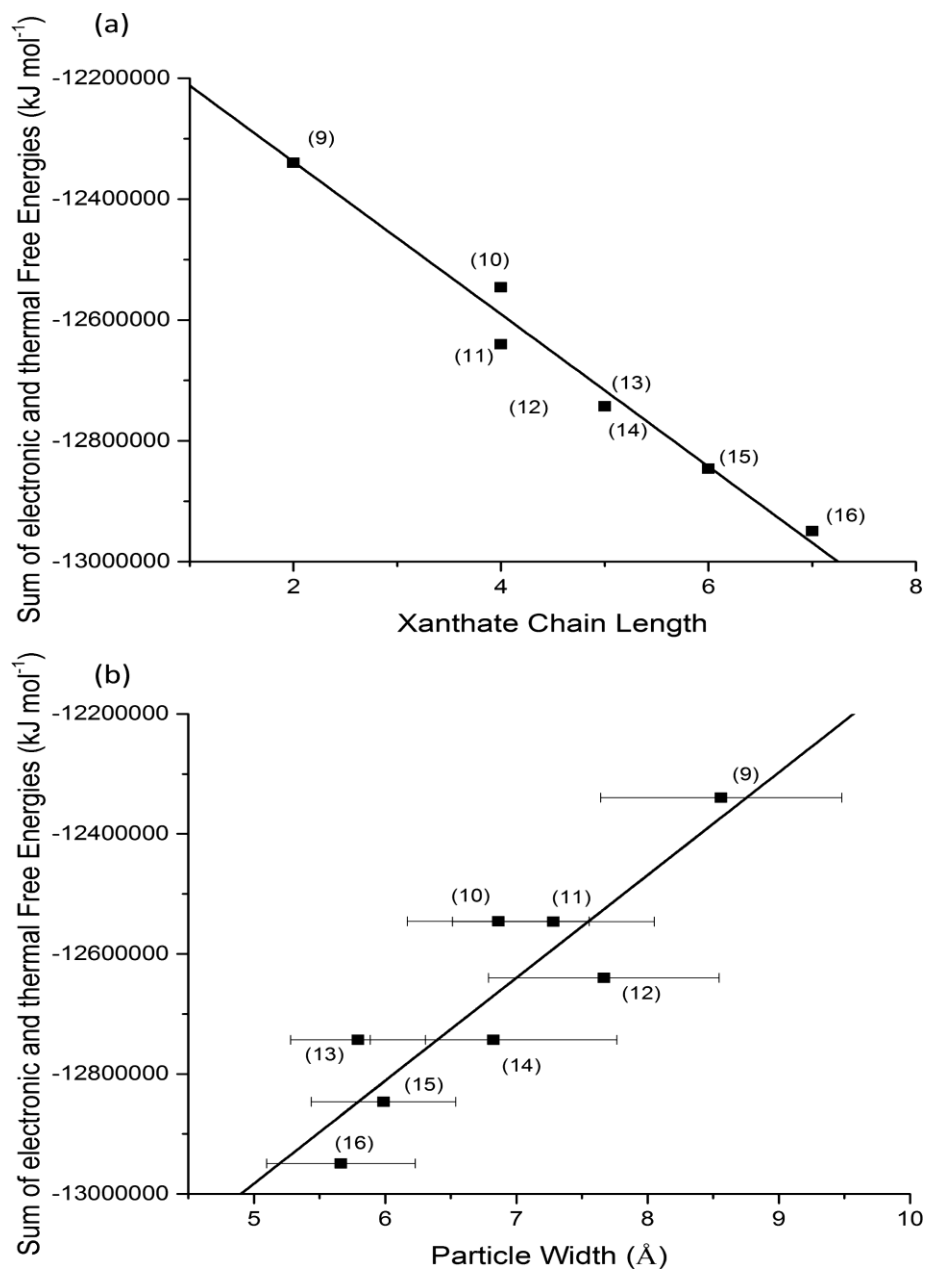


Figure 3.11. (a) The ground-state energies of 9–16 as a function of the chain length. (b) The width of the obtained nanorod compared to the sum of the electronic and thermal energy of the xanthate precursor.

3.4.5 Conclusions

The synthesis and single-crystal characterization of six novel triphenyl copper(I) xanthate complexes [isobutylxanthate (**11**), 2-methoxyethylxanthate (**12**), 2-ethoxyethylxanthate (**13**), 1-methoxy-2-propylxanthate (**14**), 3-methoxy-1-butylxanthate (**15**), and 3-methoxy-3-methyl-1-butylxanthate (**16**)] has been reported. These six complexes, in addition to the ethyl and nbutyl analogues have been tested as single-source precursors for the formation of copper sulfide nanorods. At long reaction times heavily aggregated Cu_2S is formed, while short times result in $\text{Cu}_{1.74}\text{S}$ nanorods. The longer-chain xanthates lead to the formation of rods of decreased width, which has been confirmed with a DFT study.

3.4.6 References

1. P. D. Matthews, P. D. McNaughter, D. J. Lewis and P. O'Brien, *Chem. Sci.*, 2017, **8**, 4177-4187.
2. Y. Wu, C. Wadia, W. Ma, B. Sadler and A. P. Alivisatos, *Nano Lett.*, 2008, **8**, 2551-2555.
3. I. Grozdanov and M. Najdoski, *J. Solid State Chem.*, 1995, **114**, 469-475.
4. E. Dilena, D. Dorfs, C. George, K. Miszta, M. Povia, A. Genovese, A. Casu, M. Prato and L. Manna, *J. Mater. Chem.*, 2012, **22**, 13023-13031.
5. Y. Zhao, H. Pan, Y. Lou, X. Qiu, J. Zhu and C. Burda, *J. Am. Chem. Soc.*, 2009, **131**, 4253-4261.
6. Y. Xie, L. Carbone, C. Nobile, V. Grillo, S. D'Agostino, F. Della Sala, C. Giannini, D. Altamura, C. Oelsner and C. Kryschi, *ACS nano*, 2013, **7**, 7352-7369.
7. W. van der Stam, A. C. Berends and C. de Mello Donega, *Chemphyschem*, 2016, **17**, 559-581.
8. S. Goel, F. Chen and W. Cai, *Small*, 2014, **10**, 631-645.
9. G. Ku, M. Zhou, S. Song, Q. Huang, J. Hazle and C. Li, *Acs Nano*, 2012, **6**, 7489-7496.
10. A. L. Abdelhady, K. Ramasamy, M. A. Malik, P. O'Brien, S. J. Haigh and J. Raftery, *J. Mater. Chem.*, 2011, **21**, 17888-17895.
11. S. Djurle and X. An, *Acta Chem. Scand*, 1958, **12**, 1415-1426.
12. W. G. Mumme, R. W. Gable and V. Petříček, *The Canadian Mineralogist*, 2012, **50**, 423-430.
13. H. T. Evans, *Z. Kristallogr. Cryst. Mater.*, 1979, **150**, 299-320.
14. R. J. Goble, *The Canadian Mineralogist*, 1985, **23**, 61-76.
15. M. Buerger and B. J. Wuensch, *Science*, 1963, **141**, 276-277.
16. P. L. Saldanha, R. Brescia, M. Prato, H. Li, M. Povia, L. Manna and V. Lesnyak, *Chem. Mater.*, 2014, **26**, 1442-1449.
17. S. Deka, A. Genovese, Y. Zhang, K. Miszta, G. Bertoni, R. Krahne, C. Giannini and L. Manna, *J. Am. Chem. Soc.*, 2010, **132**, 8912-8914.
18. A. Ghezelbash and B. A. Korgel, *Langmuir*, 2005, **21**, 9451-9456.
19. A. E. Saunders, A. Ghezelbash, D.-M. Smilgies, M. B. Sigman and B. A. Korgel, *Nano Lett.*, 2006, **6**, 2959-2963.

20. S. C. Riha, D. C. Johnson and A. L. Prieto, *J. Am. Chem. Soc.*, 2010, **133**, 1383-1390.
21. Q. Lu, F. Gao and D. Zhao, *Nano Lett.*, 2002, **2**, 725-728.
22. J. B. Rivest and P. K. Jain, *Chem. Soc. Rev.*, 2013, **42**, 89-96.
23. C. de Mello Donega, *Chem. Soc. Rev.*, 2011, **40**, 1512-1546.
24. W. P. Lim, C. T. Wong, S. L. Ang, H. Y. Low and W. S. Chin, *Chem. Mater.*, 2006, **18**, 6170-6177.
25. L. Jia, H. Ji, J. Lai, J. Wang, H. Chen, X. Zheng, H. Liu and Z. Jin, *Mater. Des.*, 2017, **123**, 39-45.
26. M. Akhtar, Y. Alghamdi, J. Akhtar, Z. Aslam, N. Revaprasadu and M. A. Malik, *Mater. Chem. Phys.*, 2016, **180**, 404-412.
27. T. H. Larsen, M. Sigman, A. Ghezelbash, R. C. Doty and B. A. Korgel, *J. Am. Chem. Soc.*, 2003, **125**, 5638-5639.
28. M. Afzaal, C. L. Rosenberg, M. A. Malik, A. J. White and P. O'Brien, *New J. Chem.*, 2011, **35**, 2773-2780.
29. T. Wei, Y. Liu, W. Dong, Y. Zhang, C. Huang, Y. Sun, X. Chen and N. Dai, *ACS Appl. Mater. Interfaces*, 2013, **5**, 10473-10477.
30. K. Ramasamy, M. A. Malik, N. Revaprasadu and P. O'Brien, *Chem. Mater.*, 2013, **25**, 3551-3569.
31. M. Al-Shakban, Z. Xie, N. Savjani, M. A. Malik and P. O'Brien, *J. Mater. Sci.*, 2016, **51**, 6166-6172.
32. P. D. Matthews, M. Akhtar, M. A. Malik, N. Revaprasadu and P. O'Brien, *Dalton Trans.*, 2016, **45**, 18803-18812.
33. M. Afzaal, M. A. Malik and P. O'Brien, *J. Mater. Chem.*, 2010, **20**, 4031-4040.
34. M. Kemmler, M. Lazell, P. O'Brien, D. Otway, J.-H. Park and J. Walsh, *J. Mater. Sci. Mater. Electron.*, 2002, **13**, 531-535.
35. P. D. McNaughter, S. A. Saah, M. Akhtar, K. Abdulwahab, M. A. Malik, J. Raftery, J. A. Awudza and P. O'Brien, *Dalton Trans.*, 2016, **45**, 16345-16353.
36. E. A. Lewis, P. D. McNaughter, Z. Yin, Y. Chen, J. R. Brent, S. A. Saah, J. Raftery, J. A. Awudza, M. A. Malik and P. O'Brien, *Chem. Mater.*, 2015, **27**, 2127-2136.

37. A. A. Mohamed, I. Kani, A. O. Ramirez and J. P. Fackler, *Inorg. Chem.*, 2004, **43**, 3833-3839.
38. G. Bowmaker, D. Camp, R. Hart, P. Healy, B. Skelton and A. White, *Aust. J. Chem.*, 1992, **45**, 1155-1166.
39. M. Frisch, G. Trucks, H. Schlegel, G. Scuseria, M. Robb, J. Cheeseman, G. Scalmani, V. Barone, B. Mennucci and G. Petersson, 2009.
40. C. Bianchini, C. A. Ghilardi, A. Meli, S. Midollini and A. Orlandini, *Inorg. Chem.*, 1985, **24**, 932-939.
41. H. Qiaofeng, W. Ying, Y. Xujie, L. Lude and W. Xin, *Chemistry Peking*, 2006, **69**, 148.
42. M. A. Buckingham, A. L. Catherall, M. S. Hill, A. L. Johnson and J. D. Parish, *Cryst. Growth Des.*, 2017, **17**, 907-912.

3.4.7 Supporting information

Table S3.2. The unit cell parameters for the nanorods synthesised with a 1 h reaction time, with ICDD 00-009-0328 as the Cu₂S reference pattern.

	a (Å)	b (Å)	c (Å)	α (°)	β (°)	γ (°)
00-009-0328	11.82	27.05	13.43	90	90	90
9	11.8271(3)	26.9538(60)	13.4106(10)	90	90	90
10	11.8184(37)	27.0457(102)	13.4190(53)	90	90	90
11	11.8038(42)	27.0791(90)	13.4382(72)	90	90	90
12	11.8111(60)	27.0503(129)	13.4428(93)	90	90	90

Table S3.3. The unit cell parameters for the nanorods synthesised with a 5 s reaction time, with ICDD 00-064-0278 as the Cu_{1.74}S reference pattern.

	a (Å)	b (Å)	c (Å)	α (°)	β (°)	γ (°)
00-064-0278	13.387	13.395	15.481	89.8	89.98	90.08
9	13.3859(10)	13.3883(82)	15.4737(14)	89.72(26)	90.07(3)	89.99(4)
10	13.3908(10)	13.3925(82)	15.4827(14)	89.81(26)	89.99(3)	90.09(4)
11	13.3839(10)	13.4014(82)	15.4842(14)	89.75(26)	89.99(3)	90.07(4)
12	13.3744(10)	13.3922(82)	15.4945(14)	89.76(26)	90.03(3)	90.09(4)
13	13.3993(10)	13.4118(82)	15.4737(14)	89.745(26)	89.852(34)	90.022(44)
14	13.3997(10)	13.4034(82)	15.4804(14)	89.764(26)	89.831(34)	90.052(44)
15	13.4005(10)	13.4054(82)	15.4797(14)	89.747(26)	89.814(34)	90.046(44)
16	13.3999(10)	13.4077(82)	15.4805(14)	89.766(26)	89.821(34)	90.037(44)

Table S3.4. Ground state energies of compounds **9-16**.

Compound	Chain length	Energy (Hartree)
9	2	-4699.91
10	4	-4778.42
11	4	-4778.55
12	4	-4814.32
13	5	-4853.58
14	5	-4853.59
15	6	-4892.845
16	7	-4932.10

Table S3.5. Ground state energies of **17-R** and **18-R'**.

Chain length	17-R		18-R'	
	R	Energy (Hartree)	R'	Energy (Hartree)
4	Me	-4814.32	ⁿ Bu	-4778.42
5	Et	-4853.58	ⁿ Pen	-4817.67
6	ⁿ Pr	-4892.84	ⁿ Hex	-4856.92
7	ⁿ Bu	-4932.09	ⁿ Hep	-4896.18

Table S3.6. Cu-S bond lengths for **17-R** and **18-R'**.

Chain length	17-R			18-R'		
	Cu-S(1) (Å)	Cu-S(2) (Å)	Difference (Å)	Cu-S(1) (Å)	Cu-S(2) (Å)	Difference (Å)
4	2.384	2.423	0.039	2.389	2.395	0.006
5	2.390	2.426	0.036	2.39	2.403	0.013
6	2.390	2.432	0.042	2.391	2.398	0.007
7	2.387	2.429	0.042	2.39	2.396	0.006

Table S3.7. C-S bond lengths for **17-R** and **18-R'**.

Chain length	17-R			18-R'		
	C-S(1) (Å)	C-S(2) (Å)	Difference (Å)	C-S(1) (Å)	C-S(2) (Å)	Difference (Å)
4	1.714	1.704	0.01	1.707	1.708	0.001
5	1.709	1.705	0.004	1.707	1.705	0.002
6	1.709	1.705	0.004	1.704	1.707	0.003
7	1.708	1.703	0.005	1.707	1.708	0.001

Table S3.8. Mulliken population of the S atoms in **17-R** and **18-R'**.

Chain length	17-R		18-R'	
	S(1)	S(2)	S(1)	S(2)
4	-0.204474	-0.150537	-0.162405	-0.144633
5	-0.19824	-0.158799	-0.158684	-0.155687
6	-0.201386	-0.15825	-0.163184	-0.154492
7	-0.20827	-0.15131	-0.161812	-0.146702

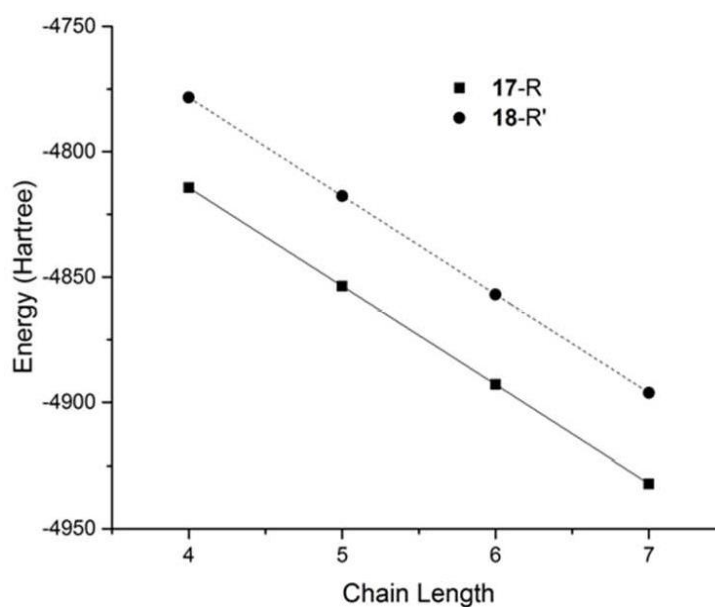
**Figure S3.12.** A comparison of the ground state energies of the linear chain xanthates [(PPh₃)₂Cu(S₂CO(CH₂)₂OR)] (**17-R**, R = Me, Et, ⁿPr, ⁿBu, ■) and [(PPh₃)₂Cu(S₂COR')] (**18-R'**, R' = ⁿBu, ⁿPen, ⁿHex, ⁿHep, ●).

Table S3.9. Band gap values for the nanorods synthesized from the decomposition of **9-16**.

Precursor	Eg (nm)	Eg (eV)
9	930.69 ± 1.11	1.332 ± 0.002
10	902.32 ± 1.12	1.373 ± 0.002
11	884.02 ± 2.17	1.402 ± 0.003
12	888.09 ± 1.61	1.396 ± 0.003
13	861.59 ± 1.66	1.439 ± 0.003
14	835.43 ± 2.97	1.484 ± 0.005
15	821.16 ± 3.01	1.509 ± 0.006
16	807.00 ± 1.43	1.536 ± 0.003

Chapter 4 The synthesis of tin sulfide thin films from tin (II)ethylxanthate

4.1 Introduction

Tin sulfides are the most promising material and suitable as an absorber layer for photovoltaic cells due to the low toxicity.¹ SnS is a good choice for photovoltaic application compared to other material such as PbS, PbSe, and the band gap of SnS is commensurate with silicon which makes it feasible to absorb light across visible spectrum.²

Tin sulfide exists in three main forms, SnS, SnS₂, Sn₂S₃.³ It crystallizes in: cubic,⁴ hexagonal⁵ and orthorhombic form.⁶ The orthorhombic structure of tin monosulfide is composed of double layers of tightly bound Sn-S atoms; the bonds between layers are Van der Waals type.⁷ Tin disulfide has a hexagonal structure composed of a three – atom layered sandwich structure formed when the tin atoms are found in octahedral environment between two hexagonally close packed sulfur slabs. Sn₂S₃ has a tetragonal structure and shares the same space group (*Pnma*) with that of tin monosulfide.^{8,9}

4.2 Author distribution

I synthesised and then characterised tin ethyl xanthate complex via IR, elemental analysis and TGA. I characterised the films by XRD, EDX, UV-Visible spectroscopy. Zhiqiang Xie uses the tin ethyl xanthate complex to deposit tin sulfide thin films. Nicky Savjani checked the characterization of complexes and materials, the project was provided by Paul O'Brien, who edited the draft. The experimental work was done in the laboratory of Paul O'Brien.

4.3 References

1. T. Rath, L. Gury, I. Sánchez-Molina, L. Martinez and S. Haque, *Chem. Commun.*, 2015, **51**, 10198-10201.
2. D. J. Lewis, P. Kevin, O. Bakr, C. A. Muryn, M. A. Malik and P. O'Brien, *Inorg. Chem. Front.*, 2014, **1**, 577-598.
3. J. H. Ahn, M. J. Lee, H. Heo, J. H. Sung, K. Kim, H. Hwang and M. H. Jo, *Nano Lett.*, 2015, **15**, 3703-3708.

4. A. Garcia-Angelmo, R. Romano-Trujillo, J. Campos-Álvarez, O. Gomez-Daza, M. Nair and P. Nair, *Phys. Status Solidi A*, 2015, **212**, 2332-2340.
5. C. Zhai, N. Du and H. Z. D. Yang, *Chem. Commun.*, 2011, **47**, 1270-1272.
6. K. R. Reddy and P. P. Reddy, *Mater. Lett.*, 2002, **56**, 108-111.
7. A. Ghazali, Z. Zainal, M. Z. Hussein and A. Kassim, *Sol. Energy Mater. Sol. Cells*, 1998, **55**, 237-249.
8. L. A. Burton and A. Walsh, *J. Phys. Chem. C*, 2012, **116**, 24262-24267.
9. S. Y. Hong, R. Popovitz-Biro, Y. Prior and R. Tenne, *J. Am. Chem. Soc.*, 2003, **125**, 10470-10474.

4.4 Manuscript 2: A facile method for the production of SnS thin films from melt reactions.

Mundher Al-Shakban¹, Zhiqiang Xie¹, Nicky Savjani², M. Azad Malik¹, and Paul O'Brien^{1,2,*}

¹ *School of Materials, University of Manchester, Oxford Road, Manchester M13 9PL, UK*

² *School of Chemistry, University of Manchester, Oxford Road, Manchester M13 9PL, UK*

4.4.1 Abstract

Tin(II)O-ethylxanthate [Sn(S₂COEt)₂] was prepared and used as a single-source precursor for the deposition of SnS thin films by a melt method. Polycrystalline, (111)-orientated, orthorhombic SnS films with controllable elemental stoichiometries (of between Sn_{1.3}S and SnS) were reliably produced by selecting heating temperatures between 200 and 400 °C. The direct optical band gaps of the SnS films ranged from 1.26 to 1.88 eV and were strongly influenced by its Sn/S ratio. The precursor [Sn(S₂COEt)₂] was characterized by thermogravimetric analysis and attenuated total reflection Fourier-transform infrared spectroscopy. The as-prepared SnS films were characterized by scanning electron microscopy, energy-dispersive X-ray spectroscopy, powder X-ray diffractometry, Raman spectroscopy, and UV–Vis spectroscopy.

4.4.2 Introduction

Tin sulfides (SnS₂, Sn₂S₃, and SnS) are members of the IV–VI family of semiconductors that have shown promise in photovoltaic and optoelectronic applications.¹⁻⁴ Tin(II) sulfide (SnS) in particular has been seen as a potential candidate as an absorber layer in photovoltaic cells due to its 1.4 eV direct band gap that can harvest the visible and near-IR regions of the EM spectrum, the lower costs and toxicity of the constituent elements as compared to other potential materials (e.g., PbS and CdS), and the simplicity of the binary system compared to multicomponent materials such as copper zinc tin sulfide (CZTS) and copper indium gallium sulfide (CIGS).⁵⁻⁸

Single-source precursors (SSPs) are compounds that are designed to decompose to materials of specific compositions, by containing the desired elements. In many

cases, the uses of SSPs have granted control of both its physical and optical properties that dual source precursors cannot.⁹⁻¹¹ In the last 20 years,¹²⁻¹⁸ many SSPs comprised of metal (*N,N*-di-alkyldithiocarbamates) $[M(S_2CNR_2)_n]$ have been used to synthesize metal sulfide nanocrystals. More recently, complexes containing (*O*-alkyl) xanthate (S_2COAk) ligands have been viewed as a potentially useful class of SSPs for the production of metal sulfide nanomaterials. The decomposition of metallo-organic xanthates is known to take place via the relatively low temperature and clean Chugaev elimination reaction.¹⁹ The use of the xanthate ligand in SSPs has permitted the formation of many metal sulfides, including, but not limited to, MoS_2 ,²⁰ CdS ,²¹ NiS , PdS ,²² and CZTS,²³ at lower temperatures than those needed by their respective (*N,N*-di-alkyldithiocarbamate) analogs. Recently, we have reported the preparations of PbS /polymer composites from both lead(II)xanthate and lead(II)dithiocarbamate complexes by a melt process,^{18, 24} finding that the decomposition of $Pb(S_2CO^nBu)_2$ in a polymer matrix produced pure cubic PbS nanocrystals at 150 °C; significantly lower temperatures than 275 °C needed to decompose $Pb(S_2CN^nBu)_2$. As a result, the xanthate-containing SSP can be used in a wider temperature window, giving greater control over nanocrystal size, shape variation, and orientation preference of the PbS crystals. Among the other known methods to SnS nanomaterials,^{18, 25} explorations of the syntheses of orthorhombic SnS nanoparticles²⁶⁻²⁸ and films,^{13, 29, 30} using Sn -SSPs such as $[Sn^{II}(S_2CNR_2)_2]$ and $[R'_2Sn^{IV}(S_2CNR_2)_2]$, have been reported. To date, however, no studies on the uses of tin(*O*-alkylxanthate) complexes have been documented.

In this report, we investigate the use of the SSP $[Sn(S_2COEt)_2]$ as a coating material for the production of herzenbergite SnS films on glass. We focus on both the annealing temperature and the role of the xanthate ligand during the decomposition process for their potential in controlling the structural and optoelectronic properties of the SnS films produced.

4.4.3 Experimental

4.4.3.1 Materials and methods

Potassium ethyl xanthate, chloroform and tetrahydrofuran were purchased from Sigma-Aldrich. Tin(II) chloride was purchased from Alfa Aesar. All chemicals were used as received. Elemental (EA) and thermogravimetric (TGA) analyses were carried out by the Microelemental Analysis service at The University of Manchester. EA was performed using a Flash 2000 Thermo Scientific elemental analyzer and TGA data obtained with Mettler Toledo TGA/DSC1 star^c system between the ranges of 30–600 °C at a heating rate of 10 °C min⁻¹ under nitrogen flow. Scanning electron microscopy (SEM) analysis was performed using a Philips XL30 FEG microscope, with energy dispersive X-ray spectroscopy (EDX) data obtained using a DX4 instrument. Thin-film X-ray diffraction (XRD) analyses were carried out using an X-Pert diffractometer with a Cu-K_{α1} source ($\lambda = 1.54059 \text{ \AA}$), the samples were scanned between 20° and 75°, the applied voltage was 40 kV, and the current was 30 mA. Raman spectra were measured using a Renishaw 1000 Micro-Raman System equipped with a 514 nm laser. UV–Vis measurements were made using a Shimadzu UV-1800 spectrophotometer.

4.4.3.2 Synthesis of tin(II)(*O*-ethylxanthate)

[Sn(S₂COEt)₂] was prepared by a procedure that was modified from that described in literature.^{19, 31} An aqueous solution of potassium ethylxanthate (10.0 g, 12.5 mmol) was added to a stirred solution of tin(II) chloride (5.9 g, 6.2 mmol) in distilled water (100 ml) and stirred for a further 30 min. The yellow precipitate produced was filtered by vacuum filtration, washed three times with water, and finally dried in a vacuum oven at room temperature for 2 h. Yield = 7.2 g (67 %). Melting point = 44–53 °C. Anal. Calcd for [Sn(S₂COEt)₂]: C, 19.98; H, 2.79; S, 35.45; Sn, 32.91 Found: C, 19.67; H, 2.74; S, 35.45; Sn, 32.17. FTIR data (cm⁻¹); 2986.8 (w), 2930.7 (w), 1457 (w), 1355 (w), 1195.6 (s), 1108.1(s), 1020.6 (s), 852.0(w), 801.3(w), 563.4 (w).

4.4.3.3 Preparation of SnS thin films by spin coating and heating

Glass slides were cut to 20 mm × 15 mm, cleaned by sonication in acetone (twice) and water, and allowed to dry. Three cycles of coating was performed; in each cycle, 300 μL of a 3 M [Sn(S₂COEt)₂] solution in THF was coated onto the glass slide by spin coating at 700 rpm for 60 s and allowed to dry. The resulting films were loaded into a glass tube for decomposition in a dry nitrogen environment. The tube was then heated in the furnace to the desired temperature (150 – 400 °C) at a rate of ~ 3 °C min⁻¹ and held at that temperature for 60 min; after this time had elapsed, the furnace was turned off and the tube allowed to cool to room temperature.

4.4.4 Results and discussion

The tin xanthate precursor [Sn(S₂COEt)₂] was synthesized by the literature procedure^{19, 31} and elemental analyses confirming its purity. The yellow powder is readily soluble in THF and many other common organic solvents. It was found that storage at -20 °C was necessary to limit decomposition. The thermal decomposition of [Sn(S₂COEt)₂] was studied using thermogravimetric analysis (TGA). The thermogram showed a rapid single decomposition step between 80 and 130 °C (Figure 4.1). The final weight of the residue (44.1 %) is close to the predicted value for residual SnS (41.8 %). The precursor is predicted to break down via the Chugaev elimination mechanism,¹⁹ as shown in figure S4.8. The IR spectrum of [Sn(S₂COEt)₂] shows bands corresponding to ν(C–O) (1196 and 1224 cm⁻¹) and ν(C–S) (1021 and 1108 cm⁻¹). A peak at 563 cm⁻¹ is also observed consistent with a ν(Sn–S) mode (Figure 4.2).

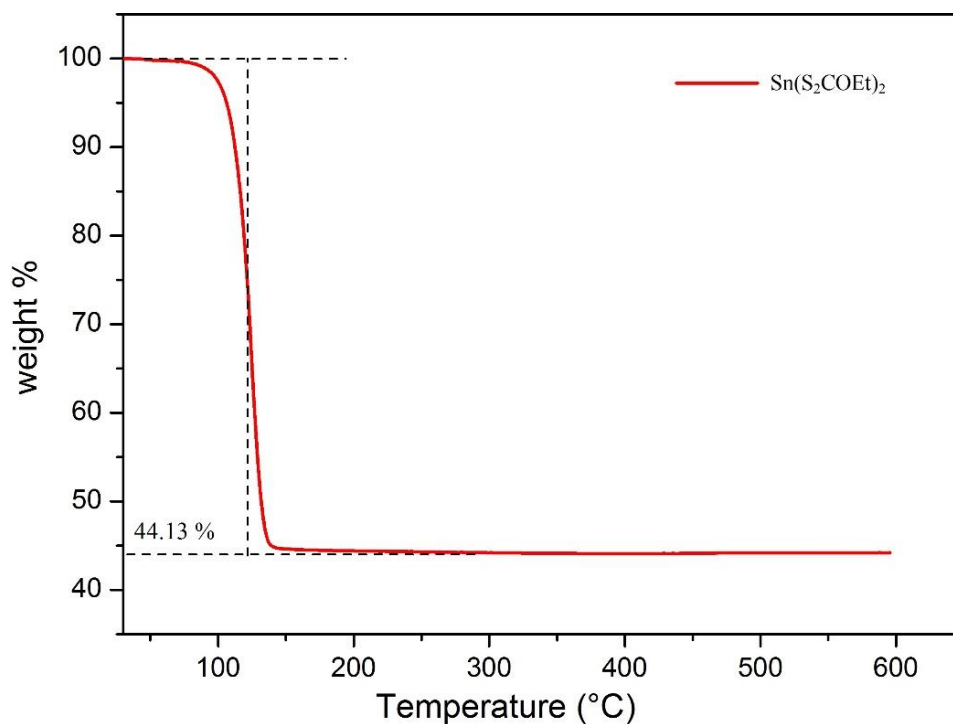


Figure 4.1. Thermogram for the decomposition of $[\text{Sn}(\text{S}_2\text{COEt})_2]$. The final residual weight (44.1 %) is close to the predicted value for residual SnS (41.8%).

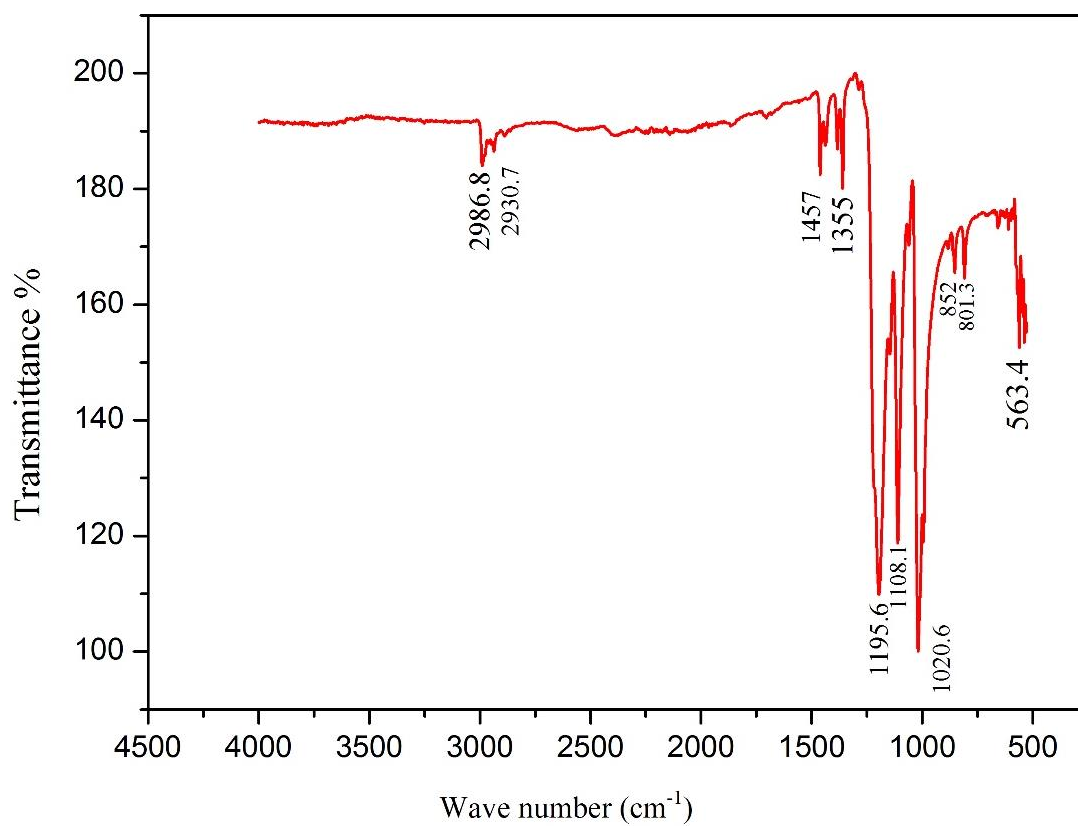


Figure 4.2. FTIR spectrum of the precursor $[\text{Sn}(\text{S}_2\text{COEt})_2]$

SnS films were prepared by coating glass slides with the $[\text{Sn}(\text{S}_2\text{COEt})_2]$ precursor, followed by a heating step in an N_2 environment, at 150, 200, 250, 300 and 400 °C for 1 h. The resulting films were gray and uniform at all the heating temperatures (Figure S4.9); the films were found to be between 2.2 and 2.9 μm thick. Both the morphology and composition of the SnS films produced showed a dependence on the heating temperature.

The films contained nearly spherical structures with some flakes (Figure 4.3 a, b, c and d). Elemental maps for the film produced at all temperatures (elemental maps for 300 °C shown in Figure 4.3 e, f; maps for the other films in Fig. S4.9) demonstrate the uniform distribution of these elements among the films. The Sn/S ratio within the films steadily decreased when higher reaction temperatures were used (Table 4.1, Figure 4.4): Sn/S ratios of 1.31 and 1.32 ($\text{Sn}_{1.31}\text{S}$ and $\text{Sn}_{1.32}\text{S}$) were seen in the films produced at 150 and 200 °C (sulfur deficient). Increasing the heating temperature also increased the sulfur content in the film, reactions performed at 250 and 300 °C produced SnS films with reduced sulfur deficiency (Sn/S ratios of 1.15:1 ($\text{Sn}_{1.15}\text{S}$) and 1.11:1 ($\text{Sn}_{1.11}\text{S}$), respectively), and a stoichiometric SnS film was obtained upon heating at 400 °C (Sn/S ratio 1.03:1; ($\text{Sn}_{1.03}\text{S}$)). Such control of the stoichiometry in SnS nanomaterials has previously been observed.^{32, 33} The p-XRD patterns of the SnS thin films produced at temperatures between 200 and 400 °C gave peaks that can be indexed to herzenbergite-SnS with the expected orthorhombic crystal structure (matches ICDD pattern No. 00-039-0354; see figure 4.5a); no other peaks are observed that correspond to other tin oxide or sulfide species. The calculated unit cell parameters of the herzenbergite SnS films (shown in Table 4.1) match the expected (Pbnm) space group, with lattice parameters that closely match with those reported in literature.^{34, 35} The films heated at 400 °C have strong, well-defined diffraction peaks. At lower temperatures, however, the films were found to exhibit broader peaks, possibly due to the increasing sulfur deficiency within the crystalline film. The temperature during $[\text{Sn}(\text{S}_2\text{COEt})_2]$ decomposition seems crucial; at lower temperatures, the rate at which the precursor decomposes will be slowed considerably, with the resulting intermediate species exposed to temperatures that may promote evaporation.

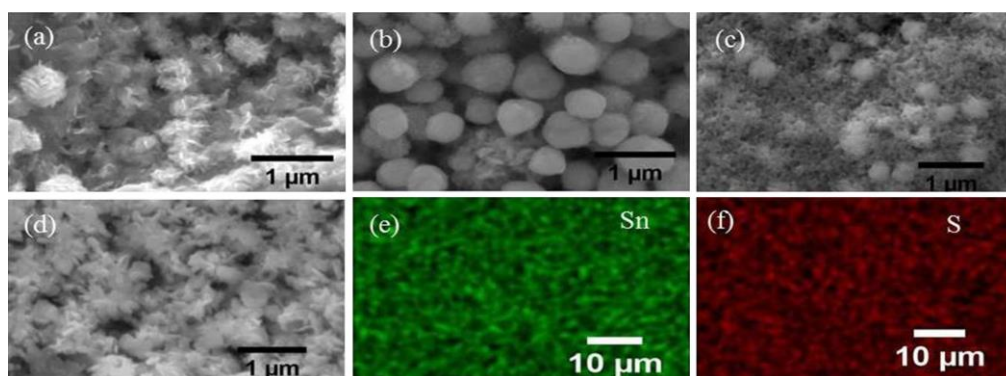


Figure 4.3. SEM images of SnS films grown on glass substrates from $[\text{Sn}(\text{S}_2\text{COEt})_2]$ at (a) 200 °C, (b) 250 °C, (c) 300 °C, and (d) 400 °C (scale bars represent 1 μm); (e) and (f) the elemental maps of the SnS film produced at 300 °C (scale bars represent 10 μm).

Table 4.1. Thicknesses, compositions, and unit cell parameters of the SnS films produced by the melt method.

Heating Temp. (°C)	Thickness (μm)	Sn atomic (%) ^a	S atomic (%) ^a	Sn/S ratio	Unit cell parameters (orthorhombic, Å) ^{bc}
150	–	56.8	43.2	1.31:1 (\pm 0.07)	$a = 4.355, b = 11.232, c = 3.985$
200	2.2	56.99	43.0	1.32:1 (\pm 0.07)	$a = 4.324, b = 11.237, c = 3.980$
250	2.9	53.4	46.4	1.15:1 (\pm 0.06)	$a = 4.324, b = 11.231, c = 3.984$
300	2.8	52.5	47.5	1.11:1 (\pm 0.06)	$a = 4.324, b = 11.236, c = 3.986$
400	2.5	50.7	49.3	1.03:1 (\pm 0.05)	$a = 4.324, b = 11.219, c = 3.986$

^a Determined by SEM–EDX

^b Determined by p-XRD

^c Rock-salt SnS phase also observed in the films produced at 150 °C (unit cell parameter: $a = 5.801$ Å)

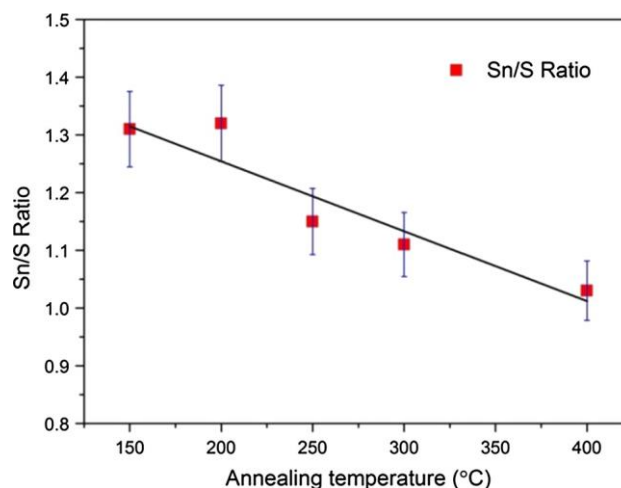


Figure 4.4. The Sn/S ratio by EDX for samples heated for 60 min at temperatures between 150 and 400 °C.

In contrast, the $\text{Sn}_{1.31}\text{S}$ film produced at 150 °C was found to consist of a mixture of orthorhombic and cubic phases, with the latter phase matching well with a rock-salt SnS phase (space group $\text{Fm}\bar{3}\text{m}$; ICDD pattern No. 04-004-8426) recently discussed by first-principle calculations.^{36, 37} In addition, Raman spectroscopy of all of the SnS films (Figure 4. 5b) revealed Raman bands at 94, 160, 188, and 218 cm^{-1} , in good agreement with the herzenbergite SnS phase reported previously.³⁸⁻⁴⁰

The optical band gaps (E_g) of the SnS films (produced at temperatures between 200 and 400 °C) were determined from optical absorption measurements by the Tauc method (Figure 4.7a).^{41, 42} All of the films analyzed have high absorption coefficients ($\alpha > 10^4 \text{ cm}^{-1}$ above the fundamental absorption) (figure 4.6). The band gaps were evaluated by extending the linear part of the plots of $(\alpha h\nu)^2$ versus $h\nu$.⁴³ The band gap of the $\text{Sn}_{1.32}\text{S}$ films formed at 200 °C is 1.88 eV. Increased decomposition temperatures gave smaller band gaps; 250 ($\text{Sn}_{1.15}\text{S}$), 300 ($\text{Sn}_{1.11}\text{S}$), and 400 °C ($\text{Sn}_{1.03}\text{S}$) gave band gaps at 1.75, 1.49, and 1.26 eV, respectively. It is clear that the control of the stoichiometry that we have achieved in the syntheses allows for tuning of optical band gaps. The band gaps of SnS films previously reported⁴⁴⁻⁴⁸ show similar change with sulfur deficiency (Figure 4.7b). However, care needs to be taken when comparing the results obtained from literature to our dataset, as the films produced by each citation varies from both our work and each other. These experimental variations will introduce variations in the macrostructures, elemental stoichiometries, film thicknesses, and concentrations of Sn_xS_y -based impurities

contained within the SnS films documented. The physical properties of the materials and the potential of quantum confined materials may also need to be considered.

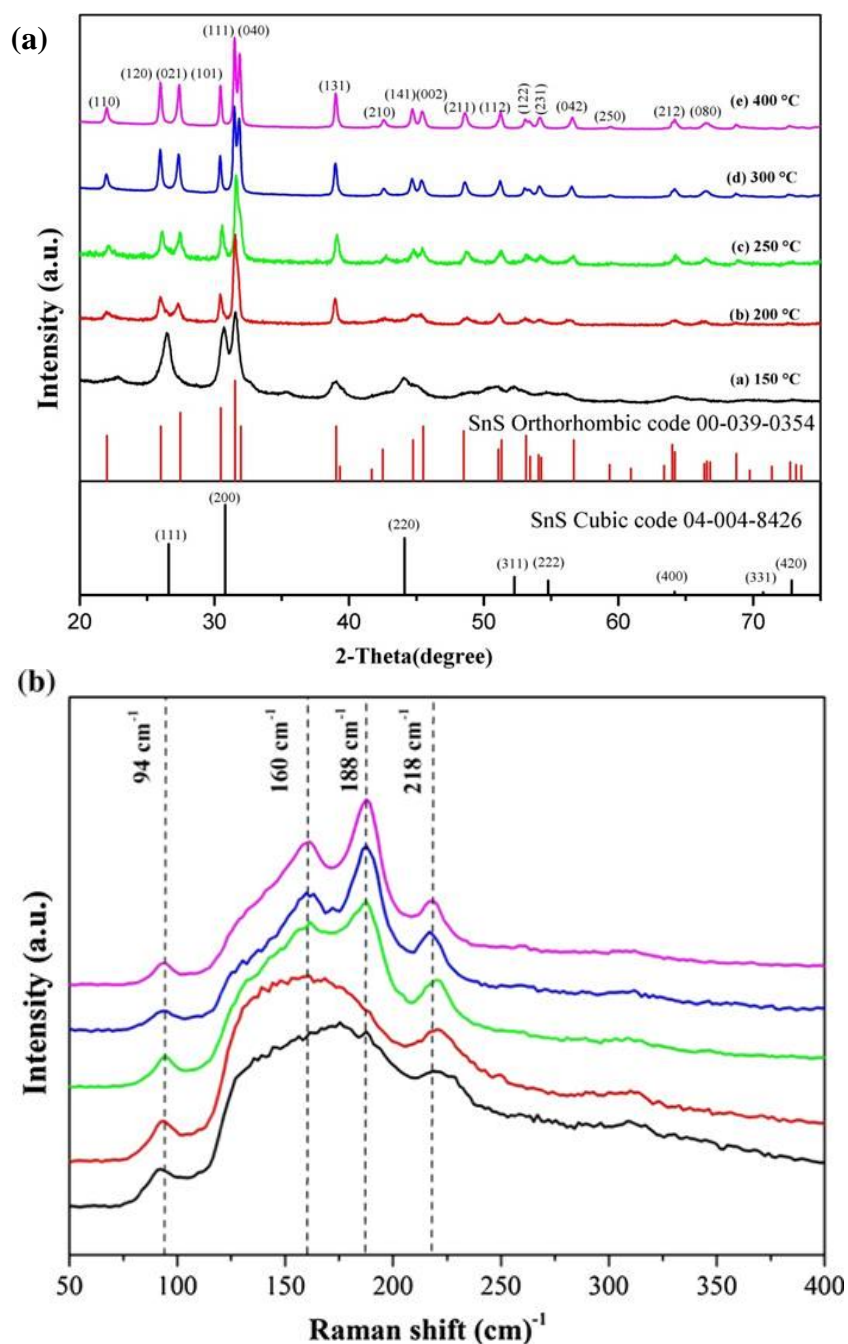


Figure 4.5. (a) p-XRD patterns of SnS films grown on glass substrate at different temperatures, accompanied by reference patterns of herzenbergite SnS (ICCD pattern No. 00-039-0354) and rock-salt SnS (ICCD pattern No. 04-004-8426). (b) Raman spectra for the SnS films grown on glass substrates from $[\text{Sn}(\text{S}_2\text{COEt})_2]$ at 150, 200, 250, 300, and 400 °C.

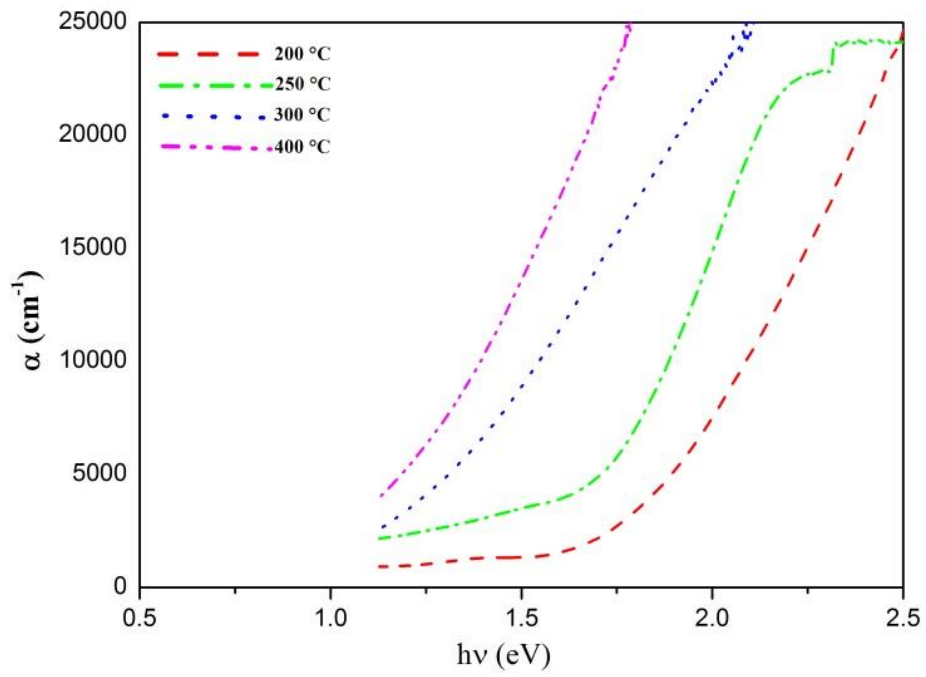


Figure 4.6. Absorption coefficient of SnS films grown on glass substrates from $[\text{Sn}(\text{S}_2\text{COEt})_2]$ decomposed at temperatures between 200 and 400 °C.

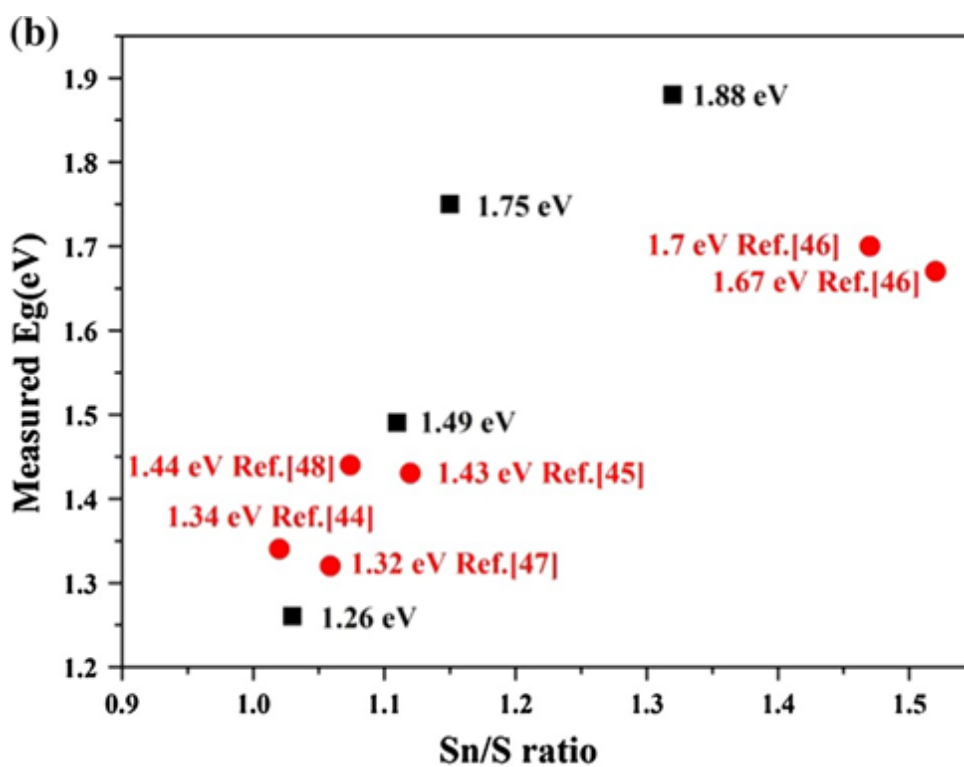
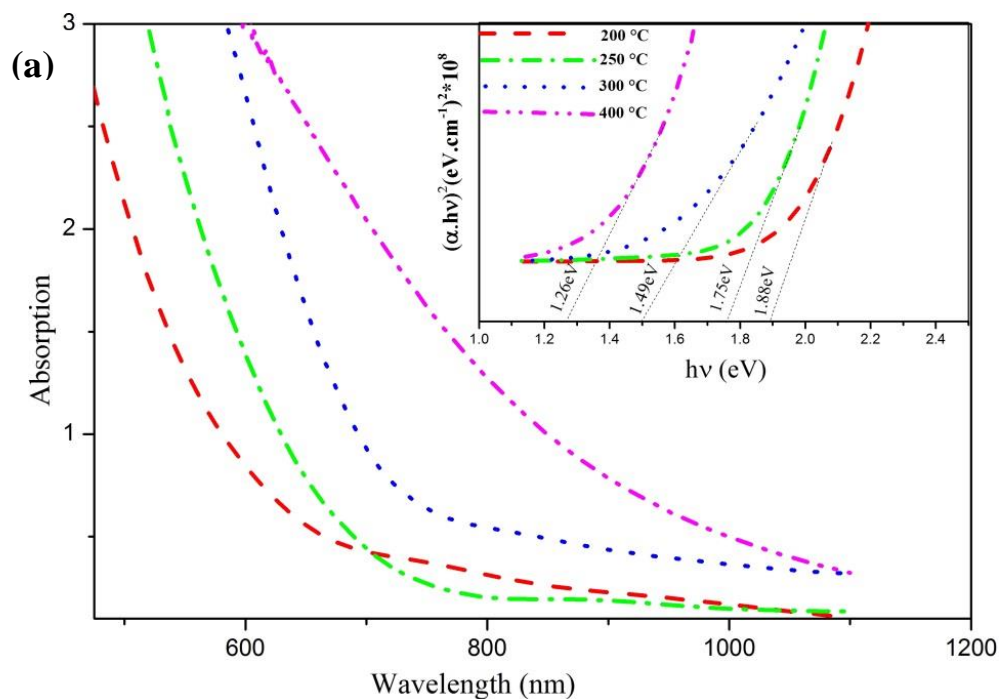


Figure 4.7. (a) UV–Vis and Tauc plots (*inset*) for the SnS films grown on glass substrates from $[\text{Sn}(\text{S}_2\text{COEt})_2]$ at 200, 250, 300, and 400 °C. (b) Graph showing the relationship between the Sn/S ratio of SnS_{1-x} materials with its measured band gap. Data in black represent the findings in this report, whereas data in *red* were obtained from literature.

4.4.5 Conclusions

A simple process has been described for the growth of SnS films. Heating of substrates spin-coated with tin(II)*O*-ethylxanthate at different temperatures between 150 and 400 °C produced SnS films mainly in orthorhombic phase with good crystallinity. Analyses of the films reveal them to be sulfur deficient with Sn/S ratio controlled by selecting the heating temperatures. In addition, a correlation was found between the optical band gap of the SnS films (as determined by UV–Vis spectroscopy) and the stoichiometry. The measured optical band gaps were lowered from 1.88 to 1.26 eV. We believe that the process described in this report could be used in the production of SnS films with tuneable band gaps for solar cell applications.

4.4.6 Acknowledgements

The authors would like to acknowledge the EPSRC Core Capability in Chemistry (CCC), Grant Number EP/K039547/1 (Director: Prof. Gareth Morris), for access to numerous analytical equipment. The authors would also like to thank Dr. Christopher Wilkins at School of Materials University of Manchester for helpful discussions on SEM and EDX. MAS acknowledges the Iraqi Culture Attaché in London for financial support. NS thanks the Parker family for funding his position.

4.4.7 References

1. K. R. Reddy, N. K. Reddy and R. Miles, *Sol. Energy Mater Sol. Cells*, 2006, **90**, 3041-3046.
2. Y. Lei, S. Song, W. Fan, Y. Xing and H. Zhang, *J. Phys. Chem. C*, 2009, **113**, 1280-1285.
3. L. Motevalizadeh, M. Khorshidifar, M. E. Abrishami and M. B. Mohagheghi, *J. Mater. Sci. Mater. Electron.*, 2013, **24**, 3694-3700.
4. H. Zhu, D. Yang, Y. Ji, H. Zhang and X. Shen, *J. Mater. Sci.*, 2005, **40**, 591-595.
5. M. Ichimura, *Sol. Energy Mater Sol. Cells*, 2009, **93**, 375-378.
6. B. Ghosh, M. Das, P. Banerjee and S. Das, *Semicond. Sci. Technol.*, 2009, **24**, 025024.
7. A. Dussan, F. Mesa and G. Gordillo, *J. Mater. Sci.*, 2010, **45**, 2403-2407.
8. V. Robles, J. Trigo, C. Guillén and J. Herrero, *J. Mater. Sci.*, 2013, **48**, 3943-3949.
9. M. Lazell, P. O'Brien, D. J. Otway and J.-H. Park, *Dalton Trans.*, 2000, 4479-4486.
10. S. L. Castro, S. G. Bailey, R. P. Raffaele, K. K. Banger and A. F. Hepp, *J. Phys. Chem. B*, 2004, **108**, 12429-12435.
11. L. Tian, H. Yao Tan and J. J. Vittal, *Cryst. Growth Des.*, 2007, **8**, 734-738.
12. T. Trindade, P. O'Brien and X.-m. Zhang, *Chem. Mater.*, 1997, **9**, 523-530.
13. P. Kevin, D. J. Lewis, J. Raftery, M. A. Malik and P. O'Brien, *J. Cryst. Growth*, 2015, **415**, 93-99.
14. T. Trindade, P. O'Brien and N. L. Pickett, *Chem. Mater.*, 2001, **13**, 3843-3858.
15. P. O'Brien and R. Nomura, *J. Mater. Chem.*, 1995, **5**, 1761-1773.
16. M. A. Malik, M. Afzaal and P. O'Brien, *Chem. Rev.*, 2010, **110**, 4417-4446.
17. K. Ramasamy, M. A. Malik, N. Revaprasadu and P. O'Brien, *Chem. Mater.*, 2013, **25**, 3551-3569.
18. D. J. Lewis, P. Kevin, O. Bakr, C. A. Muryn, M. A. Malik and P. O'Brien, *Inorg. Chem. Front.*, 2014, **1**, 577-598.
19. G. Kociok-Köhn, K. C. Molloy and A. L. Sudlow, *Can. J. Chem.*, 2014, **92**, 514-524.

20. N. Savjani, J. R. Brent and P. O'Brien, *Chem. Vap. Deposition*, 2015, **21**, 71-77.
21. N. Pradhan and S. Efrima, *J. Am. Chem. Soc.*, 2003, **125**, 2050-2051.
22. J. Cheon, D. S. Talaga and J. I. Zink, *Chem. Mater.*, 1997, **9**, 1208-1212.
23. A. Fischereder, A. Schenk, T. Rath, W. Haas, S. Delbos, C. Gougaud, N. Naghavi, A. Pateter, R. Saf and D. Schenk, *Monatsh. Chem.*, 2013, **144**, 273-283.
24. E. A. Lewis, P. D. McNaughter, Z. Yin, Y. Chen, J. R. Brent, S. A. Saah, J. Raftery, J. A. Awudza, M. A. Malik and P. O'Brien, *Chem. Mater.*, 2015, **27**, 2127-2136.
25. J. R. Brent, D. J. Lewis, T. Lorenz, E. A. Lewis, N. Savjani, S. J. Haigh, G. Seifert, B. Derby and P. O'Brien, *J. Am. Chem. Soc.*, 2015, **137**, 12689-12696.
26. N. Petkov, J. Xu, M. A. Morris and J. D. Holmes, *J. Phys. Chem. C*, 2008, **112**, 7345-7355.
27. J. Ning, K. Men, G. Xiao, L. Wang, Q. Dai, B. Zou, B. Liu and G. Zou, *Nanoscale*, 2010, **2**, 1699-1703.
28. S. Y. Hong, R. Popovitz-Biro, Y. Prior and R. Tenne, *J. Am. Chem. Soc.*, 2003, **125**, 10470-10474.
29. K. Ramasamy, V. L. Kuznetsov, K. Gopal, M. A. Malik, J. Raftery, P. P. Edwards and P. O'Brien, *Chem. Mater.*, 2013, **25**, 266-276.
30. Z. Xu and Y. Chen, *Semicond. Sci. Technol.*, 2012, **27**, 035007.
31. C. Raston, P. Tennant, A. White and G. Winter, *Aust. J. Chem.*, 1978, **31**, 1493-1500.
32. V. Robles, J. F. Trigo, C. Guillén and J. Herrero, *Thin Solid Films*, 2015, **582**, 249-252.
33. M. Ichimura, K. Takeuchi, Y. Ono and E. Arai, *Thin Solid Films*, 2000, **361**, 98-101.
34. H. Wiedemeier and H. Schnering, *Z. Kristallogr. Cryst. Mater.*, 1978, **148**, 295-303.
35. M. El-Nahass, H. Zeyada, M. Aziz and N. El-Ghamaz, *Opt. Mater.*, 2002, **20**, 159-170.
36. L. A. Burton and A. Walsh, *J. Phys. Chem. C*, 2012, **116**, 24262-24267.

37. Y. Sun, Z. Zhong, T. Shirakawa, C. Franchini, D. Li, Y. Li, S. Yunoki and X.Q. Chen, *Phys. Rev. B*, 2013, **88**, 235122.
38. H. Chandrasekhar, R. Humphreys, U. Zwick and M. Cardona, *Phys. Rev. B*, 1977, **15**, 2177.
39. P. Sinsermsuksakul, J. Heo, W. Noh, A. S. Hock and R. G. Gordon, *Adv. Energy Mater.*, 2011, **1**, 1116-1125.
40. L. S. Price, I. P. Parkin, A. M. Hardy, R. J. Clark, T. G. Hibbert and K. C. Molloy, *Chem. Mater.*, 1999, **11**, 1792-1799.
41. P. Jain and P. Arun, *Thin Solid Films*, 2013, **548**, 241-246.
42. D. S. Koktysh, J. R. McBride and S. J. Rosenthal, *Nanoscale Res. Lett.*, 2007, **2**, 144-148.
43. A. Tanuševski and D. Poelman, *Sol. Energy Mater Sol. Cells*, 2003, **80**, 297-303.
44. G. Yue, D. Peng, P. Yan, L. Wang, W. Wang and X. Luo, *J. Alloys Compd.*, 2009, **468**, 254-257.
45. B. Ghosh, M. Das, P. Banerjee and S. Das, *Appl. Surf. Sci.*, 2008, **254**, 6436-6440.
46. M. Calixto-Rodriguez, H. Martinez, A. Sanchez-Juarez, J. Campos-Alvarez, A. Tiburcio-Silver and M. Calixto, *Thin Solid Films*, 2009, **517**, 2497-2499.
47. N. K. Reddy and K. R. Reddy, *Thin Solid Films*, 1998, **325**, 4-6.
48. Z. Xu and Y. Chen, *Energy Procedia*, 2011, **10**, 238-242.

4.4.8 Supplementary information

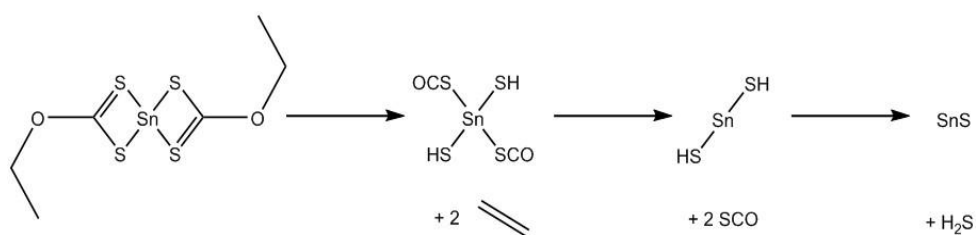


Figure S4.8. The proposed decomposition mechanism of $[\text{Sn}(\text{S}_2\text{COEt})_2]$, which is thought to break down following the Chugaev elimination mechanism of metal xanthates.

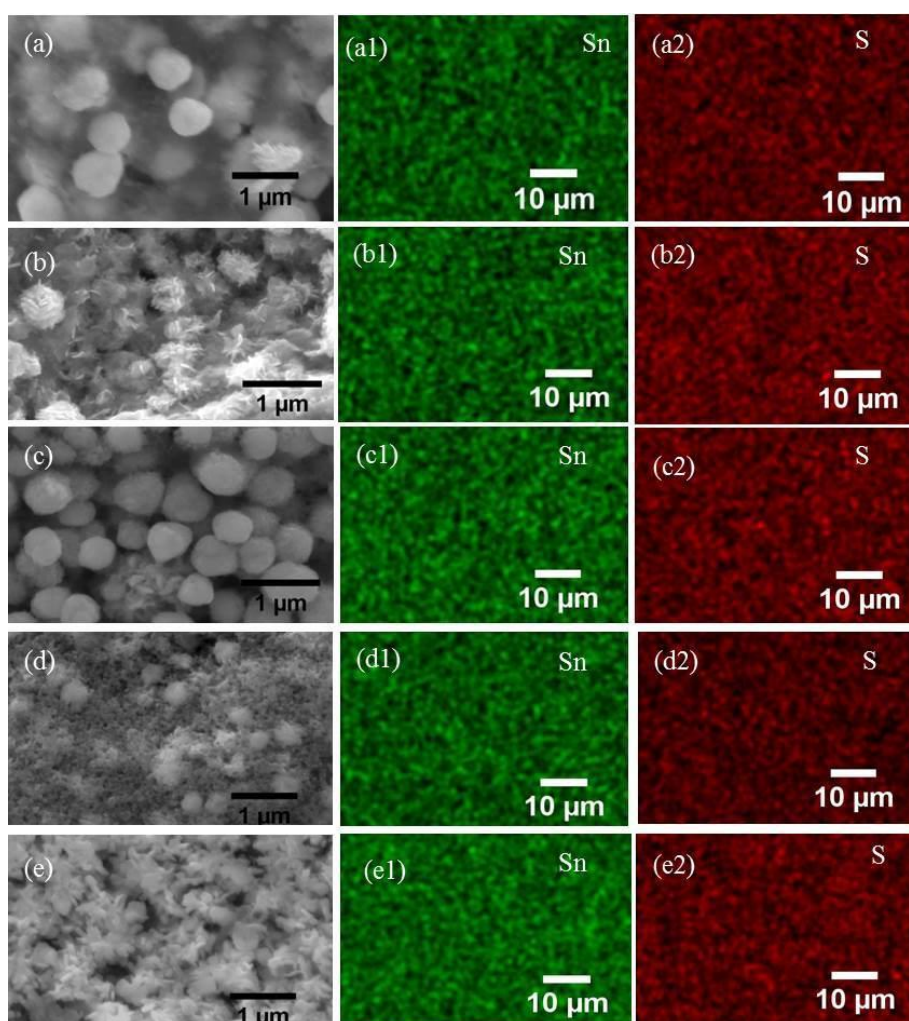


Figure S4.9. (a-e) SEM images of SnS films grown on glass substrates from $[\text{Sn}(\text{S}_2\text{COEt})_2]$ at (a) 150 °C, (b) 200 °C (c) 250 °C (d) 300 °C and (e) 400 °C. (a1-e1) and (a2-e2) are the elemental maps of the SnS film produced at the given temperatures.

Chapter 5 Phase selective synthesis of CuInS₂ from xanthate complexes

5.1 Introduction

Copper Indium sulfide (CuInS₂) is widely studied as absorber materials for efficient,¹ low toxicity,² a large absorption coefficient ($\alpha \geq 10^4 \text{ cm}^{-1}$)³ and a direct band gap about 1.53eV.⁴ CIS nanoparticles have been prepared using different precursors such as (PPh₃)₂CuIn(SEt)₄, by thermal decomposition of complex in dioctylphthalate; Castro *et al.* prepared CIS nanocrystal at 200 °C.⁵ Dutta *et al* used solvent thermolysis of In(S₂COEt)₃ and Cu(S₂COEt) mixture in ethylene glycol at 196 °C for up to 4 h to form a brown solution of nanocrystalline CuInS₂.⁶ Trimmel *et al.* added a solution of sulfur in oleylamine to an equimolar solution of copper iodide and indium chloride in oleylamine, they used microwave energy to produce CIS nanoparticles.⁷

CuInS₂ exists in three modifications, a chalcopyrite form at temperatures up to 980°C, zincblende from 980°C to 1045°C and an unknown modification from 1045°C up to the melting point at 1090°C.⁸ In the chalcopyrite structure, in the (112) plane, the Cu and In atoms zigzag in the directions [221] along alternate lines. (112) Sulfur planes can be seen to alternate with metallic ones.⁹ CuInS₂ can be regarded as the ternary analogs of the II-VI binary compounds. If Cu and In atoms were replaced by II-atoms, the result is that chalcopyrite structure is derived from the zincblende structure.¹⁰

5.2 Author distribution

I synthesised and characterised the xanthate complexes via IR, NMR, elemental analysis and TGA. The experimental work to obtain CuInS₂ nanoparticles was carried out by me, I characterised the nanoparticles via XRD, Raman spectroscopy and EDX. The TEM for the CuInS₂ samples were carried out by Xiang L. Zhong. Peter D. Matthews checked the characterization of complexes and materials. The crystallographic data of the complexes has been collected by James Raftery and Inigo Vitorica-Yrezabal. The project was provided by Paul O'Brien, who edited the draft. The experimental work was done in the laboratory of Paul O'Brien.

5.3 References

1. R. Scheer, T. Walter, H. Schock, M. Fearheiley and H. Lewerenz, *Appl. Phys. Lett.*, 1993, **63**, 3294-3296.
2. P. Guha, D. Das, A. Maity, D. Ganguli and S. Chaudhuri, *Sol. Energy Mater. Sol. Cells*, 2003, **80**, 115-130.
3. H. Neumann, W. Hörig, V. Savelev, J. Lagzdonis, B. Schumann and G. Kühn, *Thin Solid Films*, 1981, **79**, 167-171.
4. J. Jaffe and A. Zunger, *Phys. Rev. B*, 1983, **28**, 5822.
5. S. L. Castro, S. G. Bailey, R. P. Raffaele, K. K. Banger and A. F. Hepp, *J. Phys. Chem. B*, 2004, **108**, 12429-12435.
6. D. P. Dutta and G. Sharma, *Mater. Lett.*, 2006, **60**, 2395-2398.
7. A. Pein, M. Baghbanzadeh, T. Rath, W. Haas, E. Maier, H. Amenitsch, F. Hofer, C. O. Kappe and G. Trimmel, *Inorg. Chem.*, 2010, **50**, 193-200.
8. J. Binsma, L. Giling and J. Bloem, *J. Cryst. Growth*, 1980, **50**, 429-436.
9. L. Kazmerski, M. Ayyagari, G. Sanborn, F. White and A. Merrill, *Thin Solid Films*, 1976, **37**, 323-334.
10. D. Su, W. Neumann, R. Hunger, P. Schubert-Bischoff, M. Giersig, H. Lewerenz, R. Scheer and E. Zeitler, *Appl. Phys. Lett.*, 1998, **73**, 785-787.

5.4 Manuscript 3: On the Phase Control of CuInS₂ Nanoparticles from Cu-/In-Xanthates

Mundher Al-Shakban,^a Peter D Matthews,^b Xiang L. Zhong,^a Inigo Vitorica-Yrezabal,^b James Raftery^b and Paul O'Brien*^{a,b}

^a School of Materials, University of Manchester, Oxford Road, Manchester M13 9PL, UK

^b School of Chemistry, University of Manchester, Oxford Road, Manchester M13 9PL, UK

5.4.1 Abstract

In this paper we report the synthesis and single-crystal X-ray characterisation of seven novel indium(III) xanthate complexes. These xanthates have been used as an In-source for the synthesis of highly crystalline CuInS₂ nanoparticles in conjunction with a Cu(I)-xanthate. In synthesising the nanoparticles we have also demonstrated an ability to control the phase of the material through choice of solvent.

5.4.2 Introduction

Transition metal chalcogenides (TMCs) have witnessed a remarkable surge in interest in recent years, owing to extensive investigations into their exciting properties and wide ranging applications. These applications, which include playing key roles in sensors, photovoltaics, photocatalysts and other electronics, are driven by the presence of a controllable band gap which causes the semi-conductor properties of TMCs.¹⁻³

I-III-VI₂ ternary TMCs, such as CuInS₂ (CIS), offer an environmentally benign alternative to the more common II-VI binary systems like PbS or CdS.⁴ CIS has been explored as the active light harvesting component in photovoltaic devices⁵⁻⁷ as it has a direct band gap of 1.5 eV, an absorption coefficient $>10^5$ cm⁻¹ and a good defect tolerance.⁸⁻¹⁰ However, it is synthetically challenging to make pure CIS owing to the difference in reactivity of Cu(I) (soft Lewis acid) and In(III) (hard Lewis acid) to sulfur. Additionally, the phase diagram of CuInS₂ is complex, and the window to form CuInS₂ at temperatures lower than 800 °C is narrow.¹¹ These challenges mean that the formation of contaminating Cu_xS_y phases is often observed.¹²

The challenge that we address in this manuscript is one of how to reliably and easily synthesise CuInS₂, whilst demonstrating a certain level of control. In order to do this, we turned to a combination of copper(I) xanthates¹³ and novel indium(III) xanthates. Metal xanthates [M(S₂COR)_x] have been shown to be excellent precursors to an array of metal chalcogenides previously, including complex materials such as alkaline earth metal sulfides.¹⁴⁻²⁵ The xanthates break down cleanly to form metal sulfides via a Chugaev elimination mechanism, in which volatile gases are the only by-products.²⁶

Previous synthetic routes to CIS nanoparticles have included the reaction of metal salts (e.g. CuI, CuOAc, In(OAc)₃ or indium stearate) with thiols/elemental sulfur,²⁷⁻³¹ or cation exchange of Cu⁺¹ for In⁺³ into previously prepared Cu_xS_y nanoparticles.³²⁻³⁴ However, these procedures are relatively complex, requiring fine control of the reaction conditions. Here we present a robust synthetic route which demonstrates control over the phase of the obtained CIS through choice of the reaction solvent.

5.4.3 Experimental

5.4.3.1 Materials and synthesis

All chemicals were purchased from Sigma Aldrich, and were used as received. Elemental analysis (EA) and Thermogravimetric analysis (TGA) were carried out by the Microelemental Analysis service at the University of Manchester. EA was performed using a Flash 2000 Thermo Scientific elemental analyzer and TGA data were obtained with Mettler Toledo TGA/DSC1 star^c system between the range of 30 - 600 °C at a heating rate of 10 °C min⁻¹ under nitrogen flow. NMR spectra were recorded in CDCl₃ and D₂O solutions on a Bruker Ascend spectrometer operating at 400 MHz. Transmission electron microscope (TEM) images were collected using an FEI Tecnai G2 F30 with Schottky Field Emitter operated at 300 keV. Powder X-ray diffraction (pXRD) analyses were carried out using an X-Pert diffractometer with a Cu-Kα1 source ($\lambda = 1.54059 \text{ \AA}$), the samples were scanned between 10 and 80°, the applied voltage was 40 kV and the current 30 mA. Raman spectra were measured using a Renishaw 1000 Micro-Raman System equipped with a 514 nm laser. UV-Vis spectra were collected on a Shimadzu UV-1800, using 3.09 mM solution of CuInS₂ nanoparticles in methanol.

Potassium iso-butylxanthate (**3**), potassium 2-methoxyethylxanthate (**4**), potassium 2-ethoxyethylxanthate (**5**), potassium 3-methoxy-3-methyl-1-butylxanthate (**6**), potassium 1-methoxy-2-propylxanthate (**7**) and triphenylphosphine copper(I) 2-ethoxyethylxanthate (**15**) were all prepared according to our previously published procedure.¹³

5.4.3.1.1 Synthesis of Potassium *n*-propylxanthate (**1**):

Potassium *n*-propylxanthate was prepared following a literature method.³⁵ Potassium hydroxide (11.2 g, 0.20 mol) and *n*-propanol (150 ml) were stirred for 2 h at room temperature and then CS₂ (15.2 g, 12.0 ml, 0.20 mol) was added dropwise to the reaction, resulting in an orange solution. The unreacted alcohol was removed *in vacuo* and the yellow solid product was dried to give [K(S₂CO^{*n*}Pr)] (27.3 g, 0.1568 mol, 78.4% yield). M.p. = 228 - 230 °C. Calc. for C₄H₇KOS₂ (%): C 27.6, H 4.05, S 36.7, K 22.5; found: C 27.8, H 3.99, S 37.0, K 22.9. FT-IR (cm⁻¹): 2965 (m), 2937(w), 2873 (w), 1453 (m), 1445 (w), 1270 (m), 1148 (s), 1087 (s), 1061 (s), 925 (m), 902 (m), 765.0 (s), 660.1 (s), 544 (s). ¹H NMR (400 MHz, D₂O) δ (ppm) = 0.89 (t, J = 7.3 Hz, 3H, CH₃), 1.68 (m, J = 7.3 Hz, 2H, CH₂CH₂CH₃), 4.31 (t, J = 6.5 Hz, 2H, OCH₂CH₂).

5.4.3.1.2 Synthesis of potassium *iso*-propylxanthate (**2**):

[K(S₂CO^{*i*}Pr)] was prepared via the same method as **1**, using *iso*-propanol (150 ml). (25.8 g, 0.148 mol, 74.1% yield). M.p. = 223 - 227 °C. Calc. for C₄H₇KOS₂ (%): C 27.6, H 4.05, S 36.7, K 22.5; found: C 27.6, H 3.96, S 36.6, K 23.3. FT-IR (cm⁻¹): 2970 (m), 1460 (w), 1370 (m), 1182 (m), 1048 (s), 901 (s), 1092 (s), 662 (w), 583 (w). ¹H NMR (400 MHz, D₂O) δ (ppm) = 1.25 (d, J = 6.3 Hz, 6H, CH(CH₃)₂), 5.44 (sep, J = 6.3 Hz, 1H, CH(CH₃)₂).

5.4.3.1.3 Synthesis of indium(III) *n*-propylxanthate (**8**):

A solution of potassium *n*-propylxanthate (2.35 g, 0.0135 mol) in water (60 ml) was added to a solution of InCl₃ (1g, 0.0045 mol) in the same amount of water. A white precipitate was obtained after continuous stirring for 30 min at room temperature. The solid was collected by vacuum filtration and washed three times with water. The product was dried in *vacuo* and recrystallized from chloroform at room temperature

to give (1.96 g, 0.0038 mol, 83.76% yield). M.p. = 102-104 °C. Calc. for $C_{12}H_{21}InO_3S_6$ (%): C 27.7, H 4.07, S 36.9, In 22.1; found: C 27.8, H 3.98, S 36.1, In 22.0. FT-IR (cm^{-1}): 2970 (m), 2875(w), 1453 (m) 1245 (s), 1217 (s), 1136 (m), 1039 (s), 1034 (s), 937.5 (m), 899.2 (w), 755.2 (m), 648.8 (m), 561.6 (w). 1H NMR (400 MHz, $CDCl_3$) δ (ppm) = 1.06 (t, J = 7.5 Hz, 3H, CH_3), 1.91 (m, J = 6.8 Hz, 2H, $CH_2CH_2CH_3$), 4.43 (t, J = 6.8 Hz, 2H, OCH_2CH_2).

5.4.3.1.4 Synthesis of indium(III) *iso*-propylxanthate (9):

$[In(S_2CO^iPr)_3]$ was synthesized via the same method as **8**, using potassium *iso*-propylxanthate (2.35 g, 0.0135 mol). (1.85 g, 0.0035 mol, 79.0% yield). M.p. = 142-144 °C. Calc. for $C_{12}H_{21}InO_3S_6$ (%): C 27.7, H 4.07, S 36.9, In 22.1; found: C 27.8, H 3.98, S 36.7, In 22.5. FT-IR (cm^{-1}): 2976 (m), 2930 (w), 1461 (m), 1373 (m), 1232 (s), 1142 (m), 1083 (s), 1011 (s), 899.3 (m), 808.4 (w), 645.2 (m), 567.7 (w). 1H NMR (400 MHz, $CDCl_3$) δ (ppm) = 1.5 (d, J = 6.3 Hz, 6H, $CH(CH_3)_2$), 5.14 (sep, J = 6.3 Hz, 1H, $CH(CH_3)_2$).

5.4.3.1.5 Synthesis of indium(III) *iso*-butylxanthate (10):

$[In(S_2CO^iBu)_3]$ was synthesized via the same method as **8**, using potassium *iso*-butylxanthate (2.54 g, 0.0135 mol). (1.94 g, 0.0034 mol, 76.7% yield). M.p. = 109 -113 °C. Calc. for $C_{15}H_{27}InO_3S_6$ (%): C 32.0, H 4.84, S 34.1, In 20.4; found: C 32.0, H 4.79, S 34.1, In 20.2. FT-IR (cm^{-1}): 2955 (m), 2870 (w), 1466 (m), 1454 (m), 1372 (m), 1221 (s), 1197 (m), 1025 (s), 958.3 (s), 822.5 (w), 654.6 (m), 575.3 (w). 1H NMR (400 MHz, $CDCl_3$) δ (ppm): 0.96 (d, J = 6.5 Hz, 6H, $CH(CH_3)_2$), 2.12 (sep, J = 6.8 Hz, 1H, $CH(CH_3)_2$), 4.15 (d, J = 6.5 Hz, 2H, OCH_2CH).

5.4.3.1.6 Synthesis of indium(III) 2-ethoxyethylxanthate (11):

$[In(S_2CO(CH_2)_2OEt)_3]$ was synthesized via the same method as **8**, using potassium 2-ethoxyethylxanthate (2.75 g, 0.0135 mol). (2.25 g, 0.0037 mol, 82% yield). M.p. = 81-84 °C. Calc. for $C_{15}H_{27}InO_6S_6$ (%): C 29.5, H 4.46, S 31.5, In 18.8; found: C 29.5, H 4.36, S 31.2, In 18.7. FT-IR (cm^{-1}): 2971 (m), 2865 (w), 1441 (m), 1384 (m), 1352 (w), 1214 (s), 1116 (s), 1035 (s), 998.5 (s), 936.1 (m), 863.3 (m), 836.1 (m). 1H NMR (400 MHz, $CDCl_3$) δ (ppm): 1.17 (t, J = 7 Hz, 3H, OCH_2CH_3), 3.51 (q, J = 7

Hz, 2H, OCH₂CH₃), 3.74 (t, J = 4.8 Hz, 2H, CH₂CH₂O), 4.49(t, J = 4.8 Hz, 2H, CH₂CH₂O).

5.4.3.1.7 Synthesis of indium(III) 2-methoxyethylxanthate (12):

[In(S₂CO(CH₂)₂OMe)₃] was synthesized via the same method as **8**, using potassium 2-methoxyethylxanthate (2.56 g, 0.0135 mol). (2.2 g, 0.0038 mol, 86.1% yield). M.p. = 95 - 98 °C. Calc. for C₁₂H₂₁InO₆S₆ (%): C 25.4, H 3.73, S 33.8, In 20.2; found: C 25.4, H 3.66, S 33.5, In 19.8. FT-IR (cm⁻¹): 2922 (m), 1438 (m), 1392 (m), 1367 (m), 1212 (s), 1120 (s) 1092 (s), 1036 (s), 1021 (s), 976.2 (s), 845.6 (s), 661.6 (m), 575.8 (w). ¹H NMR (400 MHz, CDCl₃) δ (ppm): 3.36 (s, 3H, OCH₃), 3.71 (t, J = 4.5 Hz, 2H, CH₂CH₂O), 4.50 (t, J = 4.5 Hz, 2H, CH₂CH₂O).

5.4.3.1.8 Synthesis of indium(III) 3-methoxy-3-methyl-1-butylxanthate (13):

[In(S₂CO(CH₂)₂C(OMe)(Me)₂)₃] was synthesized via the same method as **8**, using potassium 3-methoxy-3-methyl-1-butylxanthate (3.13 g, 0.0135 mol). (2.3 g, 0.0033 mol, 73.6% yield). M.p. = 78-81 °C. Calc. for C₂₁H₃₉InO₆S₆ (%): C 36.3, H 5.66, S 27.6, In 16.6; found: C 36.5, H 5.67, S 27.3, In 16.5. FT-IR (cm⁻¹): 2975 (m), 2825 (w), 1466 (m), 1381 (m), 1366 (m), 1310 (w), 1227 (s), 1210 (s), 1173 (s), 1155 (s), 1074 (s), 1040 (s), 1019 (s), 933.7 (m), 871.4 (m), 788.1 (w), 751.9 (m), 644.7 (w), 568.2 (w). ¹H NMR (400 MHz, CDCl₃) δ (ppm): 1.24 (s, 6H, CH₂C(CH₃)₂OCH₃), 2.09 (t, J = 7.3 Hz, 2H, CH₂C(CH₃)₂OCH₃), 3.23 (s, 3H, CH₂C(CH₃)₂OCH₃), 4.59 (t, J = 7.3 Hz, 2H, CH₂CH₂C(CH₃)₂OCH₃).

5.4.3.1.9 Synthesis of indium(III) 1-methoxy-2-propylxanthate (14):

[In(S₂COC(H)(Me)CH₂OMe)₃] was synthesized via the same method as **8**, using potassium 1-methoxy-2-propylxanthate (2.75 g, 0.0135 mol). (2.25g, 0.0036 mol, 82% yield). M.p. = 109-112 °C. Calc. for C₁₅H₂₇InO₆S₆ (%): C 29.5, H 4.46, S 31.5, In 18.8; found: C 29.3, H 4.26, S 29.3, In 19.4. FT-IR (cm⁻¹): 2984 (m), 2938(w), 1448.6 (m), 1392.6(w), 1344(w), 1236.8 (s), 1198.5(s), 1161(m), 1121 (w), 1092(w), 1055(s), 1009.2 (s), 943.94(m), 815.6(m), 643.1 (w), 574.04(w). ¹H NMR (400 MHz, CDCl₃) δ (ppm): 1.39 (d, J = 6.3 Hz, 3H, CHCH₃), 3.35 (s, 3H, OCH₃), 3.50-3.59 (m, 2H, CH₂O), 5.08 (m, 1H, CHCH₃).

5.4.3.2 X-ray Crystallography:

Single crystal X-ray diffraction was performed using a Bruker diffractometer with a Cu-K α source ($\lambda = 1.5418 \text{ \AA}$) (10, 12, 13) and XtaLAB AFC11 (RINC): Kappa single diffractometer with a Mo-K α source ($\lambda = 0.71073 \text{ \AA}$) (7, 8, 9, 14) SuperNova, Single source at offset, Eos diffractometer with a Mo-K source (11). Crystallographic data available from the CCDC.

5.4.3.3 Synthesis of CuInS₂ nanoparticles:

CuInS₂ nanocrystals were synthesized via the hot injection method and a typical procedure is described. A stoichiometric mixture of **15** (0.0752 g, 0.0001 mol) and **11** (0.0609 g, 0.0001 mol) were used. The reactions were performed under nitrogen. To obtain a hexagonal phase, the mixture was suspended in octadecene (2 ml) and injected into 20 ml castor oil preheated to 260 °C. To form a zinc blende CuInS₂, the precursors were dissolved into trioctylphosphine (1 ml) and oleylamine (1 ml) and injected into oleylamine (20 ml) preheated to 260 °C. After a set period of time (10 or 45 min), the solution was cooled to room temperature with the addition of *iso*-propanol and the particles separated by centrifugation. The nanoparticles were extracted by diluting the resultant product with 30 ml methanol (three times) and 30 ml acetone (two times).

5.4.4 Results and discussion

5.4.4.1 Precursors

We report here the synthesis and single crystal structures of seven novel indium xanthates: [In(S₂COⁿPr)₃] (**8**), [In(S₂COⁱPr)₃] (**9**), [In(S₂CO^tBu)₃] (**10**), [In(S₂CO(CH₂)₂OEt)₃] (**11**), [In(S₂CO(CH₂)₂OMe)₃] (**12**), [In(S₂CO(CH₂)₂C(OMe)(Me)₂)₃] (**13**) and [In(S₂COC(H)(Me)CH₂OMe)₃] (**14**). as well as [K(S₂CO(CH₂)₂C(OMe)(Me)₂)] (Tables A3 and A4, figure A40). These complexes were prepared from the reaction of a previously prepared potassium xanthate (from the insertion of CS₂ into the relevant potassium alkoxide) and indium(III) chloride. Crystals suitable for X-ray analysis can be grown from the slow evaporation of chloroform at room temperature.

Compounds **8**, **9**, **11**, **12** and **13** adopt a monoclinic crystal system with space groups $P2_1/c$, $P2_1$, $C2/c$, $P2_1/n$, and $P2_1/n$ respectively, whilst **10** is orthorhombic $Pbca$ and **14** is trigonal $R\bar{3}$.

In all cases the central In atoms are 6-coordinate, bound by three chelating xanthate ligands in a distorted octahedral manner (Figure 5.1). The In-S bond lengths show little variation across the series: 2.5650(8)-2.6166(8) Å (**8**), 2.564(2)-2.626(2) Å (**9**), 2.575(1)-2.626(1) Å (**10**), 2.5577(9)-2.655(1) Å (**11**), 2.5683(6)-2.6298(6) Å (**12**), 2.558(2)-2.634(2) Å (**13**) and 2.576(2)-2.63(2) Å (**14**). This is also mirrored in the S-In-S bond angles of 69.93(2)-70.51(3)° (**8**), 69.72(5)-70.30(5)° (**9**), 69.68(3)-70.27(3)° (**10**), 69.71(3)-70.30(3)° (**11**), 70.06(2)-70.44(2)° (**12**), 69.72(6)-70.03(5)° (**13**) and 69.66(3)° (**14**) and S-C-S bond angles of the xanthates: 122.0(2)-122.2(2)° (**8**), 121.6(4)-122.7(4)° (**9**), 121.3(2)-122.4(3)° (**10**), 122.1(2)-123.2(2)° (**11**), 121.8(1)-122.4(1)° (**12**), 121.4(4)-123.0(4)° (**13**) and 121.9(3)° (**14**).

The decomposition of the indium complexes were assessed via thermogravimetric analysis (Figure 5.2 and Table S5.1). Complexes **8-10**, i.e. those with a pure hydrocarbon xanthate backbone, decompose cleanly in one-step to form InS at 120-150 °C. In contrast, **11-14**, which have an ether moiety within the xanthate chain undergo a two-step process, initially forming In_2S_3 before the remaining sulfur is driven off to leave InS.

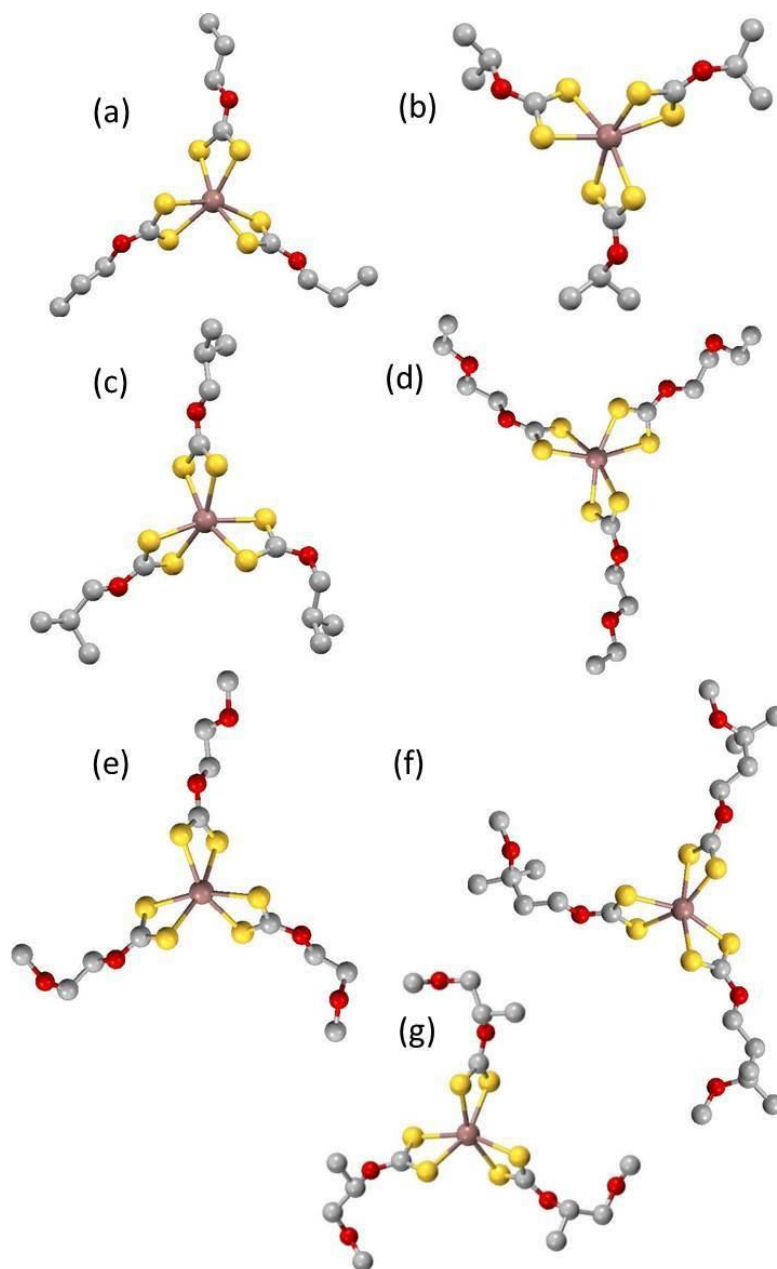


Figure 5.1. The structures of the indium xanthates. (a) $[\text{In}(\text{S}_2\text{CO}^i\text{Pr})_3]$ (**8**), (b) $[\text{In}(\text{S}_2\text{CO}^i\text{Pr})_3]$ (**9**), (c) $[\text{In}(\text{S}_2\text{CO}^i\text{Bu})_3]$ (**10**), (d), $[\text{In}(\text{S}_2\text{CO}(\text{CH}_2)_2\text{OEt})_3]$ (**11**), (e) $[\text{In}(\text{S}_2\text{CO}(\text{CH}_2)_2\text{OMe})_3]$ (**12**), (f) $[\text{In}(\text{S}_2\text{CO}(\text{CH}_2)_2\text{C}(\text{OMe})(\text{Me})_2)_3]$ (**13**) and (g) $[\text{In}(\text{S}_2\text{COC}(\text{H})(\text{Me})\text{CH}_2\text{OMe})_3]$ (**14**). H atoms are omitted for clarity. Bronze = In, yellow = S, red = O, grey = C.

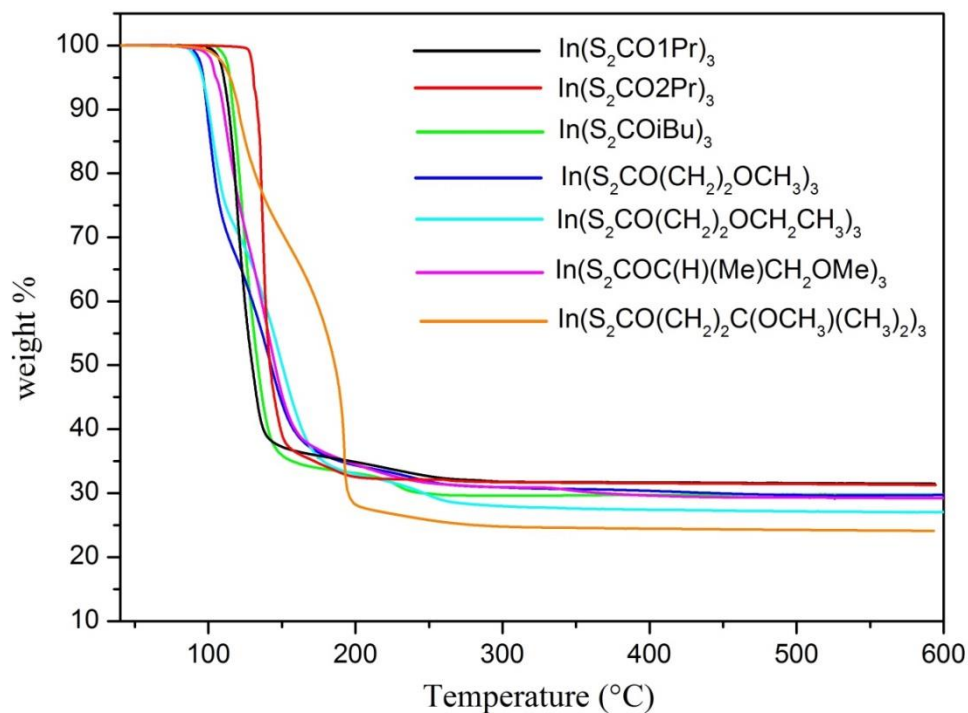


Figure 5.2. TGA of Indium xanthates complexes.

5.4.4.2 Synthesis of Nanoparticles

We initially chose complex **11**, $[\text{In}(\text{S}_2\text{CO}(\text{CH}_2)_2\text{OEt})_3]$, as our source of In, reasoning that the two-step decomposition process would give rise to a control handle for the phase produced. We selected triphenylphosphine copper(I) 2-ethoxyethylxanthate (**15**)¹³ as the copper source to avoid any potential problems involving ligand exchange.

We prepared CuInS_2 nanoparticles using the hot-injection method in two distinct solvent systems. Firstly, we suspended a 1:1 ratio of **11**:**15** in octadecene and injected it into castor oil preheated to 260 °C. This resulted in the formation of hexagonal phase CuInS_2 (Figure 5.3a), with unit cells comparable to the literature (ESI Table S5.2).

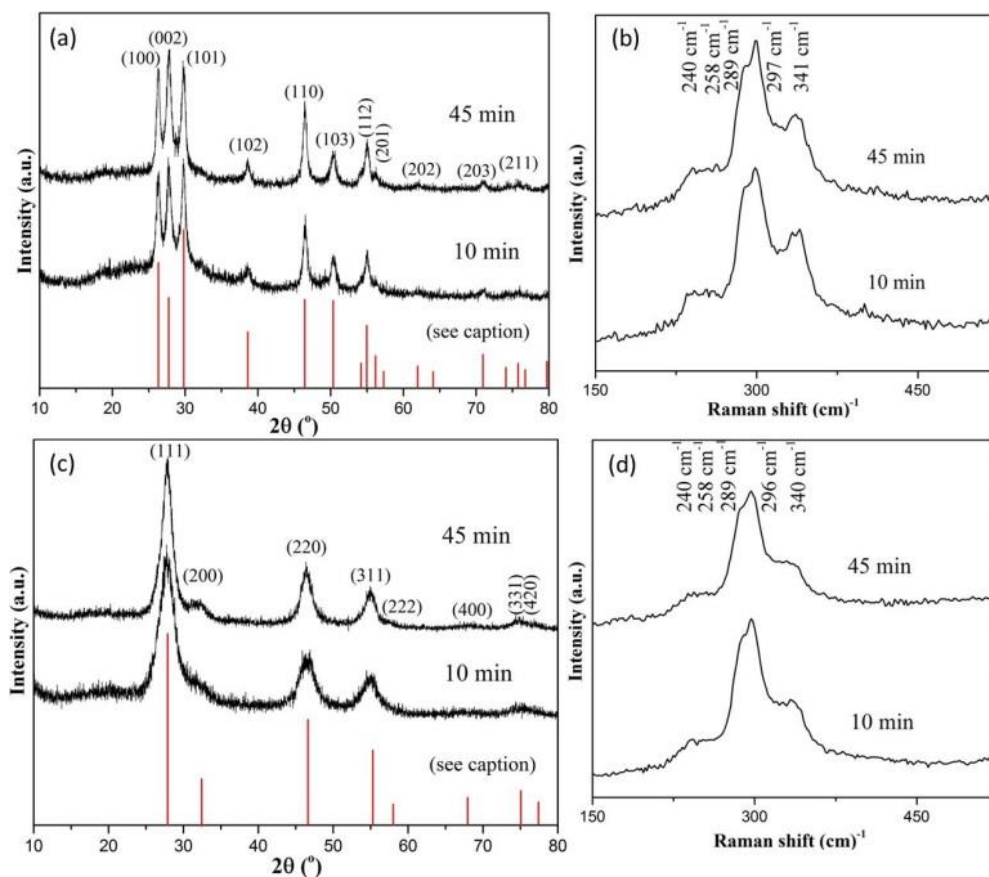


Figure 5.3. The pXRD patterns and Raman spectra of (a, b) hexagonal CIS and (c, d) cubic CIS. In each case the upper pattern corresponds to a 45 minute reaction, whilst the lower corresponds to a 10 minute reaction length. Hexagonal CIS reference pattern generated from Tang's³⁶ work, cubic CIS reference pattern generated from Yang's³⁷ work,

Secondly, we dissolved the precursors **11** and **15** in separate mixtures of trioctylphosphine (1 ml) and oleylamine (1 ml). These two solutions were then injected into oleylamine (20 ml) that had been preheated to 260 °C and held at that temperature for a set length of time before quenching. This resulted in the formation of cubic CIS (i.e. zinc blende structure (Figure 5.3c)) again with unit cells comparable to the literature (ESI Table S5.2).

This intriguing result indicates that the choice of solvent has a remarkable impact on the phase that is formed. Octadecene is of course a non-coordinating solvent, but the main component of castor oil is the triester of glycerol and ricinoleic acid, which does have pendant hydroxyl groups on the backbone and has been previously used as a 'green' capping ligand.^{38, 39} Oleylamine on the other hand is a well-known capping

ligand. In order to be sure that there was no exchange of the alkoxy group of the xanthates for oleylamine (to make a dithiocarbamate) we heated a solution of **11** in oleylamine to 100 °C (i.e. just below the initial breakdown temperature) and then ran a ^1H NMR of the resulting mixture (Figures A41 and A42). For **11** + oleylamine, there was no evidence of any exchange occurring with the oleylamine signals remaining identical after heating (Figure A41). There is some slight shifting of the xanthate signals after heating (Figure A42) but this is most likely due to the beginnings of decomposition. We have previously conducted a similar experiment for **15** and seen no ligand exchange either.¹³

Figures 5.3b and 5.3d show Raman spectra of CuInS₂ nanoparticles, the peaks are observed at 240, 258, 289, 297 and 341 cm⁻¹ for hexagonal CuInS₂, 240 cm⁻¹ and 341 cm⁻¹ are assigned to E and B₂ modes of CIS respectively, 258 cm⁻¹ is assigned to E/B₂ modes, A mode appears at 289 cm⁻¹. Similar peak positions were observed for Cubic CIS with slight shift for some individual peaks.

The particles themselves are highly crystalline, though of an indeterminate shape for both solvent systems (Figures 5.4 and 5.5). Lattice fringes for hexagonal CuInS₂ can be indexed to the (100) plane (Figure 5.4b), and for cubic CuInS₂ can be indexed to the (111) plane. There is little discernible difference from a 10 min reaction (Figure 5.4) and a 45 min reaction (Figure 5.5).

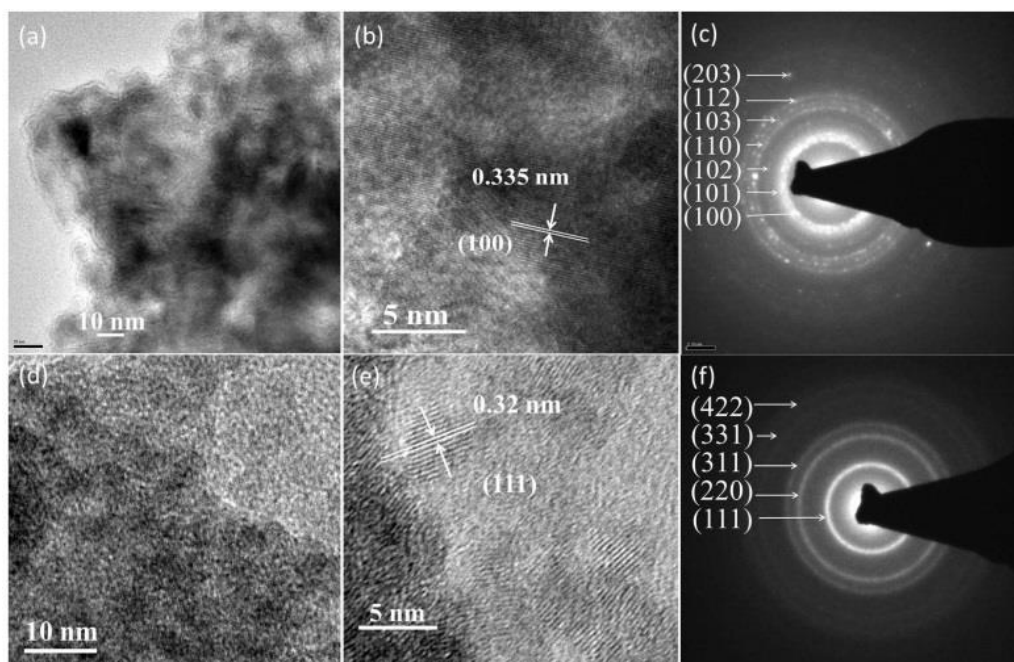


Figure 5.4. TEM images and associated selected area electron diffraction (SAED) patterns for (a)-(c) hexagonal CuInS_2 from a 10 min reaction and (d)-(f) cubic CuInS_2 from a 10 min reaction.

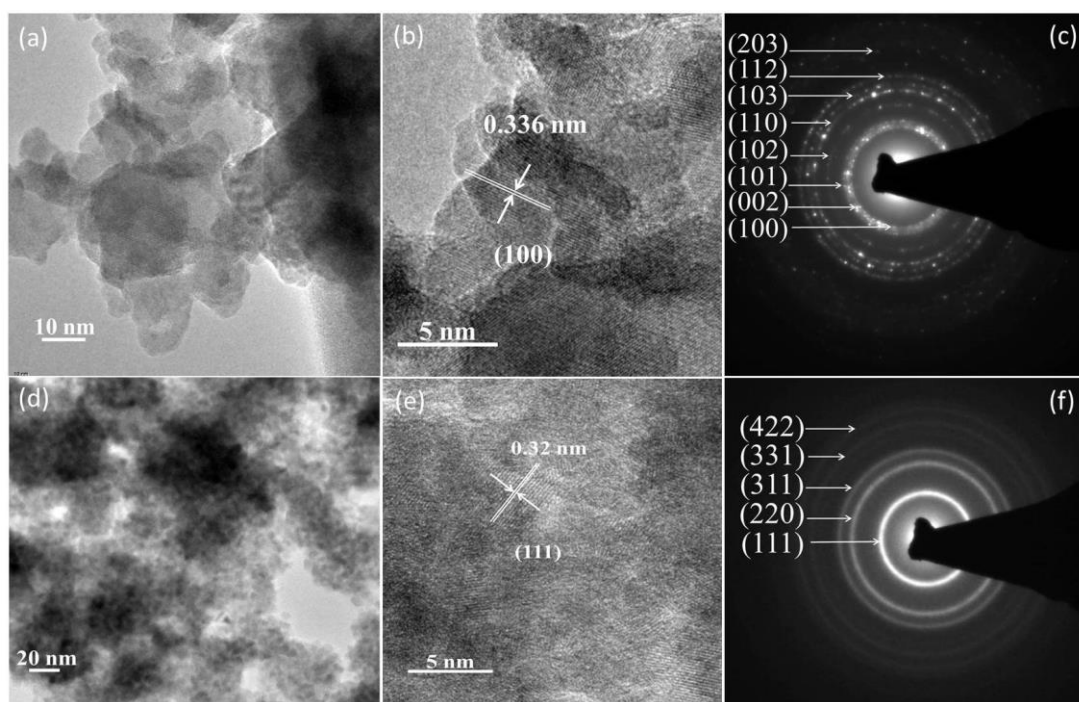


Figure 5.5. TEM images and associated selected area electron diffraction (SAED) patterns for (a)-(c) hexagonal CuInS_2 from a 45 min reaction and (d)-(f) cubic CuInS_2 from a 45 min reaction.

Energy dispersive X-ray spectroscopy (EDX) indicates that the composition of the particles is consistent across the different solvent systems and reaction times (ESI Table S5.3), close to the ideal CuInS_2 ratios. Raman spectroscopy gave additional confirmation as to the purity of the phases (Figures 5.3b and 5.3d). We have also measured the optical properties of the nanoparticles and found them to be in the range 1.47-1.53 eV, but all within error of each other (Figure 5.6). This result is consistent with the literature.^{40, 41}

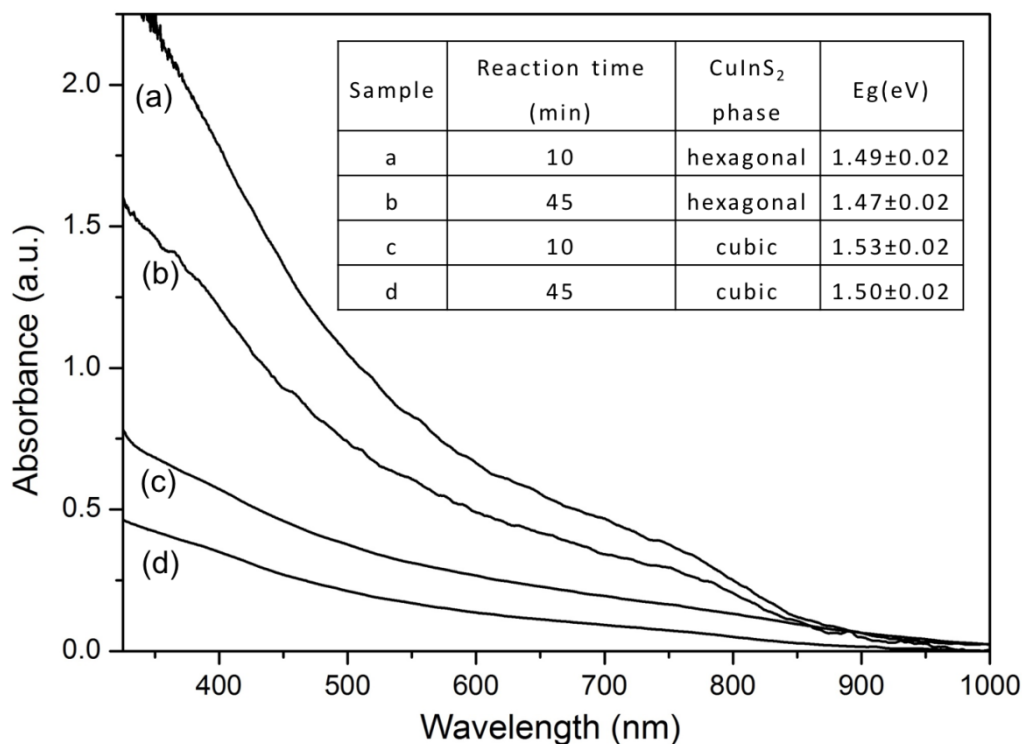


Figure 5.6. UV-vis spectra and associated band gaps of the CIS nanoparticles.

In order to confirm the consistency of the phase control, we also performed the experiment using the equivalent 2-methoxyethylxanthate (i.e. **12** and the corresponding copper(I) analogue). We found that the precursors behaved identically as **11** and **14** (Figures 5.7 and 5.8).

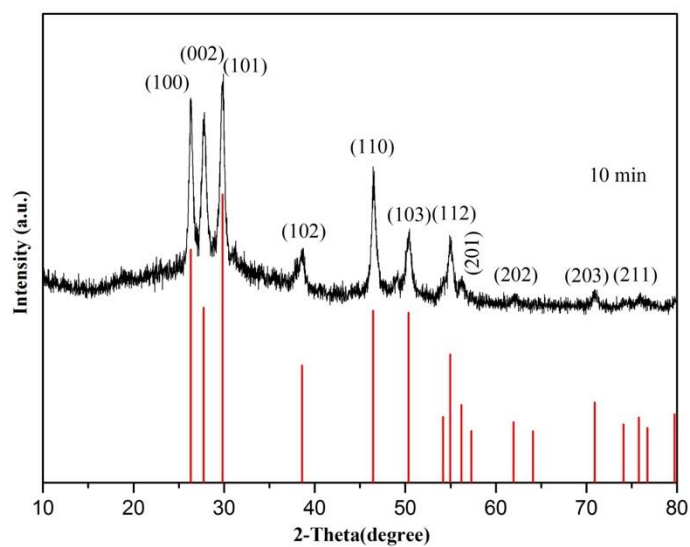


Figure 5.7. pXRD pattern of hexagonal CIS from reacting **12** and $[(\text{PPh}_3)_2\text{Cu}(\text{S}_2\text{CO}(\text{CH}_2)_2\text{OMe})]$ in octadecene/castor oil.

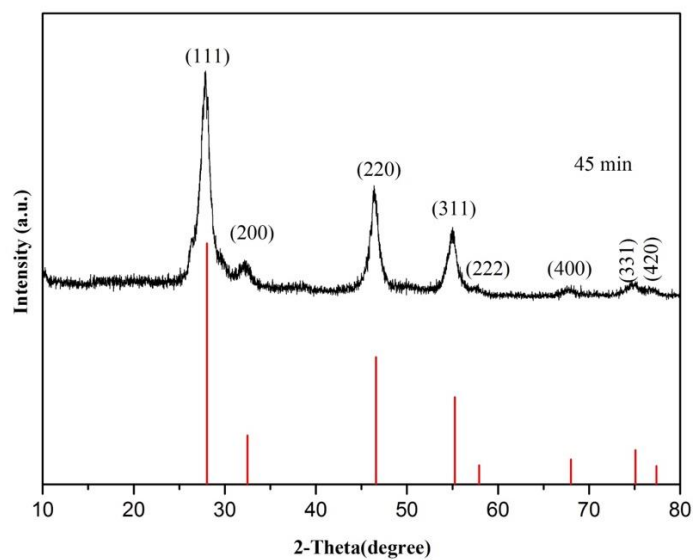


Figure 5.8. pXRD pattern of cubic CIS from reacting **12** and $[(\text{PPh}_3)_2\text{Cu}(\text{S}_2\text{CO}(\text{CH}_2)_2\text{OMe})]$ in trioctylphosphine/oleylamine.

5.4.5 Conclusions

We have demonstrated an ability to generate highly crystalline CuInS₂ from indium and copper xanthate precursors, whilst exhibiting phase control through choice of solvent. We have reported the crystal structures of seven novel indium xanthates, comprehensively extending this family of compounds.

5.4.6 Acknowledgements

The authors would like to acknowledge the Iraqi Culture Attaché in London for financial support (M.A.S.) and the EPSRC (Doctoral Prize for P.D.M., grant EP/M507969/1). Some of the equipment used in this study was provided by the EPSRC Core Capability in Chemistry grant EP/K039547/1.

5.4.7 References

1. P. D. Matthews, P. D. McNaughter, D. J. Lewis and P. O'Brien, *Chem. Sci.*, 2017, **8**, 4177-4187.
2. M. V. Kovalenko, L. Manna, A. Cabot, Z. Hens, D. V. Talapin, C. R. Kagan, V. I. Klimov, A. L. Rogach, P. Reiss and D. J. Milliron, *ACS Nano*, 2015, **9**, 1012-1057.
3. A. A. Tedstone, D. J. Lewis and P. O'Brien, *Chem. Mater.*, 2016, **28**, 1965-1974.
4. A. D. Leach and J. E. Macdonald, *J. Phys. Chem. Lett.*, 2016, **7**, 572-583.
5. S. Wagner, J. Shay, P. Migliorato and H. Kasper, *Appl. Phys. Lett.*, 1974, **25**, 434-435.
6. L. Kazmerski and G. Sanborn, *J. Appl. Phys.*, 1977, **48**, 3178-3180.
7. L. Kazmerski, F. White and G. Morgan, *Appl. Phys. Lett.*, 1976, **29**, 268-270.
8. N. Syrbu, R. Cretu and V. Tezlevan, *Cryst. Res. Technol.*, 1998, **33**, 135-144.
9. W. Yue, S. Han, R. Peng, W. Shen, H. Geng, F. Wu, S. Tao and M. Wang, *J. Mater. Chem.*, 2010, **20**, 7570-7578.
10. H. Y. Ueng and H. Hwang, *J. Phys. Chem. Solids*, 1989, **50**, 1297-1305.
11. J. Binsma, L. Giling and J. Bloem, *J. Cryst. Growth*, 1980, **50**, 429-436.
12. J. Kolny-Olesiak and H. Weller, *ACS Appl. Mater. Interfaces*, 2013, **5**, 12221-12237.

13. M. Al-Shakban, P. D. Matthews, G. Deogratias, P. D. McNaughter, J. Raftery, I. Vitorica-Yrezabal, E. B. Mubofu and P. O'Brien, *Inorg. Chem.*, 2017, **56**, 9247-9254.
14. M. Afzaal, C. L. Rosenberg, M. A. Malik, A. J. White and P. O'Brien, *New J. Chem.*, 2011, **35**, 2773-2780.
15. P. S. Nair, T. Radhakrishnan, N. Revaprasadu, G. A. Kolawole and P. O'Brien, *Polyhedron*, 2003, **22**, 3129-3135.
16. M. Afzaal, M. A. Malik and P. O'Brien, *J. Mater. Chem.*, 2010, **20**, 4031-4040.
17. E. Lewis, S. Haigh and P. O'Brien, *J. Mater. Chem. A*, 2014, **2**, 570-580.
18. E. A. Lewis, P. D. McNaughter, Z. Yin, Y. Chen, J. R. Brent, S. A. Saah, J. Raftery, J. A. Awudza, M. A. Malik and P. O'Brien, *Chem. Mater.*, 2015, **27**, 2127-2136.
19. P. D. McNaughter, S. A. Saah, M. Akhtar, K. Abdulwahab, M. A. Malik, J. Raftery, J. A. Awudza and P. O'Brien, *Dalton Trans.*, 2016, **45**, 16345-16353.
20. P. D. Matthews, M. Akhtar, M. A. Malik, N. Revaprasadu and P. O'Brien, *Dalton Trans.*, 2016, **45**, 18803-18812.
21. N. Alam, M. S. Hill, G. Kociok-Köhn, M. Zeller, M. Mazhar and K. C. Molloy, *Chem. Mater.*, 2008, **20**, 6157-6162.
22. J. M. Clark, G. Kociok-Köhn, N. Harnett, M. Hill, R. Hill, K. C. Molloy, H. Saponia, D. Stanton and A. Sudlow, *Dalton Trans.*, 2011, **40**, 6893-6900.
23. M. Al-Shakban, P. D. Matthews, N. Savjani, X. L. Zhong, Y. Wang, M. Missous and P. O'Brien, *J. Mater. Sci.*, 2017, **52**, 12761-12771.
24. T. Rath, A. J. MacLachlan, M. D. Brown and S. A. Haque, *J. Mater. Chem. A*, 2015, **3**, 24155-24162.
25. M. Al-Shakban, P. D. Matthews and P. O'Brien, *Chem. Commun.*, 2017, **53**, 10058-10061.
26. M. A. Buckingham, A. L. Catherall, M. S. Hill, A. L. Johnson and J. D. Parish, *Cryst. Growth Des.*, 2017, **17**, 907-912.
27. Y. su Kim, Y. Lee, Y. Kim, D. Kim, H. S. Choi, J. C. Park, Y. S. Nam and D. Y. Jeon, *RSC Adv.*, 2017, **7**, 10675-10682.

28. A. C. Berends, F. T. Rabouw, F. C. Spoor, E. Bladt, F. C. Grozema, A. J. Houtepen, L. D. Siebbeles and C. de Mello Donegá, *J. Phys. Chem. Lett.*, 2016, **7**, 3503-3509.
29. L. Li, A. Pandey, D. J. Werder, B. P. Khanal, J. M. Pietryga and V. I. Klimov, *J. Am. Chem. Soc.*, 2011, **133**, 1176-1179.
30. R. Xie, M. Rutherford and X. Peng, *J. Am. Chem. Soc.*, 2009, **131**, 5691-5697.
31. H. Zang, H. Li, N. S. Makarov, K. A. Velizhanin, K. Wu, Y.-S. Park and V. I. Klimov, *Nano Lett.*, 2017, **17**, 1787-1795.
32. C. Xia, J. D. Meeldijk, H. C. Gerritsen and C. de Mello Donegá, *Chem. Mater.*, 2017, **29**, 4940-4951.
33. A. D. Leach, X. Shen, A. Faust, M. C. Cleveland, A. D. La Croix, U. Banin, S. T. Pantelides and J. E. Macdonald, *J. Phys. Chem. C*, 2016, **120**, 5207-5212.
34. A. Leach, L. Mast, E. Hernandez-Pagan and J. Macdonald, *J. Mater. Chem. C*, 2015, **3**, 3258-3265.
35. A. M. Hounslow and E. R. Tiekink, *J. Chem. Crystallogr.*, 1991, **21**, 133-137.
36. Y. Qi, Q. Liu, K. Tang, Z. Liang, Z. Ren and X. Liu, *J. Phys. Chem. C*, 2009, **113**, 3939-3944.
37. D. Pan, L. An, Z. Sun, W. Hou, Y. Yang, Z. Yang and Y. Lu, *J. Am. Chem. Soc.*, 2008, **130**, 5620-5621.
38. G. B. Shombe, E. B. Mubofu, S. Mlowe and N. Revaprasadu, *Mater. Sci. Semicond. Process.*, 2016, **43**, 230-237.
39. E. B. Mubofu, *Sustain. chem. process.*, 2016, **4**, 11.
40. M. G. Panthani, V. Akhavan, B. Goodfellow, J. P. Schmidtke, L. Dunn, A. Dodabalapur, P. F. Barbara and B. A. Korgel, *J. Am. Chem. Soc.*, 2008, **130**, 16770-16777.
41. D. Pan, L. An, Z. Sun, W. Hou, Y. Yang, Z. Yang and Y. Lu, *J. Am. Chem. Soc.*, 2008, **130**, 5620-5621.

5.4.8 Electronic Supplementary Information

Table S5.1. TGA data analyses of indium xanthate complexes.

Indium complexes	M.W. g mol ⁻¹	Metal sulfides	M.W. g mol ⁻¹	% calculated	% from TGA
In(S ₂ CO ⁱ Pr) ₃	519.80	In ₂ S ₃	325.56	62.63	31.5 at 298.1 °C
		InS	146.79	28.24	
In(S ₂ CO ⁱ Pr) ₃	519.80	In ₂ S ₃	325.56	62.63	31.8 at 302.5 °C
		InS	146.79	28.24	
In(S ₂ CO ⁱ Bu) ₃	561.85	In ₂ S ₃	325.56	56.94	29.6 at 257.5 °C
		InS	146.79	26.12	
In(S ₂ CO(CH ₂) ₂ OMe) ₃	567.79	In ₂ S ₃	325.56	57.33	Step(1) 58.76 at 131.3 °C
		InS	146.79	25.85	Step (2) 29.15 at 468 °C
In(S ₂ CO(CH ₂) ₂ OEt) ₃	609.83	In ₂ S ₃	325.56	53.38	Step(1) 54.10 at 146.1 °C
		InS	146.79	24.10	Step(2)26.89 at 438 °C
In(S ₂ COC(H)(Me)CH ₂ OMe) ₃	609.83	In ₂ S ₃	325.56	53.38	Step(1) 46.4 at 148.4 °C
		InS	146.79	24.10	Step(2)29.2 at 480 °C
In(S ₂ CO(CH ₂) ₂ C(OMe)(Me) ₂) ₃	693.93	In ₂ S ₃	325.56	46.91	Step(1) 48.17 at 187.5 °C
		InS	146.79	21.15	Step(2) 24.15at 374 °C

Table S5.2. The lattices parameters of CuInS₂ samples calculated from X-Ray diffraction, lattice parameter (a) of zincblende CuInS₂ is 5.523 Å,¹ and lattice parameters of hexagonal CuInS₂ are a = 3.9065 Å and c= 6.4290 Å.²

Samples	Reaction time(min)	a(Å)	b(Å)	c(Å)
Zinc blende CuInS ₂	10	5.523(3)	5.523(3)	5.523(3)
	45	5.522(3)	5.522(3)	5.522(3)
Hexagonal CuInS ₂	10	3.907(3)	3.907(3)	6.441(1)
	45	3.907(3)	3.907(3)	6.442(1)

Table S5.3. Chemical compositions of CuInS₂ nanoparticles calculated by energy dispersive X-ray spectroscopy (EDX).

Samples	Reaction time(min)	Cu (at%)	In (at%)	S (at%)
Zinc blende CuInS ₂	10	25.88	26.46	47.66
	45	25.62	26.57	47.81
Hexagonal CuInS ₂	10	25.35	26.77	47.88
	45	25.56	26.38	48.04

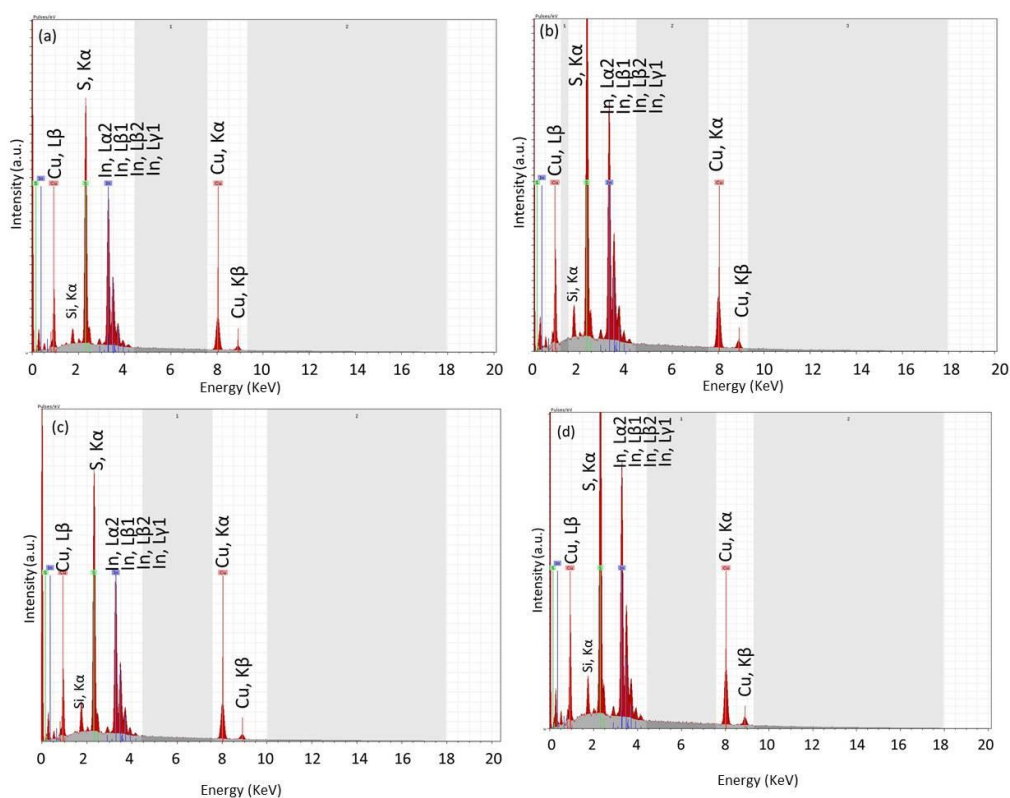


Figure S5.9. X-ray emissions lines of zinc blend CuInS₂ prepared at (a)10 min, (b) 45 min and hexagonal CuInS₂ prepared at (c) 10 min, (d) 45 min.

5.4.8.1 References

1. D. Pan, L. An, Z. Sun, W. Hou, Y. Yang, Z. Yang and Y. Lu, *J. Am. Chem. Soc.*, 2008, **130**, 5620-5621.
2. Y. Qi, Q. Liu, K. Tang, Z. Liang, Z. Ren and X. Liu, *J. Phys. Chem. C*, 2009, **113**, 3939-3944.

Chapter 6 Alkaline-Transition metal sulfides

6.1 Introduction

Alkaline-transition metal sulfides are used as phosphor¹ and thermoelectric materials.² Binary compounds like SrS and CaS emit a bright and homogeneous photoluminescence at 610 nm and 650 nm respectively, if they are doped with Eu.³ In addition ternary compounds for instance Eu²⁺ doped II-III₂S₄ (II = Ba, Sr and Ca. III = Al, Ga and In) present the wavelength range from 470 nm for BaAl₂S₄⁴ to 510 and 680 nm for CaIn₂S₄.⁵ Alkaline-transition metal sulfides have been prepared using different methods such as variation of a sol-gel process, this method has used by Petrykin *et al.*⁶ to produce Sr₂ZnS₃, the method involves two steps, synthesis of Sr_{2-x}Eu_xS₂ intermediate product by the polymerizable complex method and reaction between this intermediate and zinc sulfide under 5 GPa for 90 minutes at 1000 °C.

In the Ba-Cu-S system, a series of compounds have been found with the composition BaCu₂S₂ and BaCu₄S₃. BaCu₂S₂ shows good semiconducting properties,⁷ this compound is found into two forms orthorhombic (α - BaCu₂S₂) and tetragonal (β - BaCu₂S₂), orthorhombic phase has a one dimension tetrahedral chain of CuS₄, the Cu - Cu separation is 2.71 Å, which is a short interatomic distance. Keszler *et al.*⁸ suggested that α - BaCu₂S₂ has a good electrical conductivity, because of the shorter distances resulting in broader bands. They found that α - BaCu₂S₂ films deposited onto glass and KBr substrates show a conductivity of 17 S. cm⁻¹ and a Hall mobility of 3.5 cm²v⁻¹s⁻¹, the polarity of the films is *p*-type, also the conductivity of α -BaCu₂S₂ has been studied by Huang *et al.*⁷ The films show the value of 33.6 S cm⁻¹ at room temperature. In the crystal of β - BaCu₂S₂, however, Cu₂S₂ layers are sandwiched by Ba sheets.⁹ Kurosaki *et al.*¹⁰ suggested that the β - BaCu₂S₂ maybe a good thermoelectric material. They prepared β - BaCu₂S₂ samples by the solid state reactions, the electrical resistivity test shows that the samples have a metallic behaviour. The value of resistivity at room temperature is 3.88×10⁻⁴ Ω m.

BaCu₄S₃ also crystallises into two structures, low temperature phase (α - BaCu₄S₃) and high temperature phase (β - BaCu₄S₃). An α to β phase transition obtained at 640 ± 10 °C.¹¹ The resistivity of the α - BaCu₄S₃ is 0.2 Ω

cm, this phase shows temperature independence over the range 123°C to 227°C. The resistivity of β -BaCu₄S₃ is characteristic of a weak semiconductor over the temperature range 37°C to 157°C.¹²

6.2 Author distribution

I synthesised and characterised the xanthate complexes via IR, NMR, elemental analysis and TGA. The experimental work to obtain CaS, BaS, CaCu₂S₂, β -BaCu₂S₂ and β -BaCu₄S₃ thin films was carried out by me, I characterised the films via XRD, SEM and EDX. Peter D. Matthews checked the characterization of complexes and materials. The project was provided by Paul O'Brien, who edited the draft. The experimental work was done in the laboratory of Paul O'Brien.

6.3 References

1. P. Smet, D. Poelman and R. Van Meirhaeghe, *J. Appl. Phys.*, 2004, **95**, 184-190.
2. G. Liu, X. Wang, X. Kuang and A. L. He, *Physica B*, 2010, **405**, 4582-4585.
3. P. Smet and D. Poelman, *J. Phys. D*, 2009, **42**, 095306.
4. R. Guo, N. Miura, H. Matsumoto and R. Nakano, *Jpn. J. Appl. Phys.*, 2010, **49**, 012401.
5. J. Ding, X. Li, L. Chen, X. Zhang, S. Sun, J. Bao, C. Gao and X. Tian, *J. Mater. Chem. A*, 2016, **4**, 12630-12637.
6. V. Petrykin, M. Okube, H. Yamane, S. Sasaki and M. Kakihana, *Chem. Mater.*, 2010, **22**, 5800-5802.
7. Y. Wang, M. Liu, F. Huang, L. Chen, H. Li, X. Lin, W. Wang and Y. Xia, *Chem. Mater.*, 2007, **19**, 3102-3104.
8. S. Park, D. A. Keszler, M. M. Valencia, R. L. Hoffman, J. P. Bender and J. F. Wager, *Appl. Phys. Lett.*, 2002, **80**, 4393-4394.
9. M. Saeki, M. Onoda and H. Nozaki, *Mater. Res. Bull.*, 1988, **23**, 603-608.
10. K. Kurosaki, H. Uneda, H. Muta and S. Yamanaka, *J. Alloy. Comp.*, 2004, **385**, 312-315.
11. J. Iglesias, K. Pachali and H. Steinfink, *Mater. Res. Bull.*, 1972, **7**, 1247-1258.
12. Z. Eliezer and H. Steinfink, *Mater. Res. Bull.*, 1976, **11**, 385-388.

6.4 Manuscript 4: A Simple Route to Complex Materials: the Synthesis of Alkaline – Transition Metal Sulfides

Mundher Al-Shakban,^a Peter D. Matthews^b and Paul O'Brien^{*ab}

^a School of Materials, The University of Manchester, Oxford Road, M13 9PL

^b School of Chemistry, The University of Manchester, Oxford Road, M13 9PL

6.4.1 Abstract

We report the simple, low - temperature synthesis of a family of alkaline metal chalcogenide thin films that have previously only been produced from a high temperature, high pressure reaction system. The decomposition of calcium, barium and copper xanthates leads to the clean formation of CaS, BaS, CaCu₂S₂, β - BaCu₂S₂ and β - BaCu₄S₃ as desired.

6.4.2 Introduction

The synthesis of potentially useful complex materials is a key area for research, and one class of these, metal chalcogenides, is of particular interest to the semiconductor industry. Transition metal chalcogenides have been shown to make promising photovoltaic devices, energy storage, electronics and lubricants.¹⁻⁸ The introduction of an alkaline earth metal to make mixed metal chalcogenides produces a broad variety of structures with distinctive properties.⁹⁻¹⁵

Many complex metal chalcogenides provide significant synthetic challenges and often rely on very high temperature and/or pressure. Synthetic routes that involve more benign conditions will represent a major step forward. The mixed alkali/transition metal compound CaCu₂S₂ has previously only been synthesized by a challenging ammonothermal process,¹⁶ whilst BaCu₂S₂ has been reported via a hydrothermal method or in a flux of potassium thiocyanate.^{17, 18} Here we report a much simpler and potentially cheaper approach making use of metal xanthates in melt reactions.

We, and others, have previously described the use of transition metal xanthates [M(S₂COR)_x] (M = transition metal, R = alkyl chain) to generate nanostructured metal sulfides via aerosol - assisted chemical vapour deposition (AA-CVD), melt reactions and hot-injection reactions.¹⁹⁻²⁹ Metal xanthates are

a good choice as single-source precursors to metal sulfides, as they decompose cleanly at low temperature. One potential decomposition pathway is the Chugaev elimination mechanism (Scheme 1), from which the only by-products are gases that are readily removed from the reaction system.³⁰

We report here the simple, low-temperature synthesis of AS, ACu₂S₂ and ACu₄S₃ (A = Ca, Ba; Figure 6.1) from [Ca(S₂COⁱPr)₂(ⁱPrOH)₃] (**1**) [Ba(S₂COⁱPr)₂] (**2**) and [(PPh₃)₂Cu(S₂CO(CH₂)₂OMe)] (**3**). The calcium and copper xanthates were synthesized according to literature methods,^{31, 32} whilst we report a novel barium xanthate.

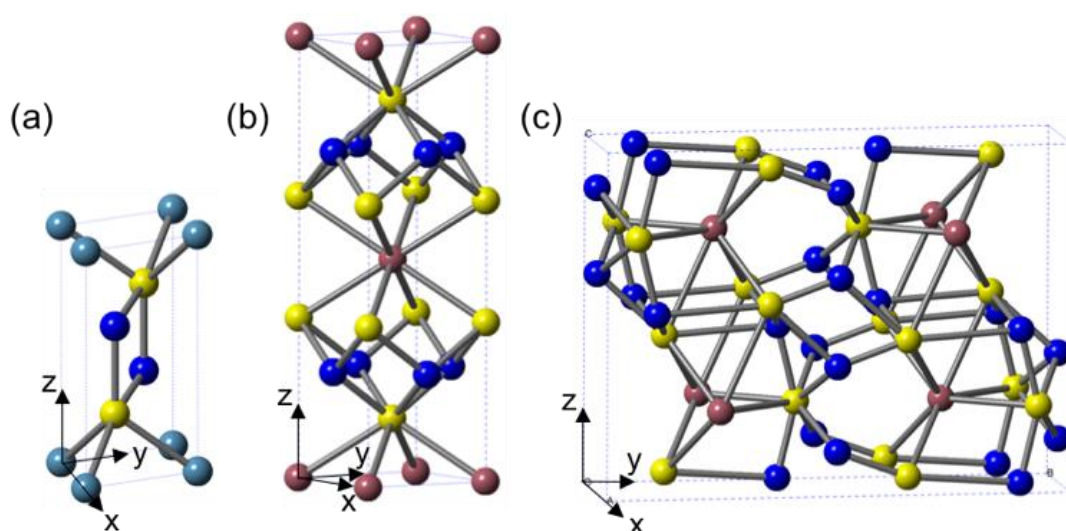
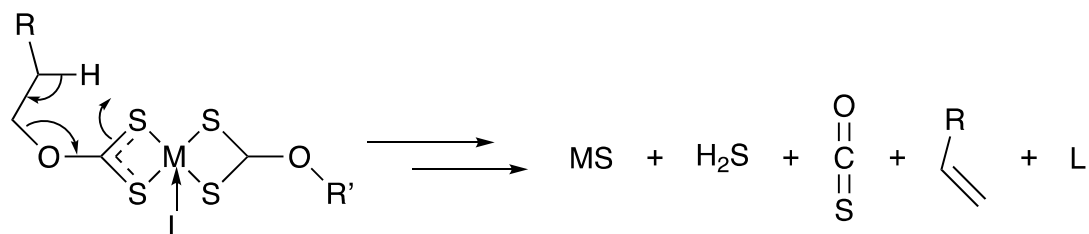


Figure 6.1. Schematic drawing of the structure of (a) CaCu₂S₂, (b) β -BaCu₂S₂ and (c) β -BaCu₄S₃. Teal = Ca, brown = Ba, blue = Cu, yellow = S.



Scheme 1. The proposed breakdown mechanism of the xanthate precursors.

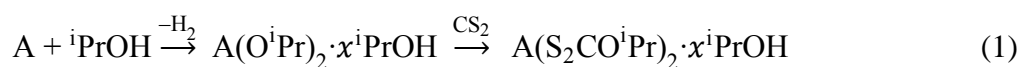
6.4.3 Experimental

6.4.3.1 Analytical equipment

Elemental analysis of the complex was carried out using Flash 2000 Thermo Scientific elemental analyzer in School of Chemistry, The University of Manchester. Thermogravimetric Analysis (TGA) of the complex was carried out by METTLER TOLEDO TGA/DSC 1 star^e system for the complexes under an atmosphere of dry nitrogen. NMR spectra were recorded in CDCl₃ and D₂O solutions on a Bruker Ascend spectrometer operating at 400 MHz, NMR samples for compounds **1** and **2** were prepared under N₂ in glove box. Scanning Electron Microscope images (SEM) were observed using a Philips XL 30FEG and FEI Quanta 200 ESEM, EDX analysis of the films was studied using EDAX Genesis V4.61 with an accelerated voltage of 20 Kv and working distance of 10mm; also, the molar and atomic ratios were analysed using a DX4 instrument. Structural properties of the films were studied using a Bruker D8 Advance diffractometer (Cu - K α , $\lambda = 1.5418 \text{ \AA}$), the applied voltage was 40 kV and the current 40 mA.

6.4.3.2 Synthesis of xanthate complexes

The Ca and Ba xanthates were synthesized from the insertion of CS₂ into the metal-alkoxide bond, according to the procedure of Bezougli³¹ (Equation 1). The Cu xanthate was prepared from CuCl, PPh₃ and potassium 2-methoxyethylxanthate in a method that we have previously reported.³²



6.4.3.2.1 Synthesis of [Ca(S₂COⁱP)₂(ⁱPrOH)₃](1)

Calcium metal (1.28 g, 16.0 mmol) was suspended in dry ⁱPrOH (100 ml) and the mixture heated to reflux under N₂ for 24 h which resulted in dissolution of the metal and evolution of hydrogen gas, yielding a slightly grey solution. The reaction was cooled to 0 °C and carbon disulfide (2.41 ml, 40 mmol) was added. A clear yellow solution started forming soon after the addition of carbon disulfide. The solution was stirred for 1 h at room temperature and then the solvent was removed *in vacuo*. The product was isolated as powder and

stored under N_2 at $0\text{ }^\circ\text{C}$ (yield: 5.3 g, 67.6%). M.p. = $48\text{-}51\text{ }^\circ\text{C}$. Calc. for $C_{17}H_{38}CaO_5S_4$ (%): C 41.6, H 7.8, S 26.0, Ca 8.17; found: C 41.5, H 7.75, S 25.6, Ca 8.53. FT-IR (cm^{-1}): 3311 (w), 2974 (m), 1459 (m), 1370 (m), 1300 (w), 1185 (s), 1156 (m), 1136 (m), 1081 (s), 1039 (s), 940 (s), 904 (w), 814 (m), 659 (w), 534 (w). ^1H NMR (400 MHz, CDCl_3) δ ppm: 1.27 (d, $J = 6.3$ Hz, 6H, $(\text{CH}_3)_2\text{CHOH}$), 1.41 (d, $J = 6$ Hz, 6H, $\text{S}_2\text{COCH}(\text{CH}_3)_2$), 2.24 (s, 1H, $(\text{CH}_3)_2\text{CHOH}$), 4.16 (sep, $J = 6$ Hz, 1H, $(\text{CH}_3)_2\text{CHOH}$), 5.61 (sep, $J = 6.3$ Hz, 1H, $\text{S}_2\text{COCH}(\text{CH}_3)_2$). ^{13}C NMR (400 MHz, CDCl_3) δ ppm: 13.60 ($\text{S}_2\text{COCH}(\text{CH}_3)_2$), 16.61 ($(\text{CH}_3)_2\text{CHOH}$), 57.33 ($(\text{CH}_3)_2\text{CHOH}$), 70.18 ($\text{S}_2\text{COCH}(\text{CH}_3)_2$), 232.80 ($\text{S}_2\text{COCH}(\text{CH}_3)_2$).

6.4.3.2.2 Synthesis of $[\text{Ba}(\text{S}_2\text{CO}^i\text{Pr})_2]$ (2)

Barium metal (1.34 g, 9.76 mmol) was suspended in dry $^i\text{PrOH}$ (100 ml) and the mixture heated to reflux for 16 h under N_2 which resulted in dissolution of the metal and evolution of hydrogen gas, yielding a slightly grey solution. The reaction was cooled to $0\text{ }^\circ\text{C}$ and carbon disulfide (1.47 ml, 24.4 mmol) added. The solution was stirred for 1 h at room temperature and then the solvent was removed *in vacuo*. The product was isolated as white powder and stored under N_2 at $0\text{ }^\circ\text{C}$ (yield: 3.32 g, 83.6%). M.p. = $168\text{-}173\text{ }^\circ\text{C}$. Calc. for $C_8H_{14}BaO_2S_4$ (%): C 23.5, H 3.94, S 31.3, Ba 33.5; found: C 23.8, H 3.89, S 31.4, Ba 33.6. FT-IR (cm^{-1}): 2972 (w), 2931 (m), 1442 (w), 1381 (m), 1373 (m), 1186 (s), 1158 (s), 1136 (m), 1085 (s), 1035 (s), 926 (s), 904 (w), 813 (m), 654 (w), 585 (w). ^1H NMR (400 MHz, D_2O) δ ppm: 1.24 (d, $J = 6.3$ Hz, 6H, $\text{OCH}(\text{CH}_3)_2$), 5.44 (sep, $J = 6.3$ Hz, 1H, $\text{OCH}(\text{CH}_3)_2$). ^{13}C NMR (400 MHz, D_2O) δ ppm: 20.71 ($\text{OCH}(\text{CH}_3)_2$), 77.38 ($\text{OCH}(\text{CH}_3)_2$), 231.98 (S_2CO).

6.4.3.2.3 Synthesis of $[\text{KS}_2\text{CO}(\text{CH}_2)_2\text{OCH}_3]$

Potassium hydroxide (11.22 g, 0.20 mol) was dissolved in 2-methoxyethanol (75 ml) and the reactors were stirred for 6 h at $0\text{ }^\circ\text{C}$, before a solution of carbon disulfide (15.23 g, 12 ml, 0.20 mol) in 2-methoxyethanol (25 ml) was added dropwise to the reaction, resulting in a clear yellow solution. $[\text{K}(\text{S}_2\text{CO}(\text{CH}_2)_2\text{OCH}_3)]$ was isolated from solution by the addition of THF

(100 ml) and shaking the mixture for 15 min. The yellow solid product was dried and recrystallized from 2-methoxyethanol to give $[\text{K}(\text{S}_2\text{CO}(\text{CH}_2)_2\text{OCH}_3)]$ (19.8g, 52.1 % yield). M.p. = 216 - 219 °C. Calc. for $\text{C}_4\text{H}_7\text{KO}_2\text{S}_2$ (%): C 25.3, H 3.71, S 33.6, K 20.6; found: C 25.5, H 3.79, S 33.5, K 20.8. FT-IR (cm^{-1}): 2935 (w), 2888 (w), 1442 (m), 1445 (w), 1230 (m), 1134 (m), 1099 (m), 1066 (s), 1018 (m), 844.3 (w), 676.7 (m), 532.5 (m). ^1H NMR (400 MHz, D_2O) δ (ppm) = 3.35 (s, 3H, OCH_3), 3.72 (t, $J = 4.5$ Hz, 2H, $\text{CH}_2\text{CH}_2\text{O}$), 4.50 (t, $J = 4.3$ Hz, 2H, $\text{CH}_2\text{CH}_2\text{O}$). ^{13}C NMR (400 MHz, D_2O) δ ppm: 58.15 (OCH_3), 70.18 ($\text{CH}_2\text{CH}_2\text{O}$), 72.09 ($\text{CH}_2\text{CH}_2\text{O}$), 232.52 (S_2CO).

6.4.3.2.4 Synthesis of $[(\text{PPh}_3)_2\text{Cu}(\text{S}_2\text{CO}(\text{CH}_2)_2\text{OCH}_3)]$ (3)

A solution of $[\text{K}(\text{S}_2\text{CO}(\text{CH}_2)_2\text{OCH}_3)]$ (0.76 g, 4.0 mmol) in chloroform (40 ml) was added to a solution of triphenylphosphine (2.09 g, 8.0 mmol) and CuCl (0.40 g, 4.0 mmol) in the same amount of chloroform. A white precipitate was obtained after continuous stirring for 1 h at room temperature. The solution was filtered to obtain a clear yellow solution. Cooling the yellow solution to -20 °C gave yellow crystals of (O-2-methoxyethanol-dithiocarbomato) copper (I) triphenyl-phosphine. (2.03 g, 67.79% yield). M.p. = 139-143 °C. Calc. for $\text{C}_{40}\text{H}_{37}\text{CuO}_2\text{P}_2\text{S}_2$ (%): C 64.98, H 5.05, S 8.66, P 8.39, Cu 8.60; found: C 64.54, H 4.99, S 8.39, P 8.01, Cu 8.25. FT-IR (cm^{-1}): 2876 (w), 1478 (m), 1432 (m), 1235 (w), 1170 (m), 1094 (s), 1065(m), 851 (w), 740 (m), 691 (s), 618 (w). ^1H NMR (400 MHz, CDCl_3) δ ppm: 3.42 (s, 3H, OCH_3), 3.69 (t, $J = 5.2$ Hz, 2H, $\text{CH}_2\text{CH}_2\text{O}$), 4.52 (t, $J = 5$ Hz, 2H, $\text{CH}_2\text{CH}_2\text{O}$), 7.05-7.47 (m, 30H, Ph). ^{13}C NMR (400 MHz, CDCl_3) δ ppm: 59.15 (OCH_3), 70.24 ($\text{CH}_2\text{CH}_2\text{O}$), 71.90 ($\text{CH}_2\text{CH}_2\text{O}$), 128.40 (Ph), 129.46 (Ph), 133.66 (Ph), 133.94 (Ph), 226.84 (S_2CO).

6.4.3.3 Preparation of thin films

For the deposition of the CaCu_2S_2 thin films, The precursor was prepared by sequentially dissolving (0.118, 0.00016 mol) $[(\text{PPh}_3)_2\text{Cu}(\text{S}_2\text{CO}(\text{CH}_2)_2\text{OMe})]$ and (0.0392 g, 0.00008 mol) $[\text{Ca}(\text{S}_2\text{CO}^i\text{Pr})_2(^i\text{PrOH})_3]$ in 4 mL dry THF under an N_2

atmosphere in glove box. A clear yellow solution was obtained, precursors were directly coated on glass substrates, which were cleaned by ultra-sonication for 15 min in water and then 15 min in acetone. The prepared precursors were spin-coated at a spinning speed of 1000 rpm for CaCu_2S_2 followed by immediate annealing for 1 h at 300 °C. CaS , BaS , CuS , CaCu_2S_2 , β - BaCu_2S_2 , and β - BaCu_4S_3 were deposited by the same method. The experimental conditions are summarised in table 6.1.

6.4.4 Results and discussion

An assessment of the thermogravimetric profile of **1** and **2** (Figure 6.2) suggests that the complexes breakdown cleanly in the region of 100-200 °C and 180-200 °C respectively. The final weight of the residue is in good agreement with the formation of CaS , BaS and CuS respectively. The suggested breakdown pathway is shown in Scheme 1.

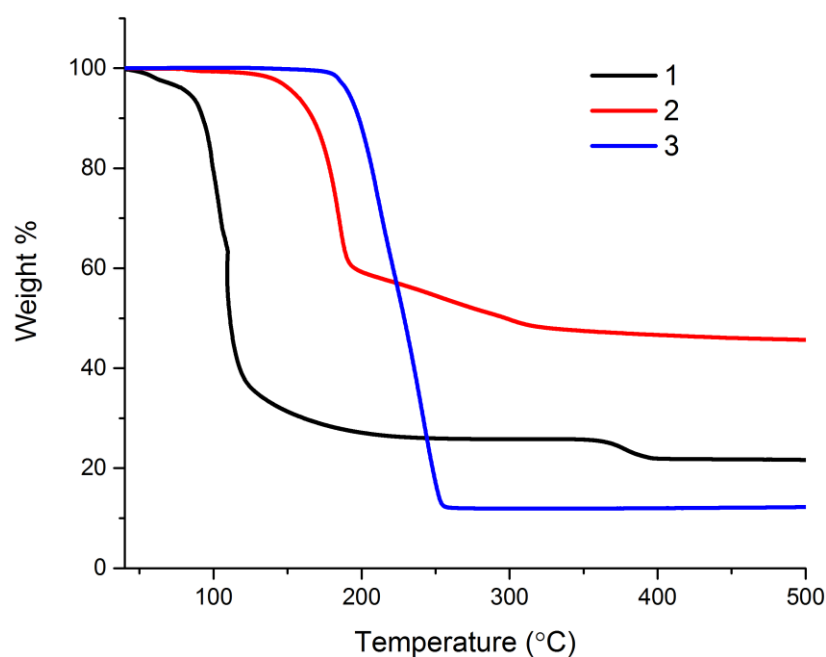

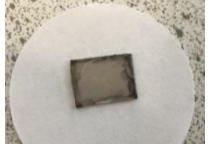
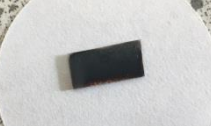
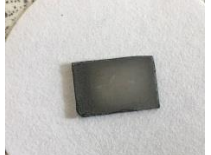
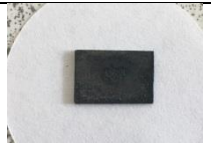
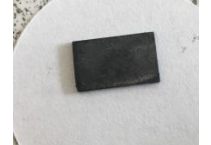


Figure 6.2. Thermogravimetric analysis of $[\text{Ca}(\text{S}_2\text{CO}^i\text{Pr})_2(^i\text{PrOH})_3]$ (**1**, black), $[\text{Ba}(\text{S}_2\text{CO}^i\text{Pr})_2]$ (**2**, red) and $[(\text{PPh}_3)_2\text{Cu}(\text{S}_2\text{CO}(\text{CH}_2)_2\text{OMe})]$ (**3**, blue).

Table 6.1. The experimental conditions of preparation of CaS, BaS, CuS, CaCu₂S₂, β- BaCu₂S₂, and β - BaCu₄S₃ films heated at different temperatures for 1 h. The picture of β - BaCu₂S₂ is obtained for the film deposited onto glass substrate and heated at 550 °C.

Compound	Complex(1) (g, mol)	Complex (2) (g, mol)	Complex (3) (g, mol)	THF (ml)	R.P.M	Temperature (°C)	Pictures of films
CaS	(0.245, 0.0005)			4	3000	300	
BaS		(0.2, 0.0005)		4	1200	550	
CuS			(0.147, 0.0002)	4	1000	300	
CaCu ₂ S ₂	(0.0392, 0.00008)		(0.118, 0.00016)	4	1000	300	
β- BaCu ₂ S ₂		(0.0366, 0.00009)	(0.132, 0.00018)	4	1000	550	
β- BaCu ₄ S ₃		(0.0126, 0.0000311)	(0.0916, 0.000124)	4	1000	580	

Thin films of the metal sulfides were prepared by spin - coating a solution of the precursor xanthates in dry THF onto a clean glass slide, followed by thermolysis in a tube furnace at different temperatures under an inert nitrogen atmosphere (Table 6.1).

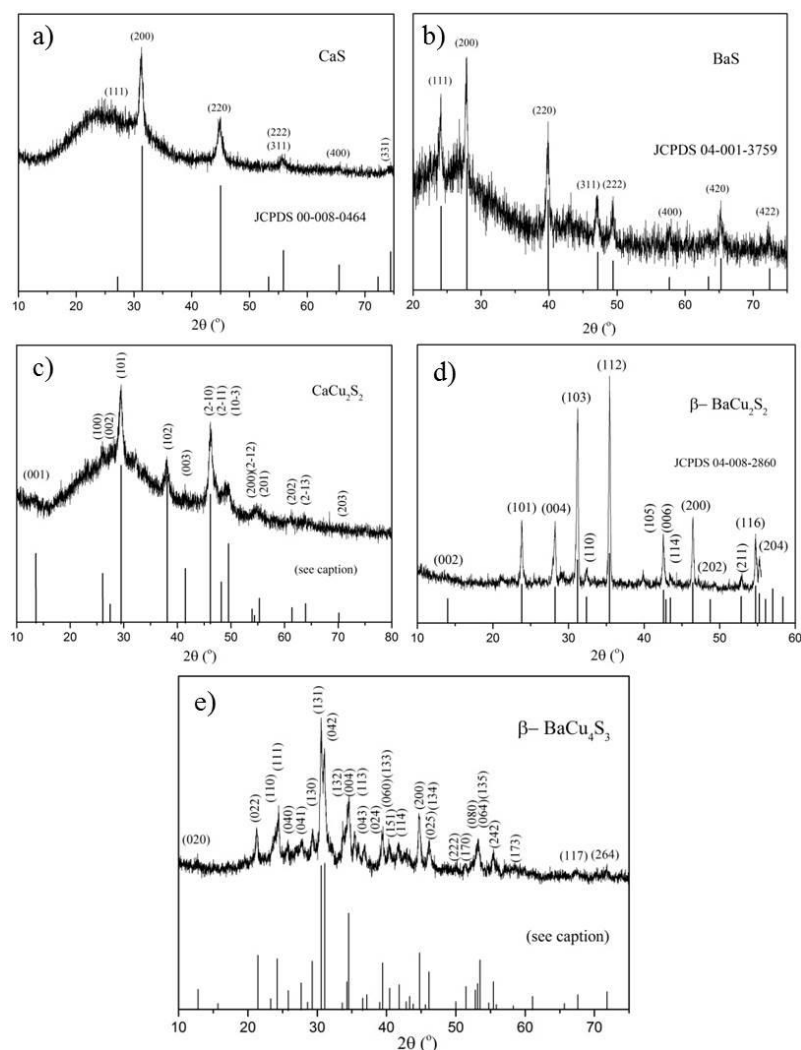


Figure 6.3 The p-XRD patterns of the thin films. (a) cubic CaS and reference pattern JCPDS 00-08-0464, (b) cubic BaS and reference pattern JCPDS 04-001-3759, (c) hexagonal CaCu_2S_2 and reference pattern generated from Purdy's work,¹⁶ (d) β - BaCu_2S_2 with reference pattern JCPDS 04-008-2860 and (e) orthorhombic β - BaCu_4S_3 and reference pattern generated from the work of Iglesias *et al.*³³

1 decomposes cleanly at 300 °C to form cubic CaS, with the powder X-ray diffraction (p-XRD) pattern agreeing well with the phase formed being that of oldhamite (JCPDS 00-08-0464, Figure 6.3a). The unit cell of $a = 5.699(2)$ Å is a close match to the literature ($a = 5.694$ Å). The decomposition of the barium xanthate **2** requires higher temperatures to form a pure phase. At 550 °C, cubic BaS is formed (Figure 6.3b) - the unit cell is $a = 6.392(6)$ Å, which is a good match with the literature ($a = 6.388$ Å). CaS and BaS both adopt the cubic structure of NaCl.

In order to generate the mixed alkali/transition metal compounds the appropriate molar ratios of **1/2** and **3** were dissolved in dry THF and spin coated onto glass slides and annealed in a N₂ atmosphere. For the Ca-Cu system an annealing temperature of 300 °C was used. The p-XRD pattern of the obtain films matches that of hexagonal CaCu₂S₂ as reported by Purdy¹⁶ (Figure 6.3c) and the unit cell parameters of $a = 3.949(3) \text{ \AA}$, $c = 6.520(3) \text{ \AA}$ are consistent with that data.¹⁶ In this structure, planes of a double layer, puckered six member Cu-S rings are separated by Ca²⁺ (Figure 6.1a). Energy-dispersive X-ray spectroscopy (EDX) analysis gives a formula consistent with the formula of CaCu₂S₂ and EDX mapping reveals a homogenous dispersion of the elements (Figure S6.7 and Table 6.2).

Unlike CaCu₂S₂, which exists as only one phase, there are two phases for BaCu₂S₂: an α (orthorhombic) and a β (tetragonal) phase. We find at 550 °C, the temperature required to breakdown **2**, that we form a mixture of α - and β -BaCu₂S₂ from a 2:1 ratio of **3:2** (ESI Figure S6.5). Increasing the temperature to 650 °C leads to a loss of the orthorhombic phase, leaving pure tetragonal β -BaCu₂S₂ (Figure 6.3d, JCPDS 04-008-2860) with a unit cell of $a = 3.907(3) \text{ \AA}$, $c = 12.648(3) \text{ \AA}$ (literature values: $a = 3.907 \text{ \AA}$, $c = 12.640 \text{ \AA}$). Note that in this case we switched to a silicon substrate to reflect the high temperature of deposition. Compositional analysis through EDX indicates an appropriate ratio of Ba:Cu:S, which is evenly distributed across the sample (Figure S6.8 and Table 6.2).

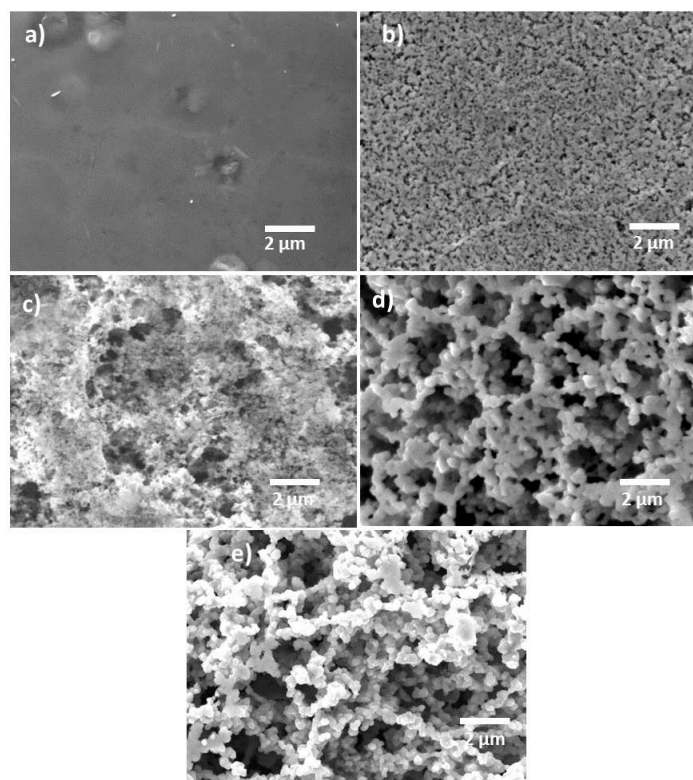


Figure 6.4. SEM images of thin films of (a) CaS, (b) BaS, (c) hexagonal CaCu₂S₂ (d) β -BaCu₂S₂ and (e) β -BaCu₄S₃.

Table 6.2. Compositional analysis of films determined by EDX.

Compound	Ca (%)	Ba (%)	Cu (%)	S (%)
CaS	49.9			50.1
BaS		50.1		49.9
CuS			63.4	36.6
CaCu ₂ S ₂	19.6		42.8	37.6
β - BaCu ₂ S ₂		22.2	39.9	37.9
β - BaCu ₄ S ₃		12.1	49.5	38.4

CaCu₂S₂ is the only known calcium copper sulfide, but for the barium family there is another: BaCu₄S₃. This also has an α and β phase, though in this case they are both orthorhombic.³⁴ The structure consists of BaS₆ triangular face

sharing trigonal prisms (Figure 6.1c). The key difference between the α and β phases is that S caps a rectangular face in β - BaCu₄S₃ and a triangular face in β - BaCu₄S₃.^{33, 34} Previous work has focused on the synthesis of these materials through a vapour transport method, and Iglesias *et al.* noted an α to β phase transition at $640 \pm 10^\circ\text{C}$.^{33, 34} We have successfully synthesised the high temperature phase, β -BaCu₄S₃, at 580°C on glass (Figure 6.3e). The unit cell of $a = 4.053(1) \text{ \AA}$, $b = 13.848(3) \text{ \AA}$ and $c = 10.377(2) \text{ \AA}$ agrees with the literature values of $a = 4.058 \text{ \AA}$, $b = 13.863 \text{ \AA}$ and $c = 10.373 \text{ \AA}$ and the EDX values are consistent with the target formula (Figure S6.9 and Table 6.2).

There is little difference in the morphology of the films that can be discerned by scanning electron microscopy (SEM), other than that of CaS (Figure 6.4). The alkali metal copper sulfides consist of conjoined spheres 0.1-0.5 μm in diameter, whereas CaS appears to be much smoother. Optical images of the films (Table 6.1) indicate that the CaS/BaS films are a lighter brown colour, whilst the others are a dark black.

6.4.5 Conclusion

We have presented a simple, efficient route to three complex alkali metal-copper sulfides; CaCu₂S₂, β - BaCu₂S₂ and β -BaCu₄S₃. This has been achieved through a melt reaction of calcium isopropylxanthate and the novel compounds barium isopropylxanthate and bis(triphenylphosphine)copper 2-methoxyethylxanthate.

6.4.6 Acknowledgements

The authors would like to acknowledge the Iraqi Culture Attaché in London for financial support (M.A.S.) and the EPSRC (Doctoral Prize for P.D.M., grant EP/M507969/1). Some of the equipment used in this study were provided by the Engineering and Physical Sciences Research Council (Core Capability in Chemistry, EPSRC grant number EP/K039547/1).

6.4.7 Reference

1. P. D. Matthews, P. D. McNaughter, D. J. Lewis and P. O'Brien, *Chem. Sci.*, 2017, **8**, 4177-4187.
2. K. Woo, Y. Kim and J. Moon, *Energy Environ. Sci.*, 2012, **5**, 5340-5345.
3. Y. C. Wang, D. Y. Wang, Y. T. Jiang, H. A. Chen, C. C. Chen, K. C. Ho, H. L. Chou and C. W. Chen, *Angew. Chem. Int. Ed.*, 2013, **52**, 6694-6698.
4. D. J. Lewis, P. Kevin, O. Bakr, C. A. Muryn, M. A. Malik and P. O'Brien, *Inorg. Chem. Front.*, 2014, **1**, 577-598.
5. A. A. Tedstone, D. J. Lewis and P. O'Brien, *Chem. Mater.*, 2016, **28**, 1965-1974.
6. Q. H. Wang, K. Kalantar-Zadeh, A. Kis, J. N. Coleman and M. S. Strano, *Nat. Nanotechnol.*, 2012, **7**, 699-712.
7. D. B. Mitzi, *Adv. Mater.*, 2009, **21**, 3141-3158.
8. S.-L. Li, K. Tsukagoshi, E. Orgiu and P. Samorì, *Chem. Soc. Rev.*, 2016, **45**, 118-151.
9. S.-M. Kuo, Y.-M. Chang, I. Chung, J.-I. Jang, B.-H. Her, S.-H. Yang, J. B. Ketterson, M. G. Kanatzidis and K.-F. Hsu, *Chem. Mater.*, 2013, **25**, 2427-2433.
10. K. Feng, W. Yin, Z. Lin, J. Yao and Y. Wu, *Inorg. Chem.*, 2013, **52**, 11503-11508.
11. A. Mesbah, E. Ringe, S. b. Lebègue, R. P. Van Duyne and J. A. Ibers, *Inorg. Chem.*, 2012, **51**, 13390-13395.
12. A. Mesbah, S. Lebègue, J. M. Klingsporn, W. Stojko, R. P. Van Duyne and J. A. Ibers, *J. Solid State Chem.*, 2013, **200**, 349-353.
13. A. Mesbah, J. Prakash and J. A. Ibers, *Dalton Trans.*, 2016, **45**, 16067-16080.
14. M.-C. Chen, L.-M. Wu, H. Lin, L.-J. Zhou and L. Chen, *J. Am. Chem. Soc.*, 2012, **134**, 6058-6060.
15. A. Assoud, N. Soheilnia and H. Kleinke, *Chem. Mater.*, 2005, **17**, 2255-2261.
16. A. P. Purdy, *Chem. Mater.*, 1998, **10**, 692-694.
17. Z. Ma, F. Weng, Q. Wang, Q. Tang, G. Zhang, C. Zheng, R. P. Han and F. Huang, *RSC Adv.*, 2014, **4**, 28937-28940.

18. J. Huster and W. Bronger, *Z. Anorg. Allg. Chem.*, 1999, **625**, 2033-2040.
19. M. Afzaal, C. L. Rosenberg, M. A. Malik, A. J. White and P. O'Brien, *New J. Chem.*, 2011, **35**, 2773-2780.
20. P. S. Nair, T. Radhakrishnan, N. Revaprasadu, G. A. Kolawole and P. O'Brien, *Polyhedron*, 2003, **22**, 3129-3135.
21. M. Afzaal, M. A. Malik and P. O'Brien, *J. Mater. Chem.*, 2010, **20**, 4031-4040.
22. E. Lewis, S. Haigh and P. O'Brien, *J. Mater. Chem. A*, 2014, **2**, 570-580.
23. E. A. Lewis, P. D. McNaughter, Z. Yin, Y. Chen, J. R. Brent, S. A. Saah, J. Raftery, J. A. Awudza, M. A. Malik and P. O'Brien, *Chem. Mater.*, 2015, **27**, 2127-2136.
24. P. D. McNaughter, S. A. Saah, M. Akhtar, K. Abdulwahab, M. A. Malik, J. Raftery, J. A. Awudza and P. O'Brien, *Dalton Trans.*, 2016, **45**, 16345-16353.
25. P. D. Matthews, M. Akhtar, M. A. Malik, N. Revaprasadu and P. O'Brien, *Dalton Trans.*, 2016, **45**, 18803-18812.
26. N. Alam, M. S. Hill, G. Kociok-Köhn, M. Zeller, M. Mazhar and K. C. Molloy, *Chem. Mater.*, 2008, **20**, 6157-6162.
27. J. M. Clark, G. Kociok-Köhn, N. Harnett, M. Hill, R. Hill, K. C. Molloy, H. Saponia, D. Stanton and A. Sudlow, *Dalton Trans.*, 2011, **40**, 6893-6900.
28. T. Lutz, A. MacLachlan, A. Sudlow, J. Nelson, M. S. Hill, K. C. Molloy and S. A. Haque, *Phys. Chem. Chem. Phys.*, 2012, **14**, 16192-16196.
29. T. Rath, A. J. MacLachlan, M. D. Brown and S. A. Haque, *J. Mater. Chem. A*, 2015, **3**, 24155-24162.
30. M. A. Buckingham, A. L. Catherall, M. S. Hill, A. L. Johnson and J. D. Parish, *Cryst. Growth Des.*, 2017, **17**, 907-912.
31. I. Bezougli, *Dalton Trans.*, 1998, 2671-2678.
32. M. Al-Shakban, P. D. Matthews, G. Deogratias, P. D. McNaughter, J. Raftery, I. Vitorica-Yrezabal, E. B. Mubofu and P. O'Brien, *Inorg. Chem.*, 2017, **56**, 9247-9254.
33. J. Iglesias, K. Pachali and H. Steinfink, *Mater. Res. Bull.*, 1972, **7**, 1247-1258.
34. Z. Eliezer and H. Steinfink, *Mater. Res. Bull.*, 1976, **11**, 385-388.

6.4.8 Supporting information

Table S6.3. Lattice parameters of the thin films as determined by p-XRD.

Compound	structure	Lattice constant (Å)	
		Experimental	Literature
CaS	cubic	a = 5.699 (2)	a = 5.694
CaCu ₂ S ₂	Hexagonal	a = 3.949 (3) c = 6.520 (3)	a = 3.940 c = 6.523
BaS	cubic	a = 6.392(6)	a = 6.388
BaCu ₂ S ₂ at 550 °C (mixture of α and β)	Orthorhombic	a = 9.215 (1) b = 4.059 (1) c = 10.387 (1)	a = 9.273 b = 4.053 c = 10.380
	Tetragonal	a = 3.907(7) b = 3.907(7) c = 12.648(7)	a = 3.907 b = 3.907 c = 12.640
β - BaCu ₂ S ₂	Tetragonal	a = 3.907 (3) b = 3.907 (3) c = 12.648(3)	a = 3.907 b = 3.907 c = 12.640
β - BaCu ₄ S ₃	Orthorhombic	a = 4.053(1) b = 13.848(3) c = 10.377(2)	a = 4.058 b = 13.863 c = 10.373

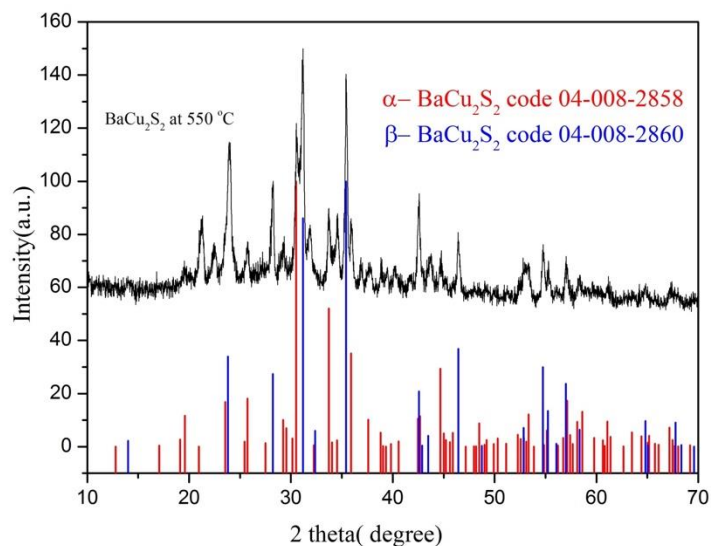


Figure S6.5 p-XRD of BaCu₂S₂ showing the mixed α (orthorhombic) and β (tetragonal) phases present in films prepared at 550 °C.

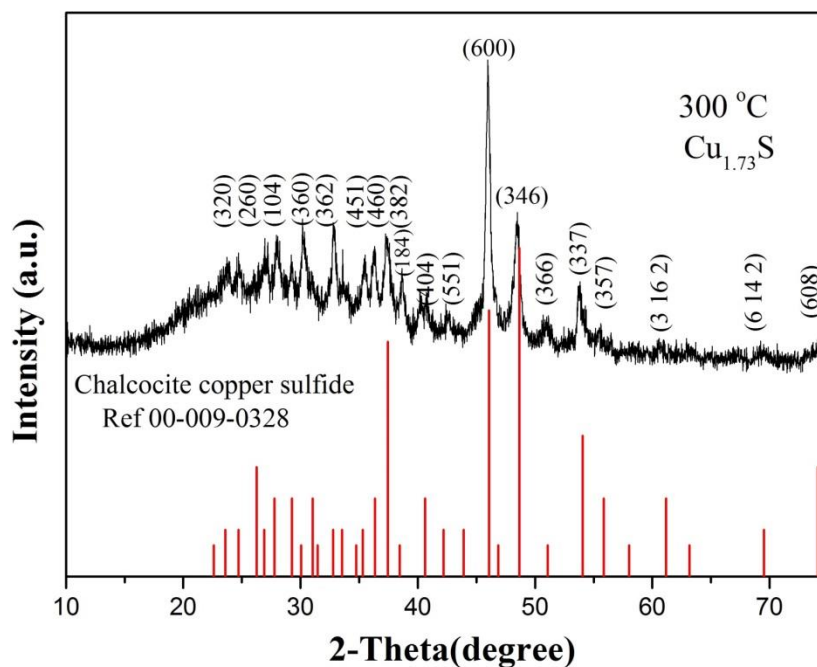


Figure S6.6. p-XRD of Cu₂S showing the chalcocite copper sulfide phase present in film prepared at 300 °C.

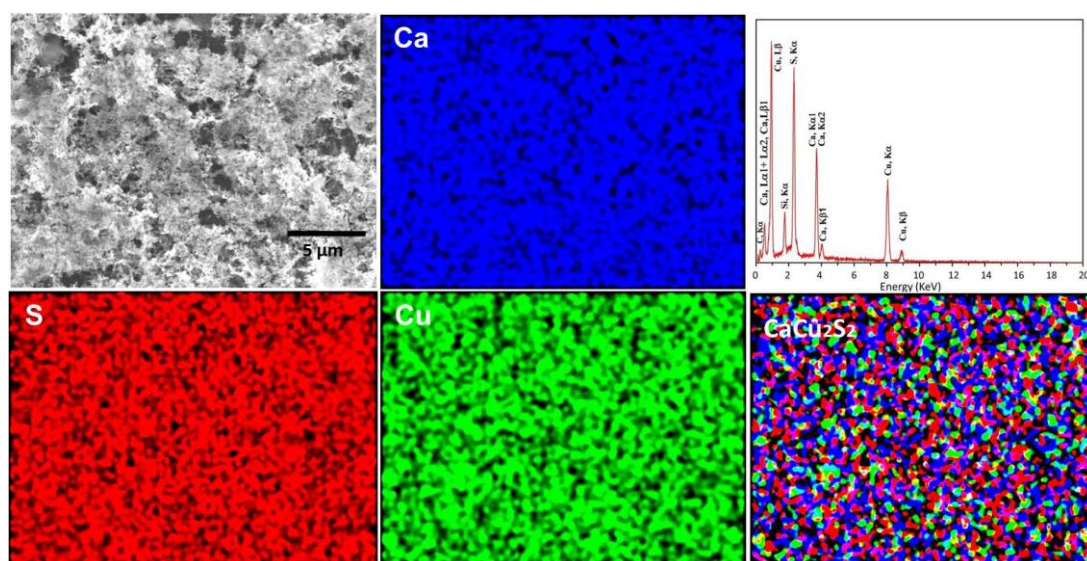


Figure S6.7. EDX elemental mapping for CaCu_2S_2 showing a homogeneous distribution of the elements.

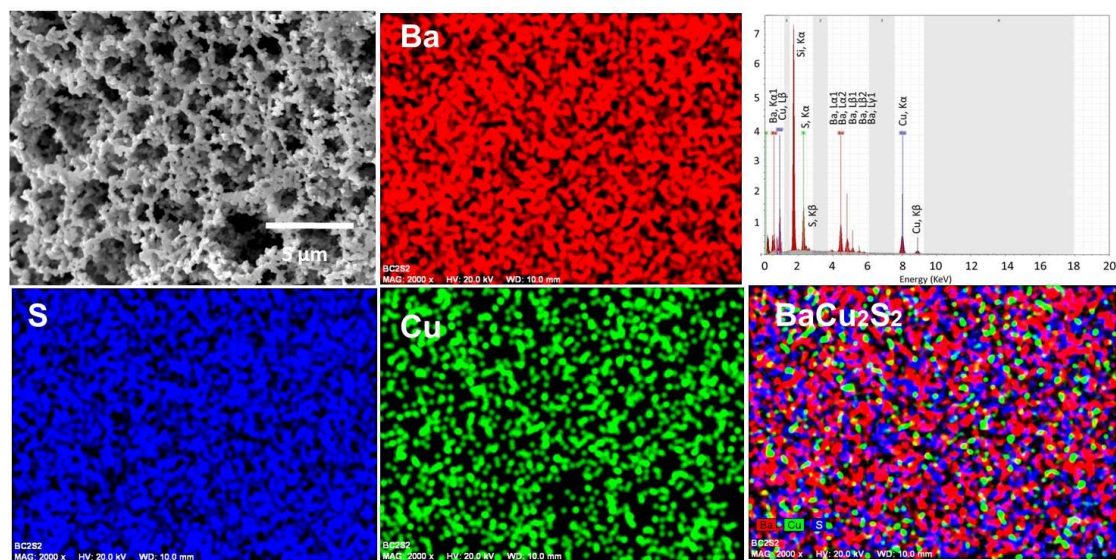


Figure S6.8. EDX elemental mapping for BaCu_2S_2 showing a homogeneous distribution of the elements.

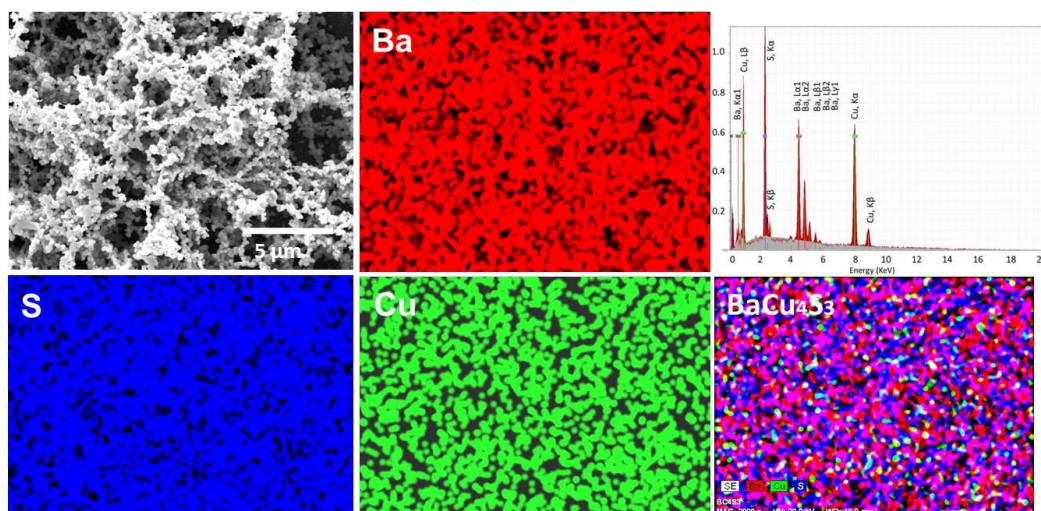


Figure S6.9. EDX elemental mapping for BaCu_4S_3 showing a homogeneous distribution of the elements.

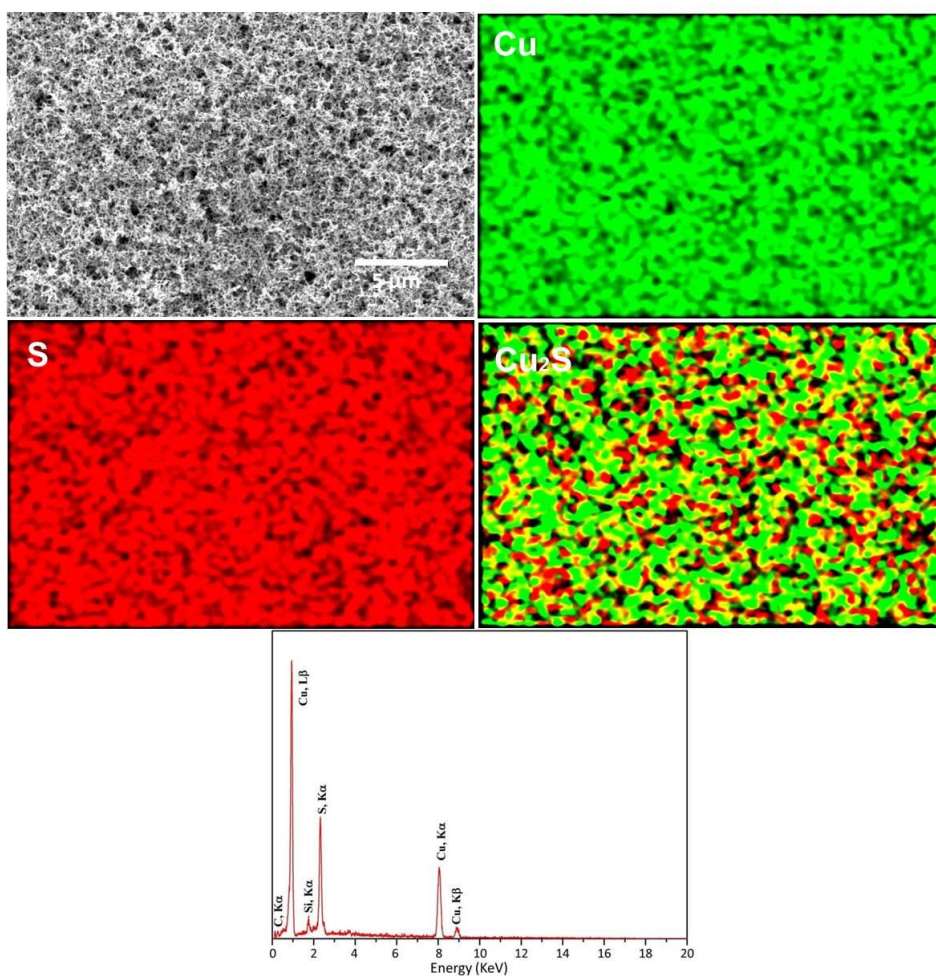


Figure S6.10. EDX elemental mapping for Cu_2S showing a homogeneous distribution of the elements

Chapter 7 The synthesis and characterization of $\text{Cu}_2\text{ZnSnS}_4$ thin films from melt reactions using xanthate precursors

7.1 Introduction

Copper zinc tin sulfide ($\text{Cu}_2\text{ZnSnS}_4$, CZTS) is a favourable material for use as an absorber layer in photovoltaic cells due to low toxicity and a large absorption coefficient ($\alpha \geq 10^4 \text{ cm}^{-1}$). The performance of CZTS absorber layer is commensurate with silicon which makes it feasible to absorb light across the visible spectrum.¹ CZTS thin films have been prepared using several techniques such as vacuum deposition techniques which has the advantage of easily controlling chemical composition in thin films, pulsed laser deposition technique, chemical vapor deposition (CVD), co-sputtering continued with sulfuration from vapor phase method, chemical bath deposition, successive ionic layer adsorption and reaction (SILAR) method, and solvothermal treatment of layered elemental copper/zinc/tin film with sulfur powder.^{2,3}

The synthesis and characterization of $\text{M}(\text{S}_2\text{COR})_2$, $\text{M}(\text{S}_2\text{COR})_4$ and $(\text{R}'_3\text{P})_2\text{CuS}_2\text{COR}$ [$\text{R}' = \text{Ph}$, $\text{R} = \text{Et}$, ^nBu ; $\text{M} = \text{Cu}$, Zn , Sn complexes are described. By the coating of $(\text{Ph}_3\text{P})_2\text{CuS}_2\text{COEt}$, $[\text{Zn}(\text{S}_2\text{CO}^n\text{Bu})_2]$ and $[\text{Sn}(\text{S}_2\text{COEt})_2]$ precursors, the temperature-dependent phase of $\text{Cu}_2\text{ZnSnS}_4$ films were prepared successfully. The X-ray diffraction patterns and Raman spectra of films annealed between 375 and 475 °C showed that films had a tetragonal structure with space group $\Gamma 42m$. The resistivity, carrier concentration, mobility and Hall coefficient of films heated at 225, 375 and 450 °C were calculated by the four probes method. The conduction type of film was p-type.

7.2 Author distribution

In this article, I synthesised and characterised the xanthate complexes via IR, elemental analysis and TGA. The experimental work to produce $\text{Cu}_2\text{ZnSnS}_4$ thin films was carried out by me, I characterised the films via XRD, Raman spectroscopy, TEM, SEM and EDX. The electrical properties were measured by Yuekun Wang and I calculated the Hall coefficient, conductivity and sheet resistance. Peter D. Matthews and Nicky Savjani checked the characterization

of complexes and materials. The project was provided by Paul O'Brien, who edited the draft. The experimental work was done in the laboratory of Paul O'Brien

7.3 Reference

1. M. A. Green, K. Emery, Y. Hishikawa, W. Warta and E. D. Dunlop, *Prog. Photovolt. Res. Appl.*, 2015, **23**, 1-9.
2. M. Suryawanshi, G. Agawane, S. Bhosale, S. Shin, P. Patil, J. Kim and A. Moholkar, *Mater. Technol.*, 2013, **28**, 98-109.
3. S. Delbos, *EPJ Photovoltaics*, 2012, **3**, 35004.

7.4 The synthesis and characterization of $\text{Cu}_2\text{ZnSnS}_4$ thin films from melt reactions using xanthate precursors

Mundher Al-Shakban¹, Peter D. Matthews², Nicky Savjani², Xiang L.

Zhong¹, Yuekun Wang³, Mohamed Missous³, and Paul O'Brien^{1,2},

¹ *School of Materials, University of Manchester, Oxford Road, Manchester M13 9PL, UK*

² *School of Chemistry, University of Manchester, Oxford Road, Manchester M13 9PL, UK*

³ *School of Electrical and Electronic Engineering, University of Manchester, Oxford Road, Manchester M13 9PL, UK*

7.4.1 Abstract

Kesterite, $\text{Cu}_2\text{ZnSnS}_4$ (CZTS), is a promising absorber layer for use in photovoltaic cells. We report the use of copper, zinc and tin xanthates in melt reactions to produce $\text{Cu}_2\text{ZnSnS}_4$ (CZTS) thin films. The phase of the as-produced CZTS is dependent on decomposition temperature. X-ray diffraction patterns and Raman spectra show that films annealed between 375 and 475 °C are tetragonal, while at temperatures < 375 °C hexagonal material was obtained. The electrical parameters of the CZTS films have also been determined. The conduction of all films was p-type, while the other parameters differ for the hexagonal and tetragonal materials: resistivity (27.1 vs 1.23 Ω cm), carrier concentration (2.65×10^{15} vs 4.55×10^{17} cm^{-3}) and mobility (87.1 vs 11.1 $\text{cm}^2 \text{V}^{-1} \text{s}^{-1}$). The Hall coefficients were 2.36×10^3 versus 13.7 $\text{cm}^3 \text{C}^{-1}$.

7.4.2 Introduction

Copper zinc tin sulfide ($\text{Cu}_2\text{ZnSnS}_4$, CZTS) is a promising absorber layer for use in photovoltaic cells and is composed of low toxicity¹⁻³ and earth-abundant elements.⁴⁻⁶ It has a large absorption coefficient ($\alpha \geq 10^4 \text{ cm}^{-1}$) and a direct band gap of about 1.45 eV.⁷⁻¹⁰ The performance of CZTS absorber layers is still less than that of silicon,¹¹ which is the current industrial standard; however, unlike silicon, it has the advantage of a direct and tunable band gap.¹²

CZTS thin films have been prepared using several techniques, including: chemical vapor deposition (CVD),¹³ co-sputtering followed by sulfurization from the vapor phase,¹⁴ chemical bath deposition (CBD),¹⁵ successive ionic layer adsorption and reaction (SILAR)¹⁶ and solvothermal treatment of a layered elemental (copper, zinc and tin) film with sulfur powder.¹⁷ However, there are two major problems with routes that involve the deposition of the individual components (either as metal M or M_xS_y) followed by high-temperature annealing in a sulfur atmosphere. The first issue is the loss of volatile components such as SnS. The photoelectrical performance of CZTS is highly dependent on good stoichiometric control, and such evaporation can make it difficult to control the composition of the target phase.¹⁸⁻²² The second issue is the stability of the Mo electrode that the CZTS is often deposited on; this can react with sulfur to form a MoS_2 layer between the electrode and the CZTS, resulting in a dramatic decrease in performance of the photovoltaic device.^{23, 24} These two problems indicate a requirement for a new synthetic route to CZTS that avoids higher temperatures.

The Cu_2ZnSnS_4 unit cell is based on zinc blende: It is related to the chalcopyrite structure of $CuInS_2$ by changing indium for zinc and tin, with the metals in tetrahedral coordination.²⁵ There are three different phases of CZTS: kesterite, stannite and primitive mixed CuAu-like structure (PMCA).²⁶⁻²⁸ Zunger *et al.*^{29, 30} have established that strain energy is responsible for the stability of the CZTS crystal structure. They found that for large lattice mismatches, the kesterite structure has a lower strain energy, which means that chalcopyrite is more stable than the CuAu-like structure; as a result, the stability of kesterite is higher than that of stannite and PMCA, but there is little difference in strain energy between the kesterite and stannite structures (≈ 3 meV/atom).

Walsh *et al.* have performed calculations on the total energy of CZTS and other quaternary semiconductors of the form $I_2-II-IV-VI_4$ (I=Cu, Ag; II=Zn, Cd; IV=Si, Ge, Sn; VI=S, Se). They found that the kesterite structure is thermodynamically more stable than stannite, wurtzite-kesterite and wurtzite-stannite.³¹⁻³³ In stannite, (Cu/Fe)Sn layers alternate with Cu_2 layers in the unit cell, whereas for kesterite CuSn alternates with CuZn. The similar lattice constants and total energy values for

kesterite and stannite CZTS mean that there is often the possibility of both phases existing together depending on the methods used to prepare the material.³⁴

A big disadvantage of CZTS in photovoltaic applications is its ability to crystallize in these different forms. Schorr *et al.*³⁵ synthesized tetragonal CZTS at 860 °C and the cubic phase of CZTS at temperatures 885 °C by the solid-state reaction of the pure elements in sealed evacuated silica tubes. Brandl *et al.*³⁶ synthesized CZTS nanoparticles in a disordered cubic structure by the hot injection of CuCl₂, Zn(OAc)₂ and SnCl₂ with S in oleylamine at 225 °C, and they found that a disordered cubic phase changed to the tetragonal CZTS phase at 275 °C. Cattley *et al.*³⁷ have also observed a temperature dependent phase change from tetragonal kesterite to hexagonal wurtzite during their synthesis of quantum dots from Cu(acetylacetonate)₂, Zn(OAc)₂, SnCl₄ and S(SiMe₃)₂. Nakayama *et al.*³⁸ first successfully prepared stannite CZTS thin film via spray pyrolysis, and its electronic properties have been theoretically assessed by Marques *et al.*³⁹ and Scarpulla *et al.*⁴⁰ The development of a method for controlling the phase of the obtained CZTS would be a major step toward commercializing CZTS. We have previously reported the synthesis of CZTS and Cu₂Zn_{1-x}Fe_xSnS₄ nanoparticles and thin films from the decomposition of dithiocarbamate single-source precursors (SSPs).⁴¹⁻⁴³

Recently xanthates have been used as SSPs to metal sulfide nanocrystals.⁴⁴⁻⁴⁹ They have the general chemical formula [M(S₂COR)_n], where R is an alkyl group. Xanthates are good precursors to deposit metal sulfide thin films as the preformed M-S bonds make the conversion to a metal sulfide film straightforward.^{50, 51} They can also decompose at lower temperatures compared to other precursors, and they are usually held to decompose by the Chugaev elimination reaction.⁵² A range of xanthates and a parallel range of dithiocarbamates have been synthesized by Molloy and co-workers as sources of metal sulfides. They studied thermal decomposition profiles by thermogravimetric analysis (TGA), and their experiments show that metal xanthates are viable precursors for Cu₂ZnSnS₄, in both thin film and nanoparticulate form.⁵³

In this report, we discuss the synthesis of a range of copper, zinc and tin *O*-ethyl and *O*-*n*-butylxanthates and assessed their suitability as precursors to CZTS. On the basis

of decomposition properties $[(\text{Ph}_3\text{P})_2\text{CuS}_2\text{COEt}]$, $[\text{Zn}(\text{S}_2\text{CO}^n\text{Bu})_2]$ and $[\text{Sn}(\text{S}_2\text{COEt})_2]$ have been used as coating precursors for the production of $\text{Cu}_2\text{ZnSnS}_4$ films on glass. We focus on both the annealing temperature and the role of the xanthate ligand in the decomposition process for the potential in control of the structural and electronic properties of the CZTS films produced. The CZTS films were analyzed by powder X-ray diffraction (p-XRD), Raman spectroscopy, scanning electron microscopy (SEM) and transmission electron microscopy (TEM). We investigated the electrical properties using the van der Pauw method,⁵⁴ and the resistivity of the films was calculated from the Hall voltage and sheet resistance.

7.4.3 Experimental

All chemicals, with the exception of tin(II) chloride (Alfa Aesar), were purchased from Sigma-Aldrich and were used as received. Elemental analysis (EA) and thermogravimetric analysis (TGA) were carried out by the Microelemental Analysis service at the University of Manchester. EA was performed using a Flash 2000 Thermo Scientific elemental analyzer, and TGA data were obtained with Mettler-Toledo TGA/ DSC1 star^c system between the range of 30–600 °C at a heating rate of 10 °C min⁻¹ under nitrogen flow. Scanning electron microscopy (SEM) images were obtained using a Philips XL30 FEG, with energy-dispersive X-ray spectroscopy (EDX) data obtained using a DX4 instrument. Samples suitable for transmission electron microscopy (TEM) were prepared by exfoliating thin films in toluene and drop casting the suspension onto holey carbon support grids, which were then air-dried. TEM was performed using Philips CM20 equipped with a LaB₆ source (Figure 7.6a, b) or a FEI Tecnai G2 F30 with Schottky field emitter operated at 300 keV (Figure 7.6c). Powder X-ray diffraction (p-XRD) analyses were carried out using an X'pert diffractometer with a Cu-K α_1 source ($\lambda = 1.54059 \text{ \AA}$), the samples were scanned between 20 and 75°, and the applied voltage was 40 kV and the current 30 mA. Raman spectra were measured using a Renishaw 1000 Micro-Raman System equipped with a 514 nm laser.

7.4.3.1 Synthesis of metal xanthate complexes

7.4.3.1.1 Synthesis of potassium n-butylxanthate ligand

The synthesis of $[\text{K}(\text{S}_2\text{CO}^n\text{Bu})]$ was adapted from a literature procedure.⁵⁵ KOH (5.64 g, 0.10 mol) and $^n\text{BuOH}$ (50 ml) were stirred for 2 h at room temperature, and then, CS_2 (7.73 g, 6.11 ml, 0.10 mol) was added dropwise to the reaction, resulting in an orange solution. The unreacted alcohol was removed in *vacuo*, and the yellow solid product was dried and recrystallized from *n*-butyl alcohol to give $[\text{K}(\text{S}_2\text{CO}^n\text{Bu})]$ (13.45 g, 71.5 mmol, 71.5% yield). MPt: 232–235 °C. Calc. for $\text{C}_5\text{H}_9\text{KOS}_2$ (%): C 31.9, H 4.82, S 34.0, K 21.8; found: C 31.6, H 4.51, S 33.3, K 22.0. FT-IR (cm^{-1}): 2958 (m), 2869 (w), 1461 (m), 1445 (w), 1261 (s), 1149 (m), 1173 (m), 1062 (m), 1014 (m), 747.3 (m), 669.0 (s), 566.2 (s).

7.4.3.1.2 Synthesis of bis(O-ethylxanthato)zinc(II)

$[\text{Zn}(\text{S}_2\text{COEt})_2]$ was synthesized by adapting the literature procedure.⁵⁶ Potassium ethylxanthate (5.00 g, 0.031 mol) was dissolved in deionized water (50 ml), and ZnCl_2 (1.81 g, 0.013 mol) was dissolved in a similar amount of water. The ZnCl_2 solution was slowly added to the KS_2COEt solution and stirred for 30 minutes leading to the formation of a white precipitate. The reaction mixture was then filtered and the white solid product dried to give $[\text{Zn}(\text{S}_2\text{COEt})_2]$ (3.45g, 0.011 mol, 85% yield). MPt: 128-132 °C. Calc. for $\text{C}_6\text{H}_{10}\text{O}_2\text{S}_4\text{Zn}$ (%): C 23.4, H 3.28, S 41.6, Zn 21.3; found: C 23.8, H 3.13, S 41.8, Zn 21.1. FT-IR (cm^{-1}): 2990 (w), 1867 (w), 1189 (s), 1122 (s), 1024 (s), 867.6 (w), 817.1 (w), 657.0 (w).

7.4.3.1.3 Synthesis of bis(O-butylxanthato)zinc(II)

The complex $[\text{Zn}(\text{S}_2\text{CO}^n\text{Bu})_2]$ was synthesized by a similar method to $[\text{Zn}(\text{S}_2\text{COEt})_2]$ using $[\text{K}(\text{S}_2\text{CO}^n\text{Bu})]$ (5.00 g, 0.027 mol) and ZnCl_2 (1.81 g, 0.013 mol). Yield = 4.61 g, 0.013 mol, 97%. MPt: 105–112 °C. Calc. for $\text{C}_{10}\text{H}_{18}\text{O}_2\text{S}_4\text{Zn}$ (%): C 33.0, H 4.99, S 35.2, Zn 18.0; found: C 33.0, H 4.99, S 35.2, Zn 18.0. FT-IR (cm^{-1}): 2952 (w), 2868 (w), 1463 (w), 1189 (s), 1129 (m), 1040 (s), 939.3 (w), 736.3 (w), 665.1 (w).

7.4.3.1.4 Synthesis of bis(O-ethylxanthato)tin(II)

[Sn(S₂COEt)₂] was prepared by a procedure modified from that described in the literature.^{53, 57} An aqueous solution of potassium ethylxanthate (10.0 g, 0.062 mol) was added to a solution of tin(II) chloride (5.90 g, 0.031 mol) in distilled water (100 ml) and stirred for a further 30 min. The yellow precipitate produced was collected by vacuum filtration, washed with water (3 × 50 ml) and finally dried in a vacuum oven at room temperature for 2 h to give [Sn(S₂COEt)₂] (7.20 g, 0.020 mol, 64% yield). MPt: 46 – 49 °C. Calc. for C₆H₁₀O₂S₄Sn (%): C 20.0, H 2.79, S 35.5, Sn 32.9; found: C 19.7, H 2.74, S 35.5, Sn 32.2. FT-IR (cm⁻¹): 2986 (w), 2930 (w), 1457 (w), 1355 (w), 1196 (s), 1108 (s), 1021 (s), 852.0 (w), 801.3 (w), 563.4 (w).

7.4.3.1.5 Synthesis of tetrakis(O-ethylxanthato)tin(IV)

[Sn(S₂COEt)₄] was prepared by a procedure that was modified from that described in literature.⁵⁷ SnCl₄ (1.04 g, 0.0040 mol) was dissolved in toluene (50 ml) and added dropwise to a solution of potassium ethylxanthate (2.80 g, 0.017 mol) in toluene (50 ml) and stirred for 1 h at room temperature. After filtering, the toluene solution was evaporated under reduced pressure and the oily residue shaken with 50 ml hexane and left to crystallize to give yellow crystals of [Sn(S₂COEt)₄] (1.80 g, 0.0030 mol, 75% yield). MPt: 58-62 °C. Calc. for C₁₂H₂₀O₄S₈Sn (%): C 23.9, H 3.34, S 42.4, Sn 19.7; found: C 24.4, H 3.36, S 42.1, Sn 20.1. FT-IR (cm⁻¹): 2983 (w), 2932 (w), 1459 (w), 1365 (w), 1233 (s), 1142(m), 1020 (s), 848.1 (w), 807.8 (w), 566.8 (w).

7.4.3.1.6 Synthesis of (O-ethylxanthato)copper(I) triphenylphosphine

A solution of potassium ethylxanthate (0.641 g, 0.0040 mol) in chloroform (40 ml) was added to a solution of triphenylphosphine (2.09 g, 0.008 mol) and CuCl (0.40 g, 0.0040 mol) in the same amount of chloroform. A white precipitate was obtained after continuous stirring for 1 h at room temperature. The solution was filtered to obtain a clear yellow solution. Cooling the yellow solution to -20 °C gave yellow crystals of O-ethylxanthato copper(I) triphenylphosphine (2.40 g, 0.0033 mol, 85% yield). MPt: 185–191 °C. Calc. for C₃₉H₃₅CuOP₂S₂ (%): C 66.1, H 4.97, S 9.02, P 8.74, Cu 8.96; found: C 65.7, H 5.08, S 8.77, P 8.44, Cu 8.74. FT-IR (cm⁻¹): 3048

(w), 2992 (w), 1478 (m) 1433 (m), 1290 (s), 1142 (m), 1041 (m), 1009 (s), 849.5 (s), 740.8 (m), 617.7 (s), 559.2 (s).

7.4.3.1.7 Synthesis of (O-butylxanthato)copper(I) triphenylphosphine

A solution of potassium butylxanthate (0.75 g, 0.0040 mol) in chloroform (40 ml) was added to a solution of triphenylphosphine (2.09 g, 0.008 mol) and CuCl (0.40 g, 0.0040 mol) in the same amount of chloroform. A white precipitate was obtained after continuous stirring for 1 h at room temperature. The solution was filtered to obtain a clear yellow solution. Cooling the yellow solution to -20 °C gave yellow crystals of O-butylxanthato copper(I) triphenyl-phosphine (2.10 g, 0.0028 mol, 71% yield). MPt: 132-137 °C. Calc. for $C_{41}H_{39}CuOP_2S_2$ (%): C 66.8, H 5.33, S 8.67, P 8.40, Cu 8.62; found: C 66.3, H 5.46, S 8.00, P 8.64, Cu 8.93. FT-IR (cm^{-1}): 3061 (w), 2998 (w), 1478 (m). 1433 (m), 1313 (s), 1168 (m), 1092 (m), 1052 (s), 996.1 (s), 743.6 (m), 618.5 (s), 574.1 (s).

7.4.3.2 Preparation of thin films

Glass slides were cut to 20 mm × 15 mm, cleaned by sonication in acetone and water and allowed to dry. Coating solutions were prepared by dissolving $[(Ph_3P)_2CuS_2COEt]$ (0.82 mmol), $[Zn(S_2CO^tBu)_2]$ (0.41 mmol) and $[Sn(S_2COEt)_2]$ (0.41 mmol) in THF (6 ml). A clear yellow solution was obtained. For each sample 2 ml of solution was coated onto the glass slide by spin coating at 700 rpm for 120 s and allowed to dry. The resulting films were then annealed in an N_2 atmosphere with a heating ramp $\approx 3\text{ }^\circ C\text{ min}^{-1}$ and held at the target temperature for 120 min; after this time had elapsed, the furnace was turned off and the tube allowed to cool to room temperature. The films were kept in the N_2 atmosphere until they had cooled to room temperature.

7.4.3.3 Electrical measurements

The electrical properties of the thin films were investigated using the van der Pauw method;⁵⁴ contacts to the 7.5 × 7.5 mm CZTS thin films were obtained using pure In probes. A magnetic field of 0.088 T strength was applied during the Hall measurements. The values of resistance between each In contact pair were

homogeneous, and the four individual Hall voltages were close to each other in value giving a statistically meaningful average. The film resistivity was calculated from the Hall voltage and sheet resistance.

7.4.4 Results and discussion

A range of copper, zinc and tin ethyl- and *n*-butylxanthate complexes were synthesized by the reaction of the appropriate metal chloride with the relevant potassium xanthate. The suitability of these complexes for melt reactions was assessed through measurements of their thermal stability. Thermogravimetric analysis (TGA, Figure 7.2) demonstrates the decomposition range of the Sn, Zn and Cu xanthates in a nitrogen atmosphere. An optimum mixture of precursors for melt reactions is one in which the precursors all decompose at similar reaction temperatures.

[Sn(S₂COEt)₂] decomposes cleanly in TGA at 100 – 145 °C, whereas [Zn(S₂COⁿBu)₂] decomposes via a two-step process between 110 – 220 and 250 – 350 °C. The decomposition of [(Ph₃P)₂CuS₂COEt] shows a mass loss starting at about 140 °C and finishing at 260 °C. The TGA curves indicate that SnS and CuS are formed cleanly, while ZnS contains impurities up to 350 °C. Sn(S₂COEt)₄ and (Ph₃P)₂(Cu(S₂COⁿBu)₂) have hence been discounted as viable precursors owing to their decomposition temperatures that differ from other precursors. The ethyl xanthate of zinc [Zn(S₂COEt)₂] is much more hygroscopic than its *n*-butyl cousin. Therefore, [(Ph₃P)₂CuS₂COEt], [Zn(S₂COⁿBu)₂] and [Sn(S₂COEt)₂] were chosen to deposit CZTS films. Additionally, these complexes are readily soluble in many common organic solvents.

CZTS thin films were prepared using a solution of [(Ph₃P)₂CuS₂COEt] (0.82 mmol), [Zn(S₂COⁿBu)₂] (0.41 mmol) and [Sn(S₂COEt)₂] (0.41 mmol) dissolved in THF (6 ml) and spin coated onto a glass slide. The resulting films were then heated in an N₂ atmosphere at the desired temperature (between 200 and 475 °C) for 120 min. The CZTS films were grey for all of the heating temperatures. Scanning electron microscopy (SEM) images (Figure 7.3) reveal the surface morphology of the films to be predominantly granular for the films prepared at temperatures 300 °C, with

particles in the region of 0.25 μm in diameter. The films prepared at lower temperature have a more flake-like consistency and contain much smaller particles. Side-on SEM images (Figure 7.1) show that the films are 1.88 – 2.0 μm in thickness.

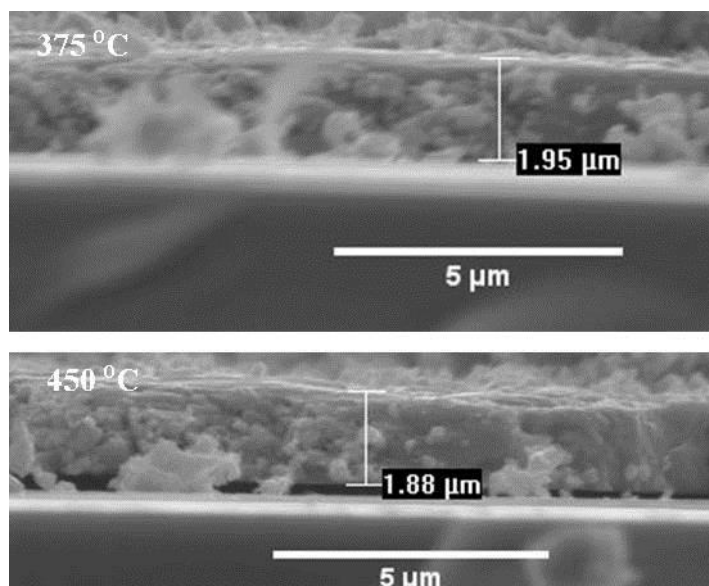


Figure 7.1. Side-on SEM image of a film prepared at 375 °C and 450 °C.

Energy-dispersive X-ray spectroscopy (EDX) analysis shows the presence of copper, zinc, tin and sulfur in the films. It is important to determine the Zn/Sn and Cu/(Zn +Sn) ratios within the films as slight changes in these values can lead to significant changes in structural/electronic properties.⁵⁸ The EDX measured compositions of the as-prepared films are shown in ESI Table S7.2.

The Cu/(Zn +Sn) ratio is in the range of 0.8 – 1.0 (ESI Table S7.2). The films heated at 225 °C gave Cu/ (Zn+Sn) [1, whereas the other films heated at high temperatures are copper deficient (ESI Table S7.2), which may reflect the volatility of the precursors. The slight copper deficiency is a promising result as solar cells made from Cu-poor films perform substantially better than those made from stoichiometric $\text{Cu}_2\text{ZnSnS}_4$.¹⁸

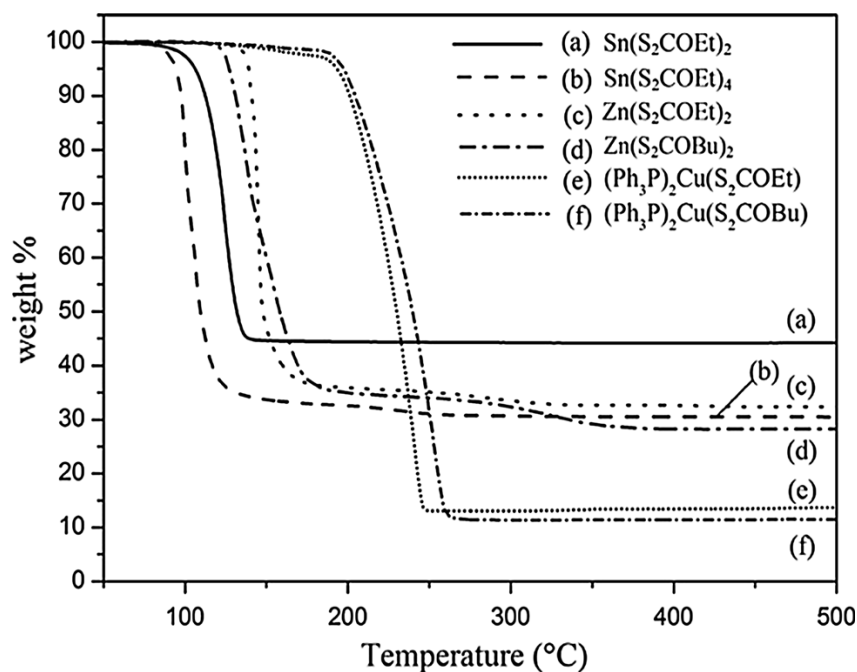


Figure 7.2. Decomposition profiles of the six potential CZTS precursors that were assessed by thermogravimetric analysis (TGA). Heating rate of $10\text{ }^\circ\text{C min}^{-1}$ under N_2 flow.

The p-XRD patterns for the samples prepared at temperatures between 200 and 475 °C are shown in figure 7.4. It is clear that the peaks sharpen with increased heating temperatures, with the width of the (002)/(112) reflection decreasing, which indicates improved crystallinity or increased crystalline size. At temperatures ≥ 375 °C simpler diffraction patterns are seen than at lower temperatures. Only KS-CZTS was observed this grows with a strongly preferred (112) orientation and matches well with the tetragonal CZTS standard (JCPDS No. 04-017-3032) which has a space group $\bar{I}4$. The lattice parameters of $a = 5.431\text{ \AA}$, $b = 5.431\text{ \AA}$ and $c = 10.844\text{ \AA}$ (ESI Tables S7.3, S7.4 and S7.5) match well with the literature values and indicate that the material is tetragonal and not cubic.⁵⁹

The films prepared at 200 – 250 °C consist of a relatively poorly crystalline hexagonal CZTS (Figure 7.6). The wurtzitic form of CZTS has previously been seen for nanoparticles and thin films.^{37, 60} The diffraction patterns of the hexagonal and orthorhombic phases are very similar. However, in orthorhombic CZTS the low angle peaks (100) and (101) in Figure 7.4a appear as ‘doublets’, representing the (210) +(020) and (211) +(021) lattice planes, respectively.⁶¹ This splitting is not

observed in our p-XRD pattern, nor is it seen in the selected area electron diffraction (SAED, Figure 7.6a and ESI Table S7.3); indeed, the patterns from TEM are very sharp and clear. Therefore, we conclude that the low temperature films result in the WZ-CZTS phase.

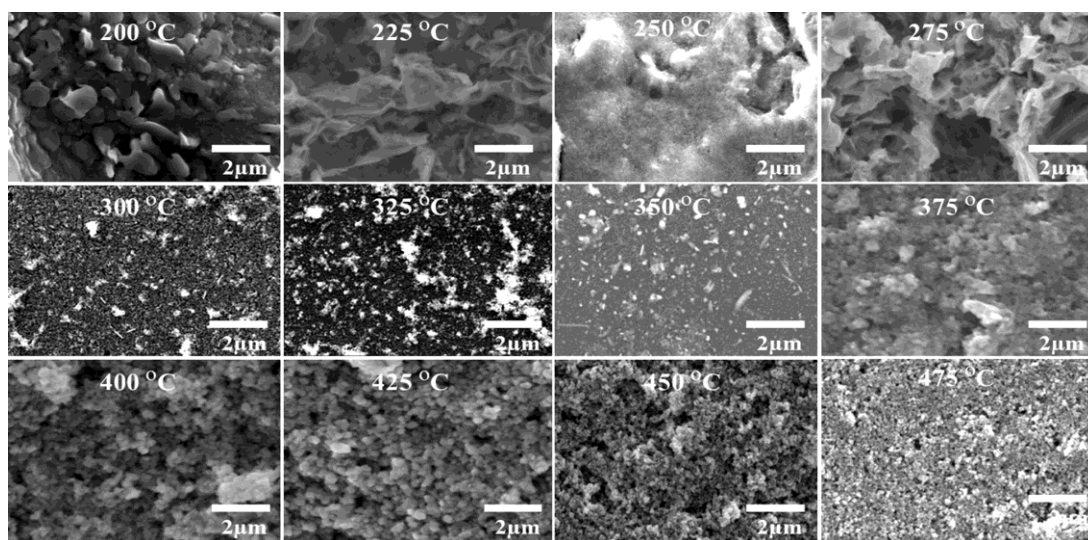


Figure 7.3. SEM images showing the surface morphology of the CZTS films obtained by heating spin-coated films at various temperatures.

Some contamination with binary or ternary phases may occur, as can be observed in the films prepared at $<300\text{ }^{\circ}\text{C}$ in which chalcocite (Cu_{2-x}S) is identifiable within the diffraction patterns.

The Raman spectra for the CZTS films give a good indication of the phase formed (Figure 7.4b). Kesteritic CZTS has a relatively narrow and dominant Raman shift at 338 cm^{-1} from the A mode, with further peaks at 288 cm^{-1} (A mode), 358 cm^{-1} (B mode) and 372 cm^{-1} (B mode).^{62, 63} This is seen in the films heated at higher temperatures ($400\text{ }^{\circ}\text{C}$). For the samples prepared at lower temperature ($<300\text{ }^{\circ}\text{C}$), the major peak has a shift of 327 cm^{-1} (Figure 7.5b). This corresponds to the WZ-CZTS A mode.⁶⁴ This indicates that the low-temperature films are wurtzite CZTS and there is a phase transition to kesterite at higher temperatures, in agreement with the p-XRD data. We note that there is also a peak in the Raman spectra for the $200\text{ }^{\circ}\text{C}$ film at 468 cm^{-1} , which corresponds to Cu_2S . Increasing the temperature leads to a gradual narrowing of the bands, and Raman bands appear with frequencies of about 331 , 333 and 337

cm^{-1} . Films heated at $475\text{ }^{\circ}\text{C}$ showed a higher intensity band at 337 cm^{-1} (Figure 7.5c), which is indicative of KS-CZTS.⁶⁵ Figure 7.5a shows the dependence of the shift of the dominant Raman peak on the heating temperatures. The WZ-CZTS films have a major peak at $326 - 327\text{ cm}^{-1}$, and this can clearly be seen for the samples prepared at $> 350\text{ }^{\circ}\text{C}$. As the annealing temperature increases, the peak moves toward 336 cm^{-1} , representing the presence of kesterite. This is demonstrated by the rapid increase in Raman shift seen from 375 to $475\text{ }^{\circ}\text{C}$. The p-XRD data show that the films prepared at $400 - 450\text{ }^{\circ}\text{C}$ are KS-CZTS too, and the downshifted peak is due to disorder in Cu and Zn atoms in the sublattice. This is because the Cu and Zn atoms have a similar size and the difference between binding energy of the cations in the sublattice is small.^{66, 67}

Samples suitable for transmission electron microscope (TEM) imaging were prepared by ultrasonication of the CZTS film (produced at 225 , 350 and $450\text{ }^{\circ}\text{C}$, Figure 7.6). Closer inspection of the CZTS produced at $225\text{ }^{\circ}\text{C}$ found that two distinct kinds of crystalline materials were present: a flake-like material and short nanorods with lattice fringes present (Figure 7.6a). Both sets of crystals were typically ≈ 40 and 20 nm in diameter, respectively. We were able to observe patches on the TEM grid that consisted mainly of either phase. The selected area electron diffraction (SAED) patterns found distinct rings indicative of polycrystalline materials, with these rings consistent with the identification of hexagonal (flake-like) and cubic (rod-like) phases of CZTS. This SAED, inset to Figure 7.6a, shows an interplanar spacing of 0.27 and 0.19 nm , which correspond to the (200) and (220) planes of cubic CZTS (ESI Table S7.4). The interplanar spacing of 0.33 and 0.32 nm relates to the (100) and (002) planes of hexagonal CZTS (ESI Table S7.3). Two phases (hexagonal and cubic) can be seen in the p-XRD pattern of the film heated at $225\text{ }^{\circ}\text{C}$ (Figure 7.4a) due to the equivalence of the (002) planes of the hexagonal structure with the (111) planes of the cubic structure. Exfoliation of CZTS films produced at $350\text{ }^{\circ}\text{C}$ showed a crystalline material ($< 20\text{ nm}$); SAED supported the formation of only the tetragonal phase of kesterite CZTS (Figure 7.6b). The interplanar spacing of 0.31 , 0.19 and 0.16 nm corresponds to the (112), [(204)(220)] and [(312)(116)] planes of kesterite CZTS (ESI Table S7.5). Likewise, for the film heated to $450\text{ }^{\circ}\text{C}$, we only observed crystalline particles $< 20\text{ nm}$, and for which the

SAED could also be indexed to tetragonal kesterite CZTS (Figure 7.6c, ESI Table S7.6).

The electrical parameters of the WZ-CZTS film prepared at 225 °C (Table A5) and the phase pure KS- CZTS samples annealed at 375 °C (Table A6) and 450 °C (Table A7) were obtained using the van der Pauw four probe configuration in Hall effect measurements at room temperature. All samples exhibited p-type conductivity, a desirable requirement for the fabrication of heterojunction solar cells.

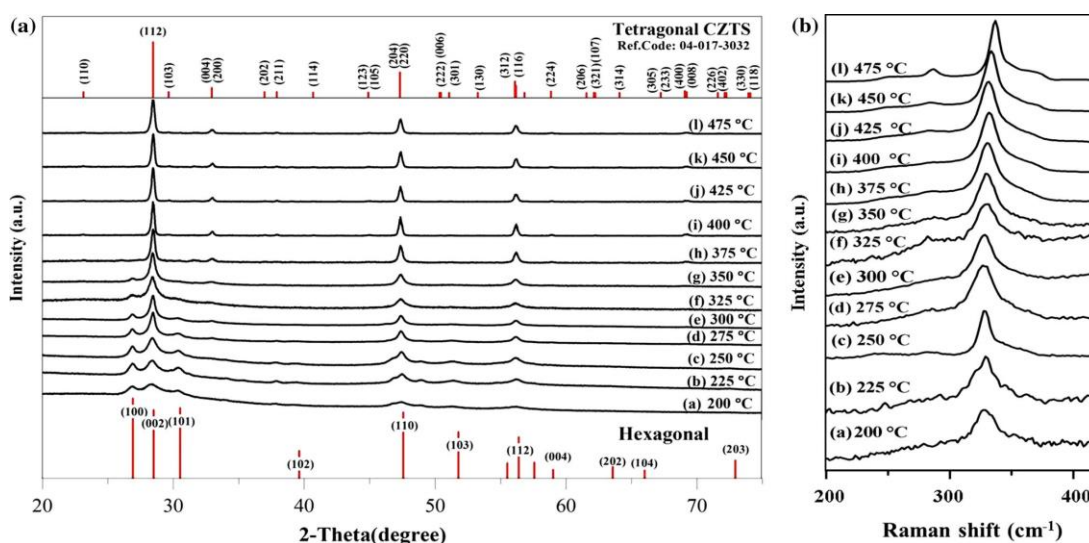


Figure 7.4. (a) p-XRD patterns and (b) Raman scattering spectra of CZTS thin films annealed in an N₂ atmosphere at the desired temperature (200–475 °C) for 120 min. Chalcocite (Cu_{2-x}S) is identifiable within the p-XRD for temperatures < 300 °C: low-intensity peaks for the (110) plane ($2\theta = 46.7^\circ$) and (103) plane ($2\theta = 48.8^\circ$).

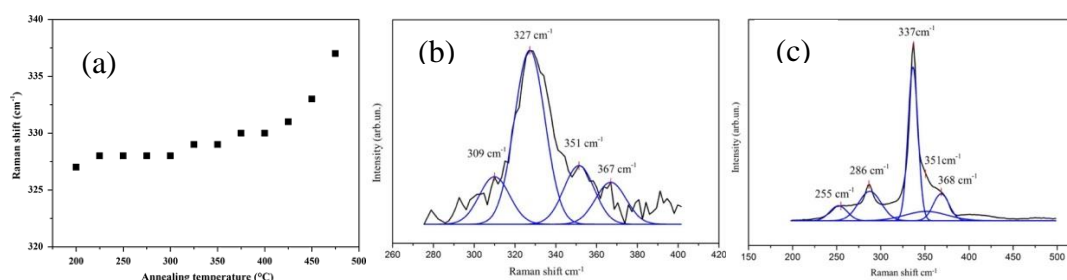


Figure 7.5. (a) The position of the dominant Raman peak at 327–336 cm⁻¹ in Figure 7.4b and its relationship to the annealing temperature of the films. (b) Raman spectrum of films prepared at 200 °C and (c) 475 °C.

The resistivity (ρ), Hall mobility (μ), carrier concentration (p) and Hall coefficient (R_H) are shown in Table 7.1. The resistivity (ρ) decreased from 27.1 Ω cm to around 1.23 Ω . cm for the transition from WZ- CZTS to KS-CZTS. In addition, we found that the Hall coefficient (R_H) decreased from $2.36 \times 10^{+3} \text{ cm}^3 \text{ C}^{-1}$ for WZ-CZTS films to 13.7 $\text{cm}^3 \text{ C}^{-1}$ for KS-CZTS $^\circ\text{C}$. We have determined that for the two phases, the Hall mobility (μ) is 87.1 and 11.1 $\text{cm}^2 \text{ V}^{-1} \text{ s}^{-1}$, respectively. The carrier concentration values were $2.65 \times 10^{+15}$ and $4.55 \times 10^{+17} \text{ cm}^{-3}$, the latter of which is an excellent value for use in practical devices. TEM images of the film prepared at 225 $^\circ\text{C}$ indicate that the film exhibited hexagonal CZTS as well as cubic (Figure 7.6a). This confirms the presence of impurities in the predominantly wurtzite phase CZTS. McGill⁶⁸ and Hall⁶⁹ previously showed that as the impurity concentration increases, the mobility decreases. This behavior has also been seen for Si⁷⁰ and GaAs.⁷¹ This model can be applied to the CZTS system, as moving from 225 to 375/450 $^\circ\text{C}$ we see a substantial decrease in mobility.

Table 7.1. Electrical properties of CZTS films prepared through melt reactions at 225, 375 and 450 $^\circ\text{C}$

T	225 $^\circ\text{C}$	375 $^\circ\text{C}$	450 $^\circ\text{C}$
μ ($\text{cm}^2 \cdot \text{V}^{-1} \cdot \text{S}^{-1}$)	87.1	5.58	11.1
p (cm^{-3})	$2.65 \times 10^{+15}$	$1.32 \times 10^{+18}$	$4.55 \times 10^{+17}$
R_H ($\text{C}^{-1} \cdot \text{cm}^3$)	$2.36 \times 10^{+3}$	4.73	13.7
ρ ($\Omega \cdot \text{cm}$)	27.1	0.85	1.23
σ ($\text{S} \cdot \text{cm}^{-1}$)	0.0369	1.18	0.81
R_S (Ω/\square)	$1.37 \times 10^{+5}$	$4.35 \times 10^{+3}$	$6.55 \times 10^{+3}$
Conductivity	p-type	p-type	p-type

T annealing temperature, μ Hall mobility, p Hall carrier density, R_H Hall coefficient, ρ resistivity, σ conductivity and R_S sheet resistance.

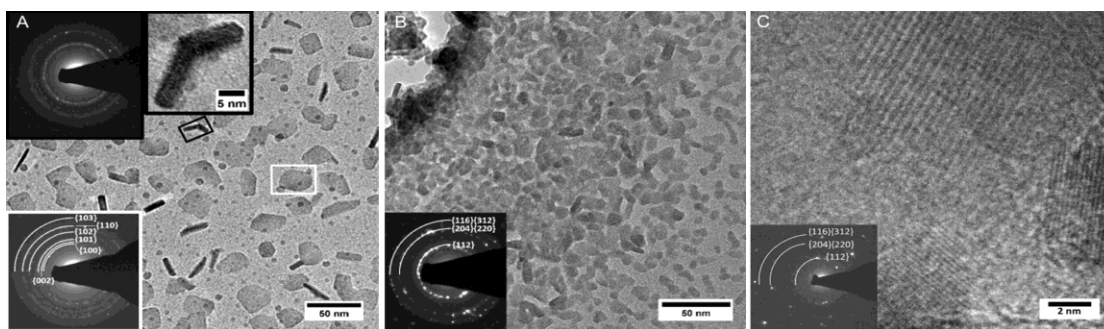


Figure 7.6. TEM images of $\text{Cu}_2\text{ZnSnS}_4$ nanocrystals. (a) A CZTS film heated at 225 °C. The insets show selected area electron diffraction (SAED) images, gray box for cubic CZTS and white box for hexagonal CZTS. (b) A film heated at 350 °C. The SAED pattern can be indexed to tetragonal CZTS. (c) A film heated at 450 °C, the inset SAED pattern is also indexed to tetragonal CZTS.

7.4.5 Conclusions

Thermogravimetric analysis was used to investigate the decomposition of a series of *O-n*-butyl and *O*-ethylxanthate complexes of copper, tin and zinc. $[(\text{Ph}_3\text{P})_2\text{CuS}_2\text{COEt}]$, $[\text{Zn}(\text{S}_2\text{CO}^n\text{Bu})_2]$ and $[\text{Sn}(\text{S}_2\text{COEt})_2]$ were found to have compatible decomposition temperatures and were used for the formation of $\text{Cu}_2\text{ZnSnS}_4$ (CZTS) by spin coating followed by heating under N_2 . The p-XRD patterns of CZTS thin films were obtained after heating at temperatures between 200 and 475 °C and revealed a temperature dependence of the CZTS phase formed. Higher temperatures give the normal tetragonal phase CZTS, while low temperatures are mixed hexagonal and cubic phases. EDX measurements show that the $\text{Cu}/(\text{Zn} + \text{Sn})$ ratio was between 1 and 0.64. The measured resistivity, carrier concentration, mobility and Hall coefficient of films heated at 225, 375 and 450 °C, indicated fairly homogenous films. In this work the wurtzite CZTS has a much higher resistivity and mobility, but a much lower charge carrier density.

7.4.6 Acknowledgements

The authors would like to acknowledge the Iraqi Culture Attache´ in London for financial support (M.A.S.) and the EPSRC (Doctoral Prize for P.D.M., EP/M507969/1). N.S. thanks Carl and Anne Parker for the fellowship that funded this work. Some of the equipment used in this study were provided by the

Engineering and Physical Sciences Research Council (Core Capability in Chemistry, EPSRC Grant Number EP/K039547/1).

7.4.7 References

1. K. Woo, Y. Kim and J. Moon, *Energy Environ. Sci.*, 2012, **5**, 5340-5345.
2. H. Katagiri, K. Jimbo, W. S. Maw, K. Oishi, M. Yamazaki, H. Araki and A. Takeuchi, *Thin Solid Films*, 2009, **517**, 2455-2460.
3. P. D. Matthews, P. D. McNaughter, D. J. Lewis and P. O'Brien, *Chem. Sci.*, 2017, **8**, 4177-4187.
4. B. Shin, O. Gunawan, Y. Zhu, N. A. Bojarczuk, S. J. Chey and S. Guha, *Prog. photovolt.*, 2013, **21**, 72-76.
5. S. K. Saha, A. Guchhait and A. J. Pal, *Phys. Chem. Chem. Phys.*, 2012, **14**, 8090-8096.
6. J. J. Scragg, P. J. Dale, L. M. Peter, G. Zoppi and I. Forbes, *Phys. Status Solidi B*, 2008, **245**, 1772-1778.
7. K. Jimbo, R. Kimura, T. Kamimura, S. Yamada, W. S. Maw, H. Araki, K. Oishi and H. Katagiri, *Thin Solid Films*, 2007, **515**, 5997-5999.
8. K. Ito and T. Nakazawa, *Jpn. J. Appl. Phys.*, 1988, **27**, 2094.
9. H. Katagiri, N. Sasaguchi, S. Hando, S. Hoshino, J. Ohashi and T. Yokota, *Sol. Energy Mater Sol. Cells*, 1997, **49**, 407-414.
10. S. W. Shin, S. Pawar, C. Y. Park, J. H. Yun, J.-H. Moon, J. H. Kim and J. Y. Lee, *Sol. Energy Mater Sol. Cells*, 2011, **95**, 3202-3206.
11. M. Suryawanshi, G. Agawane, S. Bhosale, S. Shin, P. Patil, J. Kim and A. Moholkar, *Mater. Technol.*, 2013, **28**, 98-109.
12. M. Kumar, A. Dubey, N. Adhikari, S. Venkatesan and Q. Qiao, *Energy Environ. Sci.*, 2015, **8**, 3134-3159.
13. K. Ramasamy, M. A. Malik and P. O'Brien, *Chem. Sci.*, 2011, **2**, 1170-1172.
14. R. Schurr, A. Hölzing, S. Jost, R. Hock, T. Voß, J. Schulze, A. Kirbs, A. Ennaoui, M. Lux-Steiner and A. Weber, *Thin Solid Films*, 2009, **517**, 2465-2468.
15. A. Wangperawong, J. King, S. Herron, B. Tran, K. Pangan-Okimoto and S. Bent, *Thin Solid Films*, 2011, **519**, 2488-2492.

16. Z. Su, C. Yan, K. Sun, Z. Han, F. Liu, J. Liu, Y. Lai, J. Li and Y. Liu, *Appl. Surf. Sci.*, 2012, **258**, 7678-7682.
17. L.J. Chen and Y.-J. Chuang, *Mater. Lett.*, 2013, **91**, 372-375.
18. M. C. Johnson, C. Wrasman, X. Zhang, M. Manno, C. Leighton and E. S. Aydil, *Chem. Mater.*, 2015, **27**, 2507-2514.
19. Y. Feng, B. Yu, G. Cheng, T. Lau, Z. Li, L. Yin, Q. Song, C. Yang and X. Xiao, *J. Mater. Chem. C*, 2015, **3**, 9650-9656.
20. J. J. Scragg, T. Ericson, T. Kubart, M. Edoff and C. Platzer-Björkman, *Chem. Mater.*, 2011, **23**, 4625-4633.
21. K. Yu and E. A. Carter, *Chem. Mater.*, 2015, **27**, 2920-2927.
22. K. Yu and E. A. Carter, *Chem. Mater.*, 2016, **28**, 4415-4420.
23. J. J. Scragg, T. Kubart, J. T. Wätjen, T. Ericson, M. K. Linnarsson and C. Platzer-Björkman, *Chem. Mater.*, 2013, **25**, 3162-3171.
24. F. Jiang, T. Harada, Y. Kuang, T. Minegishi, K. Domen and S. Ikeda, *J. Am. Chem. Soc.*, 2015, **137**, 13691-13697.
25. J. Chang and E. R. Waclawik, *RSC Adv.*, 2014, **4**, 23505-23527.
26. S. Chen, X. Gong, A. Walsh and S.-H. Wei, *Appl. Phys. Lett.*, 2009, **94**, 41903.
27. J. Paier, R. Asahi, A. Nagoya and G. Kresse, *Phys. Rev. B*, 2009, **79**, 115126.
28. A. Khare, B. Himmetoglu, M. Johnson, D. J. Norris, M. Cococcioni and E. S. Aydil, *J. Appl. Phys.*, 2012, **111**, 083707.
29. J. E. Bernard, L. Ferreira, S.-H. Wei and A. Zunger, *Phys. Rev. B*, 1988, **38**, 6338.
30. R. Magri, S.H. Wei and A. Zunger, *Phys. Rev. B*, 1990, **42**, 11388.
31. S. Chen, A. Walsh, Y. Luo, J.-H. Yang, X. Gong and S.-H. Wei, *Phys. Rev. B*, 2010, **82**, 195203.
32. T. Shibuya, Y. Goto, Y. Kamihara, M. Matoba, K. Yasuoka, L. A. Burton and A. Walsh, *Appl. Phys. Lett.*, 2014, **104**, 021912.
33. A. J. Jackson and A. Walsh, *J. Mater. Chem. A*, 2014, **2**, 7829-7836.
34. K. Ramasamy, M. A. Malik and P. O'Brien, *Chem. Commun.*, 2012, **48**, 5703-5714.
35. S. Schorr and G. Gonzalez-Aviles, *Phys. Status Solidi A*, 2009, **206**, 1054-1058.

36. R. Ahmad, M. Brandl, M. Distaso, P. Herre, E. Spiecker, R. Hock and W. Peukert, *CrystEngComm*, 2015, **17**, 6972-6984.
37. C. A. Cattley, C. Cheng, S. M. Fairclough, L. M. Droessler, N. P. Young, J. H. Warner, J. M. Smith, H. E. Assender and A. A. Watt, *Chem. Commun.*, 2013, **49**, 3745-3747.
38. N. Nakayama and K. Ito, *Appl. Surf. Sci.*, 1996, **92**, 171-175.
39. S. Botti, D. Kammerlander and M. A. Marque, *Appl. Phys. Lett.*, 2011, **98**, 241915.
40. E. A. Lund and M. A. Scarpulla, SPIE OPTO, 2013, 8620, 8.
41. P. Kevin, M. A. Malik and P. O'Brien, *J. Mater. Chem. C*, 2015, **3**, 5733-5741.
42. P. Kevin, M. A. Malik and P. O'Brien, *New J. Chem.*, 2015, **39**, 7046-7053.
43. P. Kevin, M. A. Malik, S. Mcadams and P. O'Brien, *J. Am. Chem. Soc.*, 2015, **137**, 15086-15089.
44. E. A. Lewis, P. D. McNaughter, Z. Yin, Y. Chen, J. R. Brent, S. A. Saah, J. Raftery, J. A. Awudza, M. A. Malik and P. O'Brien, *Chem. Mater.*, 2015, **27**, 2127-2136.
45. E. Lewis, S. Haigh and P. O'Brien, *J. Mater. Chem. A*, 2014, **2**, 570-580.
46. P. D. Matthews, M. Akhtar, M. A. Malik, N. Revaprasadu and P. O'Brien, *Dalton Trans.*, 2016, **45**, 18803-18812.
47. D. J. Lewis, A. A. Tedstone, X. L. Zhong, E. A. Lewis, A. Rooney, N. Savjani, J. R. Brent, S. J. Haigh, M. G. Burke and C. A. Muryn, *Chem. Mater.*, 2015, **27**, 1367-1374.
48. N. Savjani, J. R. Brent and P. O'Brien, *Chem. Vap. Deposition*, 2015, **21**, 71-77.
49. N. Savjani, E. A. Lewis, M. A. Bissett, J. R. Brent, R. A. Dryfe, S. J. Haigh and P. O'Brien, *Chem. Mater.*, 2016, **28**, 657-664.
50. M. Al-Shakban, Z. Xie, N. Savjani, M. A. Malik and P. O'Brien, *J. Mater. Sci.*, 2016, 1-7.
51. K. Ramasamy, M. A. Malik, N. Revaprasadu and P. O'Brien, *Chem. Mater.*, 2013, **25**, 3551-3569.
52. N. Alam, M. S. Hill, G. Kociok-Köhn, M. Zeller, M. Mazhar and K. C. Molloy, *Chem. Mater.*, 2008, **20**, 6157-6162.

53. G. Kociok-Köhn, K. C. Molloy and A. L. Sudlow, *Can. J. Chem.*, 2014, **92**, 514-524.
54. L. J. van der Pauw, *Philips Res. Rep.*, 1958, **13**, 1-9.
55. A. A. Mohamed, I. Kani, A. O. Ramirez and J. P. Fackler, *Inorg. Chem.*, 2004, **43**, 3833-3839.
56. T. Ikeda and H. Hagihara, *Acta Crystallogr.*, 1966, **21**, 919-927.
57. C. Raston, P. Tennant, A. White and G. Winter, *Aust. J. Chem.*, 1978, **31**, 1493-1500.
58. S. Zhou, R. Tan, X. Jiang, X. Shen, W. Xu and W. Song, *J. Mater. Sci. Mater. Electron.*, 2013, **24**, 4958-4963.
59. P. Bonazzi, L. Bindi, G. P. Bernardini and S. Menchetti, *The Canadian Mineralogist*, 2003, **41**, 639-647.
60. R. Mainz, A. Singh, S. Levchenko, M. Klaus, C. Genzel, K. Ryan and T. Unold, *Nat. Commun.*, 2014, **5**.
61. H. Jiang, P. Dai, Z. Feng, W. Fan and J. Zhan, *J. Mater. Chem.*, 2012, **22**, 7502-7506.
62. A.-J. Cheng, M. Manno, A. Khare, C. Leighton, S. Campbell and E. Aydil, *J. Vac. Sci. Technol. A*, 2011, **29**, 051203.
63. M. Dimitrievska, A. Fairbrother, X. Fontané, T. Jawhari, V. Izquierdo-Roca, E. Saucedo and A. Pérez-Rodríguez, *Appl. Phys. Lett.*, 2014, **104**, 021901.
64. J. M. R. Tan, Y. H. Lee, S. Pedireddy, T. Baikie, X. Y. Ling and L. H. Wong, *J. Am. Chem. Soc.*, 2014, **136**, 6684-6692.
65. M. Himmrich and H. Haeuseler, *Spectrochim. Acta A*, 1991, **47**, 933-942.
66. M. Y. Valakh, O. Kolomys, S. Ponomaryov, V. Yukhymchuk, I. Babichuk, V. Izquierdo-Roca, E. Saucedo, A. Perez-Rodriguez, J. Morante and S. Schorr, *Phys. Status Solidi RRL*, 2013, **7**, 258-261.
67. A. Walsh, S. Chen, S. H. Wei and X. G. Gong, *Adv. Energy Mater.*, 2012, **2**, 400-409.
68. T. McGill and R. Baron, *Phys. Rev. B*, 1975, **11**, 5208.
69. G. Hall, *J. Phys. Chem. Solids*, 1962, **23**, 1147-1151.
70. H. Kosina and G. Kaiblinger-Grujin, *Solid State Electron.*, 1998, **42**, 331-338.
71. C. Wolfe, G. Stillman and J. Dimmock, *J. Appl. Phys.*, 1970, **41**, 504-507.

7.4.8 Supporting information

Table S7.2. Composition percentages and ratios for CZTS films after annealing at different temperatures as determined by EDX.

T (°C)	Cu	Zn	Sn	S	Zn/Sn	Cu/(Zn+Sn)
200	28	17	14	41	1.2	0.9
225	30	13	17	40	0.8	1.0
250	29	17	14	41	1.2	1.0
275	28	18	16	38	1.1	0.8
300	30	18	13	39	1.3	1.0
325	28	15	16	41	1.0	0.9
350	28	18	14	39	1.3	0.9
375	29	16	15	40	1.1	0.9
400	27	18	15	39	1.2	0.8
425	28	19	15	38	1.3	0.8
450	28	17	16	39	1.1	0.8
475	28	18	14	39	1.3	0.9

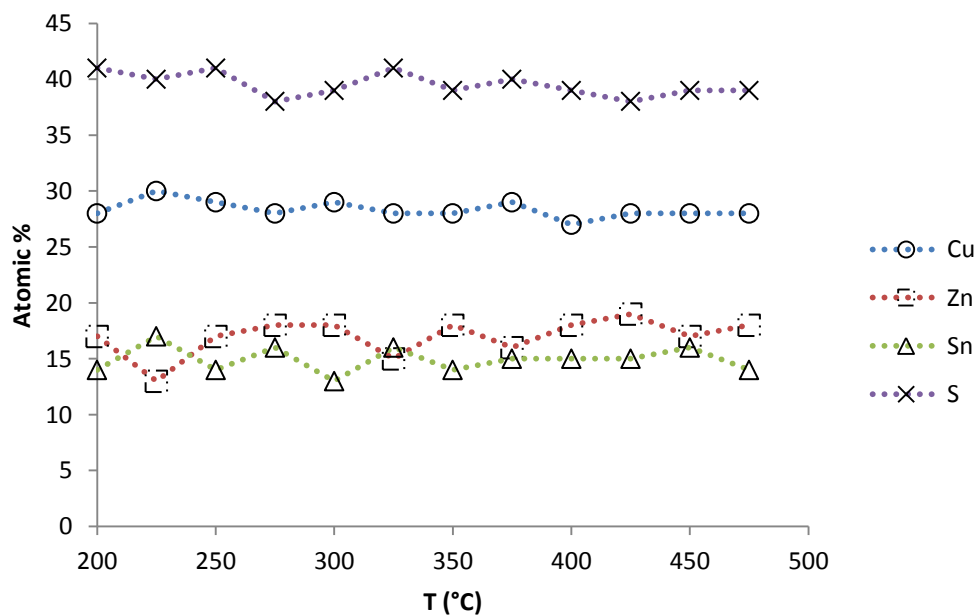


Figure S7.7. The elemental composition of the films determined by EDX.

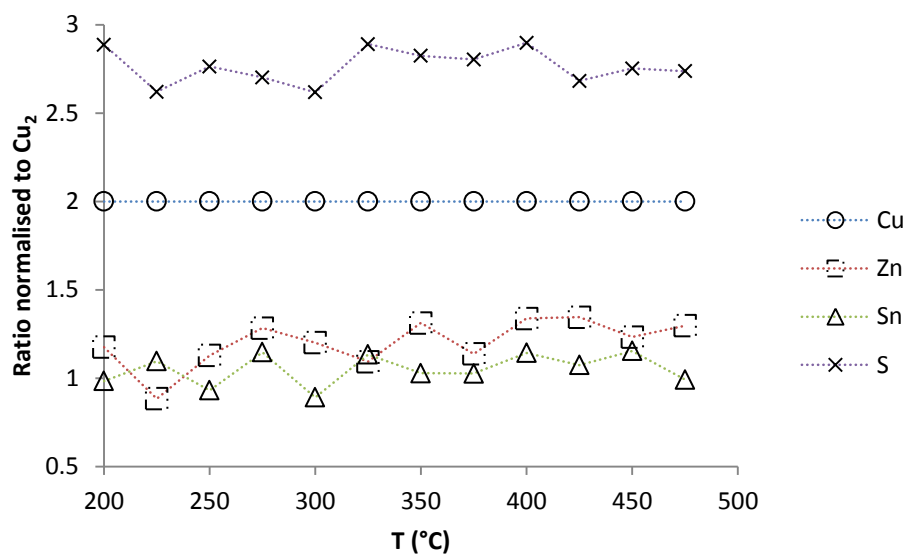


Figure S7.8. Elemental composition of the CZTS films determined by EDX normalised to Cu₂.

Table S7.3. Lattice parameters calculated from p-XRD and SAED (Figure 7.6a) for hexagonal CZTS film heated at 225 °C.

d [Å] from TEM	hkl	Calc. unit cell from TEM [Å]			Calc. unit cell from PXRD [Å]		
		a	b	c	a	b	c
3.3	(100)	3.80	3.80	6.32	3.83	3.83	6.30
3.2	(002)						
2.9	(101)						
6.3	(102)						
1.9	(110)						
1.7	(103)						

Table S7.4. Lattice parameters calculated from p-XRD and SAED (Figure 7.6a) for cubic CZTS heated at 225 °C.

d [Å]	hkl	Calc. unit cell from TEM [Å]			Calc. unit cell from PXRD [Å]		
		a	b	c	a	b	c
2.70	(200)	5.42	5.42	5.42	5.43	5.43	5.43
1.91	(220)						

Table S7.5. Lattice parameters calculated from p-XRD and SAED for tetragonal CZTS prepared at 350 °C (Figure 7.6b).

d [Å]	hkl	Calc. unit cell from TEM [Å]			Calc. unit cell from PXRD [Å]		
		a	b	c	a	b	c
3.13	(112)	5.43	5.43	10.84	5.43	5.43	10.85
1.91	(204)(220)						
1.63	(116)(312)						

Table S7.6. Lattice parameters calculated from p-XRD and SAED for tetragonal CZTS prepared at 450 °C (Figure 7.6c).

d [Å]	hkl	Calc. unit cell from TEM [Å]			Calc. unit cell from PXRD [Å]		
		a	b	c	a	b	c
3.13	(112)	5.43	5.43	10.80	5.43	5.43	10.84
1.91	(204)(220)						
1.59	(116)(312)						

Table S7.7. Lattice parameters calculated from p-XRD for tetragonal and hexagonal CZTS prepared by heating spin-coated films at various temperatures. The literature values of lattice parameters are $a = b = 5.43 \text{ \AA}$ and $c = 10.84 \text{ \AA}$ for tetragonal ¹ and $a = b = 3.83 \text{ \AA}$, $c = 6.31 \text{ \AA}$ for hexagonal.²

T (°C)	Calc. unit cell for tetragonal CZTS [\AA]			Calc. unit cell for hexagonal CZTS [\AA]		
	a	b	c	a	b	c
200				3.837	3.837	6.300
225				3.832	3.832	6.301
250				3.836	3.836	6.299
275				3.837	3.837	6.302
300				3.836	3.836	6.299
325				3.837	3.837	6.302
350				3.831	3.831	6.297
375	5.433	5.433	10.844			
400	5.429	5.429	10.845			
425	5.431	5.431	10.844			
450	5.431	5.431	10.844			
475	5.431	5.431	10.844			

7.4.8.1 References

1. P. Bonazzi, L. Bindi, G. P. Bernardini and S. Menchetti, *The Canadian Mineralogist*, 2003, **41**, 639-647.
2. M. Li, W. H. Zhou, J. Guo, Y. L. Zhou, Z. L. Hou, J. Jiao and Z. J. Zhou, *J. Phys. Chem. C*, 2012, **116**, 26507-26516.

Chapter 8 Conclusion and future work

8.1 Conclusion

Single source precursors have been employed for the formation of nanoparticles and deposition of thin films of metal sulfides. In this study, a series of novel xanthate complexes were synthesised and characterized by elemental analysis, IR, NMR and single crystal X-ray diffraction. The decomposition of the complexes was assessed by thermogravimetric analysis. The xanthate complexes were used as single source precursors for the deposition of metal sulfide thin films and formation of nanoparticles.

Chapter three explains the synthesis and single-crystal X-ray characterisation of six novel triphenyl copper(I) xanthate complexes [*iso*-butylxanthate, 2-methoxyethylxanthate, 2-ethoxyethylxanthate, 1-methoxy-2-propylxanthate, 3-methoxy-1-butylxanthate and 3-methoxy-3-methyl-1-butylxanthate]. These six complexes, in addition to the ethyl and n-butyl analogues have been tested as single-source precursors for the formation of copper sulfide nanoparticles. At 5 seconds reaction time, $\text{Cu}_{1.74}\text{S}$ nanorods are formed. The longer chain xanthates lead to the formation of particles of decreased width. In chapter four a simple process has been described for the growth of tin sulfide films. Heating of substrates spin-coated with $\text{Sn}(\text{S}_2\text{COEt})_2$ at 150, 200, 250, 300, and 400 °C produced SnS films mainly in orthorhombic phase with good crystallinity.

Chapter five describes the synthesis and single-crystal X-ray characterisation of seven novel indium(III) xanthate complexes. These xanthates as well as triphenyl copper(I) xanthate complexes have been used as an In/Cu source for the synthesis of highly crystalline CuInS_2 nanoparticles. CuInS_2 nanoparticles were formed using the hot-injection method in two solvent systems at 260 °C. $[\text{In}(\text{S}_2\text{CO}(\text{CH}_2)_2\text{OEt})_3]$ and $[(\text{Ph}_3\text{P})_2\text{Cu}(\text{S}_2\text{CO}(\text{CH}_2)_2\text{OEt})]$ in 1:1 ratio were chosen as a sources of In and Cu. The injection of the complexes into castor oil gives a hexagonal phase CuInS_2 , however same complexes injected into oleylamine formed cubic CuInS_2 . Chapter six reports a simple, efficient procedure in which xanthate complexes produce thin films of CaCu_2S_2 , β - BaCu_2S_2 and β - BaCu_4S_3 . The films were deposited using calcium isopropylxanthate and the novel compounds barium isopropylxanthate

and bis(triphenylphosphine)copper 2-methoxyethylxanthate by spin coating and were characterised using p-XRD, SEM and EDX. In chapter seven, we explain the preparation of $\text{Cu}_2\text{ZnSnS}_4$ thin films from xanthate complexes at temperatures between 200 and 475 °C. $[(\text{Ph}_3\text{P})_2\text{CuS}_2\text{COEt}]$, $[\text{Zn}(\text{S}_2\text{CO}^n\text{Bu})_2]$ and $[\text{Sn}(\text{S}_2\text{COEt})_2]$ were dissolved in toluene and deposited on glass substrates. The p-XRD patterns of the films shows hexagonal $\text{Cu}_2\text{ZnSnS}_4$ at lower temperatures, however higher temperatures give the normal tetragonal phase CZTS. The measured resistivity, carrier concentration, mobility and Hall coefficient of films heated at 225, 375 and 450 °C, indicated fairly homogenous films. In this work the wurtzite CZTS has a much higher resistivity and mobility, but a much lower charge carrier density.

8.2 Future work

Future work will concentrate on synthesis and use of other ligands in complexes such as imidophosphinato, selenophosphinato, and selenourea for the deposition of SnS, SnSe, CZTS and CZTSSe thin films. It will also be necessary to investigate deposition of $\text{Cu}_2\text{ZnSnS}_4$ (CZTS) and $\text{Cu}_2\text{FeSnS}_4$ (CFTS) from xanthato complexes by chemical vapour deposition techniques such as AACVD, LPCVD and APCVD. To improve the electrical properties of the CZTS films for solar cell applications, it is may be a good option to use polymers such as electrically active (P3HT).

A major advantage of using xanthate complexes to deposit CZTS absorber layer is that the ability of synthesis the films at low temperature. Therefore, it is possible to fabricate CZTS layer on molybdenum substrate, since this will help to avoid the growth of molybdenum disulfide and improve the efficiency of CZTS device, as a result, CZTS sample prepared at 375 °C is suitable to fabricate the CZTS pn-junction diode.

For the development of novel solar devices based on these materials more work will need to be focused on developing controllable fabrication of CZTS and testing of semiconductor devices including:

1. The measurement of forward to reverse resistance ratio and cell capacitance. The resistance ratio indicates the ability of the diode to pass current in one direction and block current in the other direction. ¹

2. The measurement of current - voltage characteristics and external quantum efficiency (EQE).²
3. Environmental tests should be verified to determine the resistance of diode to deleterious.
4. The reliability test, this test is to verify the reliability and quality of the product.

Carrying out these additional measurements on the materials will allow us to verify that they are firstly suitable for use in heterojunction solar cells in terms of their electronic properties and secondly that they have the desired stability for long term operation.

8.3 References

1. F. Jiang and H. Shen, *Appl. Surf. Sci.*, 2013, **280**, 138-143.
2. B. Shin, O. Gunawan, Y. Zhu, N. A. Bojarczuk, S. J. Chey and S. Guha, *Prog. Photovolt. Res. Appl.* , 2013, **21**, 72-76.

Appendix

Appendix

Table A1. Crystallographic data for compounds [KS₂CO(CH₂)₂OMe] (**3**), [K(S₂CO(CH₂)₂OEt)] (**4**), [K(S₂COC(H)(Me)CH₂OMe)] (**5**).

Compound	[KS ₂ CO(CH ₂) ₂ OMe] (3)	[K(S ₂ CO(CH ₂) ₂ OEt)] (4)	[K(S ₂ COC(H)(Me)CH ₂ OMe)] (5)
Empirical formula	C ₄ H ₇ KO ₂ S ₂	C ₅ H ₉ KO ₂ S ₂	C ₁₀ H ₁₈ K ₂ O ₄ S ₄
Formula weight	190.32	204.34	408.68
Temperature (K)	150	150.15	100.00(10) K
Wavelength (Å)	0.71073	0.71073	0.71073
Crystal system	Monoclinic	Orthorhombic	Triclinic
Space group	P 1 21/c 1	Pbca	P-1
Unit cell dimensions	a (Å)	9.564(4)	6.6541(3)
	b (Å)	12.667(4)	10.3045(8)
	c (Å)	6.656(3)	21.052(5)
	α (°)	90	90
	β (°)	105.17(4)°	90
	γ (°)	90	90
Volume (Å ³)	778.3(6)	1755.2(6)	879.64(9)
Z	4	8	2
Absorption coefficient (mm ⁻¹)	1.146	1.022	1.020
Crystal size (mm ³)	0.3 x 0.3 x 0.1	0.25 x 0.2 x 0.05	0.2 x 0.1 x 0.1
Reflections collected	5118	11745	12165
Independent reflections	1420 [R _(int) = 0.0557]	1605 [R _(int) = 0.0623]	3209 [R _(int) = 0.0707]
Goodness-of-fit on F ²	1.112	1.096	1.101
Final R indices [I ≥ 2σ (I)]	R1 = 0.0391, wR2 = 0.0631	R1 = 0.0485, wR2 = 0.1214	R1 = 0.0606, wR2 = 0.1299
R indices (all data)	R1 = 0.0616, wR2 = 0.0729	R1 = 0.0645, wR2 = 0.1301	R1 = 0.0796, wR2 = 0.1376

Table A2. Crystallographic data for [(Ph₃P)₂Cu(S₂COⁱBu)] (**11**), [(Ph₃P)₂Cu(S₂CO(CH₂)₂OMe)] (**12**), [(Ph₃P)₂Cu(S₂CO(CH₂)₂OEt)] (**13**), [(Ph₃P)₂Cu(S₂COC(H)(Me)CH₂OMe)] (**14**), [(Ph₃P)₂Cu(S₂CO(CH₂)₂C(H)(OMe)Me)] (**15**), [(Ph₃P)₂Cu(S₂CO(CH₂)₂C(OMe)(Me)₂)] (**16**).

Compound	(Ph ₃ P) ₂ Cu(S ₂ CO ⁱ Bu) (11)	(Ph ₃ P) ₂ Cu(S ₂ CO(CH ₂) ₂ OMe) (12)	(Ph ₃ P) ₂ Cu(S ₂ CO(CH ₂) ₂ OEt) (13)	(Ph ₃ P) ₂ Cu(S ₂ COC(H)(Me)CH ₂ OMe) (14)	(Ph ₃ P) ₂ Cu(S ₂ CO(CH ₂) ₂ C(H)(OMe)Me) (15)	(Ph ₃ P) ₂ Cu(S ₂ CO(CH ₂) ₂ C(OMe)(Me) ₂) (16)	
Empirical formula	C ₄₁ H ₃₉ CuOP ₂ S ₂	C ₄₀ H ₃₇ CuO ₂ P ₂ S ₂	C ₄₁ H ₃₇ CuO ₂ P ₂ S ₂	C ₄₁ H ₃₉ CuO ₂ P ₂ S ₂	C ₄₂ H ₄₁ CuO ₂ P ₂ S ₂	C ₄₃ H ₄₃ CuO ₂ P ₂ S ₂	
Formula weight	737.32	739.29	751.30	753.32	767.35	781.37	
Temperature (K)	180(2)	100(2)	100(2)	100(2)	100(2)	100(2)	
Wavelength (Å)	1.54178	1.5418	1.5418	1.5418	1.54178	1.54178	
Crystal system	Monoclinic	Triclinic	Monoclinic	Monoclinic	Orthorhombic	Orthorhombic	
Space group	P21/c	P-1	P 1 21/c 1	P 1 21/c 1	Pbca	Pbca	
Unit cell dimensions	a (Å)	10.81(2)	10.35(5)	11.0615(2)	10.9072(3)	18.5723(6)	18.4301(5)
	b (Å)	19.81(3)	12.67(6)	19.9867(4)	20.0812(4)	18.1083(5)	18.4629(6)
	c (Å)	17.39(2)	14.27(7)	17.1128(4)	16.9950(4)	22.2433(5)	22.5305(6)
	α (°)	90	92.01(4)	90	90	90	90
	β (°)	103.14(10)	104.70(4)	105.496(2)	104.079(3)	90	90
	γ (°)	g = 90	103.62(4)	90	90	90	90
Volume (Å ³)	3627.96(10)	1753.20(15)	3645.82(14)	3610.59(14)	7480.7(4)	7666.5(4)	
Z	4	2	4	4	8	8	
Absorption coefficient (mm ⁻¹)	2.997	3.126	3.016	3.045	2.950	2.888	
Crystal size (mm ³)	0.29x0.19x0.11	0.23x 0.15 x 0.05	0.24x0.11x0.04	0.26 x 0.16 x 0.06	0.25x0.13 x 0.05	0.25 x 0.17 x 0.07	
Reflections collected	30594	14193	22229	30402	27907	43112	
Independent reflections	7127 [R _(int) = 0.0607]	6686 [R _(int) = 0.0532]	7205 [R _(int) = 0.1235]	7195 [R _(int) = 0.0786]	7311 [R _(int) = 0.0675]	7540 [R _(int) = 0.0861]	
Goodness-of-fit on F ²	0.990	1.025	1.022	1.031	1.042	1.014	
Final R indices [I ≥ 2σ(I)]	R1 = 0.0396, wR2 = 0.1078	R1 = 0.0438, wR2 = 0.0936	R1 = 0.0637, wR2 = 0.1440	R1 = 0.0586, wR2 = 0.1364	R1 = 0.0479, wR2 = 0.1271	R1 = 0.0370, wR2 = 0.0819	
R indices (all data)	R1 = 0.0511, wR2 = 0.1164	R1 = 0.0659, wR2 = 0.1043	R1 = 0.1145, wR2 = 0.1732	R1 = 0.0814, wR2 = 0.1511	R1 = 0.0655, wR2 = 0.1379	R1 = 0.0555, wR2 = 0.0897	

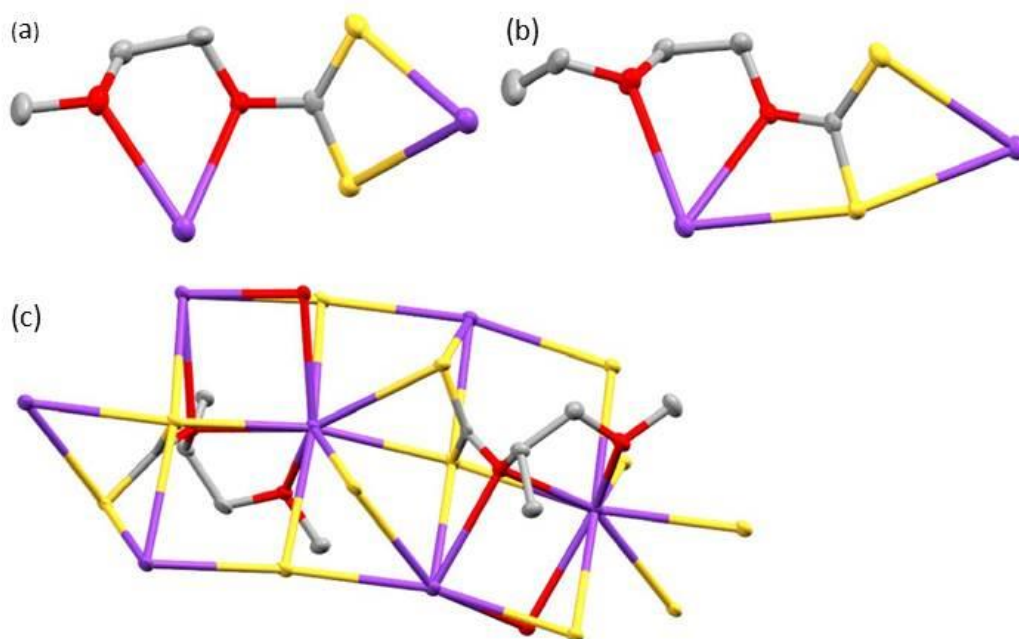


Figure A1. Structure of (a) potassium 2-methoxyethylxanthate (**3**), (b) potassium 2-ethoxyethylxanthate (**4**) and (c) potassium 1-methoxy-2-propylxanthate (**5**). Purple = K, yellow = S, red = O, grey = C. H omitted for clarity. Note that two K are shown here to demonstrate the two binding modes of the xanthate – the formula is KS_2COR .

Selected bond lengths for (**3**): S-K 3.169(2)-3.426(1) Å; C-S 1.670(4)-1.655(3) Å; K-O 2.815(2)- 3.169(2) Å.

Selected bond lengths for (**4**): S-K 3.317(1)-3.447(1) Å; C-S 1.672(3)-1.689(4) Å; K-O 2.934(3)- 3.196(3) Å.

Selected bond lengths for (**5**): S-K 3.315(2)-3.352(1) Å; C-S 1.673(5)-1.701(5) Å; K-O 2.892(3)- 3.315(2) Å.

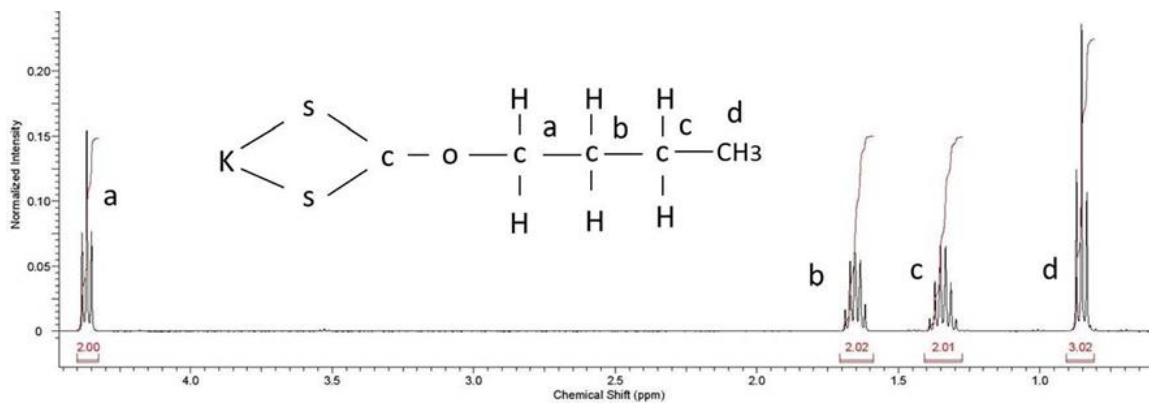


Figure A2. ^1H NMR spectrum of $[\text{K}(\text{S}_2\text{CO}^n\text{Bu})]$ (1).

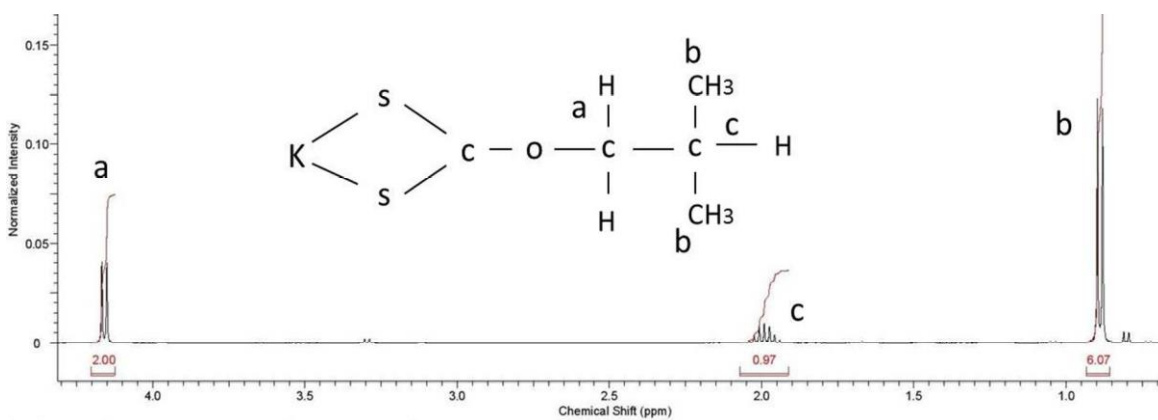


Figure A3. ^1H NMR spectrum of $[\text{K}(\text{S}_2\text{CO}^i\text{Bu})]$ (2).

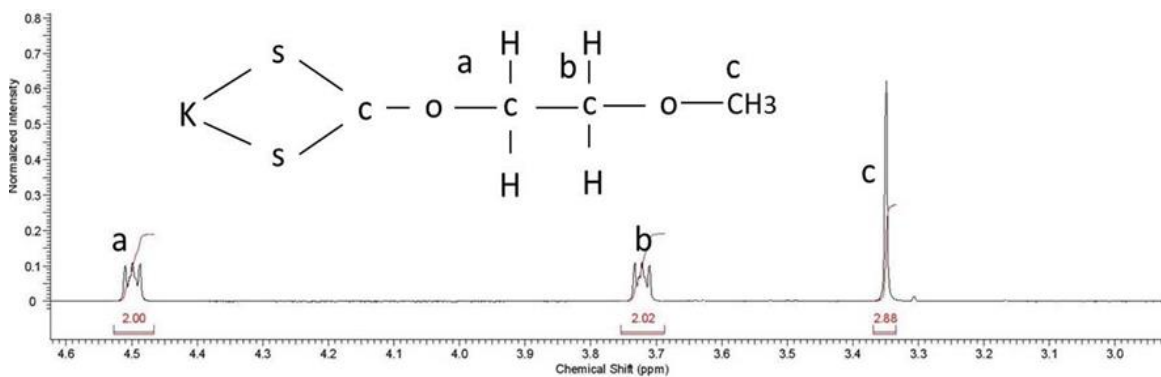


Figure A4. ^1H NMR spectrum of $[\text{KS}_2\text{CO}(\text{CH}_2)_2\text{OMe}]$ (3).

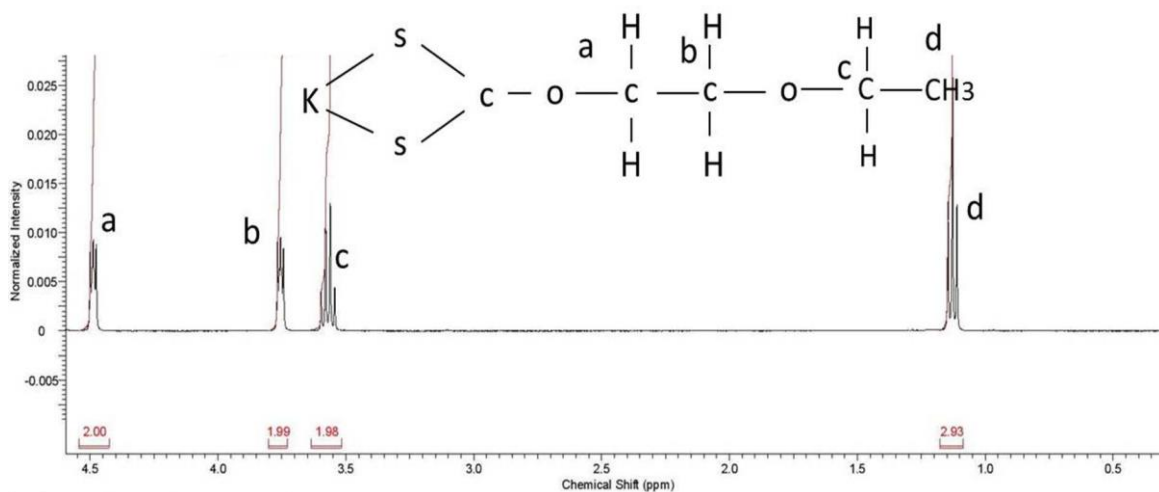


Figure A5. ^1H NMR spectrum of $[\text{K}(\text{S}_2\text{CO}(\text{CH}_2)_2\text{OEt})]$ (**4**).

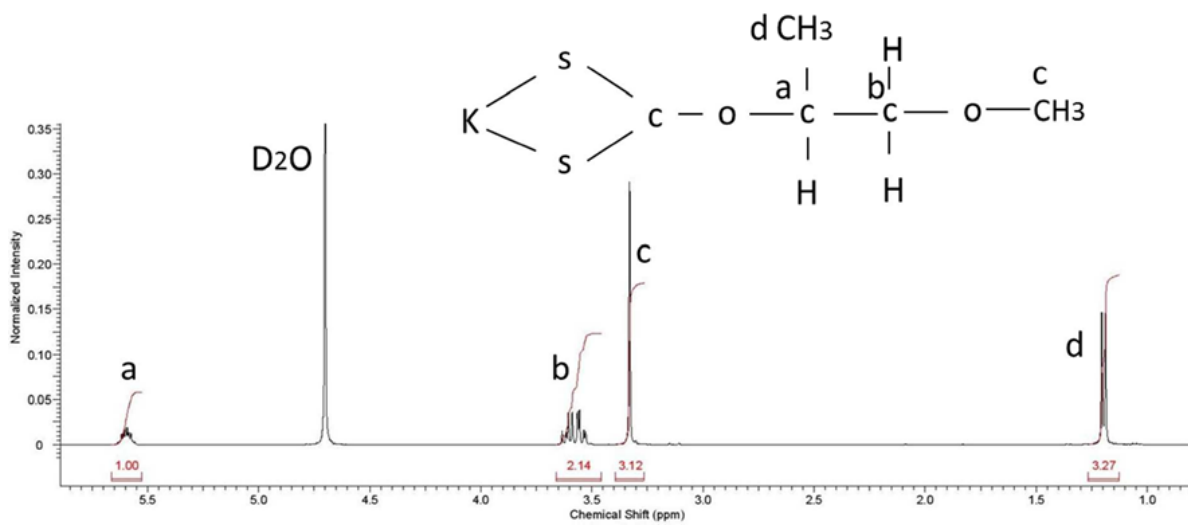


Figure A6. ^1H NMR spectrum of $[\text{K}(\text{S}_2\text{COC}(\text{H})(\text{Me})\text{CH}_2\text{OMe})]$ (**5**).

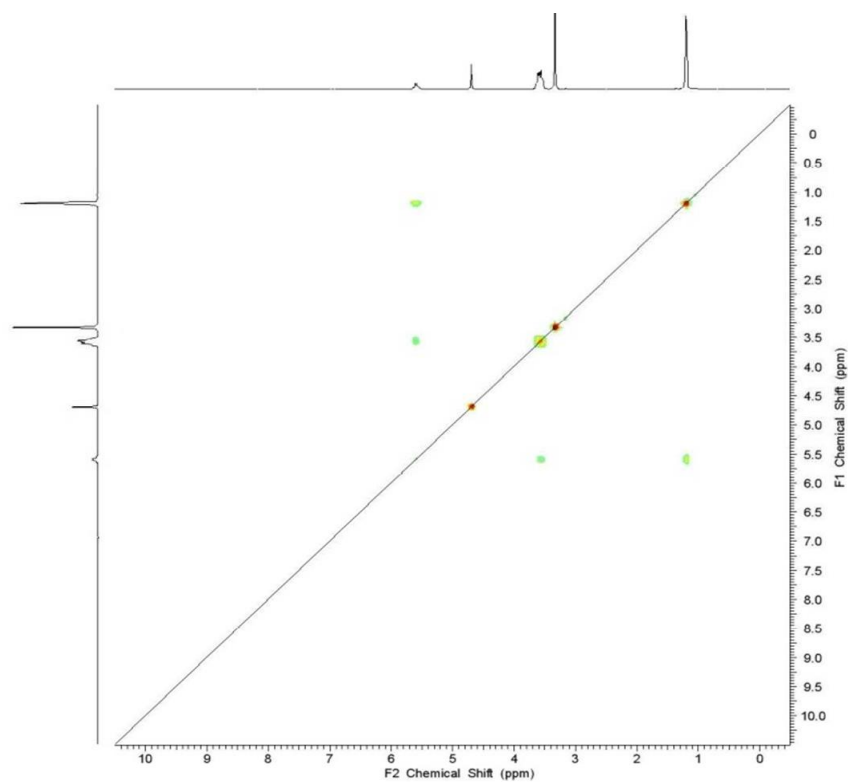


Figure A7. COSY spectrum of $[\text{K}(\text{S}_2\text{COC}(\text{H})(\text{Me})\text{CH}_2\text{OMe})]$ (**5**).

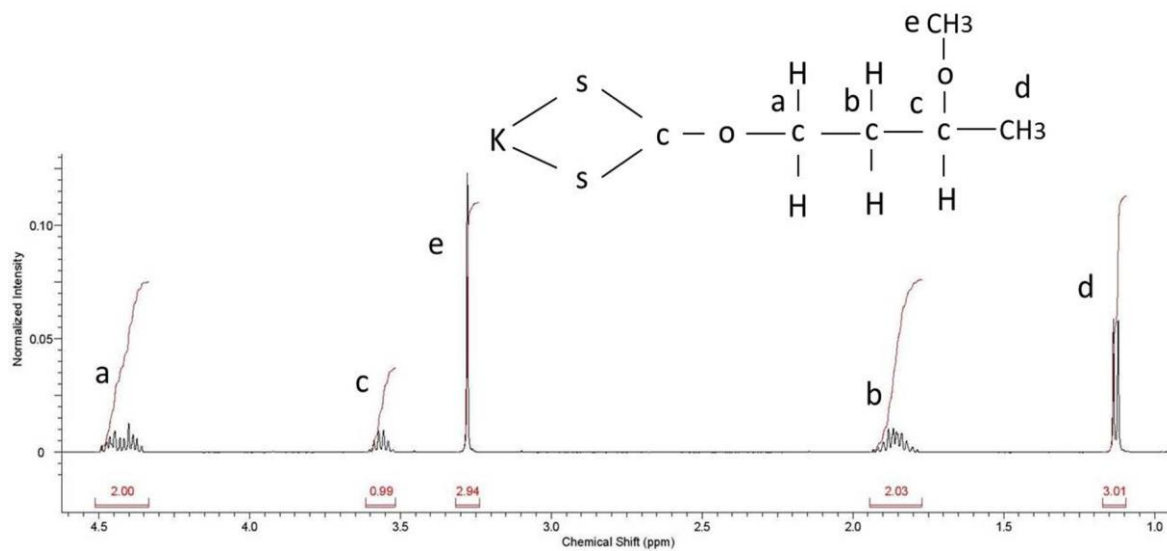


Figure A8. ^1H NMR spectrum of $[\text{K}(\text{S}_2\text{CO}(\text{CH}_2)_2\text{C}(\text{H})(\text{OMe})\text{Me})]$ (**6**).

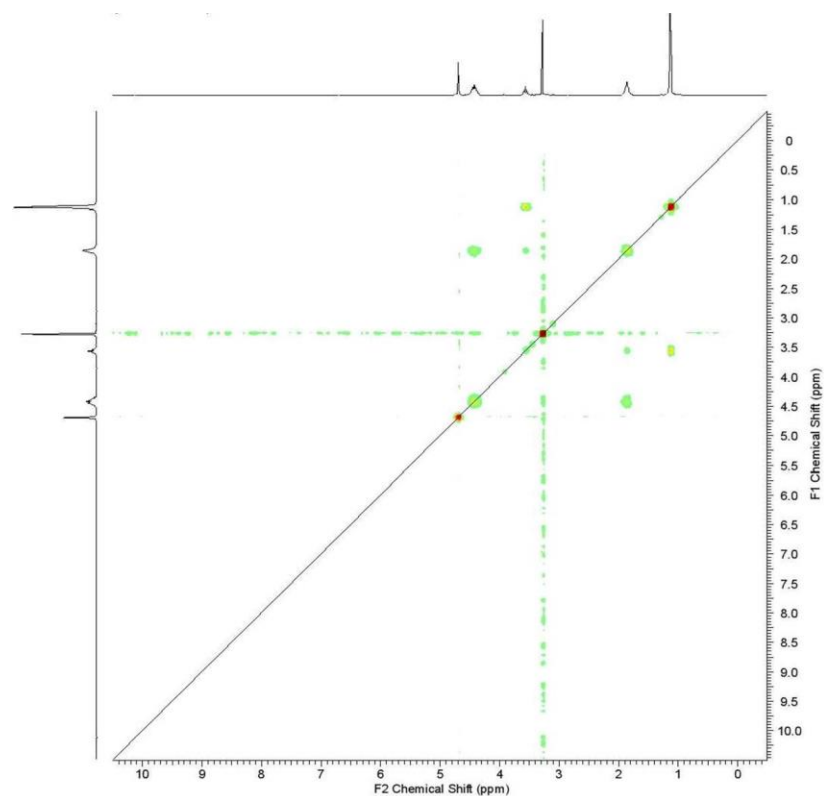


Figure A9. COSY spectrum of $[\text{K}(\text{S}_2\text{CO}(\text{CH}_2)_2\text{C}(\text{H})(\text{OMe})\text{Me})]$ (**6**).

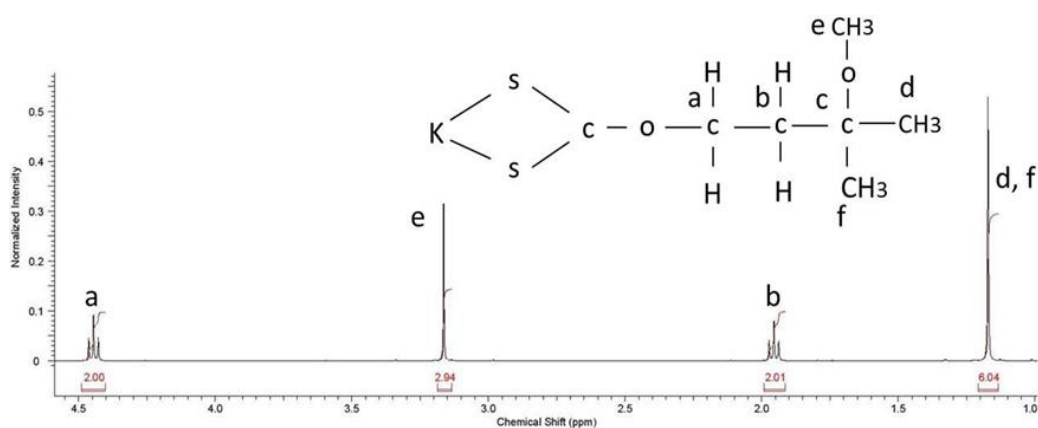


Figure A10. ^1H NMR spectrum of $[\text{K}(\text{S}_2\text{CO}(\text{CH}_2)_2\text{C}(\text{OMe})(\text{Me})_2)]$ (**7**).

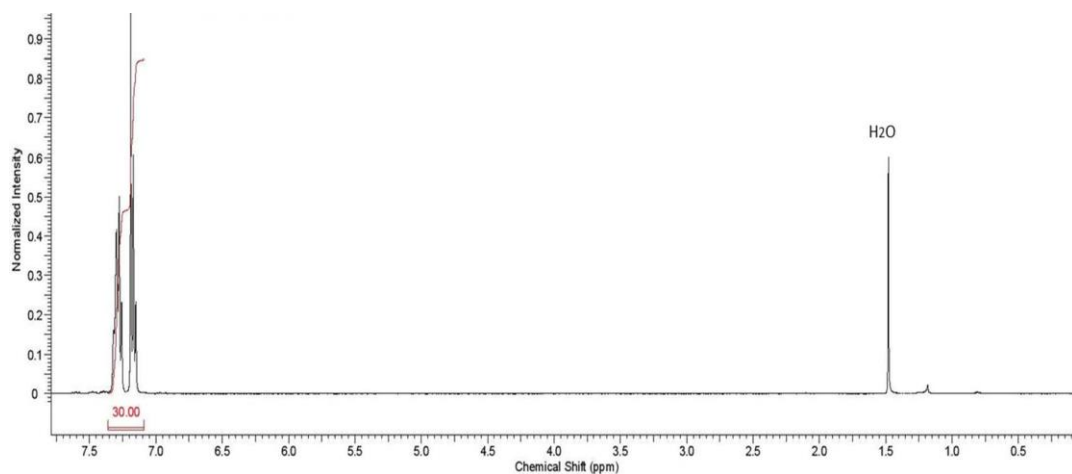


Figure A11. ^1H NMR spectrum of $[(\text{Ph}_3\text{P})_2\text{CuCl}]_2 \cdot 2\text{CHCl}_3$ (**8**).

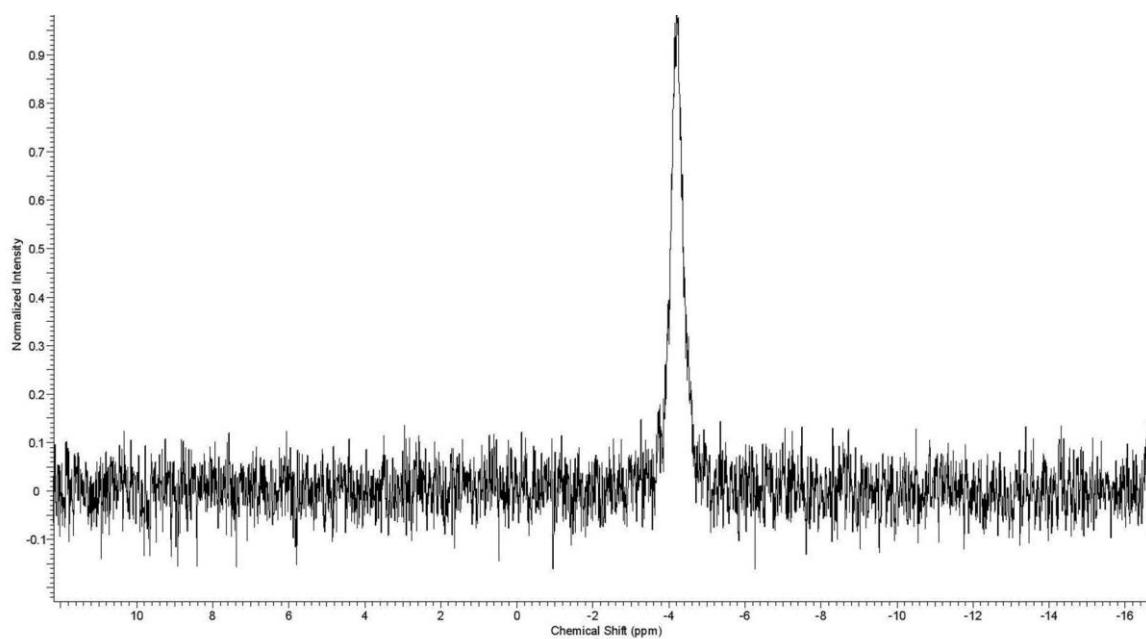


Figure A12. ^{31}P NMR spectrum of $[(\text{Ph}_3\text{P})_2\text{CuCl}]_2 \cdot 2\text{CHCl}_3$ (**8**).

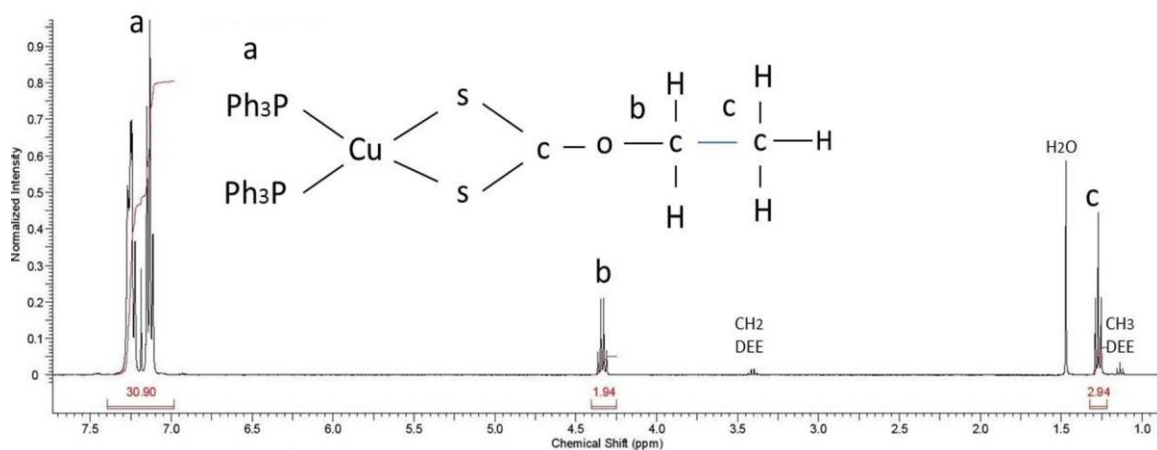


Figure A13. ^1H NMR spectrum of $[(\text{Ph}_3\text{P})_2\text{Cu}(\text{S}_2\text{COEt})]$ (**9**) (DEE = diethyl ether).

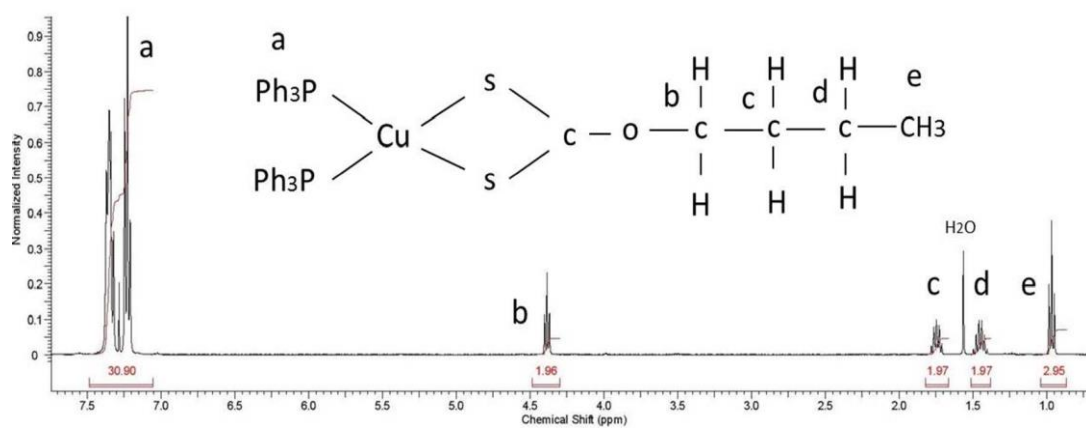


Figure A14. ^1H NMR spectrum of $[(\text{Ph}_3\text{P})_2\text{Cu}(\text{S}_2\text{COBu})]$ (**10**).

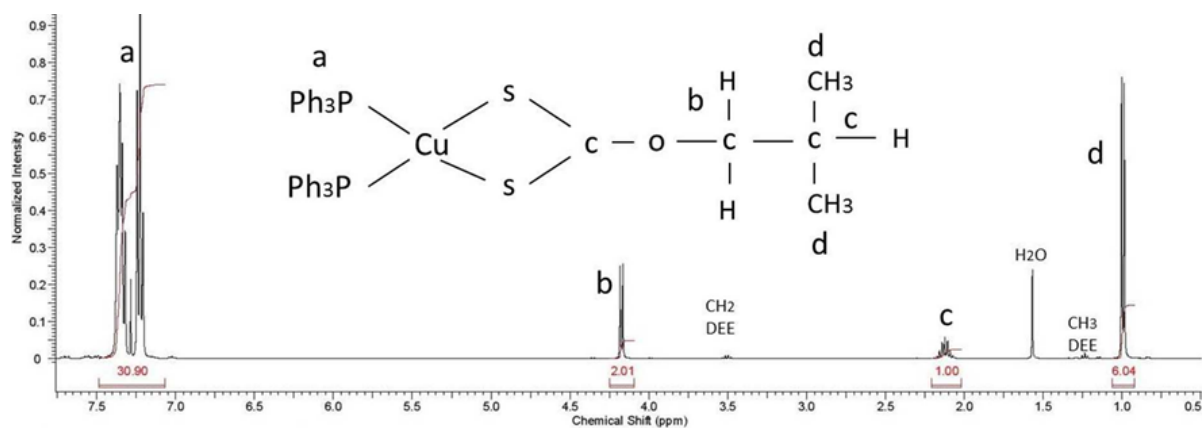


Figure A15. ^1H NMR spectrum of $[(\text{Ph}_3\text{P})_2\text{Cu}(\text{S}_2\text{CO}^i\text{Bu})]$ (**11**) (DEE = diethyl ether).

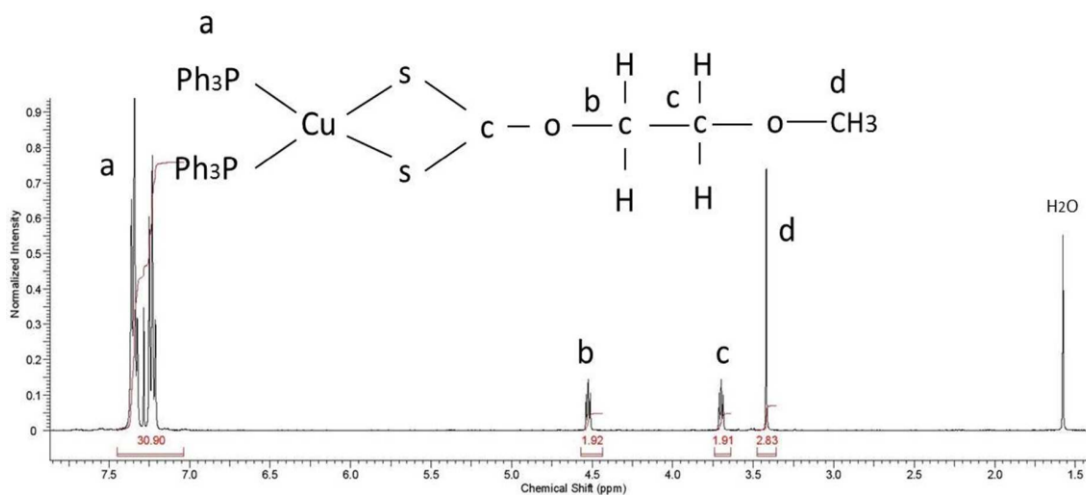


Figure A16. ^1H NMR spectrum of $[(\text{Ph}_3\text{P})_2\text{Cu}(\text{S}_2\text{CO}(\text{CH}_2)_2\text{OMe})]$ (**12**).

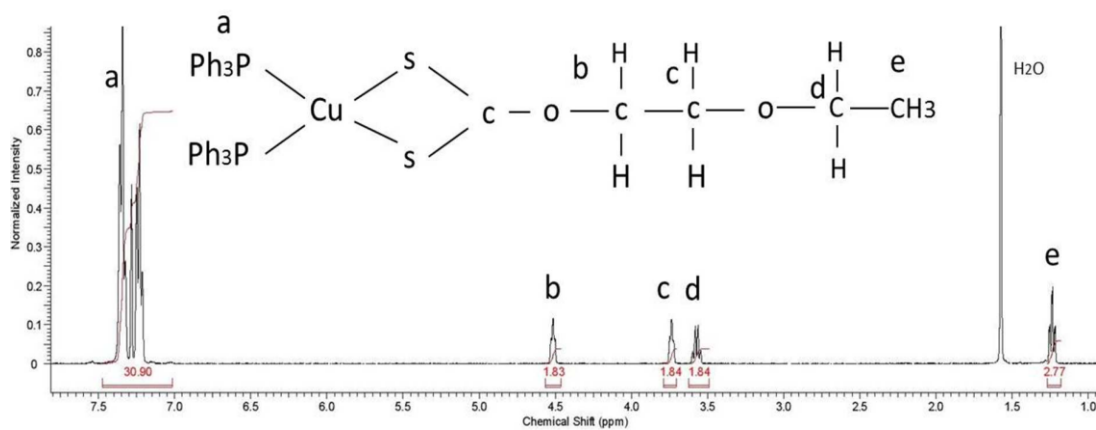


Figure A17. ^1H NMR spectrum of $[(\text{Ph}_3\text{P})_2\text{Cu}(\text{S}_2\text{CO}(\text{CH}_2)_2\text{OEt})]$ (**13**).

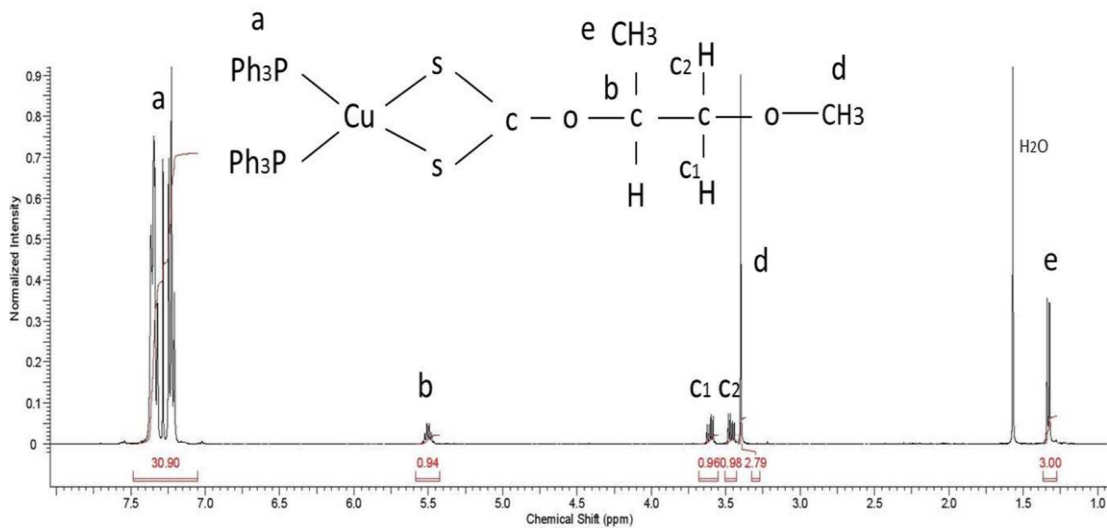


Figure A18. ^1H NMR spectrum of $[(\text{Ph}_3\text{P})_2\text{Cu}(\text{S}_2\text{COC}(\text{H})(\text{Me})\text{CH}_2\text{OMe})]$ (**14**).

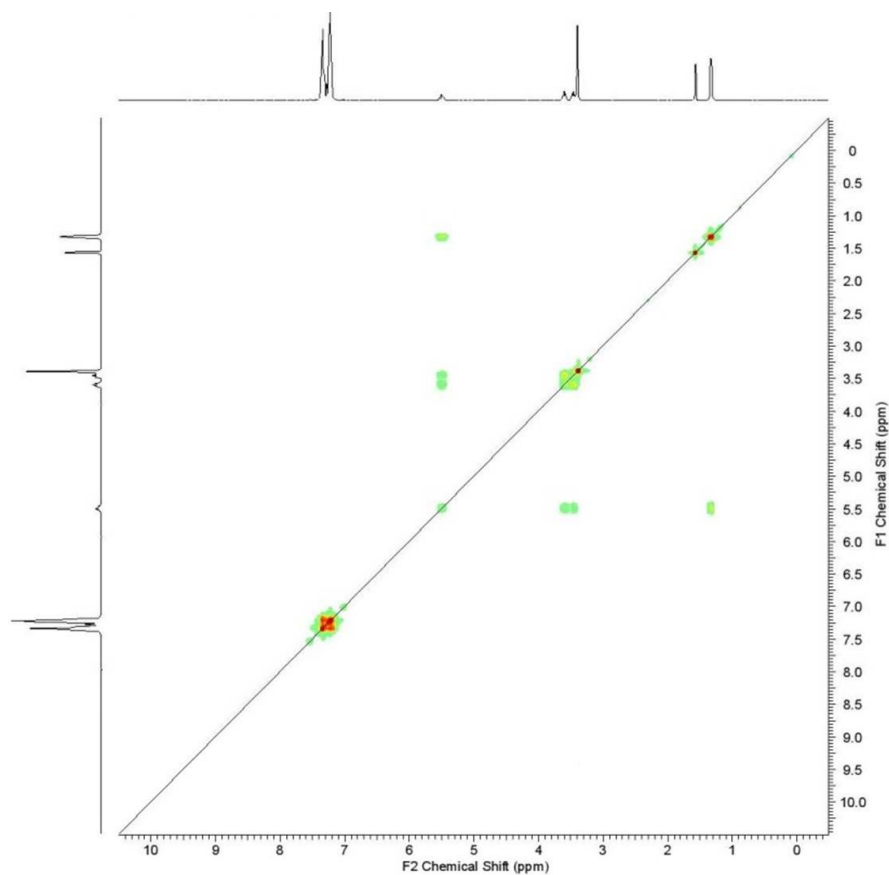


Figure A19. COSY spectrum of $[(\text{Ph}_3\text{P})_2\text{Cu}(\text{S}_2\text{COC}(\text{H})(\text{Me})\text{CH}_2\text{OMe})]$ (**14**).

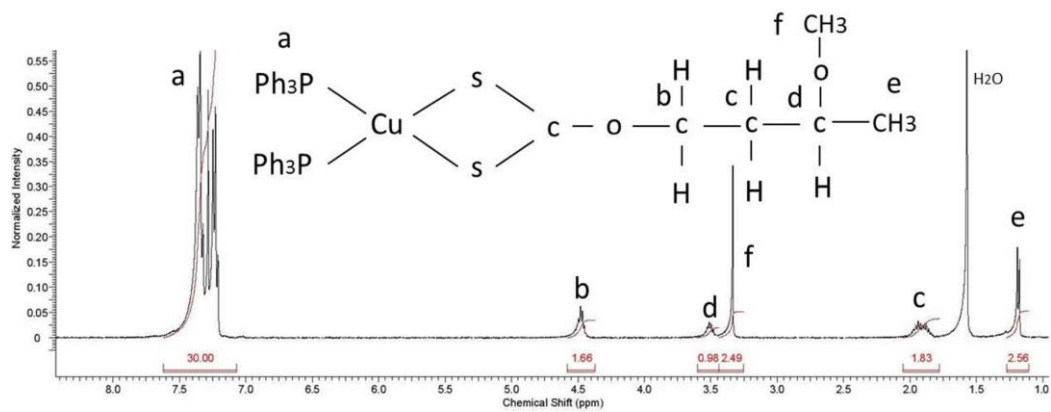


Figure A20. ^1H NMR spectrum of $[(\text{Ph}_3\text{P})_2\text{Cu}(\text{S}_2\text{CO}(\text{CH}_2)_2\text{C}(\text{H})(\text{OMe})\text{Me})]$ (**15**).

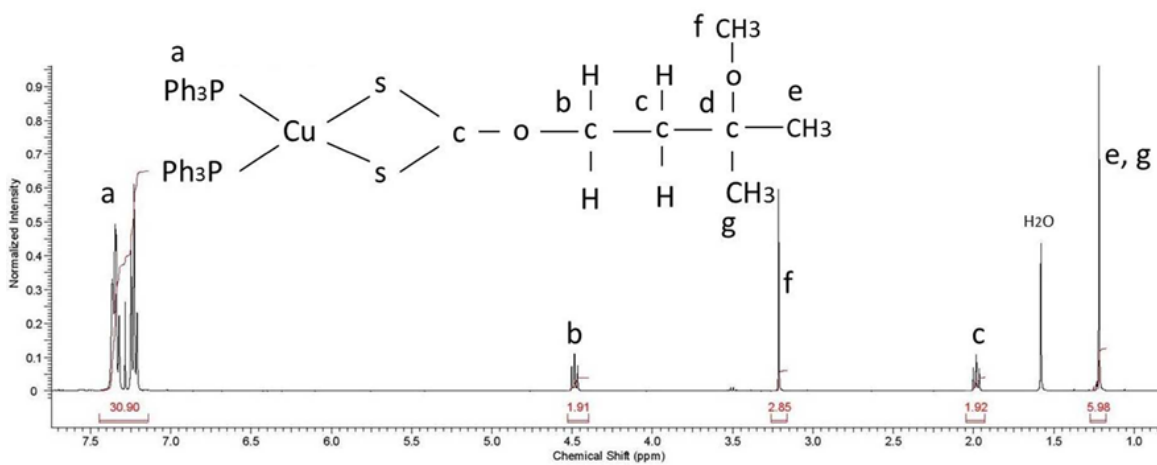


Figure A21. ^1H NMR spectrum of $[(\text{Ph}_3\text{P})_2\text{Cu}(\text{S}_2\text{CO}(\text{CH}_2)_2\text{C}(\text{OMe})(\text{Me})_2)]$ (**16**).

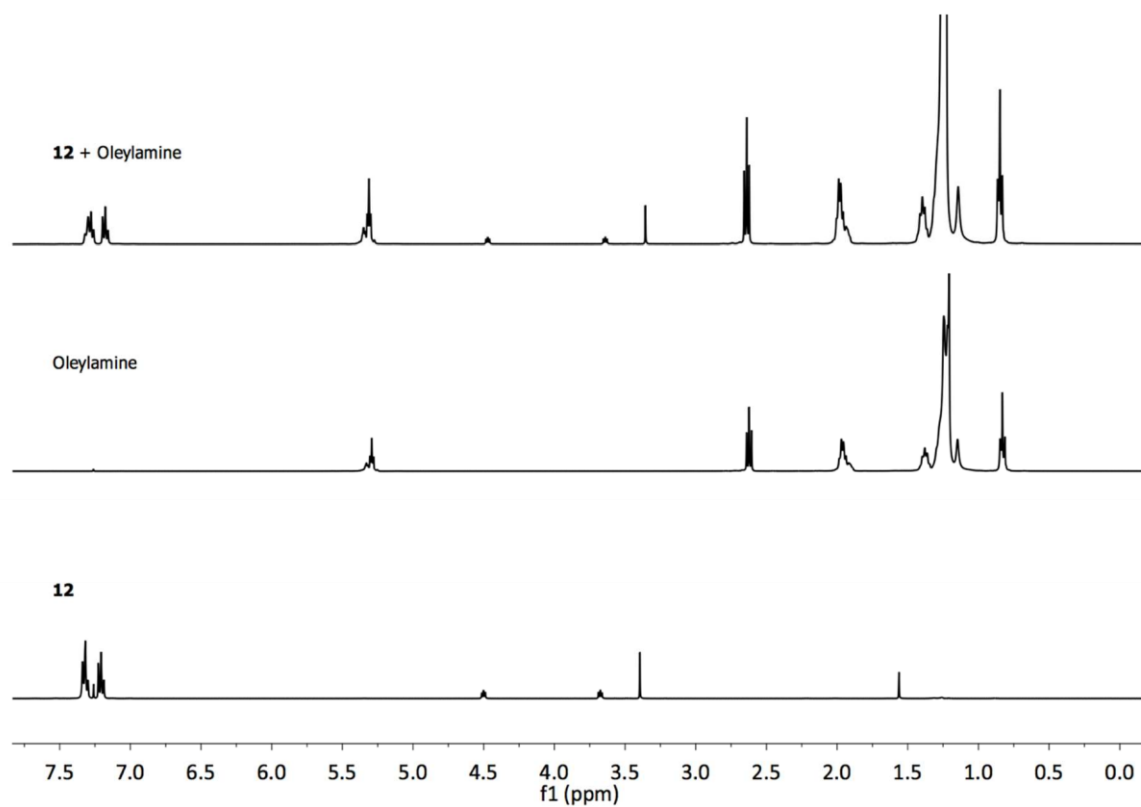


Figure A22. ^1H NMR spectra of complex **12** (triphenylphosphine copper(I) 2-methoxyethyl xanthate), oleylamine and a mixture of oleylamine and **12**, shows that the mixture is simply the sum of the two individual spectra and that no ligand exchange is observed.

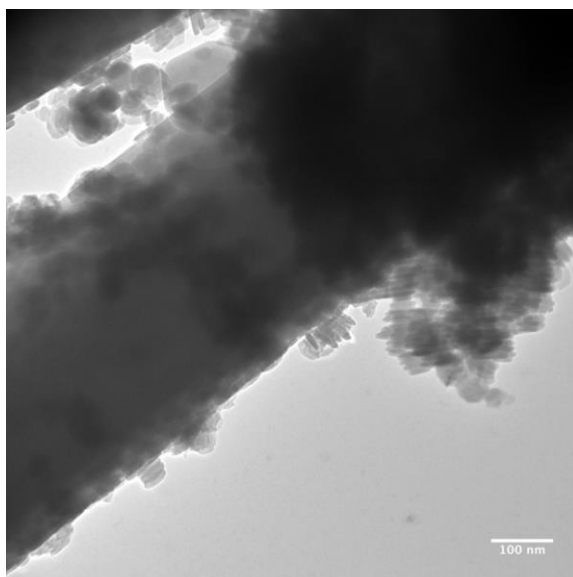


Figure A23. TEM image of the material produced from the thermal decomposition of triphenylphosphine copper(I) ethylxanthate (**9**) during a 1 h reaction.

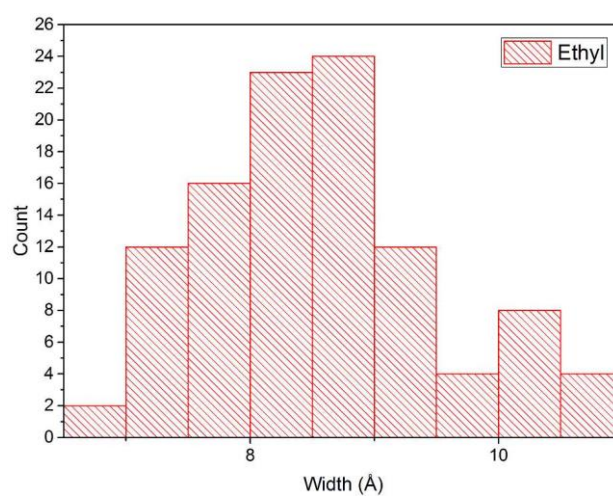


Figure A24. Size distribution of nanorods produced from the decomposition of triphenylphosphine copper(I) ethylxanthate (**9**).

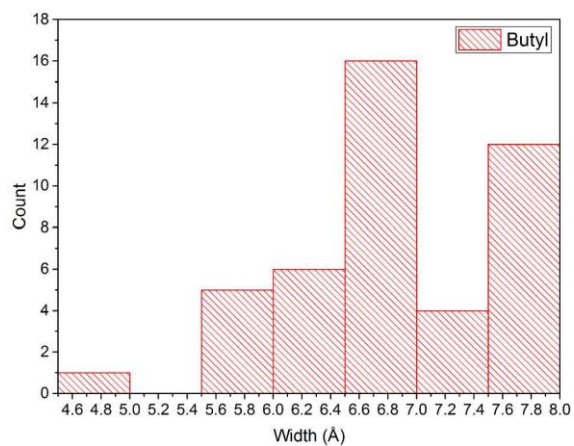


Figure A25. Size distribution of nanorods produced from the decomposition of triphenylphosphine copper(I) *n*-butylxanthate (**10**).

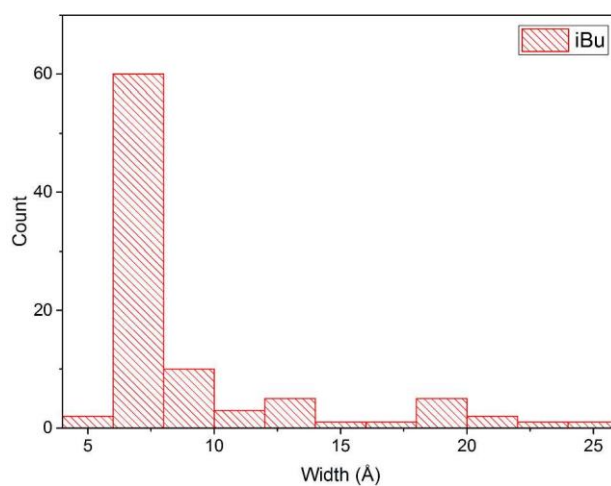


Figure A26. Size distribution of nanorods produced from the decomposition of triphenylphosphine copper(I) *iso*-butylxanthate (**11**).

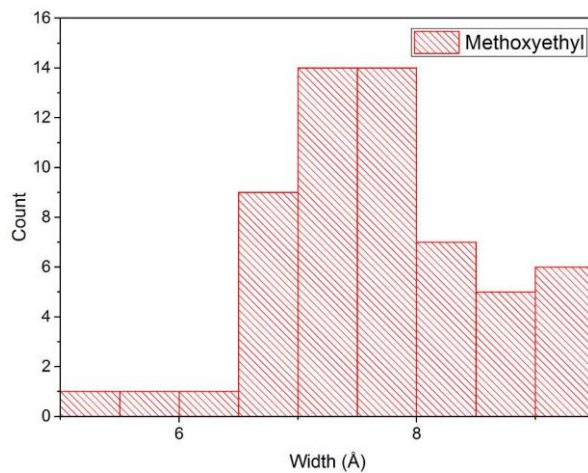


Figure A27. Size distribution of nanorods produced from the decomposition of triphenylphosphine copper(I) 2-methoxyethylxanthate (**12**).

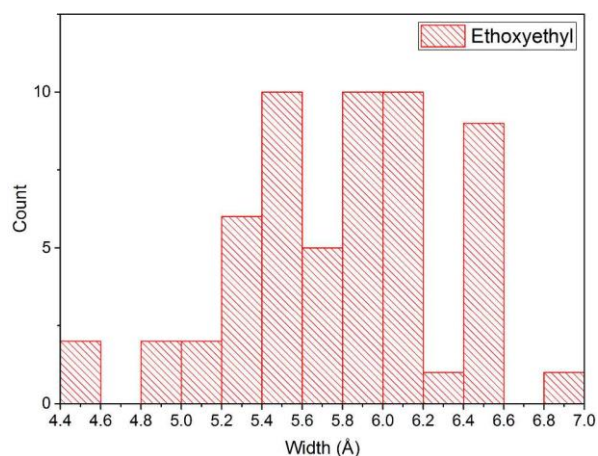


Figure A28. Size distribution of nanorods produced from the decomposition of triphenylphosphine copper(I) 2-ethoxyethylxanthate (**13**).

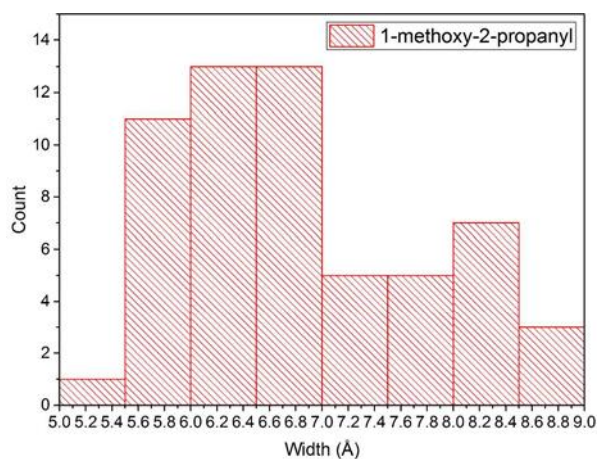


Figure A29. Size distribution of nanorods produced from the decomposition of triphenylphosphine copper(I) 1-methoxy-2-propylxanthate (**14**).

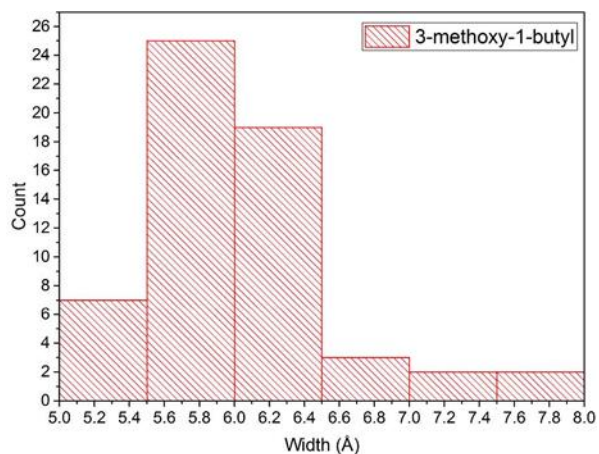


Figure A30. Size distribution of nanorods produced from the decomposition of triphenylphosphine copper(I) 3-methoxy-1-butylxanthate (**15**).

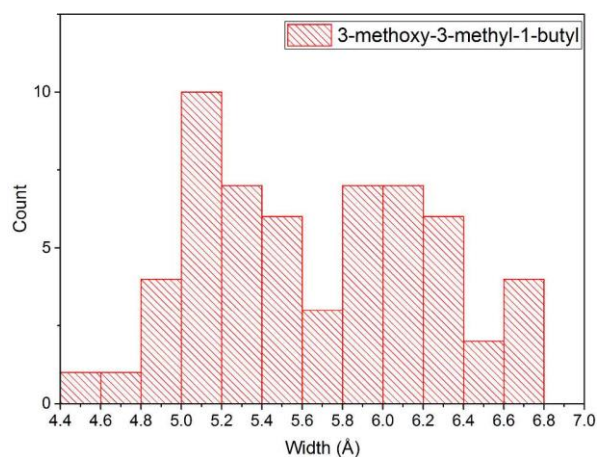


Figure A31. Size distribution of nanorods produced from the decomposition of triphenylphosphine copper(I) 3-methoxy-3-methyl-1-butylxanthate (**16**).

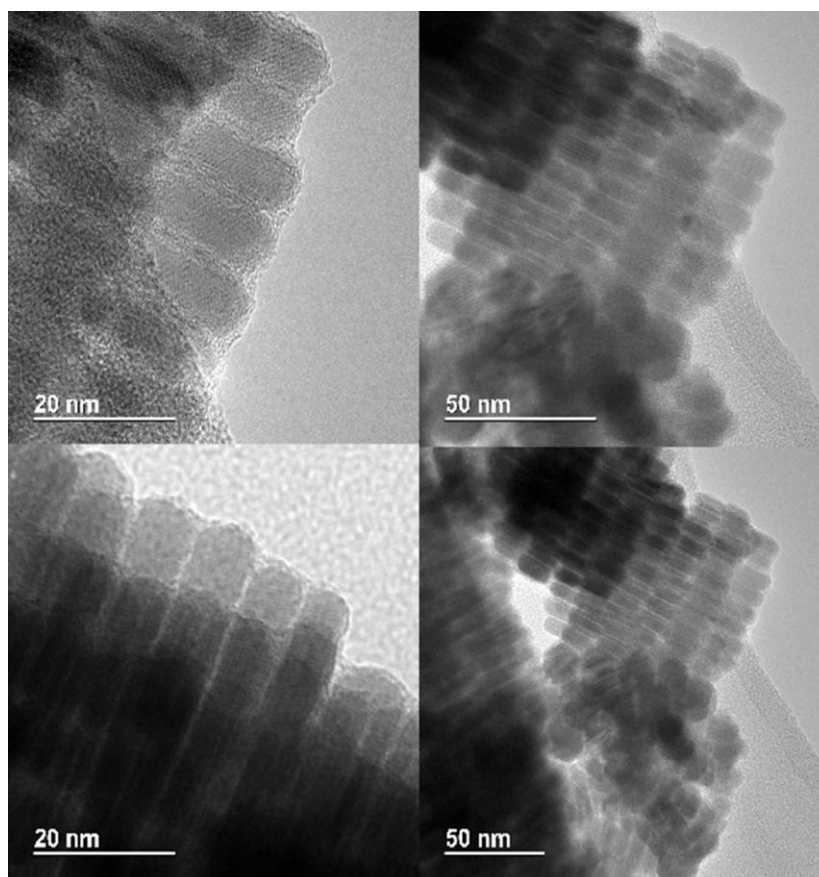


Figure A32. TEM images of nanorods produced from the decomposition of triphenylphosphine copper(I) ethylxanthate (**9**) during a 5 s reaction.

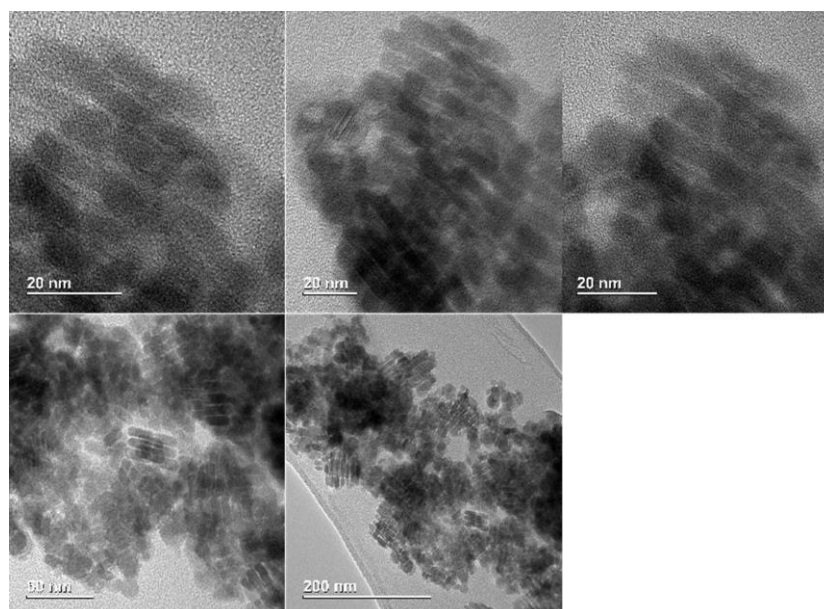


Figure A33. TEM images of nanorods produced from the decomposition of triphenylphosphine copper(I) butylxanthate (**10**) during a 5 s reaction.

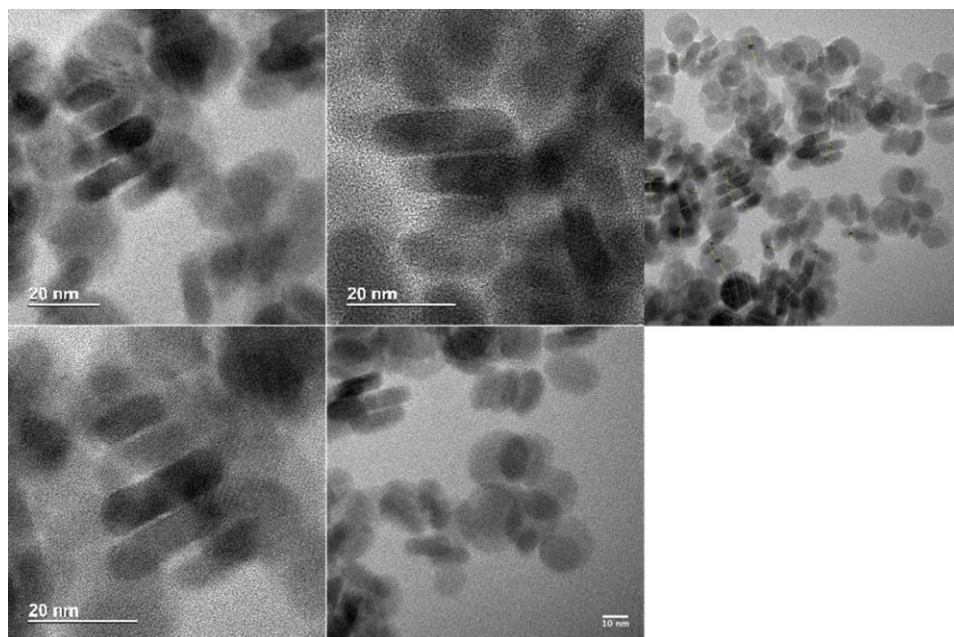


Figure A34. TEM images of nanorods produced from the decomposition of triphenylphosphine copper(I) *iso*-butylxanthate (**11**) during a 5 s reaction.

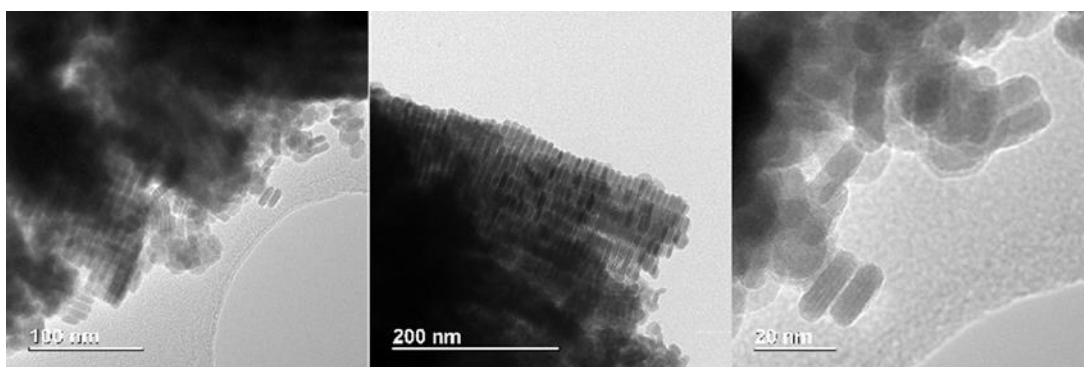


Figure A35. TEM images of nanorods produced from the decomposition of triphenylphosphine copper(I) 2-methoxyethylxanthate (**12**) during a 5 s reaction.

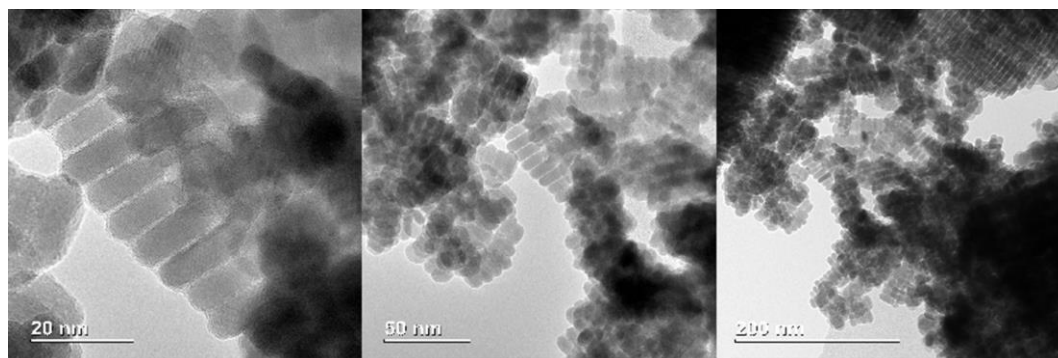


Figure A36. TEM images of nanorods produced from the decomposition of triphenylphosphine copper(I) 2-ethoxyethylxanthate (**13**) during a 5 s reaction.

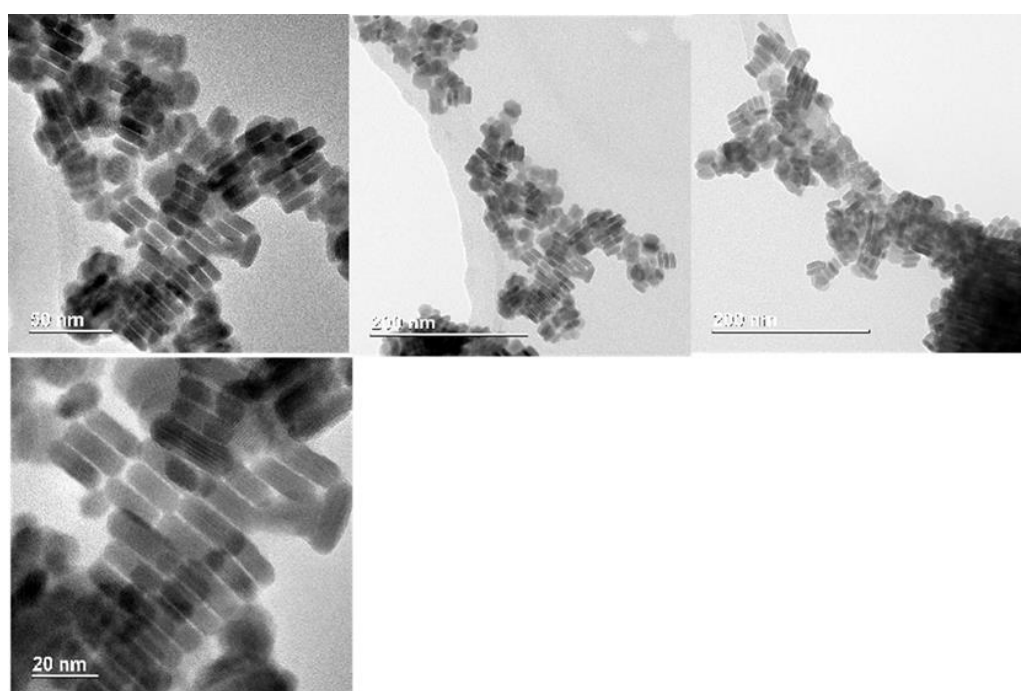


Figure A37. TEM images of nanorods produced from the decomposition of triphenylphosphine copper(I) 1-methoxy-2-propylxanthate (**14**) during a 5 s reaction

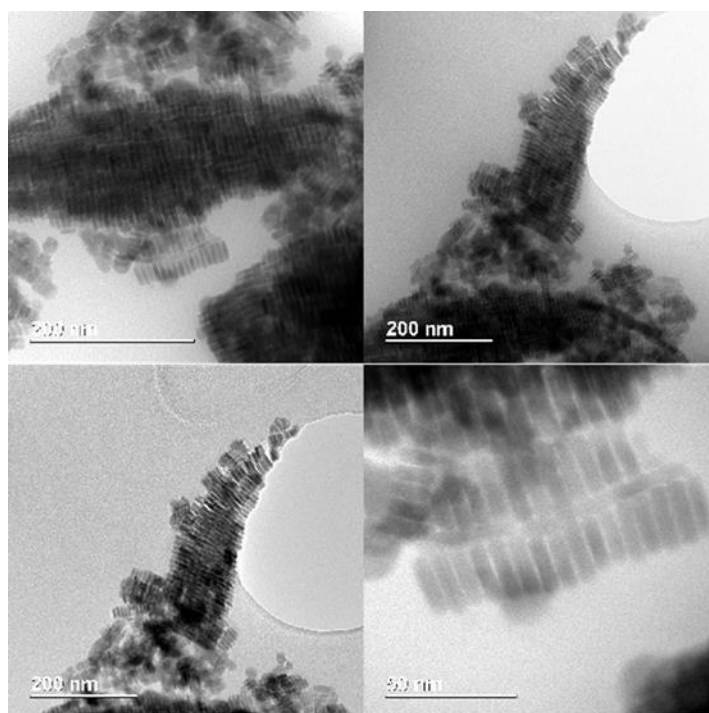


Figure A38. TEM images of nanorods produced from the decomposition of triphenylphosphine copper(I) 3-methoxy-1-butylxanthate (**15**) during a 5 s reaction.

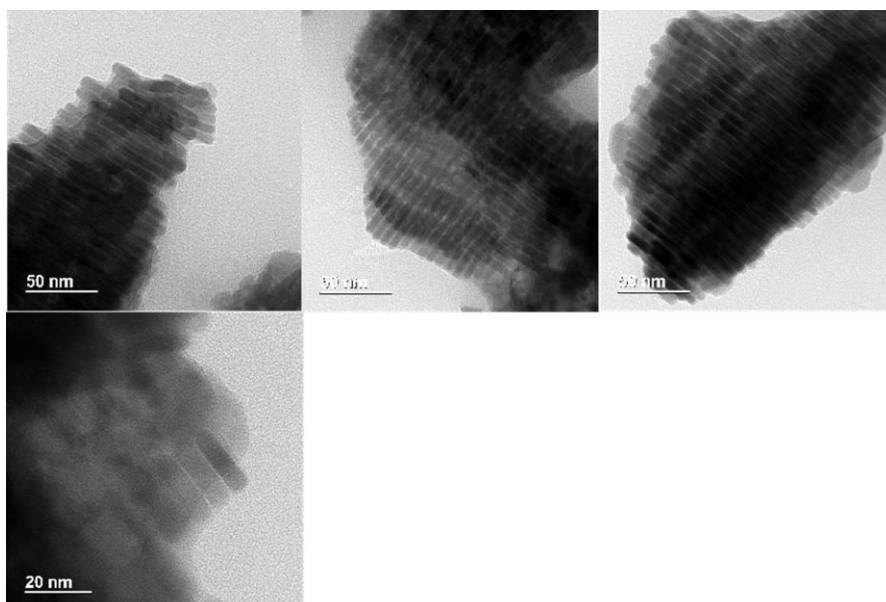


Figure A39. TEM images of nanorods produced from the decomposition of triphenylphosphine copper(I) 3-methoxy-3-methyl-1-butylxanthate (**16**) during a 5 s reaction

Table A3. Crystallographic data for [K(S₂CO(CH₂)₂C(OMe)(Me)₂)].

Chemical formula	[K(S ₂ CO(CH ₂) ₂ C(OMe)(Me) ₂)]	
Empirical formula	C ₇ H ₁₃ KO ₂ S ₂	
Formula weight	232.39	
Temperature(K)	149.9(3)	
Crystal system	monoclinic	
Space group	Cc	
Unit cell dimension	a(Å)	8.6583(2)
	b(Å)	18.7658(4)
	c(Å)	6.6572(2)
	α(°)	90
	β(°)	95.538(2)
	γ(°)	90
Volume (Å ³)	1076.61(5)	
Z	4	
ρ _{calc} (g/cm ³)	1.434	
Absorption coefficient (mm ⁻¹)	0.842	
F(000)	488.0	
Crystal size (mm ³)	0.421 × 0.072 × 0.01	
Radiation	MoKα (λ = 0.71073)	
Reflections collected	9921	
Independent reflections	2184 [R _{int} = 0.0267, R _{sigma} = 0.0216]	
Goodness-of-fit on F ²	1.158	
Final R indexes [I >= 2σ (I)]	R ₁ = 0.0548, wR ₂ = 0.1416	
Final R indexes [all data]	R ₁ = 0.0551, wR ₂ = 0.1419	

Table A4. Crystallographic data for [In(S₂COⁿPr)₃] (**8**), [In(S₂COⁱPr)₃] (**9**), [In(S₂CO^tBu)₃] (**10**), [In(S₂CO(CH₂)₂OEt)₃] (**11**), [In(S₂CO(CH₂)₂OMe)₃] (**12**), [In(S₂CO(CH₂)₂C(OMe)(Me)₂)₃] (**13**), [In(S₂COC(H)(Me)CH₂OMe)₃] (**14**).

Chemical formula	[In(S ₂ CO ⁿ Pr) ₃] (8)	[In(S ₂ CO ⁱ Pr) ₃] (9)	[In(S ₂ CO ^t Bu) ₃] (10)	[In(S ₂ CO(CH ₂) ₂ OEt) ₃] (11)	[In(S ₂ CO(CH ₂) ₂ OMe) ₃] (12)	[In(S ₂ CO(CH ₂) ₂ C(OMe)(Me) ₂) ₃] (13)	[In(S ₂ COC(H)(Me)CH ₂ OMe) ₃] (14)
Empirical formula	C ₁₂ H ₂₁ InO ₃ S ₆	C ₁₂ H ₂₁ InO ₃ S ₆	C ₁₅ H ₂₇ InO ₃ S ₆	C ₁₅ H ₂₇ InO ₆ S ₆	C ₁₂ H ₂₁ InO ₆ S ₆	C ₂₁ H ₃₉ InO ₆ S ₆	C ₁₅ H ₂₇ InO ₆ S ₆
Formula weight	520.47	520.47	562.54	610.54	568.47	694.70	610.55
Temperature(K)	100.00(10)	293.15	100(2)	150.01(10)	100(2)	180(2)	150
Crystal system	monoclinic	monoclinic	orthorhombic	monoclinic	monoclinic	monoclinic	trigonal
Space group	P2 ₁ /c	P2 ₁	Pbca	C2/c	P2 ₁ /n	P2 ₁ /n	R-3
Unit cell dimension	a(Å)	12.6914(11)	10.3260(2)	19.7328(5)	18.6588(10)	12.2235(4)	12.5836(3)
	b(Å)	16.4263(9)	11.0670(2)	9.9324(3)	11.3293(5)	11.1426(4)	22.3627(6)
	c(Å)	10.4553(8)	18.9109(4)	23.6448(6)	26.0649(11)	15.9305(5)	22.8132(6)
	α (°)	90	90	90	90	90	90
	β (°)	113.465(10)	90.621(2)	90	114.445(6)	92.748(2)	101.127(2)
	γ (°)	90	90	90	90	90	90
Volume (Å ³)	1999.4(3)	2160.97(7)	4634.2(2)	5016.0(5)	2167.26(13)	6299.0(3)	3669.3(2)
Z	4	4	8	8	4	8	5.99994
ρ _{calc} (g/cm ³)	1.729	1.600	1.613	1.617	1.742	1.465	1.658
Absorption coefficient (mm ⁻¹)	1.815	1.679	13.309	1.468	14.347	9.977	1.505
F(000)	1048.0	1048.0	2288.0	2480.0	1144.0	2864.0	1860.0
Crystal size (mm ³)	0.323 × 0.22 × 0.025	0.2 × 0.1 × 0.08	0.210 × 0.120 × 0.060	0.5 × 0.3 × 0.08	0.220 × 0.130 × 0.040	0.260 × 0.160 × 0.080	0.25 × 0.22 × 0.1
Radiation	MoKα (λ = 0.71073)	MoKα (λ = 0.71073)	CuKα (λ = 1.54178)	MoKα (λ = 0.71073)	CuKα (λ = 1.54178)	CuKα (λ = 1.54178)	MoKα (λ = 0.71073)
Reflections collected	11553	14025	26580	10603	15315	41853	18510
Independent reflections	4029 [R _{int} = 0.0426, R _{sigma} = 0.0493]	8408 [R _{int} = 0.0588, R _{sigma} = 0.0816]	4549 [R _{int} = 0.0760, R _{sigma} = 0.0465]	5144 [R _{int} = 0.0270, R _{sigma} = 0.0458]	4231 [R _{int} = 0.0412, R _{sigma} = 0.0361]	12232 [R _{int} = 0.0932, R _{sigma} = 0.0912]	2183 [R _{int} = 0.0304, R _{sigma} = 0.0182]
Goodness-of-fit on F ²	1.056	0.997	1.039	1.057	1.015	1.017	1.127
Final R indexes [I ≥ 2σ (I)]	R ₁ = 0.0315, wR ₂ = 0.0777	R ₁ = 0.0383, wR ₂ = 0.0867	R ₁ = 0.0374, wR ₂ = 0.0861	R ₁ = 0.0394, wR ₂ = 0.0752	R ₁ = 0.0233, wR ₂ = 0.0503	R ₁ = 0.0527, wR ₂ = 0.1204	R ₁ = 0.0286, wR ₂ = 0.0647
Final R indexes [all data]	R ₁ = 0.0382, wR ₂ = 0.0802	R ₁ = 0.0480, wR ₂ = 0.0915	R ₁ = 0.0478, wR ₂ = 0.0911	R ₁ = 0.0526, wR ₂ = 0.0806	R ₁ = 0.0294, wR ₂ = 0.0520	R ₁ = 0.0875, wR ₂ = 0.1392	R ₁ = 0.0340, wR ₂ = 0.0661

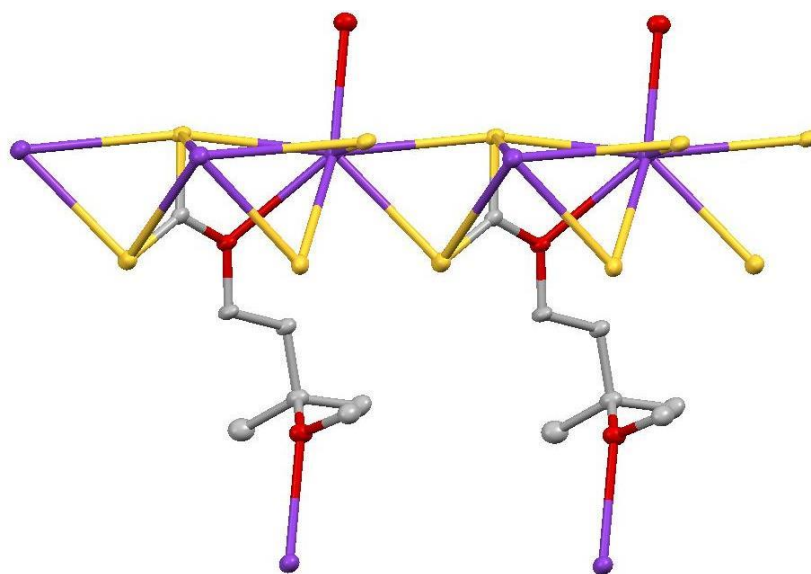


Figure A40. Structure of potassium 3-methoxy-3-methyl-1-butanol. Purple = K, yellow = S, red = O, grey = C. H omitted for clarity. Note that two K are shown here to demonstrate the two binding modes of the xanthate – the formula is KS_2COR .

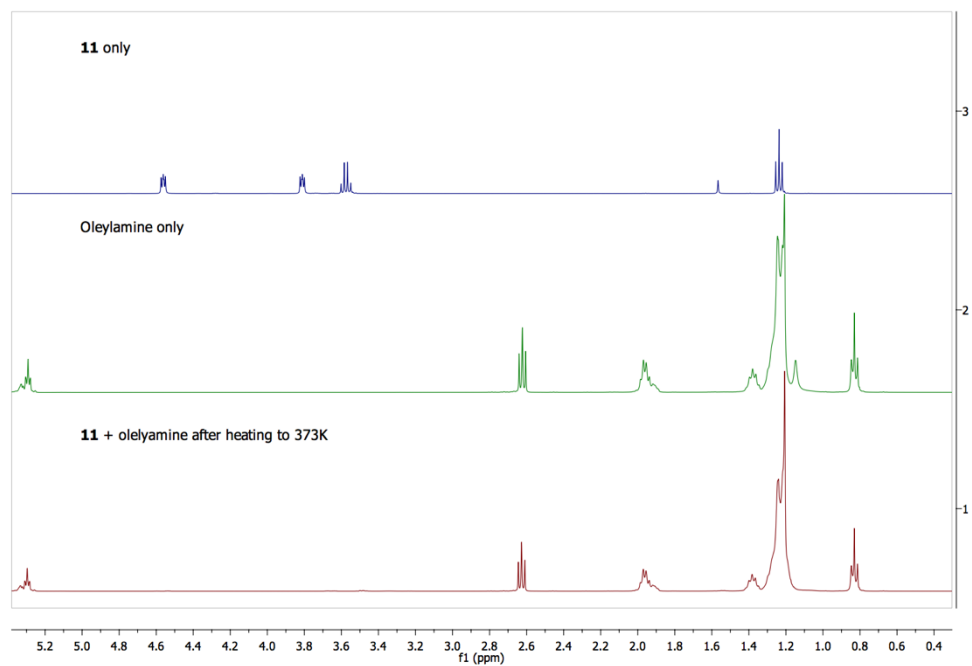


Figure A41. ^1H NMR spectra of **11**, oleylamine only and **11** + oleylamine after heating to 373 K.

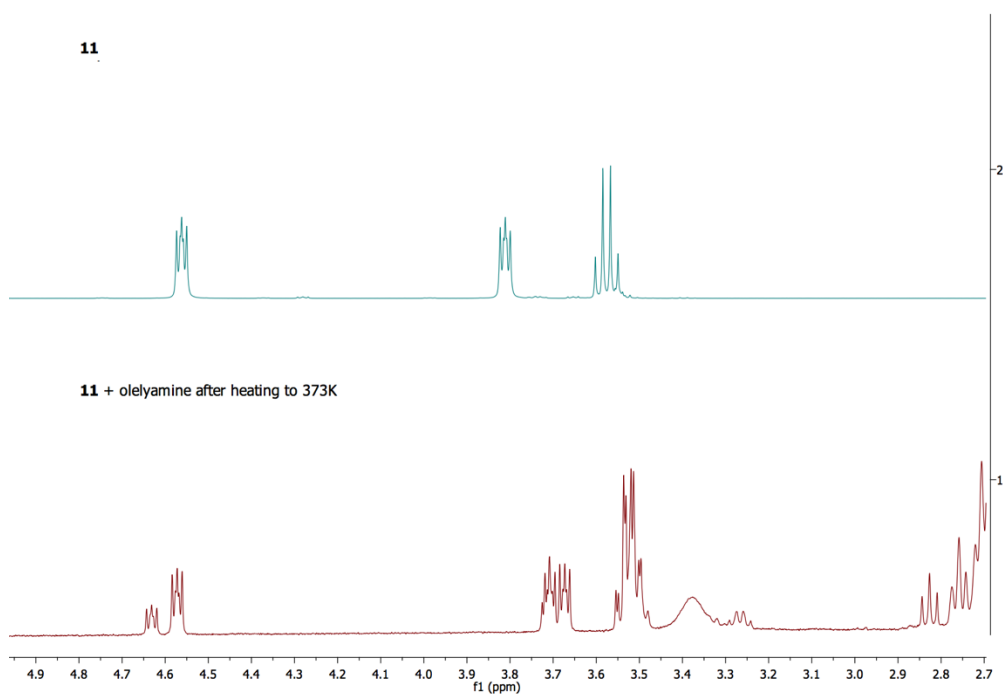


Figure A42. Expansion of the ^1H NMR spectra of **11** and **11** + oleylamine after heating to 373 K.

Table A5. Electrical measurements for the WZ-CZTS sample prepared at 225 °C.

Resistivity measurement (I = current, V = voltage, [XY] = measurement between points X and Y):

I[21] = 0.012 mA	V[43] = 463.400 mV
I[12] = 0.012 mA	V[43] = -618.100 mV
I[32] = 0.012 mA	V[41] = 891.100 mV
I[23] = 0.013 mA	V[41] = -938.200 mV
I[43] = 0.012 mA	V[12] = 497.500 mV
I[34] = 0.012 mA	V[12] = -569.600 mV
I[14] = 0.012 mA	V[23] = 829.000 mV
I[41] = 0.012 mA	V[23] = -949.600 mV

Hall measurement without magnetic field (I = current, V = voltage, [XY] = measurement between points X and Y):

I[31] = 0.012 mA	V[42] = 341.500 mV
I[13] = 0.012 mA	V[42] = -400.400 mV
I[42] = 0.012 mA	V[13] = -412.700 mV
I[24] = 0.012 mA	V[13] = 322.300 mV

Hall measurement with applied 0.088 T magnetic field (I = current, V = voltage, [XY] = measurement between points X and Y):

I[31] = 0.012 mA	V[42] = 344.200 mV
I[13] = 0.012 mA	V[42] = -403.100 mV
I[42] = 0.012 mA	V[13] = -415.300 mV
I[24] = 0.012 mA	V[13] = 324.300 mV

Hall Voltages:

Hall Voltage 1 = 2.700 mV

Hall Voltage 2 = 2.700 mV

Hall Voltage 3 = 2.600 mV

Hall Voltage 4 = 2.000 mV

Table A6. Electrical measurements results for KS-CZTS sample prepared at 375 °C.

Resistivity measurement (I = current, V = voltage, [XY] = measurement between points X and Y):

I[21] = 1.202 mA	V[43] = 2672.400 mV
I[12] = 1.205 mA	V[43] = -2674.300 mV
I[32] = 1.201 mA	V[41] = 1817.900 mV
I[23] = 1.204 mA	V[41] = -1818.600 mV
I[43] = 1.201 mA	V[12] = 2674.400 mV
I[34] = 1.205 mA	V[12] = -2674.600 mV
I[14] = 1.201 mA	V[23] = 1818.200 mV
I[41] = 1.204 mA	V[23] = -1819.300 mV

Hall measurement without magnetic field (I = current, V = voltage, [XY] = measurement between points X and Y):

I[31] = 1.201 mA	V[42] = -859.100 mV
I[13] = 1.202 mA	V[42] = 856.400 mV
I[42] = 1.203 mA	V[13] = 853.600 mV
I[24] = 1.203 mA	V[13] = -855.000 mV

Hall measurement with applied 0.088 T magnetic field (I = current, V = voltage, [XY] = measurement between points X and Y):

I[31] = 1.202 mA	V[42] = -858.100 mV
I[13] = 1.202 mA	V[42] = 856.000 mV
I[42] = 1.203 mA	V[13] = 853.300 mV
I[24] = 1.203 mA	V[13] = -854.700 mV

Hall Voltages:

Hall Voltage 1 = 1.000 mV

Hall Voltage 2 = 0.400 mV

Hall Voltage 3 = 0.300 mV

Hall Voltage 4 = 0.300 mV

Table A7. Electrical measurements results for KS-CZTS sample prepared at 450 °C.

Resistivity measurement (I = current, V = voltage, [XY] = measurement between points X and Y):

I[21] = 0.112 mA	V[43] = 214.350 mV
I[12] = 0.112 mA	V[43] = -240.240 mV
I[32] = 0.112 mA	V[41] = 379.700 mV
I[23] = 0.112 mA	V[41] = -381.900 mV
I[43] = 0.112 mA	V[12] = 227.080 mV
I[34] = 0.112 mA	V[12] = -228.920 mV
I[14] = 0.112 mA	V[23] = 376.600 mV
I[41] = 0.112 mA	V[23] = -381.700 mV

Hall measurement without magnetic field (I = current, V = voltage, [XY] = measurement between points X and Y):

I[31] = 0.112 mA	V[42] = 151.680 mV
I[13] = 0.112 mA	V[42] = -154.050 mV
I[42] = 0.112 mA	V[13] = -153.120 mV
I[24] = 0.112 mA	V[13] = 150.250 mV

Hall measurement with applied 0.088 T magnetic field (I = current, V = voltage, [XY] = measurement between points X and Y):

I[31] = 0.112 mA	V[42] = 151.770 mV
I[13] = 0.112 mA	V[42] = -154.210 mV
I[42] = 0.112 mA	V[13] = -153.280 mV
I[24] = 0.112 mA	V[13] = 150.380 mV

Hall Voltages:

Hall Voltage 1 = 0.090 mV

Hall Voltage 2 = 0.160 mV

Hall Voltage 3 = 0.160 mV

Hall Voltage 4 = 0.130 mV